Exploring and Visualizing the Nuances of Bonding in Bimetallic di-Molybdenum and Gold Complexes

By

Michael M. Aristov

A dissertation submitted in partial fulfillment

of the requirements for the degree of

Doctor of Philosophy (Chemistry)

at the

University of Wisconsin–Madison

2022

Date of final oral examination: August 29, 2022.

The dissertation is approved by the following members of the Final Oral Committee:

John F. Berry, Professor, Chemistry

Clark R. Landis, Professor, Chemistry

Thomas C. Brunold, Professor, Chemistry

Huifang Xu, Professor, Department of Geoscience

Exploring and Visualizing the Nuances of Bonding in Bimetallic di-Molybdenum and Gold Complexes

Michael M. Aristov

Under the Supervision of Professor John F. Berry

University of Wisconsin–Madison

Abstract: The work contained within this thesis describes three, loosely related projects. Chapter 2 discusses the updated synthesis and characterization of several N-heterocycles with three N atom binding sites. These ligands were further used to stabilize dimolybdenum species, and a combination of experimental and computational methods were used to understand the nuanced bonding of the ligands and how the localization in the ligand backbone affected the dimolybdenum electronic structure. Chapter 3 focuses on using computational methods to better understand three types of bonding interactions of Au atoms as observed in crystal structures. The first subchapter discusses the anti-chelate effect observed crystallographically in $[(bipy)Au(PEt_3)]^+$, the second subchapter searches for metallophilic interactions between Au and Cu atoms $[Au^I_6(Triphos)_4(Cu^ICl_2)]^{5+}$ and $[Au^I_6(Triphos)_4(Cu^IBr_2)]^{5+}$, and the third subchapter examines crystal packing effects on aurophilic Au•••Au interactions. Chapter 4 discusses two libraries of educational 3D models made and freely distributed during the pandemic. The first of these libraries provides 3D visual aids for the purpose of teaching general chemistry, whereas the second library focuses intently on teaching symmetry and crystallography. Chapter 5 is written for a general audience with the goal of garnering a feeling familiarity with many of the instruments critical for many types of analytical chemistry.

Acknowledgments

My graduate school experience at University of Wisconsin – Madison has been some of the hardest years of my life. Between the pandemic, critical and debilitating health issues, and interpersonal drama, these years quite nearly killed me. I survived till today thanks to amazing people who worked tirelessly with me every day of my graduate school career.

I thank John Berry, whose endless patience both inside and outside the lab provided me with endless support. You gave me the encouragement I needed to not only complete my synthetic-inorganic projects but to also explore entirely unrelated hobbies and convert them into viable areas of work. I will never forget the many drinks we shared while discussing these projects, and I hope you remember to continue doing your planks.

To my undergraduate Han Geng, thank you for your enthusiasm and for your years of assistance with my PhD. Your willingness and flexibility to hop between synthesis, computations, and 3D modeling during our time working together was an invaluable delight. I wish you the best of luck and endless support in your graduate school career.

I also thank Clark Landis, who sat with me several times to give me guidance on interpersonal conflicts and grievances with the Chemistry department in general. Your endlessly level-headed and patient responses, especially when my own demeanor lacked the same degree of tact, helped to guide me to be the chemist I am today.

Thank you, Judith, for your expertise in navigating the UW Heath care system. Without your knowledge and instructions, I likely would not be able to walk.

To my previous mentors Xian Carroll and Kamran Ghiassi, the two of you set me on the path that I've followed for the last 9 years. Kamran, you took a chemically illiterate first-year

undergraduate student and gave me almost all my synthetic skillset and problem-solving abilities that I rely upon daily. Xian, you taught me critical self-preservation and time management skills, both of which were instrumental to surviving graduate school.

Alan Balch and Marilyn Olmstead, although I started out as a terrified, first-year, undergraduate student in your care, you both showed me a timeless love for the ever-evolving field of chemistry. Your stories, techniques, and naming conventions live on forever in me, and I strive to give the same care and excitement to my mentees that you gave to me.

Briana, my beautiful wife, your endless care and love brightened everyday of my time in Madison. I thank you from the bottom of my heart for coming here and standing by my side through everything this University has thrown at us.

To my parents, my ultimate form of backup and support, I only completed this degree because of the invisible reassurance that you provided me. Every single day, you were here giving me the additional strength I needed to succeed.

Table Of Contents

Abstract i

Acknowledgments ii

Table of Contents iv

Chapter 1

Introduction: A PhD in Three Acts

Introduction 1

Chapter 2

Ligand Design and Dimolybdenum Chemistry

Subchapter 2.1: Clarifying the Synthesis and Characterization of Imidines: Using Crystallographic Characterization to Identify Tautomers and Localized Systems of π-Bonding

2.1.0 Author Contributions 4

2.1.1 Abstract 4

2.1.2 Chemical Context 4

2.1.3 Structural Commentary 7

2.1.4 Supramolecular Features 11

2.1.5 Synthesis, Crystallization, and Characterization 13

2.1.6 Crystallographic Refinement 16

2.1.7 References 18

2.1.8 Supporting Information 19

2.1.8.1 IR Data 20

2.1.8.2 ESI-MS Data 24

2.1.8.3 NMR Data 28

2.1.8.4 Computational Data 34

2.1.8.5 Additional Crystal Structure Images 35

2.1.8.6 References 43

Subchapter 2.2: A Study of the Unusual Absorptivity of $[Mo_2(HNNNy)_4(X)_2](X)_2$ (where x=OAc^- or Cl^- and y=5 or 6) Resulting from Ligand Contribution to a Metal Based LUMO

2.2.0 Author Contributions 44

2.2.1 Abstract 44

2.2.2 Introduction 45

2.2.3 Results and Discussion 47

2.2.3.1 Synthesis 47

2.2.3.2 Structures 48

2.2.3.3 Spectroscopic Properties 50

2.2.3.4 Computational Analysis 52

2.2.3.5 Concentration Dependent Color-Shift 54

2.2.4 Conclusion 55

2.2.5 Acknowledgements 56

2.2.6 Associated Content 56

2.2.7 References. 57

2.2.8 Supporting Information 60

2.2.8.1 Computational Methods 61

2.2.8.2 Synthesis 62

2.2.8.3.1 Characterization 66

2.2.8.3.2 NMR 67

2.2.8.3.3 IR 74

2.2.8.3.4 UV-VIS 78

2.2.8.3.5 Crystal Structures 80

2.2.8.4 Geometry Optimized Coordinates 91

2.2.8.5 References 99

Chapter 3

Computational Examination of Unusual Au Atom Bonding Environments

Subchapter 3.1: Computational studies of the stabilization of various conformers of $[(bipy)Au(PEt_3)]^+$

3.1.0 Author Contributions 100

3.1.1 Introduction 100

3.1.2 Computational Methods 100

3.1.2.1 Geometry Optimization and Frequency Calculations 100

3.1.2.2 Single Point and Natural Resonance Theory (NRT) Calculations 102

3.1.3 Computational Discussion: 102

3.1.4 Three-center Four-Electron (3c/4e) Bond and the anti-Chelate Effect 103

3.1.5 Conclusion 105

3.1.6 References 106

3.1.7 Supporting Information 108

3.1.7.1 Geometry Optimized Coordinates 108

3.1.7.2 Computational Bond Lengths 114

Subchapter 3.2: Computational Studies of d10–d10 Bonding in $[Au^{I}_6(Triphos)_4(CuIX_2)]^{5+}$ (X = Cl^- or Br^-) and their Luminescence

3.2.0 Author Contribution 116

3.2.1 Introduction 116

3.2.2 Computational Methods 116

3.2.3 Results and Discussion 117

3.2.3.1 The Nature of d10–d10 Bonding 117

3.2.3.2 The Au−Cu ground state d10–d10 bonding interaction 118

3.2.3.3 The Nature of the Luminescence 120

3.2.3.4 Origin of the Asymmetry in the Au–Cu distances 120

3.2.4 Conclusion 121

3.2.5 References 122

3.2.6 Supporting Information 125

Subchapter 3.3: Single Crystal Structural Isomers of $Au_2(DPPE)_2I_2$ and the Elongation of the Au–Au Metallophilic Interaction

3.3.0 Author Contributions 125

3.3.1 Abstract 125

3.3.2 Computational Methods 126

3.3.3 Results and Discussion 127

3.3.3.1 Structural Comparisons 127

3.3.3.2 Analysis of Au⋯Au Interactions 130

3.3.4 Conclusion 131

3.3.5 References 132

3.3.6 Supporting Information 135

3.3.6.1 Geometry Optimized Coordinates 135

Chapter 4

Using Blender to Create Educational Tools

Subchapter 1: A Library of 3D Visual Teaching Tools for Chemistry Classroom Accessible via Sketchfab and Viewable in Augmented Reality

4.1.0 Author Contributions

4.1.1 Abstract 144

4.1.2 Introduction 145

4.1.3 Methods 146

4.1.4 Workflow 147

4.1.5 Alternative Workflow Guide 147

4.1.6 Blender Implementation and Final File Export 148

4.1.7 Pedagogical Framework 149

4.1.8 Current Models and Animations 149

4.1.9 Student Implementation and Classroom Integration 152

4.1.10 Conclusion 153

4.1.11 Associated Content 154

4.1.12 References 154

Subchapter 2: A New Library of 3D Models and Problems for Teaching Crystallographic Symmetry Generated Through Blender for Use with 3D Printers or Sketchfab

4.2.0 Author Contribution 157

4.2.1 Abstract 157

4.2.2 Introduction 158

4.2.3 Technical Considerations 161

4.2.3.1 General Model Settings 161

4.2.3.2 3D Symbols for Symmetry Elements 162

4.2.3.3 3D Symbols for Objects 162

4.2.4 Static VS Animated 163

4.2.5 Availability and Expandability 163

4.2.6 File Types 164

4.2.7 3D Printing 164

4.2.8 Discussion 165

4.2.8.1 A Need for New Objects 165

4.2.9 The 3D Library 167

4.2.9.1 General Considerations 167

4.2.9.2 Example Models 167

4.2.10 Crystallography Activities 171

4.2.10.1 Unit Cell Problems 172

4.2.10.2 Point Group Problems 172

4.2.10.3 Space Group Problems 173

4.2.10.4 Block Problems 173

4.2.10.5 Miller Indices Problem 174

4.2.11 Conclusion 174

4.2.12 Disclaimer 175

4.2.13 Supporting Information 176

4.2.14 References 177

4.2.15 Additional Supporting Information 179

Chapter 1 – A PhD in Three Acts

Introduction: The work contained within describes three, separate projects.

The 2nd chapter of this work is split into two subchapters. The first subchapter explores the updated synthesis, characterization, and crystallographic novelties of several N-heterocycles dubbed HNNNx. In this subchapter the synthesis for 2-Imino-3,4-dihydro-2H-pyrrol-5-amine aka Succinimidine (HNNN5), 6-Imino-3,4,5,6-tetrahydro-2-pyridinamine aka Glutarimidine (HNNN6), 5-Amino-3,4-dihydro-2H-pyrrol-2-one (HNNO5), and 6-Amino-4,5-dihydro-2(3H)-pyridinone (HNNO6) is updated and their characterization is expanded upon. These organic molecules were originally discovered in the mid-1950's.[1, 2] The synthesis of these ligands involves an elegant, protio-neutral, ring closing reaction between a dinitrile and ammonia. The reaction is pressurized, so a sealed, thick-walled glass vessel is employed to contain the reaction. The structure of the ligand creates a five-atom chain of H_2N-C(R)=N-C(R)=NH, with a localization of sequential double-bond and single-bond occurs across five atoms. By careful inspection of their crystal structures, we were able to observe a noticeable difference in bond length resulting from these localizations. This work will be submitted as a completed manuscript to Acta Crystallographic E.[3]

In the second subchapter, these ligands were used to bridge a dimolybdenum species in the synthesis of new paddlewheel-type complexes. Four new paddlewheels, $[Mo_2(HNNN5)_4(OAc)_2](OAc)_2$ (**2(OAc)**), $[Mo_2(HNNN5)_4(Cl)_2](Cl)_2$ (**2(Cl)**), $[Mo_2(HNNN6)_4(OAc)_2](OAc)_2$ (**3(OAc)**), $[Mo_2(HNNN6)_4(Cl)_2](Cl)_2$ (**3(Cl)**), are synthesized and characterized. Unlike many previous dimolybdenum paddlewheels, the HNNNx ligands did not deprotonate during the reaction, and instead bound in the neutral form. These neutrally bound ligands resulted in fascinating electronic structure and extremely vivid colors not typically seen

in dimolybdenum chemistry. A combination of experimental and computational methods were used to understand the nuanced bonding of the ligands and how the localization in the ligand backbone gave rise to the vivid colors. This work will be submitted to the journal of Inorganic Chemistry once the HNNNx ligand paper has been accepted.[4]

The 3rd chapter is split into three subchapters, each discussing a different attempt to use computational methods to better understand unusual bonding and/or metallophilic interactions in Au(I) complexes. The first subchapter discusses the unusual Au bonding in $[(bipy)Au(PEt_3)]^+$ (bipy = 2,2′-bipyridine).[5] In this structure, the three-coordinate Au atom was noted as having two different Au-N bond distances. Through computational methods, we were able to bracket the energy of the Au-N bond and show that the asymmetry was arising from the *anti*-chelate effect and a 3 center-4 electron bond between the Au atom and the ligand. The second subchapter searches for potential metallophilic interactions between Au and Cu atoms in $[Au^I_6(Triphos)_4(Cu^ICl_2)]^{5+}$ and $[Au^I_6(Triphos)_4(Cu^IBr_2)]^{5+}$ (Triphos = bis(2-diphenylphosphino-ethyl)phenylphosphine). Through employment of computational methods, we were able to identify a clear overlap of the Au and Cu orbitals, and, through TD-DFT calculations, show that this interaction was strengthen in the excited state of this species. The third subchapter compares crystal packing effects and potential aurophilic interactions across two crystal structures of $Au_2(DPPE)_2I_2$ (DPPE= 1,2-bis(diphenylphosphino)ethane). In these crystal structures, there is a 0.25 Å difference in the Au···Au interaction, however there is no obvious origin, ie a solvatomoprh or change in counter ion, for this difference in Au···Au distances. Through computational methods, we were able to demonstrate, that this change in Au···Au distances was outside the range of aurophilic interactions and therefore was most likely a result of crystal packing effects. These projects were all completed as part of a collaboration with the Balch

research group at the University of California, Davis. Only the computational portions, completed by the Berry research group, is discussed in this thesis. The first subchapter is published and available online.[5] The second subchapter involving $[Au^{I}_{6}(Triphos)_{4}(Cu^{I}Cl_{2})]^{5+}$ and $[Au^{I}_{6}(Triphos)_{4}(Cu^{I}Br_{2})]^{5+}$ was recently resubmitted to Chemical Science.[6] The final subchapter has been sent to Prof. Alan Balch for final additions before being submitted, though our contribution to this manuscript is complete.

The 4th chapter is split into two subchapters and discusses two libraries of educational 3D models made and freely distributed during the pandemic. The first subchapter discusses the creation and distribution of a library of 3D, virtual visual aids for the purpose of teaching general chemistry.[7] These models have since been integrated into the Chem 109 oer textbook at the University of Wisconsin, Madison. The second subchapter discusses the creation, distribution, and implementation of a library of 3D virtual visual aids with a focus on teaching symmetry and crystallography.[8] These libraries of teaching models and more are freely available from Michael Aristov's Sketchfab account at https://sketchfab.com/Michael.Aristov. As of writing this thesis, these models have garnered over 25 thousand views from students and educators alike.

Citations:

1. Elvidge, J. A.; Linstead, R. P., Heterocyclic imines and amines. Part III. Succinimidine. *Journal of the Chemical Society (Resumed)* **1954,** (0), 442-448.
2. Elvidge, J. A.; Linstead, R. P.; Salaman, A. M., 37. Heterocyclic imines and amines. Part IX. Glutarimidine and the imidine from α-phenylglutaronitrile. *Journal of the Chemical Society (Resumed)* **1959,** (0), 208-215.
3. Aristov, M. M.; Geng, H.; Harris, J. W.; Berry, J. F., Updated Synthesis and Characterization of Imidines: Using Crystallographic Characterization to Identify Tautomers and Localized Systems of π-Bonding. *Manuscript in Preparation* **2022**.
4. Aristov, M. M.; Geng, H.; Harris, J. W.; Wheaton, A. M.; Berry, J. F., A Study of the Unusual Absorptivity of [Mo2(HNNNy)4(X)2](X)2 (where x=OAc- or Cl- and y=5 or 6) Resulting from Ligand Contribution to a Metal Based LUMO. *Manuscript in Preparation* **2022**.

5. Luong, L. M. C.; Aristov, M. M.; Adams, A. V.; Walters, D. T.; Berry, J. F.; Olmstead, M. M.; Balch, A. L., Unsymmetrical Coordination of Bipyridine in Three-Coordinate Gold(I) Complexes. *Inorg. Chem.* **2020,** *59* (6), 4109-4117.
6. Walters, D. T.; Aristov, M. M.; Aghakhanpour, R. B.; SantaLucia, D. J.; Costa, S.; Olmstead, M. M.; Berry, J. F.; Balch, A. L., Suspending CuX_2^- (X=Br, Cl) Anions in a Box-Like Cavity Formed from a Triphosphine Ligand with Gold(I) Connectors. *Chem. Sci.* **2022 (SUBMITTED)**.
7. Aristov, M. M.; Moore, J. W.; Berry, J. F., Library of 3D Visual Teaching Tools for the Chemistry Classroom Accessible via Sketchfab and Viewable in Augmented Reality. *J. Chem. Educ.* **2021,** *98* (9), 3032-3037.
8. Aristov, M. M.; Geng, H.; Pavelic, A.; Berry, J. F., A new library of 3D models and problems for teaching crystallographic symmetry generated through Blender for use with 3D printers or Sketchfab. *J. Appl. Crystallogr.* **2022,** *55* (1), 172-179.

Chapter 2: *Ligand Design and Dimolybdenum Chemistry*

Subchapter 2.1: Clarifying the Synthesis and Characterization of Imidines: Using Crystallographic Characterization to Identify Tautomers and Localized Systems of π-Bonding

Michael M. Aristov, Han Geng, James W. Harris, and John F. Berry

Department of Chemistry, University of Wisconsin – Madison, 1101 University Ave. Madison, WI 53703

Email: berry@chem.wisc.edu

2.1.0 Author contributions: This work was written by MMA and JFB. All experimental data and synthetic work were carried out by MMA, HG, and JWH.

2.1.1: Abstract: N-heterocycles are a class of organic ligands with extremely versatile functionality. In this paper, we report crystal structures of four N-heterocycles first synthesized in the mid 1950's, 2-imino-3,4-dihydro-2H-pyrrol-5-amine, (HNNN5), 6-imino-3,4,5,6-tetrahydro-2-pyridinamine, (HNNN6), 5-amino-3,4-dihydro-2H-pyrrol-2-one (HNNO5), and 6-amino-4,5-dihydro-2(3H)-pyridinone (HNNO6). Of these four structures, HNNN5 and HNNN6 show alternating short and long C–N bond distances across the molecule, revealing a localization of the pi-bonding system. This localized bonding is further evidenced by the structure of HNNN5·HCl, which shows a stabilized delocalization throughout the C–N backbone. These structures provide definitive evidence for the predominant form of the solid-state tautomer of these species, something that was misreported in their original synthetic report.

2.1.2: Chemical Context

Nitrogen heterocycles are of considerable interest for their ability to act as ligands in coordination chemistry, notably supporting multimetallic compounds and, in particular, compounds having metal-metal bonds,(Chipman & Berry, 2020, Beach *et al.*, 2021) 2-naphthyridylphenylamine, (DING *et al.*, 2015, Liu, Wang, *et al.*, 2009, Liu, Chen, *et al.*, 2009, Tsai *et al.*, 2013) 1,8 naphthyridin-2(1H)-one,(Chang *et al.*, 2017) 2- anilinopyridinate,(Roy *et al.*, 2022) and 2,2′-dipyridylamine.(Chipman & Berry, 2018b, a, Lescouëzec *et al.*, 2001, Berry *et al.*, 2003, Hsiao *et al.*, 2008)

We have recently explored the ability of the ligand 2,2'-dipyridylamine (Chart 1) to support linear, trimetallic metal-metal bonded compounds.(Brogden & Berry, 2016) In the search for other N-donor ligands that might support similar structures, our attention was drawn to the work of Elvidge and Linstead and their synthesis of compounds that they called "succinimidine" and "glutarimidine".(Elvidge *et al.*, 1959, Elvidge & Linstead, 1954) These compounds were so named because of their proposed structural analogy to succinimide (Chart 1) and the corresponding six-membered ring analog glutarimide. We show here that, in the solid state, the compounds "succinimidine" and "glutarimidine" adopt a different tautomeric form from those originally proposed. The structures are unsymmetric and better named systematically as 2-imino-3,4-dihydro-2H-pyrrol-5-amine and 6-imino-3,4,5,6-tetrahydro-2-pyridinamine. For simplicity, we refer to these compounds as HNNN5 and HNNN6, respectively.

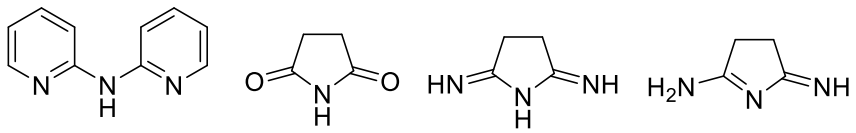

Chart 1. Structures of Hdpa, succinimide, the proposed "succinimidine" structure, and the observed structure of HNNN5.

The original syntheses described the reaction of methanol solutions of terminal dinitriles (succinonitrile, glutaronitrile, or adiponitrile) with liquid ammonia before heating,(Elvidge & Linstead, 1954, Elvidge *et al.*, 1959). We have found that similar results can be obtained by saturating a methanol solution with ammonia by sparging anhydrous ammonia gas into it. This solution, when heated for 18 hours in a sealed, bomb-flask yielded the Succinimidine. Additionally, we found that the product could be easily separated from the mother-liquor by treating it with an excess of diethyl ether. The glutarimidine reaction could be performed in an almost identical manner, however, to achieve sufficient yield, the reaction needed to be continued for 40 hours total. The product also could not be precipitated with diethyl ether. Rather, when the resulting reaction liquor was rotavaped to near dryness, yellow crystals separated from the residual stating material oil. The oil could be washed away with ether. These reaction results in a protio-neutral ring-closing to yield the N-heterocycle with two additional N-atom based functional groups. Both original papers draw all three N-atom sites as being singly protonated in a symmetric "imidine" form.(Elvidge & Linstead, 1954, Elvidge *et al.*, 1959) They additionally reported how reactions with water could sequentially replace one then both terminal N-atom functional groups with carbonyls such that "succinimidine" could be fully hydrolyzed to form succinimide.(Elvidge & Linstead, 1954, Elvidge *et al.*, 1959) While the symmetric structure of succinimide in the solid state is well established,(Yu *et al.*, 2012, Mason, 1961) the mono-hydrolyzed forms of HNNN5 and HNNN6 have not before been investigated, and they are structurally characterized here. Herein, we report an modified synthesis for 2-imino-3,4-dihydro-2H-pyrrol-5-amine, aka "succinimidine" (HNNN5), 6-imino-3,4,5,6-tetrahydro-2-pyridinamine, aka "glutarimidine" (HNNN6), 5-amino-3,4-dihydro-2H-pyrrol-2-one (HNNO5), and 6-amino-4,5-dihydro-2(3H)-pyridinone (HNNO6), see Chart 2, as well as a combination of solid-state,

liquid-phase, and computational studies to best describe the various possible tautomers of these species.

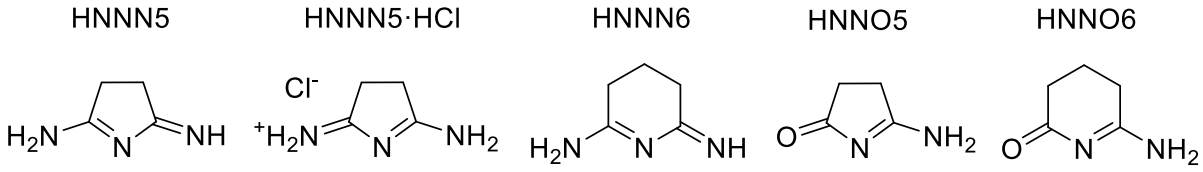

Chart 2. The structures of the most stable solid-phase tautomers of the species described in this paper. Only one resonance structure is shown for HNNN5·HCl.

2.1.3: Structural Commentary

Three of the N-heterocycles, HNNN5, HNNO5, and HNNO6 crystalize with only one molecule in the asymmetric unit with no disorder or solvent molecules. The crystal structure for HNNN6 includes two N-heterocycles and two methanol solvent molecules in the asymmetric unit. The

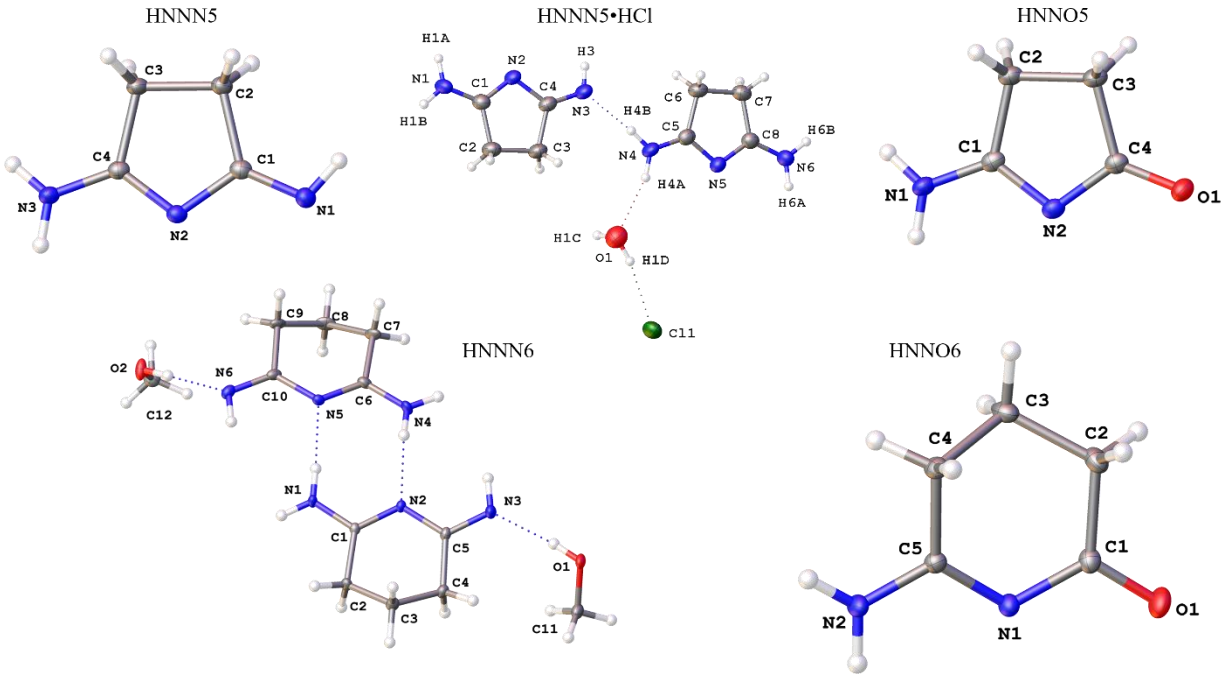

Figure 2. The asymmetric units of HNNN5 (top left), HCl•NNN5 (top middle), HNNO5 (top right), HNNN6 (bottom left), and HNNO6 (bottom right) shown with 50% probability ellipsoids. Dotted lines are used to indicated hydrogen bonding interactions. Only the major component of the ring in HNNN6 is shown.

two HNNN6 units interact via a set of two N–H···N hydrogen bonds to form a dimeric structure. A similar structural motif is seen in the structure of succinimide, (Yu *et al.*, 2012, Mason, 1961) and for some of the other compounds described here, when looking at the structures beyond just the asymmetric unit (vide infra). Additionally, one of the HNNN6 molecules displays disorder across the 3 -CH_2 units in the backbone, and one methanol shows disorder of the protons on the -CH_3 group. The structure of HNNN5•HCl contains one neutral HNNN5 molecule, one [H_2NNN5]Cl salt and one water solvent molecule. The asymmetric unit of each structure is shown in Figure 2.

In HNNN5, the NH protons are distributed such that one terminal Nitrogen atom is double protonated as an amine, the nitrogen atom in the ring is not protonated, and the other terminal nitrogen atom is singly protonated, as an imine, with the proton pointing towards the hydrophobic backbone. In HNNN6, the NH protons are distributed in a nearly identical manner, however, due to intermolecular O–H···N hydrogen bonding interactions with the solvent methanol molecules, the imine nitrogen atom of each of the two independent HNNN6 molecules has its single proton pointed away from the hydrophobic backbone. In both HNNO5 and HNNO6, the oxygen atom binds as a carbonyl, as indicated by the short C=O distances of 1.23-1.24 Å. As in the NNN structures, the nitrogen atom in the ring is unprotonated, and the terminal nitrogen atom is doubly protonated as an amine. In the HNNN5•HCl structure, both terminal nitrogen atoms are doubly protonated, with the nitrogen atom in the ring being left unprotonated. The protonation states of all complexes can be seen in Figure 2. Notably, the protonation states of all compounds differ from the structure of succinimide, which remains symmetric despite forming similarly asymmetric hydrogen bonded dimers.(Yu *et al.*, 2012, Mason, 1961) The structures of HNNN5 and HNNN6 are also notably inconsistent with their earlier structural

proposals as “succinimidine” and “glutarimidine”. And it is particularly notable that protonation of HNNN5 to form the HCl salt occurs at a terminal imine rather than the internal ring position. These observations are consistent with pK_a data for terminal vs internal imines: $(Ph)_2C=NH$ (pK_a = 31.0),(Bordwell & Ji, 1991) $PhCH_2N=C(Ph)_2$ (pK_a = 24.3).(Bordwell, 1988)

The proposed protonation states of the HNNNX and HNNOX species are further supported by the bond lengths across the heteroatoms, as seen in Figure 3. These bond distances as well as relevant comparisons are described in Table 1. We note that in the neutral form of the HNNNx complexes, there are statistically meaningful differences between the A/D and B/C bond pairs. Specifically, these differences appear to indicate a locked π-system with alternating single and double bonds where the shorter bonds are localized to B and D. Whereas in the structure of HNNN5•HCl these differences are statistically insignificant. Thus, the structure of HNNN5·HCl is best described by a delocalized electronic structure as shown by the two limiting resonance forms shown in Chart 3.

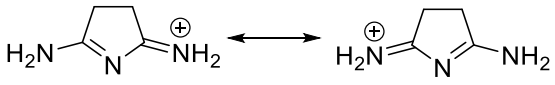

Chart 3. Limiting resonance forms for the cation in HNNN5·HCl.

To gain further insights into the protonation states of HNNN5, computational studies were performed indicating that, in the gas phase, the Gibbs free energy of the symmetric “succinimidine” tautomer is ~1.9 kcal/mol more stable than the asymmetric form observed crystallographically. The energy difference is small enough to allow for the network of hydrogen bonds in the crystal structure to dictate which tautomer of the compound is observed in the solid state. To examine which tautomer is preferred in solution, we examined a solution of HNNN5 in d_6-DMSO by ^1H NMR spectroscopy. The main signal observed is a singlet at 2.46 ppm

assignable to the CH_2 protons, consistent with the symmetric "succinimidine" tautomer. For reference, the ^1H NMR spectrum of succinimide in d_1-$CDCl_3$ consists of a singlet at 2.769 ppm. (Book) However, for HNNN5 there is also a small set of signals nearby the main singlet that could indicate the presence of a small amount of the asymmetric tautomer.

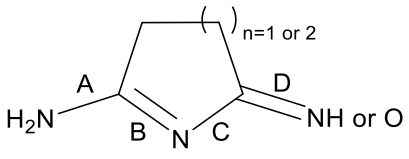

Figure 3. A generic NNNx structure used to define the bonds of interest.

Table 1: Selected bond lengths and comparisons of the structures.

Compound	A (Å)	B (Å)	C (Å)	D (Å)	Δ(A-D) (Å)	Δ(C-B) (Å)
HNNN5	1.318(2)	1.320(2)	1.387(2)	1.275(2)	0.043(4)	0.067(4)
HNNN5·HCl	1.299(3)	1.343(3)	1.349(3)	1.294(2)	0.005(5)	0.006(6)
HNNN6	1.289(2)	1.381(2)	1.323(2)	1.325(2)	0.036(4)	0.058(4)
HNNO5	1.311(2)	1.333(1)	1.379(2)	1.231(1)	NA	0.046(3)
HNNO6	1.315(2)	1.334(1)	1.366(2)	1.238(1)	NA	0.032(3)

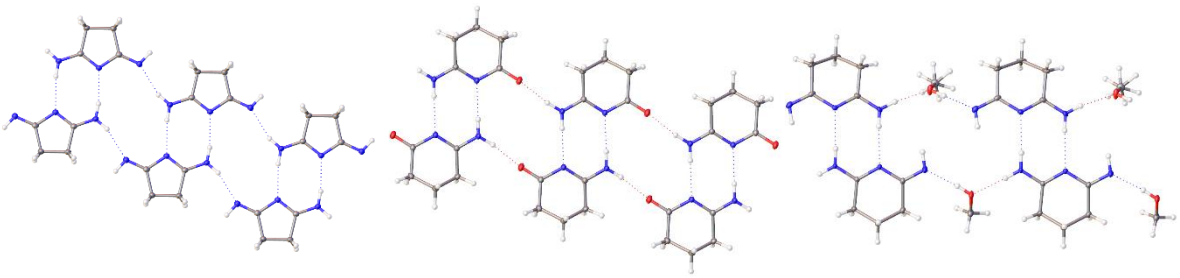

Figure 4. A comparison on the planar dimers formed by HNNN5 (left), HNNO6 (middle), and HNNN6 (right) shown with 50% probability ellipsoids. Dotted lines are used to indicated hydrogen bonding interactions. Only the major component of the ring in HNNN6 is shown.

2.1.4: Supramolecular Features

Crystal Packing. Unsurprisingly, the large amount of hydrogen bond donors and acceptors in the molecules examined here result in significant intermolecular hydrogen bonding interactions throughout the crystal structures. In HNNN5, HNNN6, and HNNO6, the hydrogen bonding interactions result in an oligomer of planar dimer units forming as the hydrophilic section of the molecules are paired together, as seen Figure 4. This creates long, 2D strands throughout the crystal lattice. For both HNNN5 and HNNO6, there are no hydrogen bonding interactions between strands either on the same plane or in between planes, as seen in Figure 5. This pattern

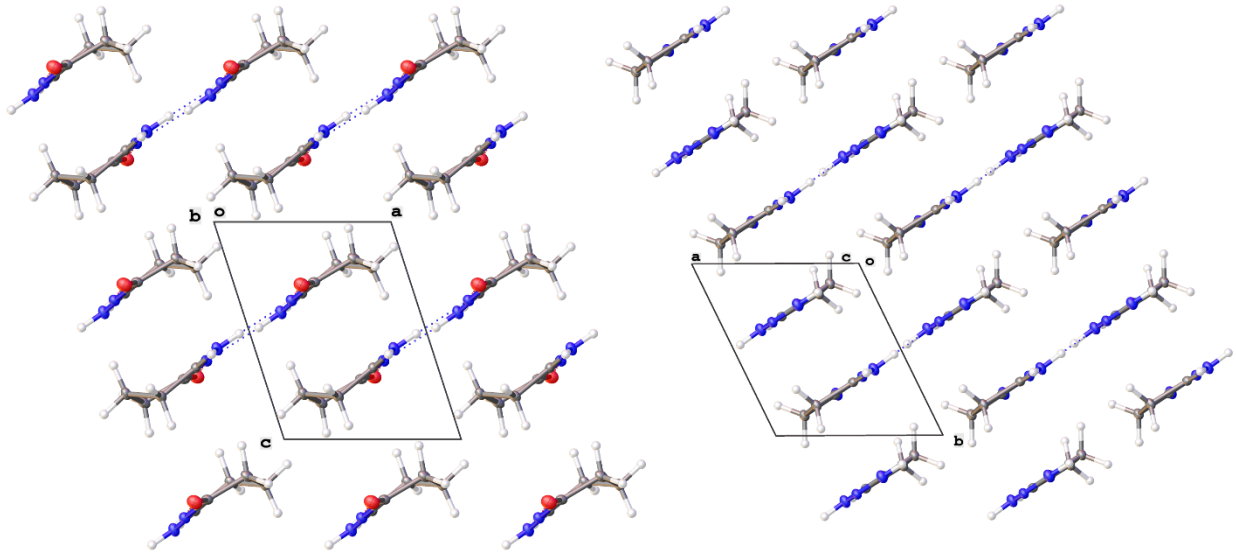

Figure 5. Left: A molecular drawing of HNNO6 viewed along the crystallographic b-axis. Right: a molecular drawing of HNNN5 viewed along the crystallographic c-axis. Both structures are drawn with 50% probability ellipsoids. Dotted lines are used to indicated hydrogen bonding interactions.

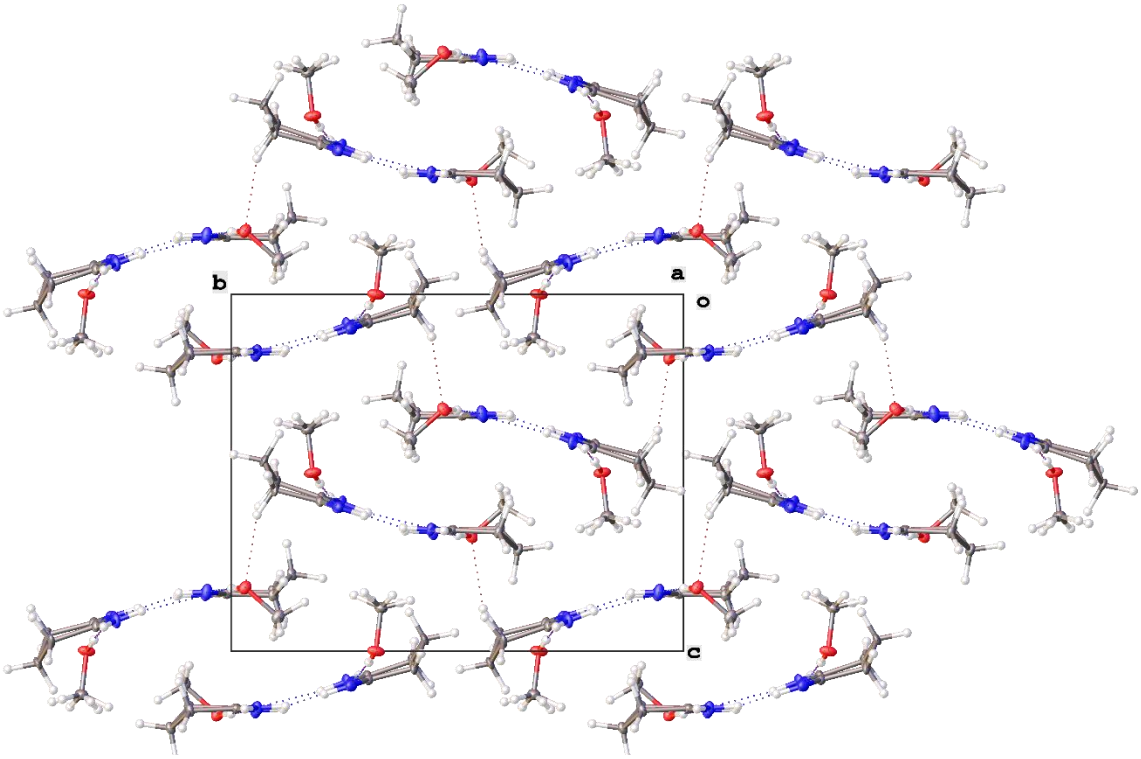

Figure 6. Left: A molecular drawing of HNNN6 viewed along the crystallographic a axis drawn with 50% probability ellipsoids. Dotted lines are used to indicated hydrogen bonding interactions.

is broken with HNNN6, where the methanol solvent molecule hydrogen bonds in between sheets. This additional hydrogen bonding interaction perpetuates through-out the packed crystal structure making a series of interlaced sheets, as seen in Figure 6. In the structure of HNNN5•HCl, the molecule's hydrophobic and hydrophilic portions alternate, as seen in previously in Figure 2 forming 2d sheets across the structure. Additionally, the water solvent

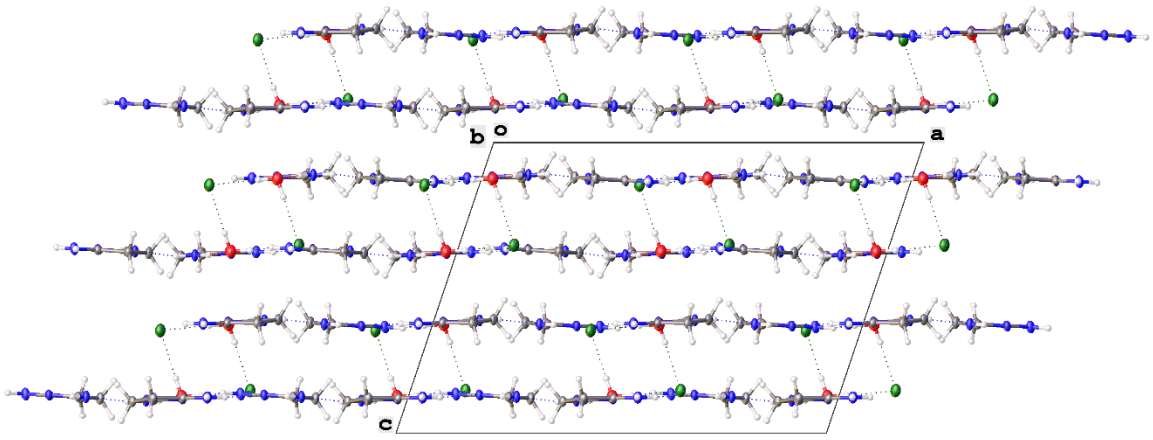

Figure 7. A molecular drawing of HNNN5•HCl viewed along the crystallographic b axis shown with 50% probability ellipsoids. Dotted lines are used to indicated hydrogen bonding interactions.

molecule in HNNN5•HCl hydrogen bonds between sheets, bridging pairs of these sheets, as seen in Figure 7. The major exception to the planar molecular sheets stabilized by a hydrogen bonding network is found in the crystal packing of HNNO5. In HNNO5 the hydrogen bonding interactions form an interconnected 3D lattice as the molecules stack perpendicular to each other, as seen in Figure 8. The introduction of the 3D hydrogen bonding lattice is likely what causes HNNO5 to be insoluble.

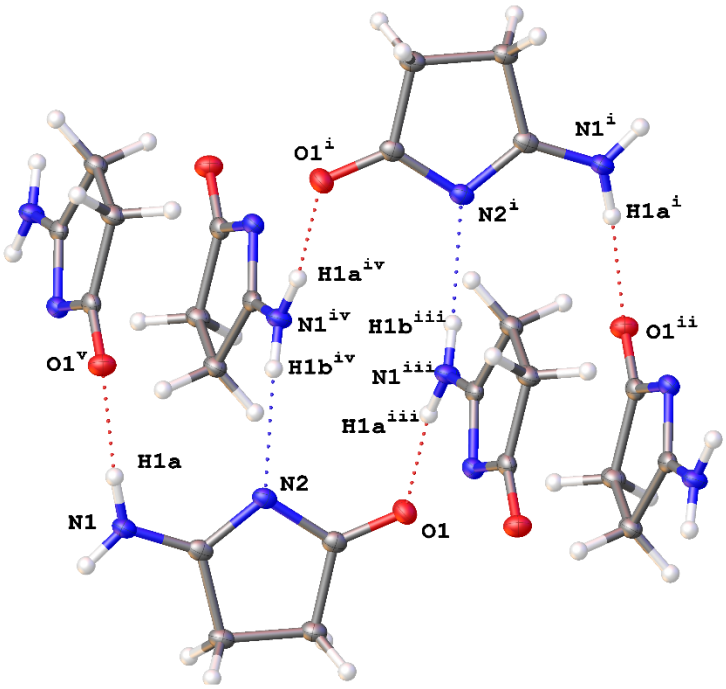

Figure 8. The stacked hydrogen-bonding network as observed in HNNO5. All atoms are drawn with 50% probability ellipsoids and dotted lines are used to indicated hydrogen bonding interactions. [Symmetry codes: (i) 1/2+X,1/2-Y,1/2+Z; (ii) 3/2-X,1/2+Y,3/2-Z; (iii) 3/2-X,-1/2+Y,3/2-Z; (iv) 2-X,1-Y,2-Z; (v) 1/2+X,3/2-Y,1/2+Z.]

2.1.5: Synthesis, Crystallization, and Characterization

General Methods

Methanol (Sigma-Aldrich) was distilled from CaH_2 under N_2 and used immediately. Succinonitrile and glutaronitrile were purchased from Sigma-Aldrich and used as received. Inhibitor-free anhydrous diethyl ether was purchased from Sigma-Aldrich and used as received. Unless otherwise noted, all manipulations were performed in air.

Synthesis of HNNN5: This product was synthesized by a modified literature method.(Elvidge & Linstead, 1954) Anhydrous methanol (70 mL), 4.02 g (50.1 mmol) of succinonitrile, and a Teflon stir bar were combined in a 250 mL heavy wall, threaded glass vessel. The solid fully dissolved, and the resulting solution was sparged with anhydrous ammonia gas until saturated. The flask was

then tightly sealed and partially submerged in an oil bath. The oil bath was programmed to heat to 70°C for 18 hours before automatically cooling to room temperature. A blast shield was placed in front of the flask, and the heating cycle was started. Upon cooling to room temperature, the pressure flask with a black solution was removed from the oil bath. Activated carbon (~3 grams), was added to the solution, and the solution was sparged with nitrogen for 10 minutes. The solution was filtered through celite to yield a pale-yellow filtrate. This filtrate was added to an excess of diethyl ether resulting in a precipitation of the product. The suspension was filtered through a glass frit and the off-white solid was washed several times with ether. The solid was dried under high-vacuum overnight and stored in a nitrogen glovebox without further purification. X-ray quality crystals were obtained by slow diffusion of diethyl ether into a saturated solution of HNNN5 in MeOH under an inert atmosphere. Crystals of HNNN5•HCl were obtained by slow diffusion of diethyl ether into a chloroform solution containing HNNN5. Yield: 2.46 g (25.3 mmol), 50.6%. MW: 97.12 g mol^{-1}. ESI (*m*/*z*): ([M+H]$^{+}$) 98.0712. IR (ATR, cm^{-1}): 3289, 3157, 3077, 2935, 2847, 1829, 1772, 1749, 1686, 1662, 1654, 1636, 1532, 1473, 1453, 1418, 1328, 1296, 1265, 1241, 1223, 1190, 1143, 1129, 1115, 996, 936, 919, 851, 822, 783, 665, 651, 641. ^{1}H NMR (400 MHz, HNNN5 in DMSO) δ 7.37 (s, 1H), 2.46 (s, 1H).

Synthesis of HNNN6: This product was synthesized by a modified literature method.(Elvidge & Linstead, 1954) Glutaronitrile (2.0299 g, 21.568 mmol), anhydrous methanol (70 mL) and an oven dried stir bar were added to an oven dried pressure flask under a constant stream of nitrogen gas. The solution was sparged with nitrogen gas for 5 minutes and then sparged with ammonia gas until saturation. The flask was sealed and heated at 70° C for 40 hours while stirring. Once the flask had cooled, the clear solution was sparged with nitrogen for ~20 minutes. The solvent was removed via rotary evaporation. The resulting yellow powder was washed with diethyl ether and filtered to

remove residual glutaronitrile. X-ray quality crystals were obtained through evaporations of a saturated MeOH solution. Yield: 0.760 g, 31.7%. MW: 111.14 g mol^{-1}. ESI (*m*/*z*): ($[M+H]^+$) 112.0868. IR (ATR, cm^{-1}): 3254, 3004, 2954, 1666, 1605, 1543, 1457, 1418, 1373, 1334, 1316, 1316, 1187, 1145, 1103, 1061, 967, 909, 886, 791, 758, 676. ^{1}H NMR (400 MHz, HNNN6 in DMSO) δ 7.05 (s, 1H), 2.20 (t, J = 6.5 Hz, 1H), 1.80 – 1.57 (q, 1H).

Synthesis of 5-Amino-3,4-dihydro-2H-pyrrol-2-one (HNNO5): A scintillation vial was filled with 1.0 g (0.010 mol) of NNN5. Then 3.4 mL of 0 °C mili-Q water was added to the vial, immediately turning the solution faint brown. The vial was stored in a 0 °C fridge overnight. The next day 0.68 g (0.0069 mol, 69% yield) of white crystal suitable for X-ray diffraction were collected from the solution. MW: 98.10 g mol^{-1}. ESI (*m*/*z*): ($[M+H]^+$) 99.0552. IR (ATR, cm^{-1}): 3220, 3135, 3019, 2938, 2918, 2851, 2360, 2341, 1686, 1627, 1526, 1456, 1437, 1418, 1397, 1338, 1294, 1251, 1221, 1161, 1009, 929, 866, 852, 827, 765, 677.^{1}H NMR (400 MHz, HNNO5 in DMSO) δ 8.30 (s, 1H), 8.07 (s, 1H), 2.67 – 2.56 (m, 2H), 2.34 – 2.25 (m, 2H). ^{13}C NMR (101 MHz, HNNO5 in DMSO) δ 193.51, 31.33, 30.72, 28.08.

Synthesis of 6-amino-4,5-dihydropyridin-2(3H)-one (HNNO6): A scintillation vial was filled with 0.1005 g (.90 mmol) of HNNN6 was added to a vial and dissolved in a minimal amount of Milli-Q water. The resulting solution was cooled overnight before allowing ether to vapor diffuse into the solution. The product precipitated out as 0.0481 g (47.4%) of white crystals suitable for X-ray diffraction with a minor 6-hydroxy-4,5-dihydropyridin-2(3H)-one (ONO6) impurity. MW: 970.52 g mol^{-1}. ESI (*m*/*z*): ($[M+NH_4]^+$) 130.0975. IR (ATR, cm^{-1}): 3381, 3185, 2967, 2947, 2920, 2886, 2823, 2774, 1644, 1534, 1506, 1458, 1426, 1418, 1349, 1299, 1274, 1222, 1153, 1120, 1071, 1056, 948, 917, 864, 807, 756, 671, 638. ^{1}H NMR (400 MHz, HNNO6 in DMSO) δ 7.72 (s, 1H), 7.18 (s, 1H), 2.50 (t, J = 7.5 Hz, 2H), 2.14 (p, J = 7.7 Hz, 1H).

2.1.6: Refinement

For the structures of HNNN5 and HNNO6 The diffraction data were consistent with the space groups $P\bar{1}$ and *P*1. The *E*-statistics strongly suggested the centrosymmetric space group $P\bar{1}$ that yielded chemically reasonable and computationally stable refinements. For the structures of HNNN6, HNNO5, and HNNN5•HCl a combination of systematic absences in the diffraction data and the *E*-statistics were used to assign the centrosymmetric space groups $P2_1/c$, $P2_1/n$, and $C2/c$, respectively.

The structures were solved via intrinsic phasing and refined by least-squares refinement of F^2 followed by difference Fourier synthesis. All non-hydrogen atoms above 70% occupancy were refined with anisotropic displacement parameters. Unless otherwise stated, all hydrogen atoms were included in the final structure-factor calculation at idealized positions and were allowed to ride on the neighboring atoms with relative isotropic displacement coefficients.

The coordinates of the H atoms bound to N atoms in, HNNO6, HNNN5, and HNNO5 were allowed to freely refine.

In the structure of HNNN6, one ring is partially disordered over two positions with a major occupancy of 85.4(6)%. The SAME command was used to restrain the lesser fraction of the disordered part of the ring to the geometry of the major fraction of the same ring. One of the methanol solvent molecules had disorder of the CH_3 protons.

Crystal data, data collections, and structure refinement details are summarized in Table 2.

Table 2. Summarized crystallographic information for all complexes discussed in this paper.					
Compound	**HNNN5**	**HNNN5•HCl**	**HNNN6**	**HNNO5**	**HNNO6**
Deposition #	2202455	2202454	2202458	2202456	2202457
Formula	$C_4H_7N_3$	$2(C_4H_7N_3) \bullet (H_2O)(HCl)$	$C_5H_9N_3 \bullet (CH_3OH)$	$C_4H_6N_2O$	$C_5H_8N_2O$
Formula weight	97.13	248.72	143.19	98.11	112.13
Temperature/K	100.02	99.99	100.00	99.99	100.0
Crystal system	triclinic	monoclinic	monoclinic	monoclinic	triclinic
Space group	$P\bar{1}$	$C2/c$	$P2_1/c$	$P2_1/n$	$P\bar{1}$
a/Å	5.9577(4)	19.294(3)	9.4887(9)	7.3685(5)	6.3296(19)
b/Å	6.7494(5)	9.4173(8)	14.5341(11)	8.0074(7)	7.0222(19)
c/Å	6.8249(5)	13.7430(12)	12.2828(10)	8.4211(9)	7.351(2)
α/°	101.641(4)	90	90	90	84.975(13)
β/°	104.225(6)	108.570(5)	111.320(8)	115.741(5)	71.693(13)
γ/°	111.425(4)	90	90	90	63.889(12)
Volume/$Å^3$	234.36(3)	2367.0(5)	1578.0(2)	447.56(7)	278.06(14)
Z	2	8	8	4	2
$\rho_{calc}g/cm^3$	1.376	1.396	1.205	1.456	1.339
μ/mm^{-1}	0.754	2.809	0.695	0.906	0.097
Radiation	CuKα (λ = 1.54178)	CuKα (λ = 1.54178)	CuKα (λ = 1.54178)	CuKα (λ = 1.54178)	MoKα (λ = 0.71073)
R_{int}	0.0191	0.0507	0.0368	0.0422	0.0336
Data/restraints/parameters	892/0/76	2322/0/151	3219/5/204	886/0/72	2048/0/79
Goodness-of-fit on F^2	1.094	1.027	1.073	1.029	1.059
Final R indexes	R_1 = 0.0342,	R_1 = 0.0435	R_1 = 0.0400	R_1 = 0.0331	R_1 = 0.0426
[I>=2σ (I)][a, b]	wR_2 = 0.0889	wR_2 = 0.1082	wR_2 = 0.1051	wR_2 = 0.0858	wR_2 = 0.1125
Final R indexes	R_1 = 0.0364	R_1 = 0.0551	R_1 = 0.0432	R_1 = 0.0386	R_1 = 0.0550
[all data]	wR_2 = 0.0916	wR_2 = 0.1160	wR_2 = 0.1077	wR_2 = 0.0888	wR_2 = 0.1195

Acknowledgments and Funding Information

MMA would like to thank Marilyn Olmstead and Ilia Guzei for the years of assistance with crystallography. We thank NSF for funding via CHE-1953294, and we thank the NSF-GRFP for

funding via DGE-1747503. NMR spectrometers were supported by NSF grant CHE-1048642 and a generous gift from Paul J. and Margaret M. Bender. The mass spectrometer was supported by NIH grant 1S10 OD020022-1. The Bruker D8 VENTURE Photon III X-ray diffractometer was partially funded by NSF Award #CHE-1919350 to the UW–Madison Department of Chemistry. The Bruker Quazar APEX2 was purchased by the UW–Madison Department of Chemistry with a portion of a generous gift from Paul J. and Margaret M. Bender.

2.1.7 References:

Beach, S. A., Rheingold, A. L. & Doerrer, L. H. (2021). *Polyhedron* **208**, 115403.
Berry, J. F., Cotton, F. A., Daniels, L. M., Murillo, C. A. & Wang, X. (2003). *Inorg. Chem.* **42**, 2418-2427.
Book, C. (2017). *Succinimide(123-56-8) 1H NMR,* https://www.chemicalbook.com/SpectrumEN_123-56-8_1HNMR.htm.
Bordwell, F. G. (1988). *Acc. Chem. Res.* **21**, 456-463.
Bordwell, F. G. & Ji, G. Z. (1991). *Journal of the American Chemical Society* **113**, 8398-8401.
Brogden, D. W. & Berry, J. F. (2016). *Comments Inorg. Chem.* **36**, 17-37.
Chang, W.-C., Chang, C.-W., Sigrist, M., Hua, S.-A., Liu, T.-J., Lee, G.-H., Jin, B.-Y., Chen, C.-h. & Peng, S.-M. (2017). *Chem. Commun.* **53**, 8886-8889.
Chipman, J. A. & Berry, J. F. (2018a). *Chemistry–A European Journal* **24**, 1494-1499.
Chipman, J. A. & Berry, J. F. (2018b). *Inorg. Chem.* **57**, 9354-9363.
Chipman, J. A. & Berry, J. F. (2020). *Chem. Rev.* **120**, 2409-2447.
DING, D.-D., XU, X., WU, Z.-W., ZHOU, W.-H., CHEN, R. & XU, Z.-G. (2015). *Acta Physico-Chimica Sinica* **31**, 1323-1330.
Elvidge, J. A. & Linstead, R. P. (1954). *Journal of the Chemical Society (Resumed)*, 442-448.
Elvidge, J. A., Linstead, R. P. & Salaman, A. M. (1959). *Journal of the Chemical Society (Resumed)*, 208-215.
Hsiao, C.-J., Lai, S.-H., Chen, I.-C., Wang, W.-Z. & Peng, S.-M. (2008). *The Journal of Physical Chemistry A* **112**, 13528-13534.
Lescouëzec, R., Marinescu, G., Muñoz, M. C., Luneau, D., Andruh, M., Lloret, F., Faus, J., Julve, M., Mata, J. A. & Llusar, R. (2001). *New J. Chem.* **25**, 1224-1235.
Liu, I. P.-C., Chen, C.-H., Chen, C.-F., Lee, G.-H. & Peng, S.-M. (2009). *Chem. Commun.*, 577-579.
Liu, I. P.-C., Wang, W.-Z. & Peng, S.-M. (2009). *Chem. Commun.*, 4323-4331.
Mason, R. (1961). *Acta Crystallographica* **14**, 720-724.
Roy, M. D., Trenerry, M. J., Thakuri, B., Macmillan, S. N., Liptak, M. D., Lancaster, K. M. & Berry, J. F. (2022). *Inorg. Chem.* **61**.
Tsai, C.-S., Liu, I. P.-C., Tien, F.-W., Lee, G.-H., Yeh, C.-Y., Chen, C.-h. & Peng, S.-M. (2013). *Inorg. Chem. Commun.* **38**, 152-155.
Yu, M., Huang, X. & Gao, F. (2012). *Acta Crystallographica Section E* **68**, o2738.

Supporting Information for Subchapter 2.1: Updated Synthesis and Characterization of Imidines: Using Crystallographic Characterization to Identify Tautomers and Localized Systems of π-Bonding

Michael M. Aristov, Han Geng, James W. Harris, and John F. Berry

Department of Chemistry, University of Wisconsin – Madison, 1101 University Ave. Madison, WI 53703

Email: berry@chem.wisc.edu

Table of Contents:

IR Data 20-23

ESI-MS Data 24-27

NMR Data 28-33

Computational Data 34

Supplemental Crystallographic Images 35-43

Reference 43

Figure S1. IR of HNNN5

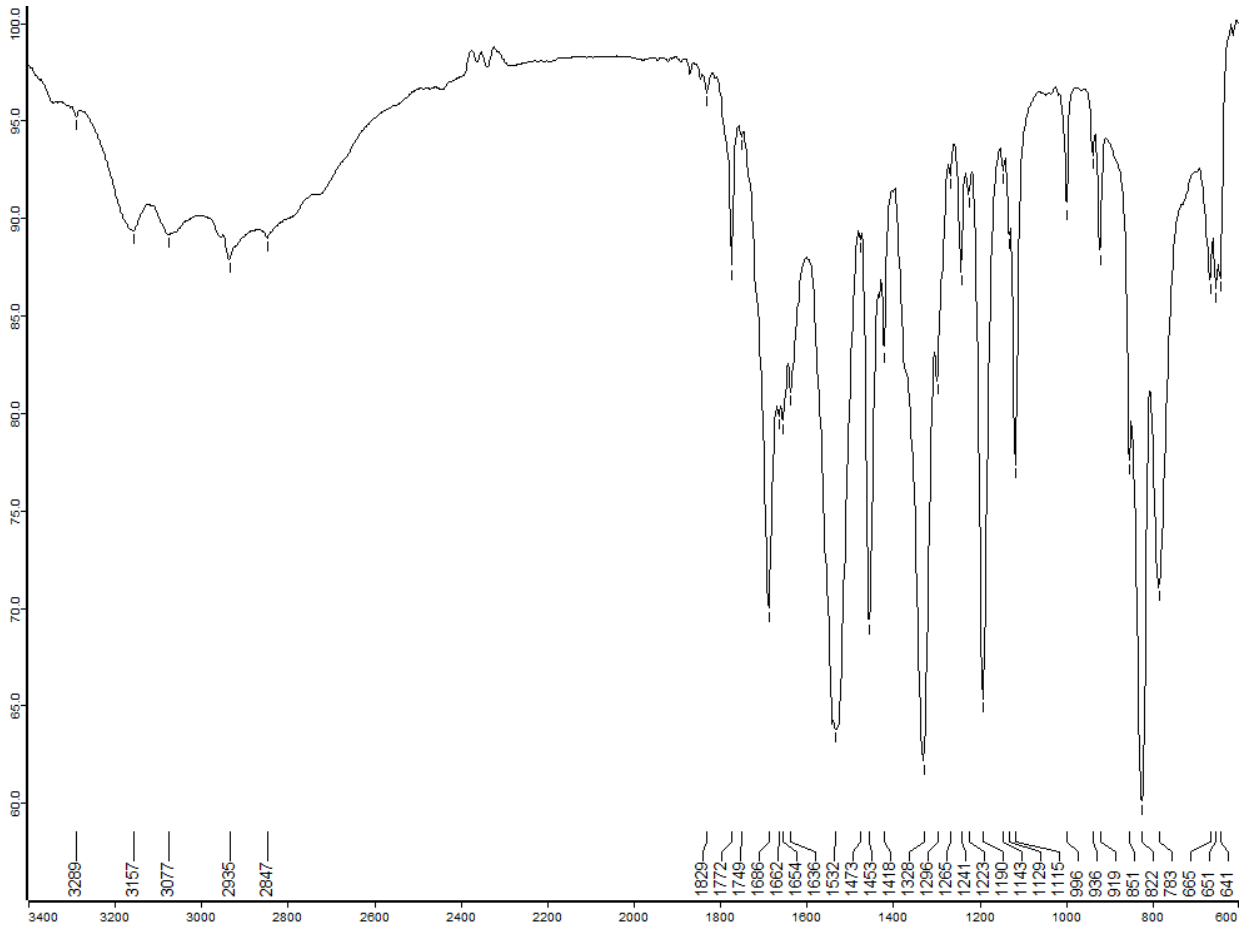

Figure S2. IR of HNNN6.

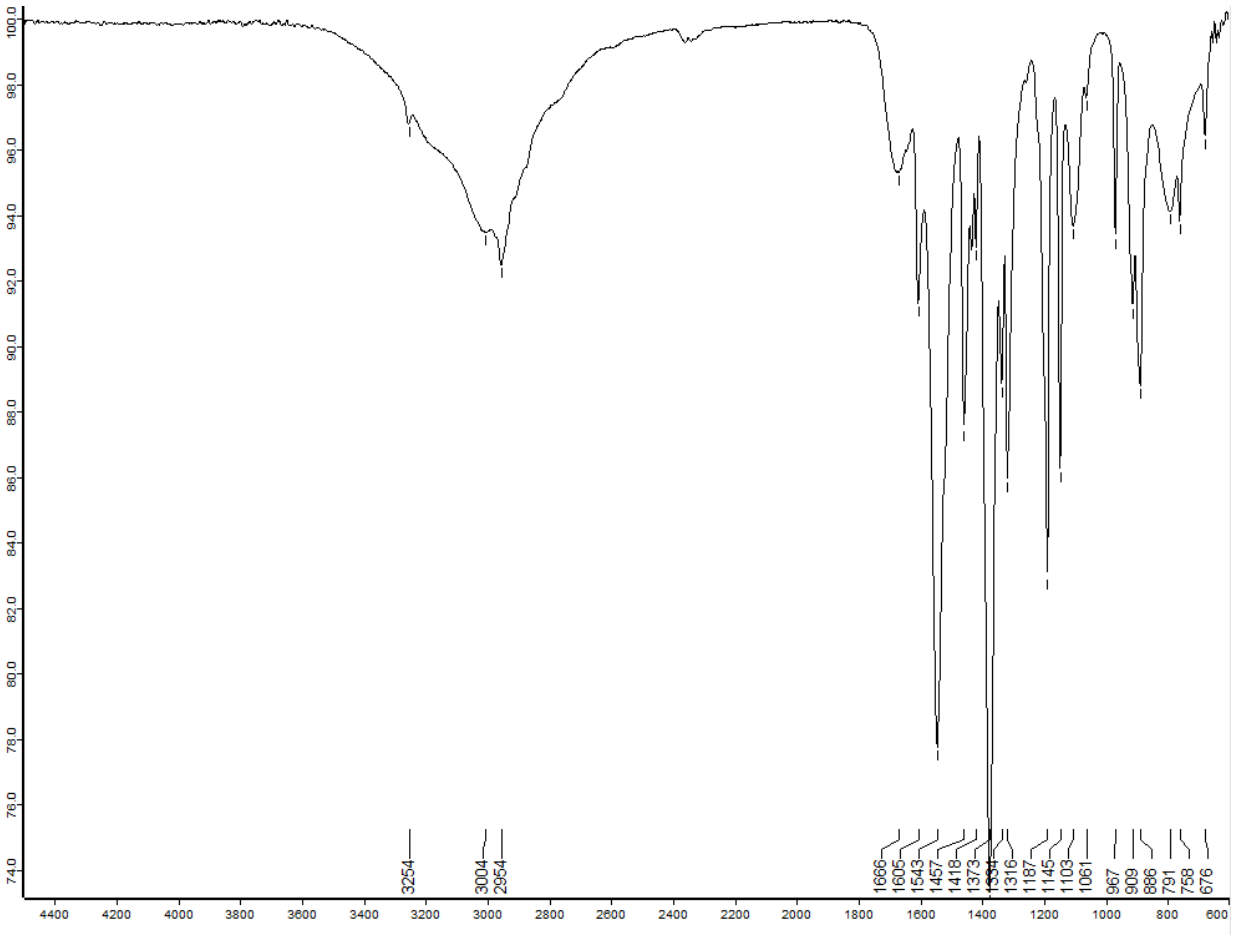

Figure S3. IR of HNNO6

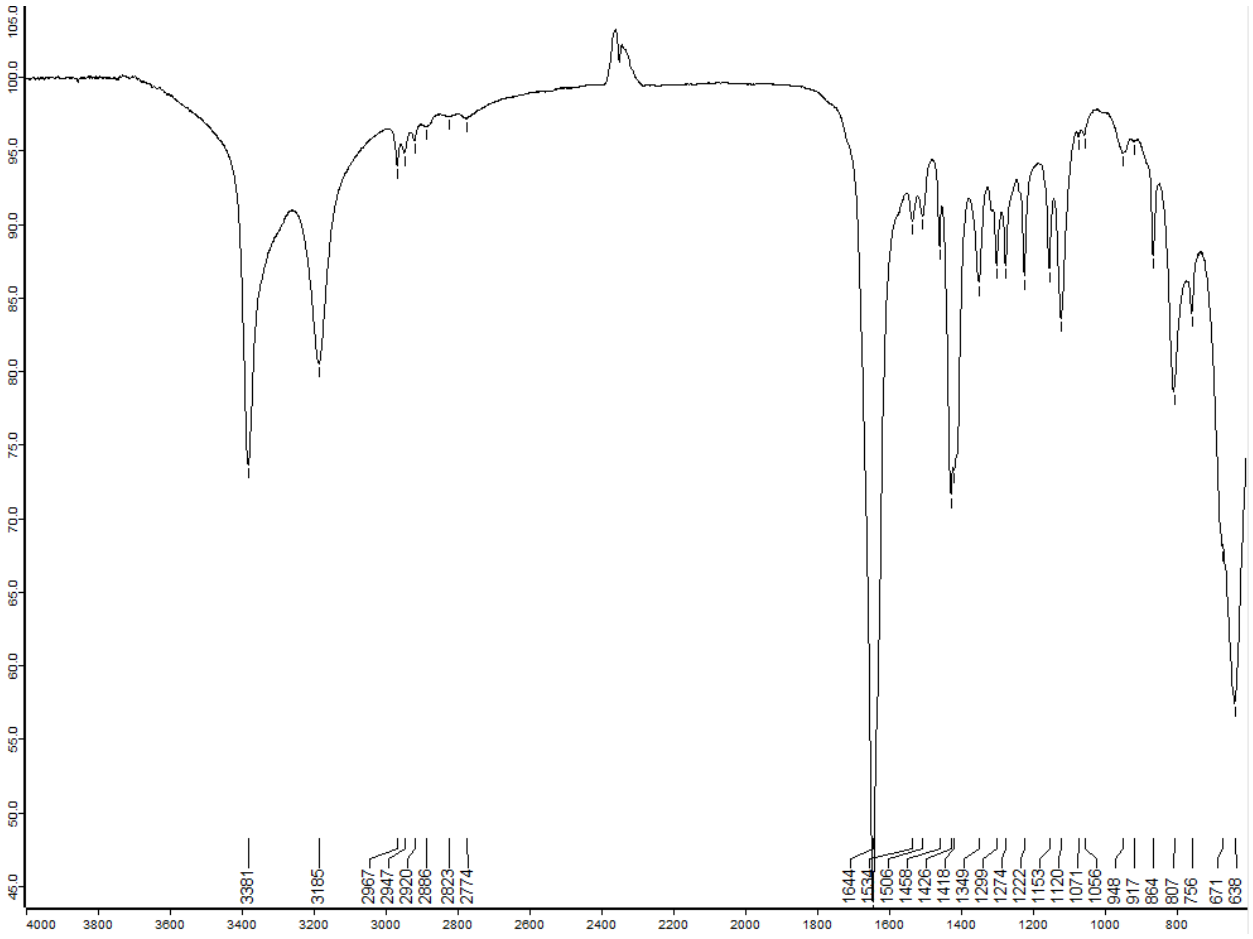

Figure S4. IR of HNNO5

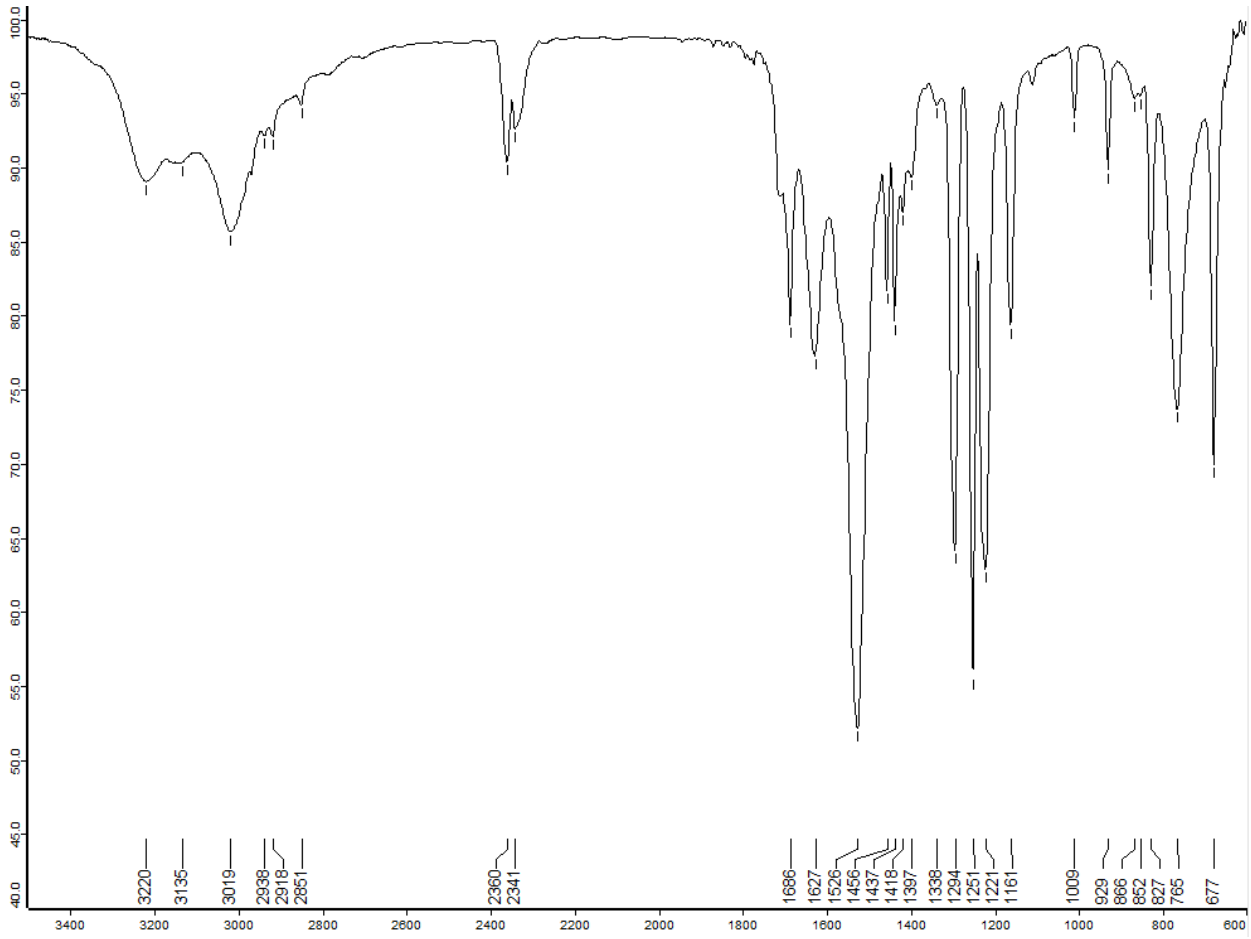

Mass Spec Data:

Figure S5. ESI-MS of HNNN5

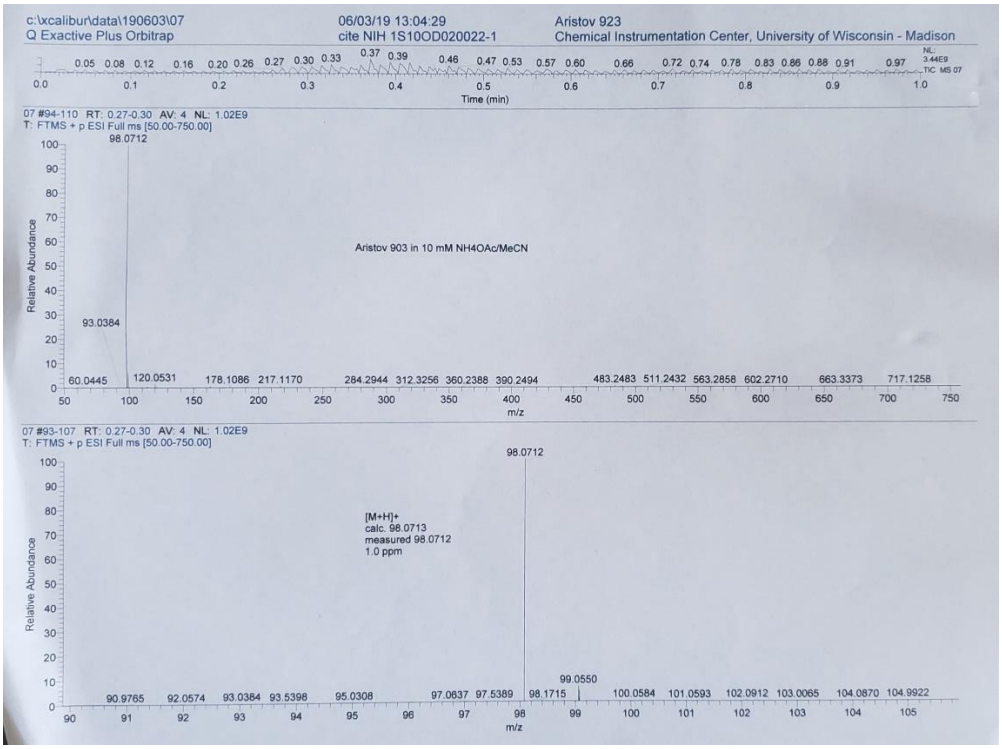

Figure S6. ESI-MS of HNNO5

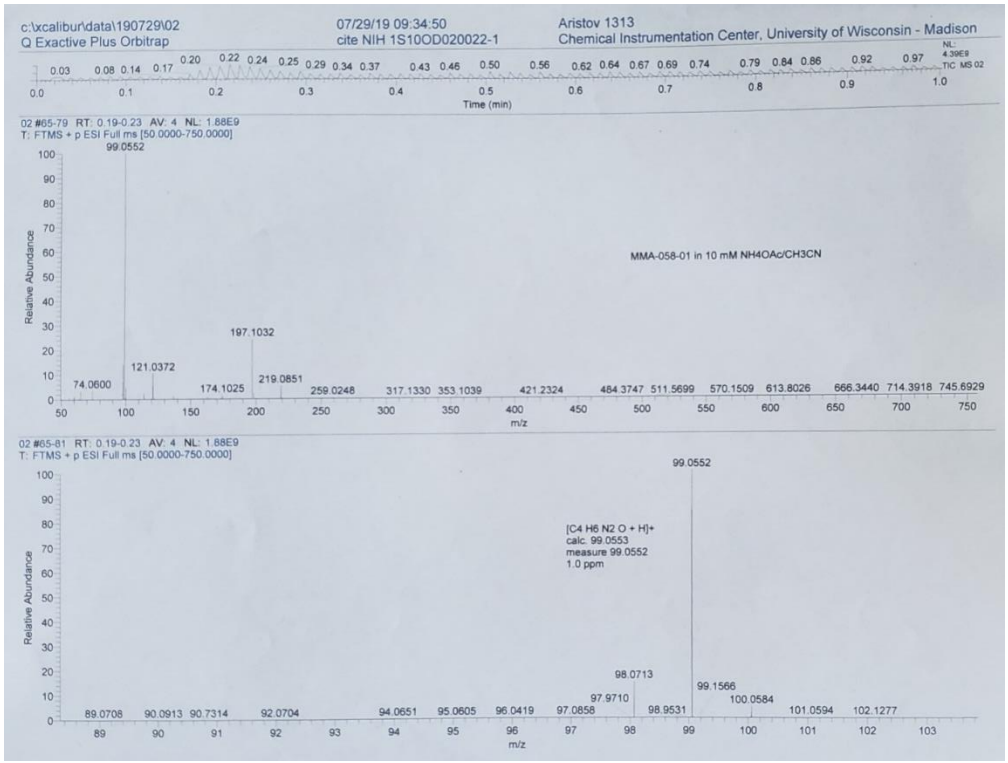

ESI (*m*/*z*): ($[C_8H_{10}N_4O](H_2O)+H]^+$) 197.1032

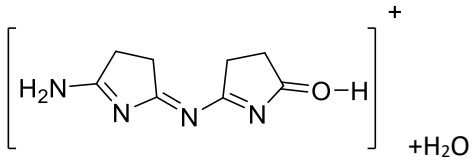

ESI (*m*/*z*): ($[HNNO5+Na]^+$) 121.0372

Figure S7. ESI-MS of HNNN6

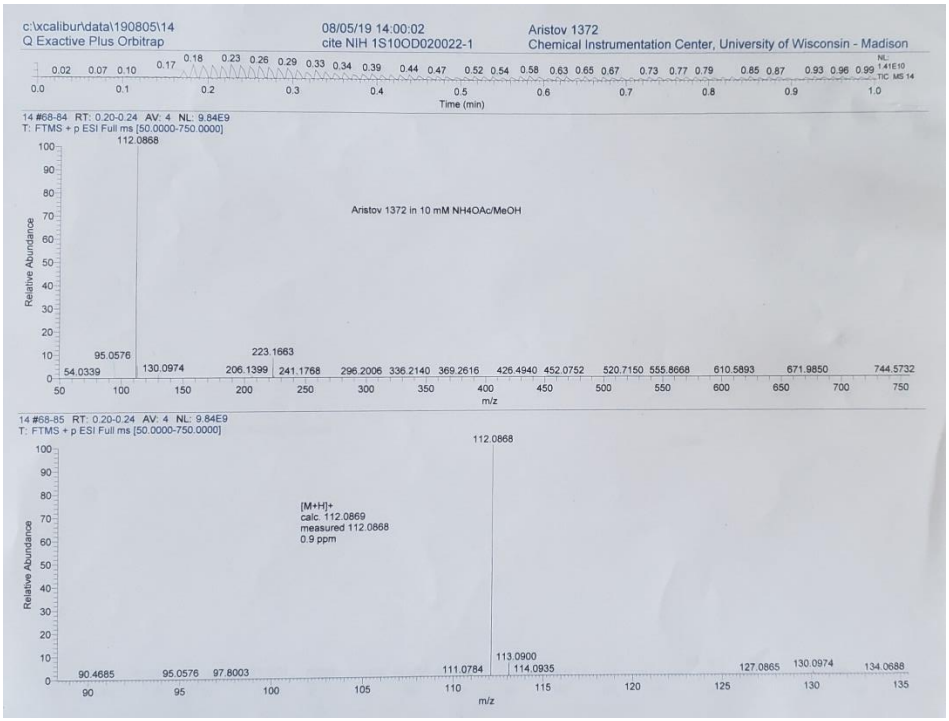

ESI (*m*/*z*): ($[C_{10}H_{15}N_5]+NH_4]^+$) 223.17

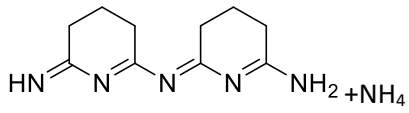

Figure S8. ESI-MS of HNNO6

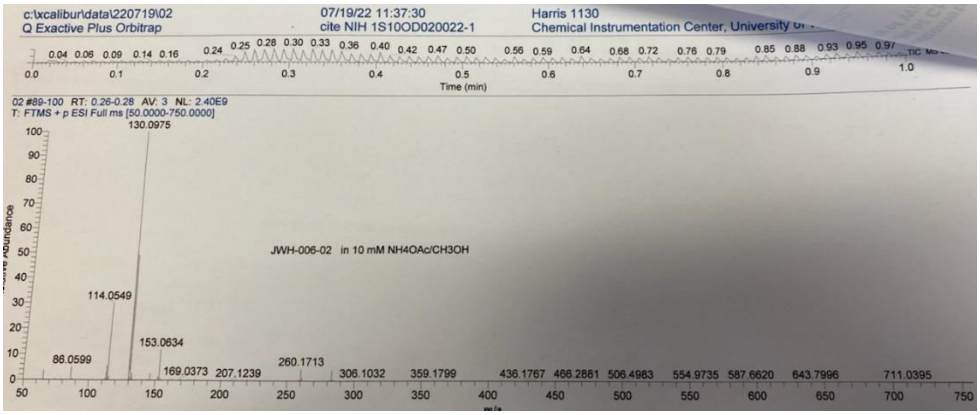

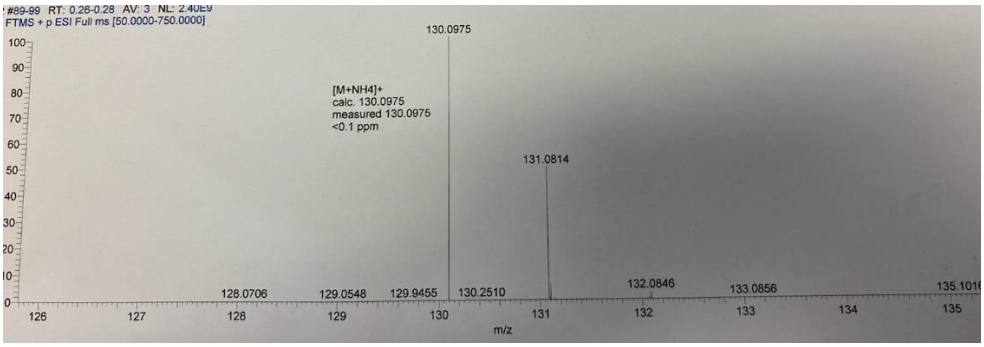

ESI (*m*/*z*): ([HONO6]+NH_4]$^+$) 131.0814

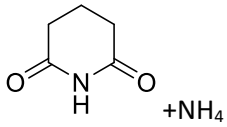

NMR Data:

Figure S9. HNNN5: ^{1}H NMR (400 MHz, HNNN5 in DMSO) δ 7.37 (s, 1H), 2.46 (s, 1H).

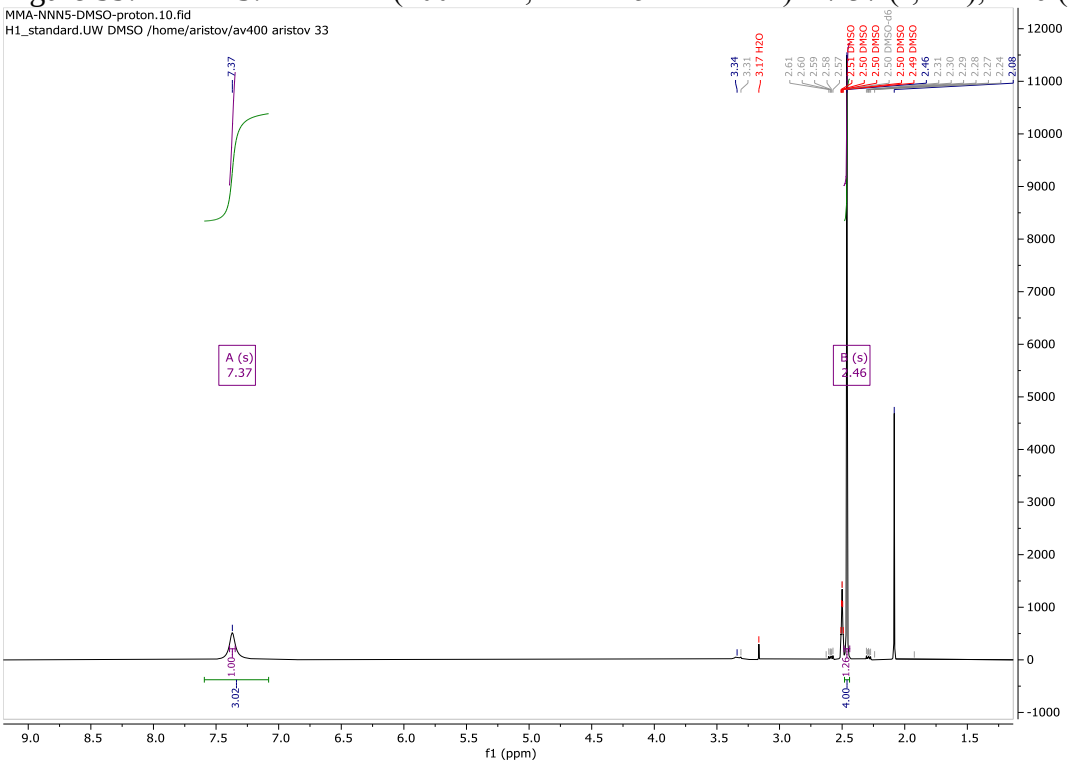

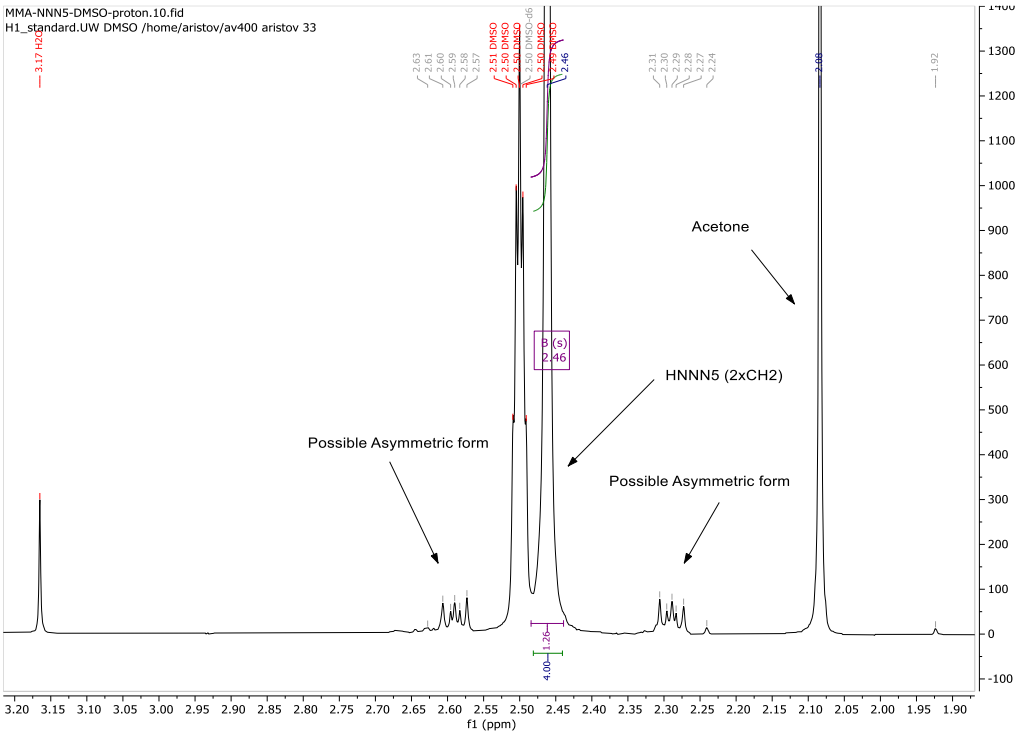

Figure S10. HNNO5: ^{1}H NMR (400 MHz, HNNO5 DMSO) δ 8.30 (s, 1H), 8.07 (s, 1H), 2.67 – 2.56 (m, 2H), 2.34 – 2.25 (m, 2H).

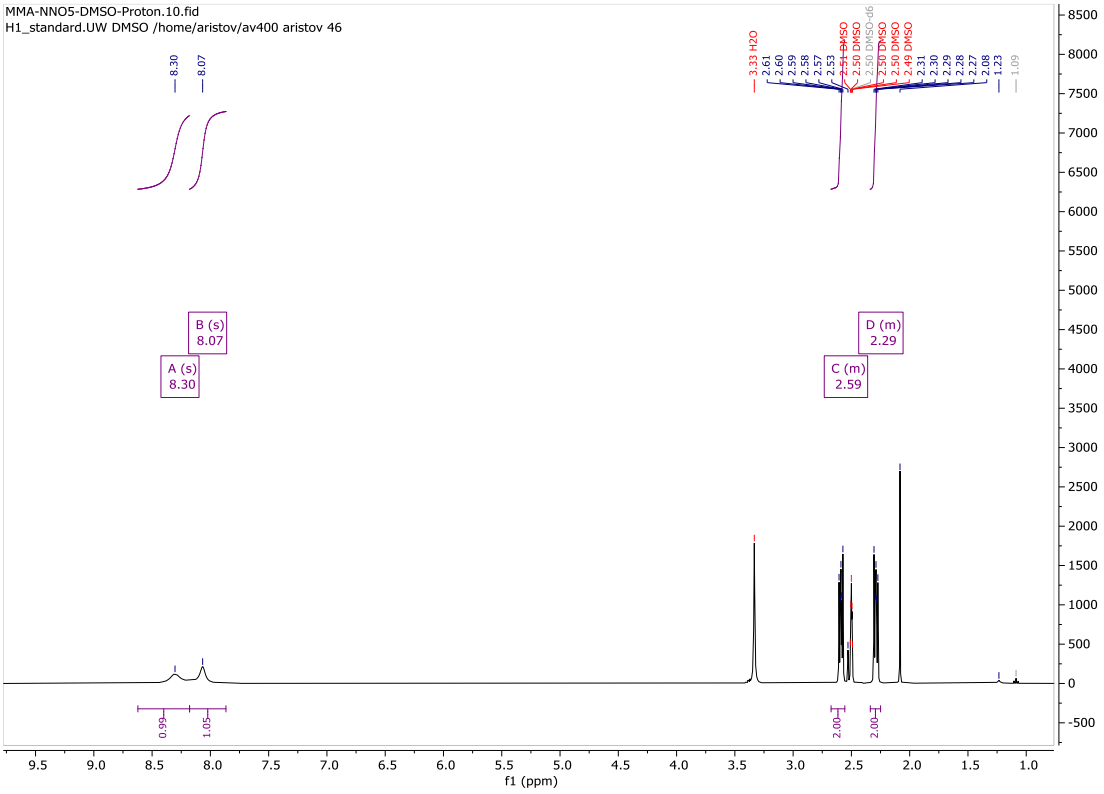

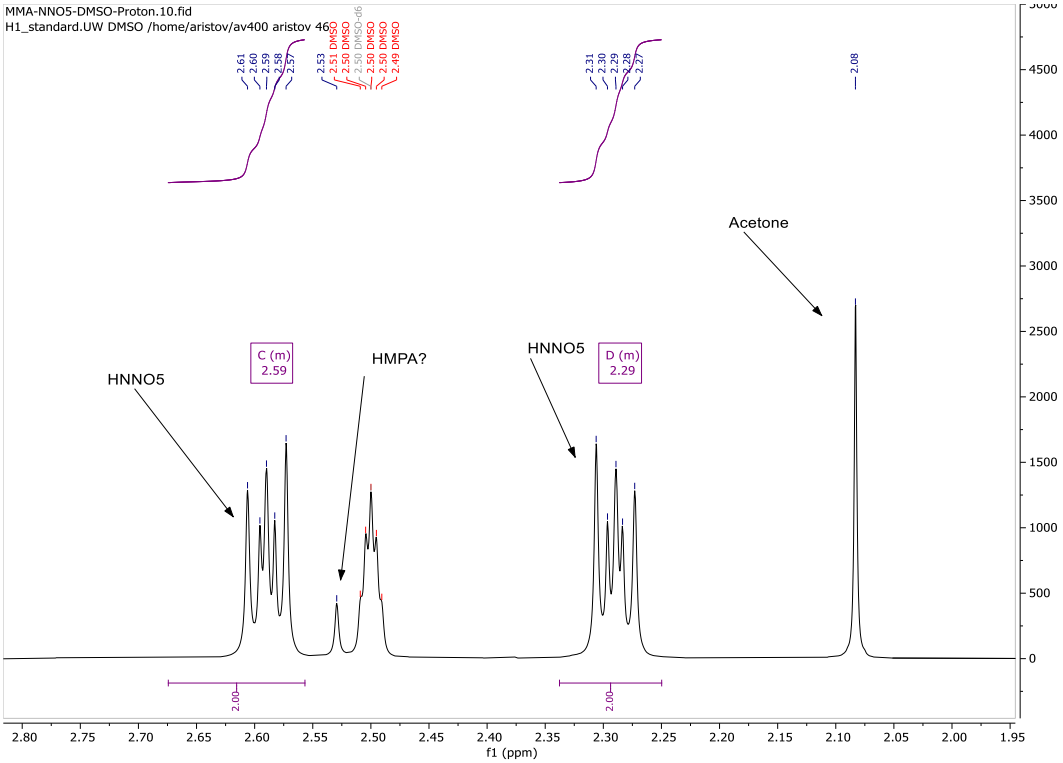

Figure S11. HNNO5: ^{13}C NMR (101 MHz, HNNO5 in DMSO) δ 193.51, 31.33, 30.72, 28.08.

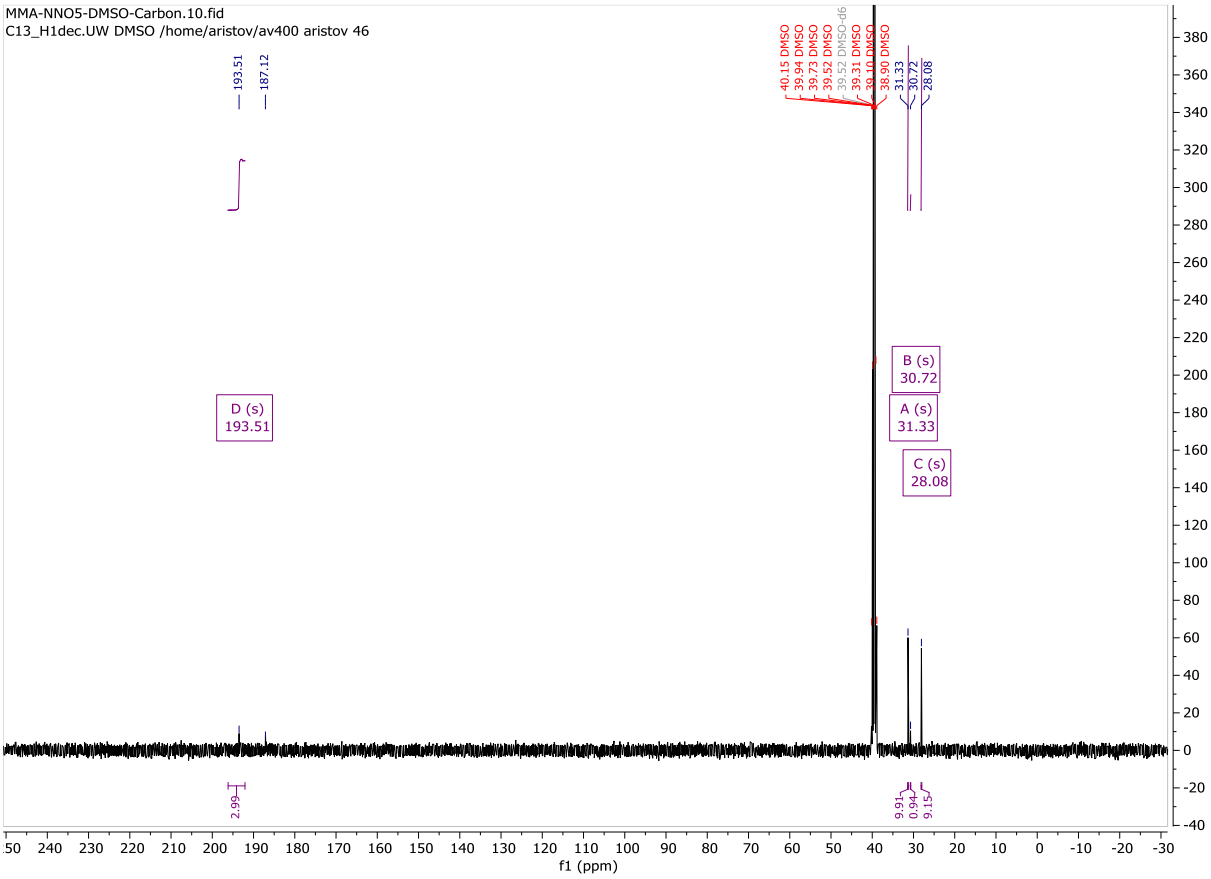

Figure S12. HNNN6: ^{1}H NMR (400 MHz, HNNN6 in DMSO) δ 7.05 (s, 1H), 2.20 (t, *J* = 6.5 Hz, 1H), 1.80 – 1.57 (q, 1H).

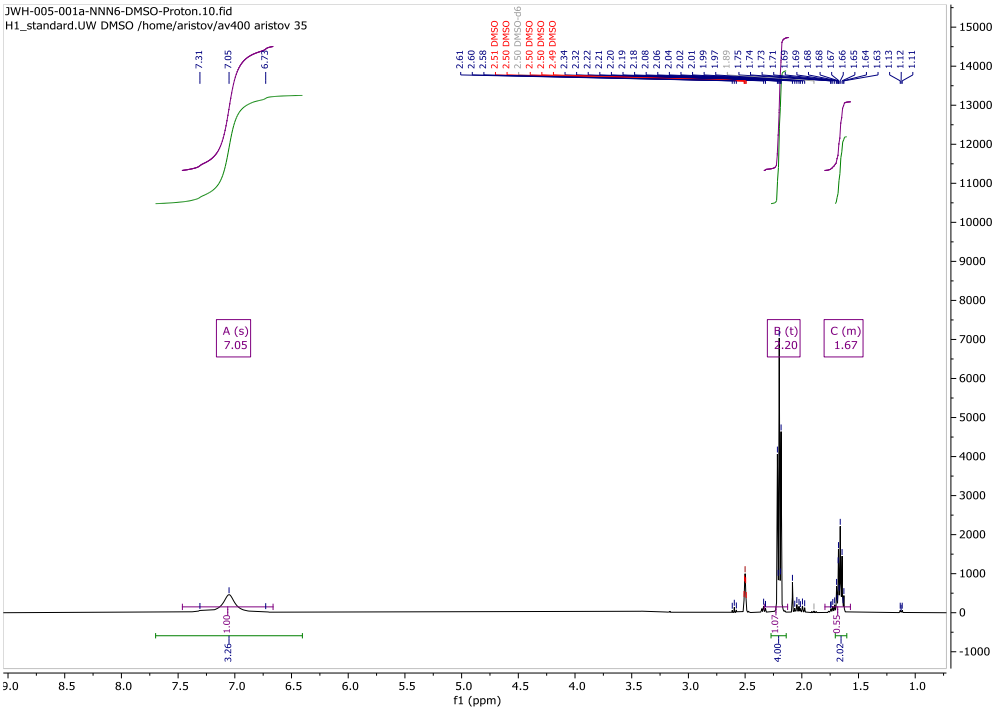

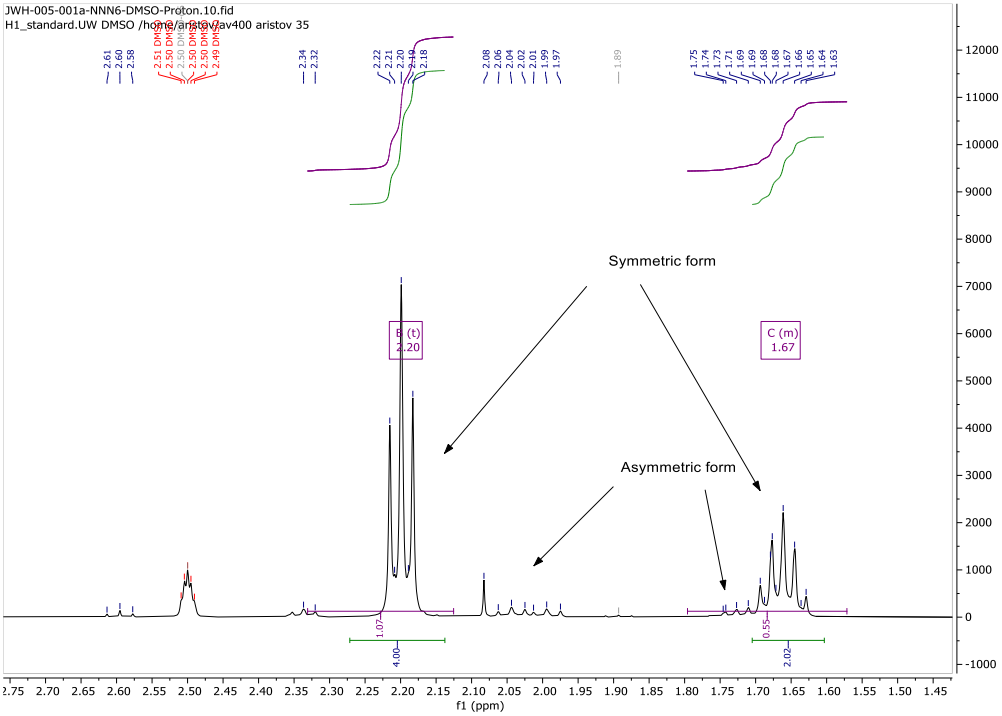

Figure S13. HNNN6: ^{13}C NMR (101 MHz, HNNN6 in DMSO) δ 168.09, 27.53, 19.45.

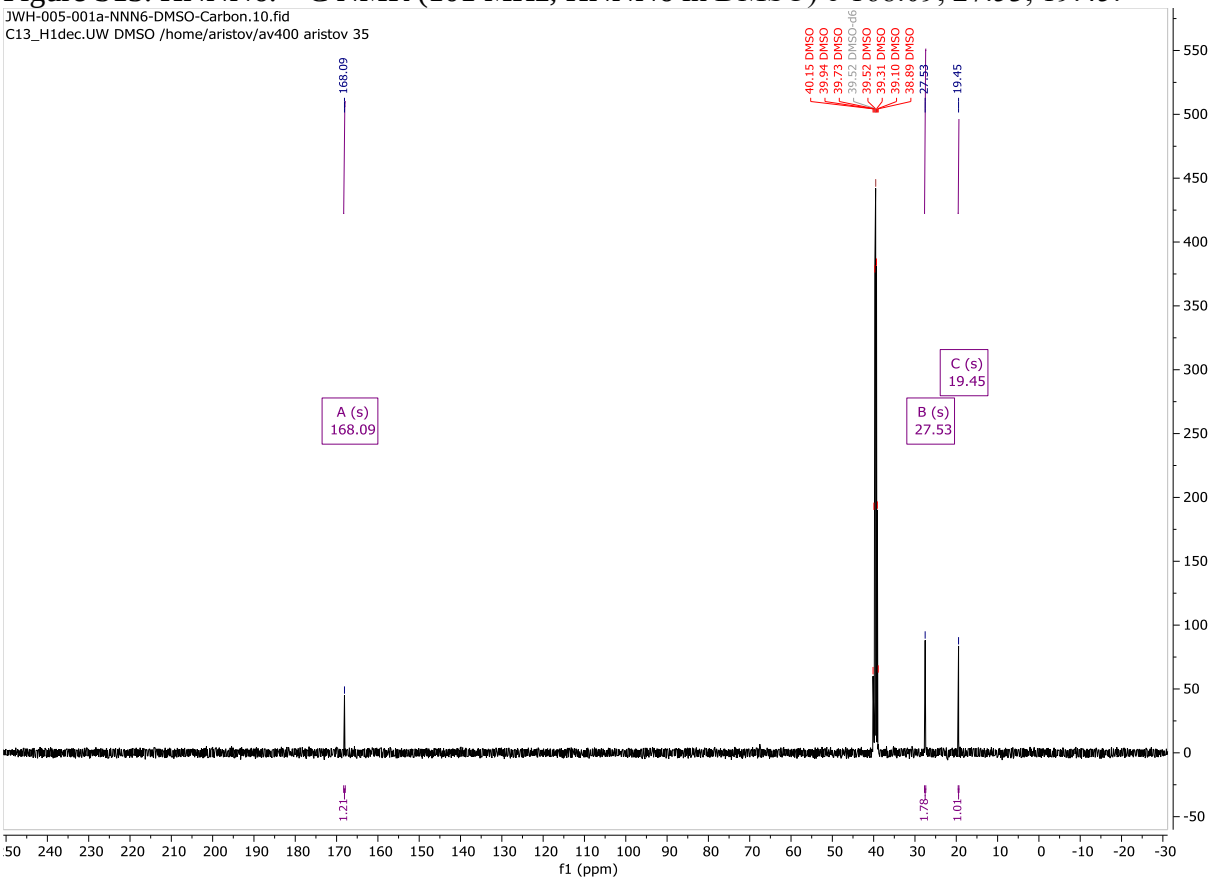

Figure S14. HNNO6: ^{1}H NMR (400 MHz, HNNO6 in DMSO) δ 7.72 (s, 1H), 7.18 (s, 1H), 2.50 (t, J = 7.5 Hz, 2H), 2.14 (p, J = 7.7 Hz, 1H)

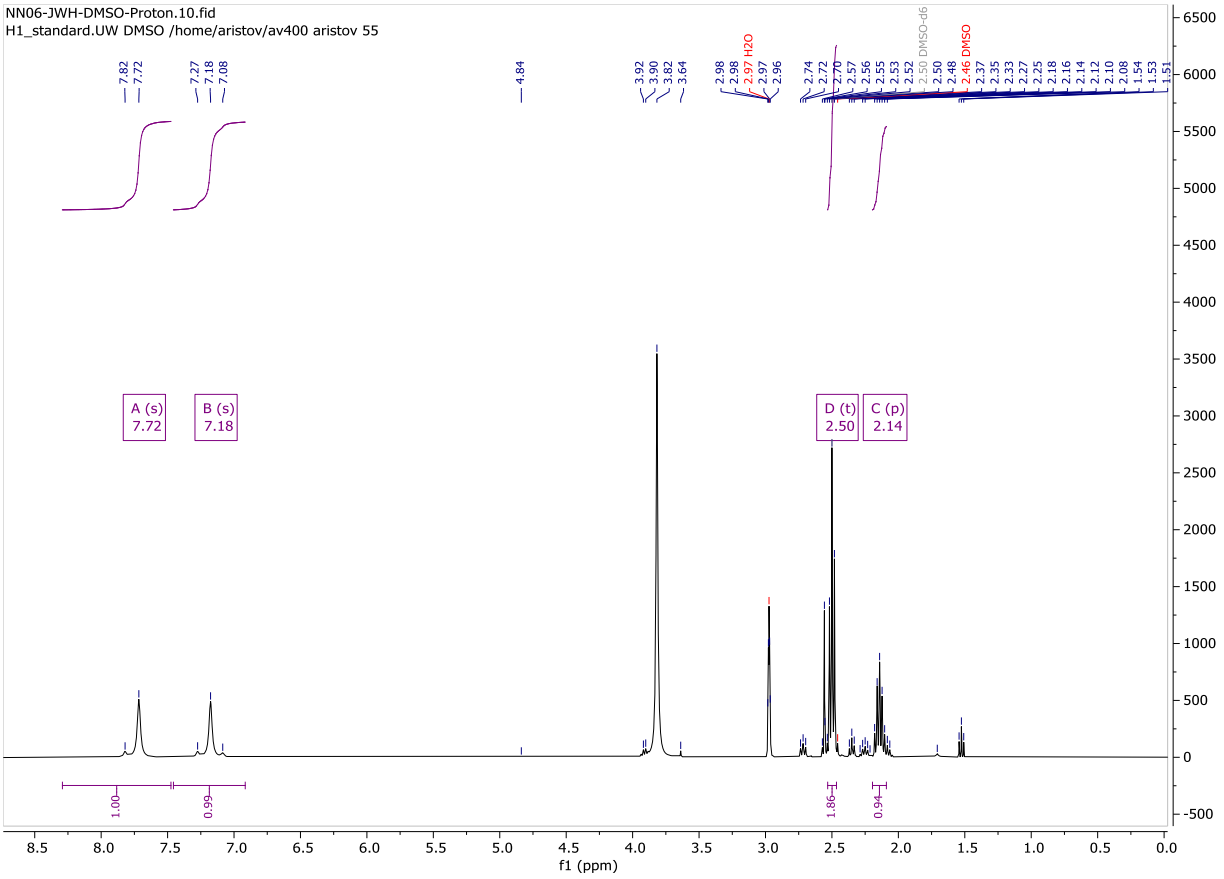

Calculations: All calculations were carried out using Gaussian 16(Frisch *et al.*, 2016), HF theory, and the 6-31g(d) basis set. Input geometries were constructed from modified crystallographic coordinates. The geometry optimized xyz coordinates for all structures are provided in Tables S1 and S2.

Table S1. XYZ coordinates from the optimized asymmetric structure of HNNN5.

Atom	X	Y	Z
C	0.649857	1.277596	-0.00554
C	-0.87957	1.208895	0.007742
C	-1.165	-0.29754	-0.00051
N	0.036009	-1.01282	-0.00076
C	1.005749	-0.19268	0.001706
N	2.298247	-0.57871	0.049523
H	2.487487	-1.54654	-0.09035
H	3.013518	0.059235	-0.21267
N	-2.28135	-0.86433	-0.00814
H	-3.02497	-0.18848	-0.00903
H	-1.30665	1.666701	0.89213
H	-1.32716	1.683164	-0.85749
H	1.050836	1.764418	-0.88898
H	1.070304	1.774916	0.861671

Table S2. XYZ coordinates from the optimized symmetric structure of HNNN5.

Atom	X	Y	Z
C	0.738432	1.272389	0.093736
C	-0.78701	1.239713	-0.0961
C	-1.1574	-0.23124	-0.00404
N	0.025415	-0.93835	0.000991
C	1.175065	-0.17634	0.005833
N	2.371288	-0.54612	-0.03507
H	2.465645	-1.54601	-0.07787
H	0.017593	-1.93459	0.010076
N	-2.27434	-0.79566	0.041777
H	-3.02215	-0.12755	0.023393
H	-1.32447	1.814511	0.647444
H	-1.08008	1.609986	-1.07252
H	1.255905	1.862327	-0.64936
H	1.016463	1.655097	1.068347

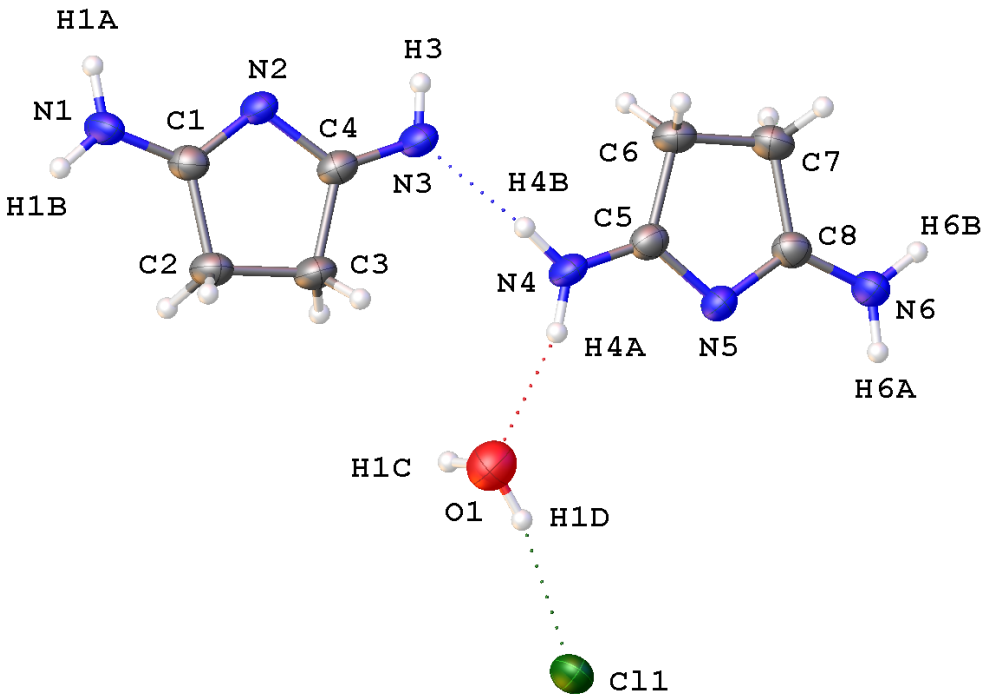

Figure S15. A molecular drawing of the structure of HNNN5•HCl shown with 50% probability ellipsoids.

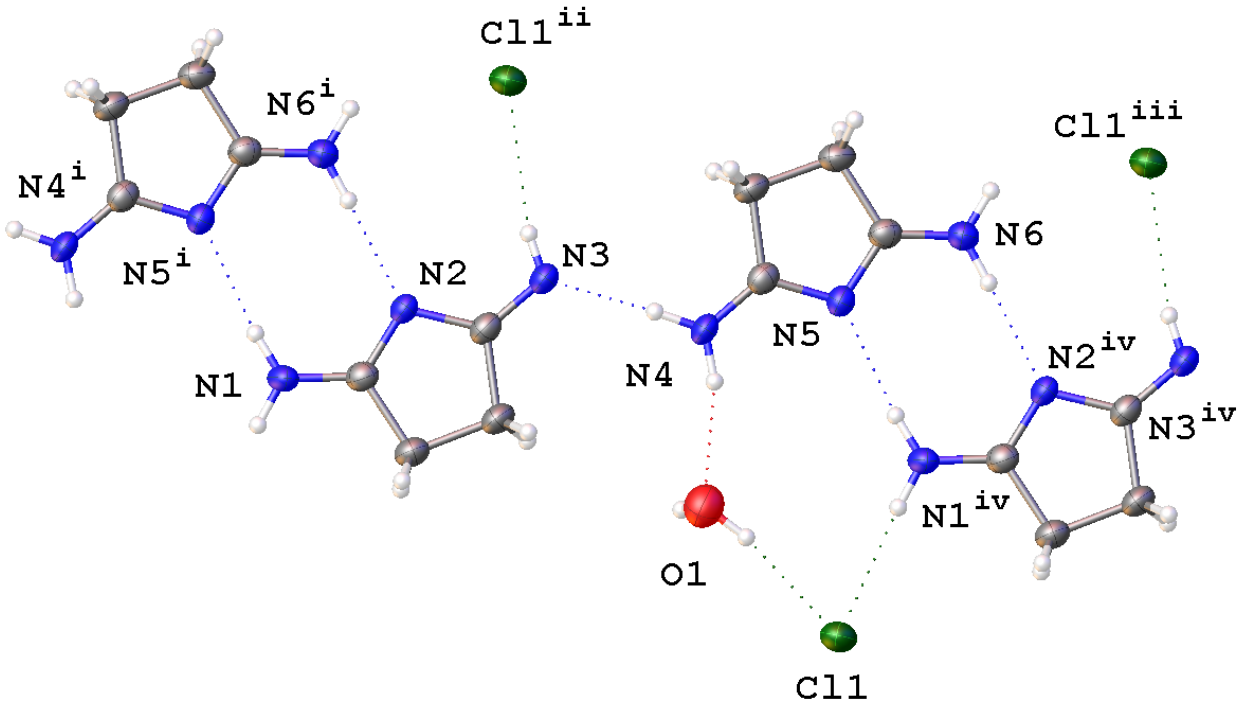

Figure S16. A molecular drawing of HNNN5•HCl shown with 50% probability ellipsoids, with emphasis placed on the layered hydrogen bonding system. [Symmetry code: i: 1/2+X,-1/2+Y,+Z; ii: 1/2+X,1/2+Y,+Z ; iii: -1/2+X,1/2+Y,+Z ; iv: +X,1+Y,+Z.]

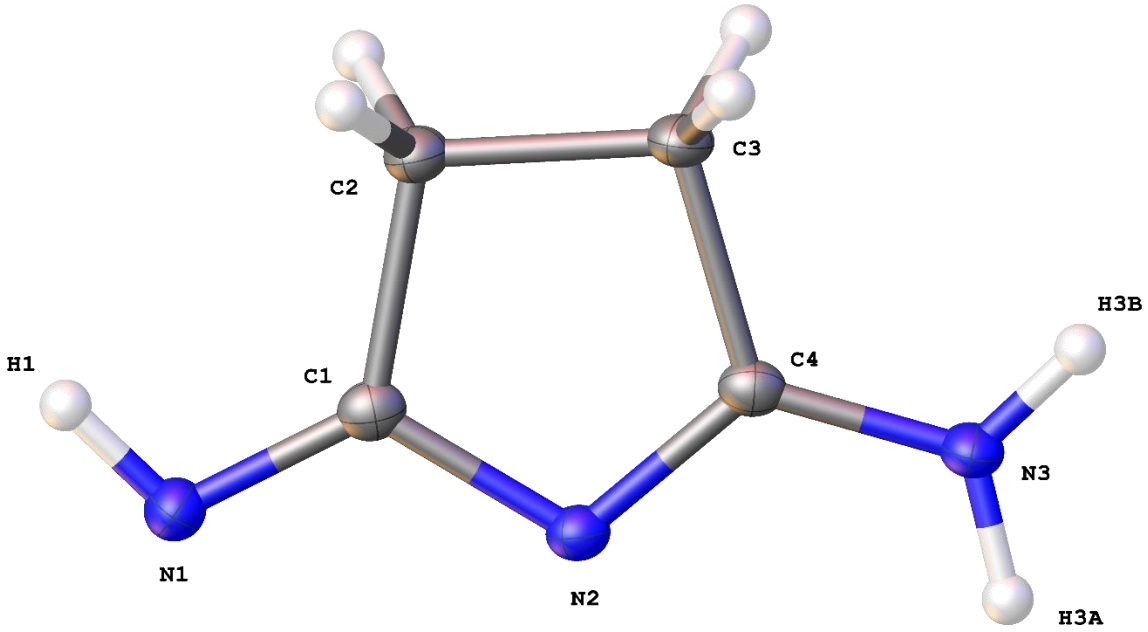

Figure S17. A molecular drawing of HNNN5 shown with 50% probability ellipsoids.

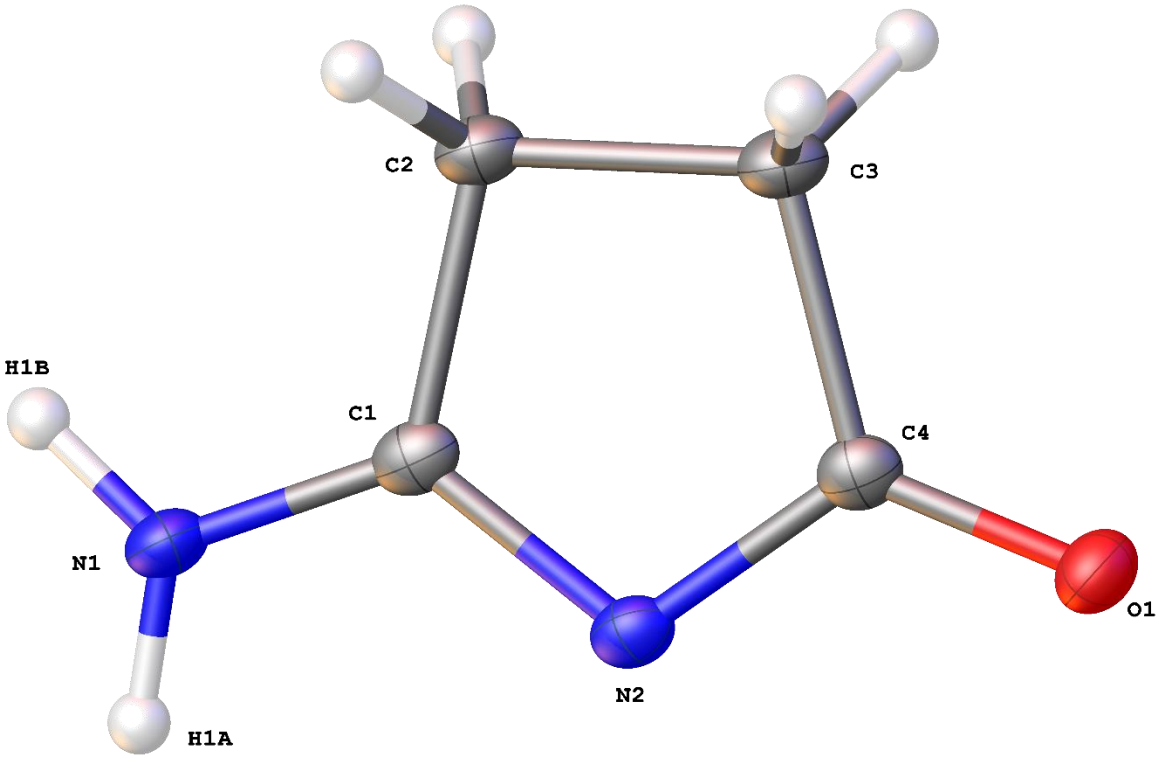

Figure S18. A molecular drawing of HNNO5 shown with 50% probability ellipsoids.

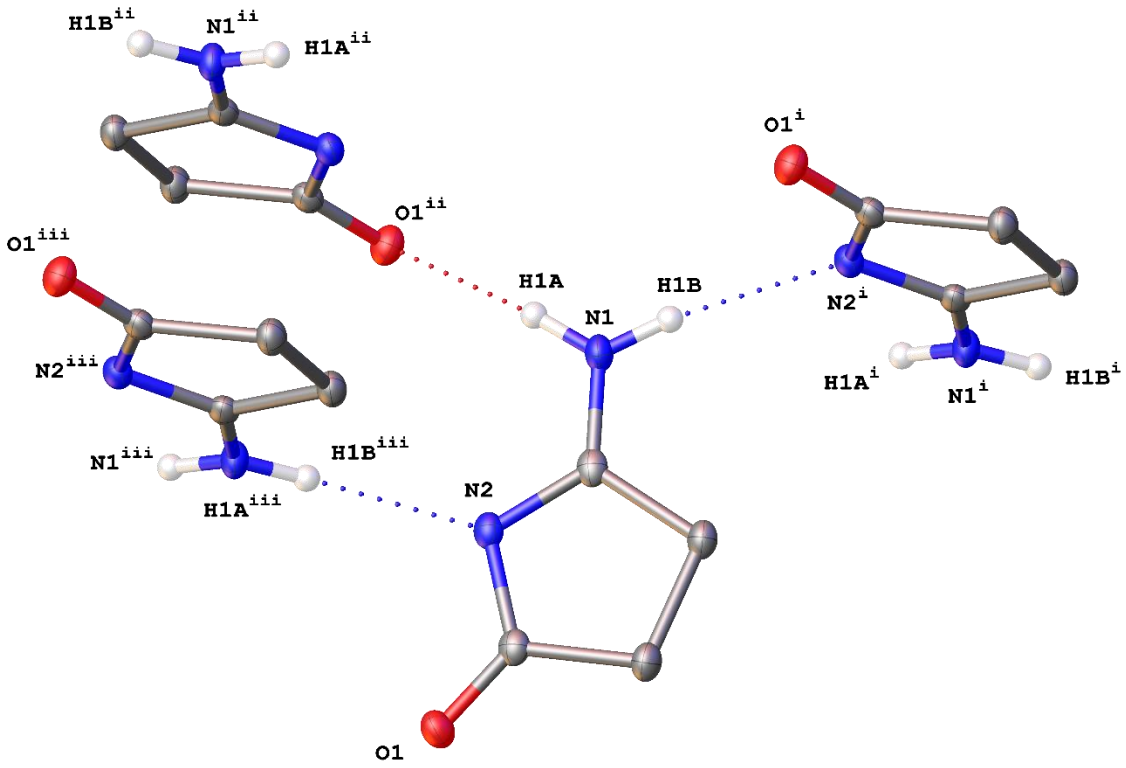

Figure S19. A molecular drawing of HNNO5 shown with 50% probability ellipsoids with emphasis placed on the hydrogen bonding interactions. All H atoms not participating in hydrogen bonding interactions are omitted. [Symmetry code: i = -1/2+X,1/2-Y,-1/2+Z; ii = 3/2-X,-1/2+Y,3/2-Z; iii = 1/2+X,1/2-Y,1/2+Z.]

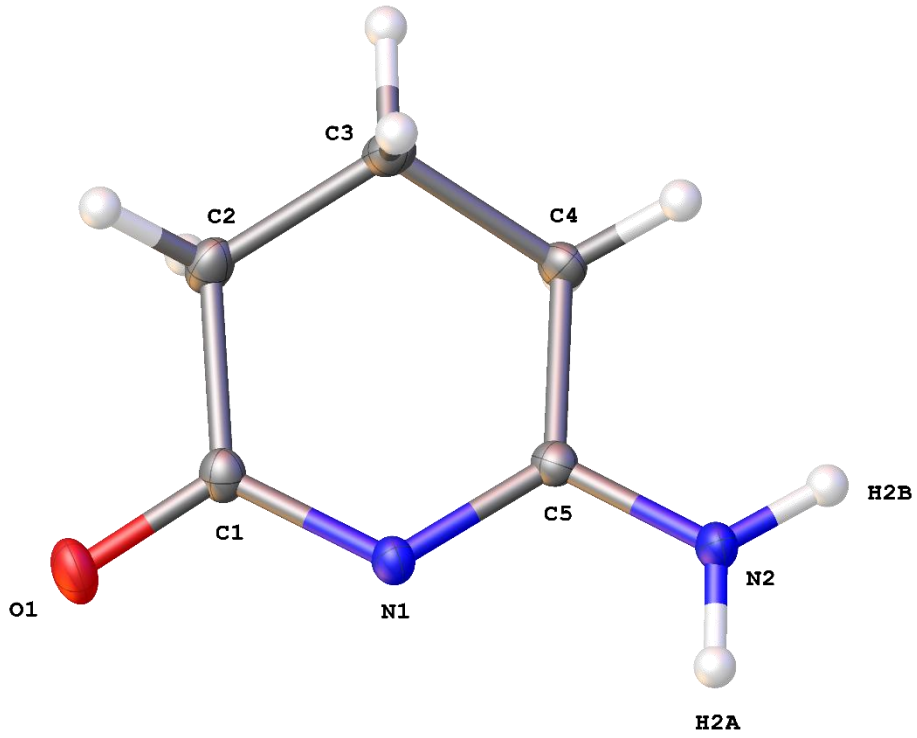

Figure S20. A molecular drawing of HNNO6 shown with 50% probability ellipsoids.

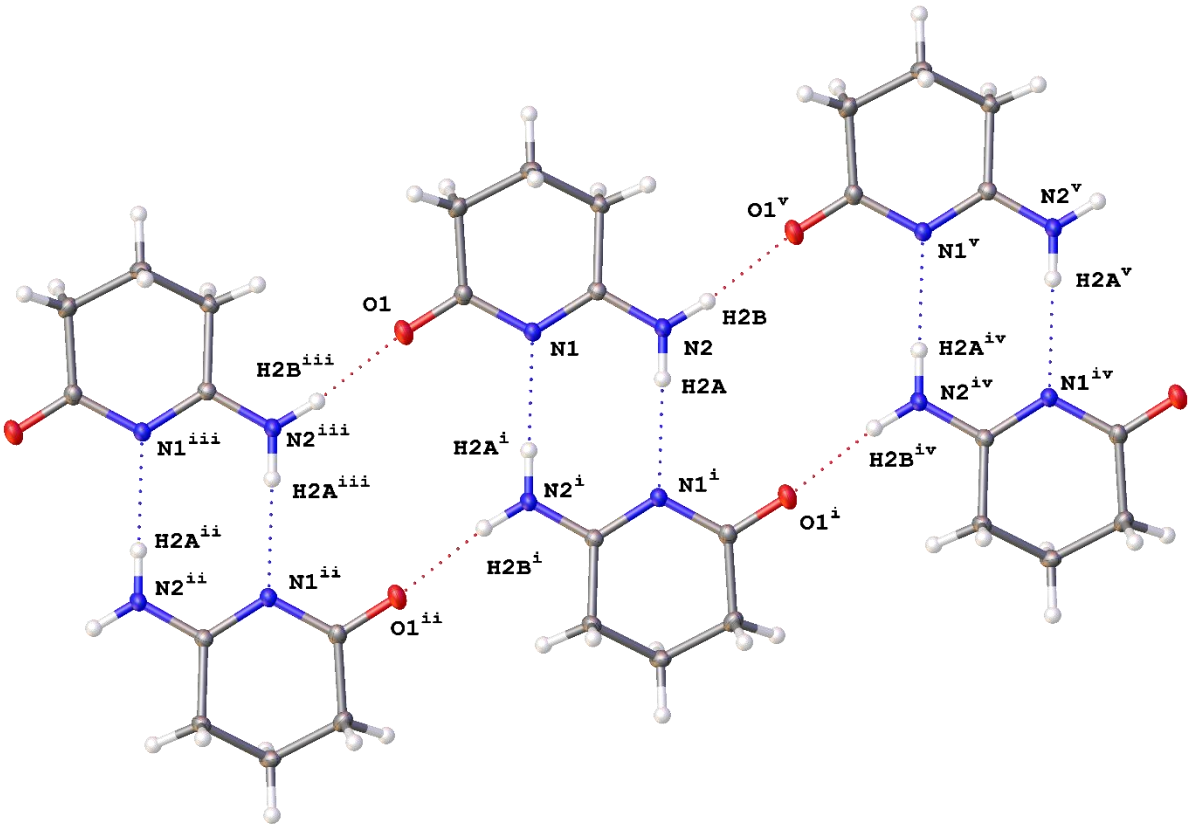

Figure S21. A molecular drawing of HNNO6 shown with 50% probability ellipsoids. Emphasis is placed on the hydrogen bonding system. [Symmetry codes: i=-X,1-Y,1-Z; ii=-X,2-Y,1-Z; iii=+X,1+Y,+Z; iv=-X,-Y,1-Z; v=+X,-1+Y,+Z.]

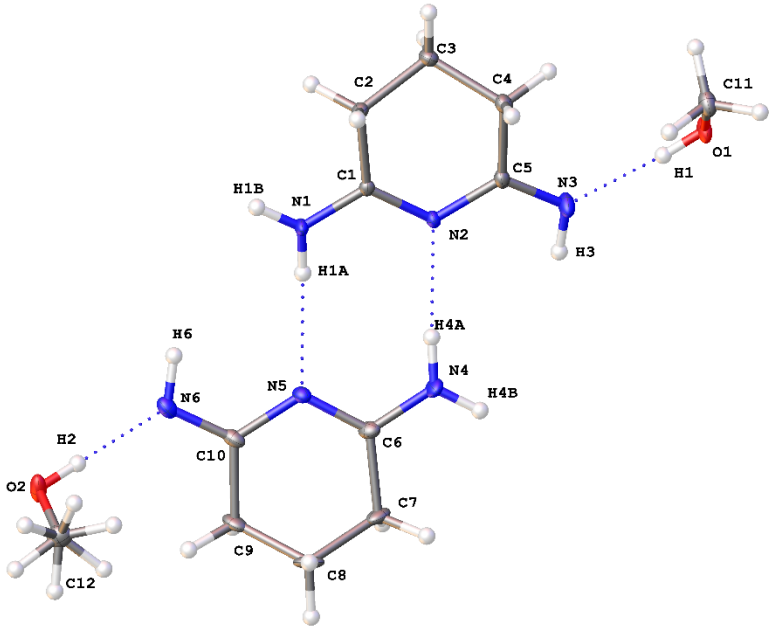

Figure S22. A molecular drawing of the major component of HNNN6 shown with 50% probability ellipsoids.

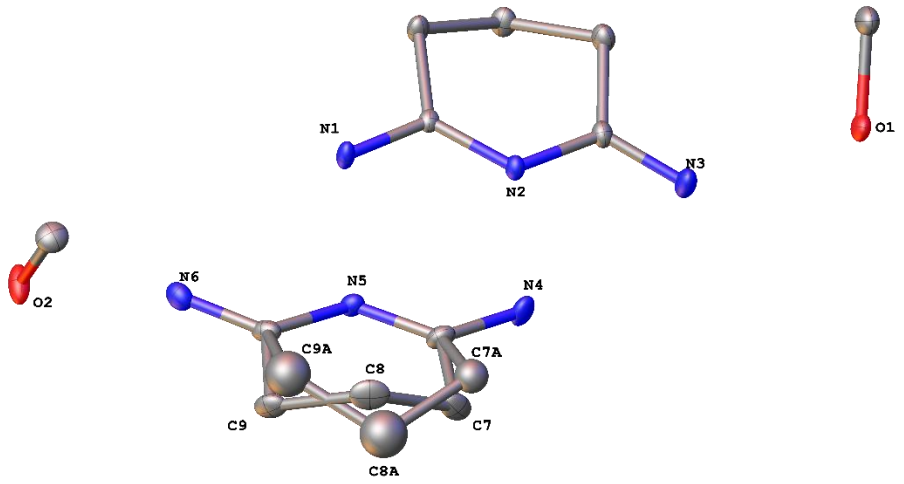

Figure S23. A molecular drawing of HNNN6 shown with 50% probability ellipsoids. All Hydrogen atoms were omitted for clarity. Emphasis was placed on the disordered portion of the ring.

Citations:

Frisch, M. J., Trucks, G. W., Schlegel, H. B., Scuseria, G. E., Robb, M. A., Cheeseman, J. R., Scalmani, G., Barone, V., Petersson, G. A., Nakatsuji, H., Li, X., Caricato, M., Marenich, A. V., Bloino, J., Janesko, B. G., Gomperts, R., Mennucci, B., Hratchian, H. P., Ortiz, J. V., Izmaylov, A. F., Sonnenberg, J. L., Williams, Ding, F., Lipparini, F., Egidi, F., Goings, J., Peng, B., Petrone, A., Henderson, T., Ranasinghe, D., Zakrzewski, V. G., Gao, J., Rega, N., Zheng, G., Liang, W., Hada, M., Ehara, M., Toyota, K., Fukuda, R., Hasegawa, J., Ishida, M., Nakajima, T., Honda, Y., Kitao, O., Nakai, H., Vreven, T., Throssell, K., Montgomery Jr., J. A., Peralta, J. E., Ogliaro, F., Bearpark, M. J., Heyd, J. J., Brothers, E. N., Kudin, K. N., Staroverov, V. N., Keith, T. A., Kobayashi, R., Normand, J., Raghavachari, K., Rendell, A. P., Burant, J. C., Iyengar, S. S., Tomasi, J., Cossi, M., Millam, J. M., Klene, M., Adamo, C., Cammi, R., Ochterski, J. W., Martin, R. L., Morokuma, K., Farkas, O., Foresman, J. B. & Fox, D. J. (2016). *Gaussian 16 Rev. C.01.*

Subchapter 2.2: A Study of the Unusual Absorptivity of $[Mo_2(HNNNy)_4(X)_2](X)_2$ (where x=OAc^- or Cl^- and y=5 or 6) Resulting from Ligand Contribution to a Metal Based LUMO

Michael M. Aristov, Han Geng, James W. Harris, Amelia M. Wheaton, John F. Berry

Department of Chemistry, University of Wisconsin-Madison, 1101 University Ave., Madison, Wisconsin 53706, United States

2.2.0 Author contributions: This work was written by MMA, JWH, and JFB. All experimental data and synthetic work were carried out by MMA, HG, and JWH. Crystallographic characterizations were performed by MMA and AMW.

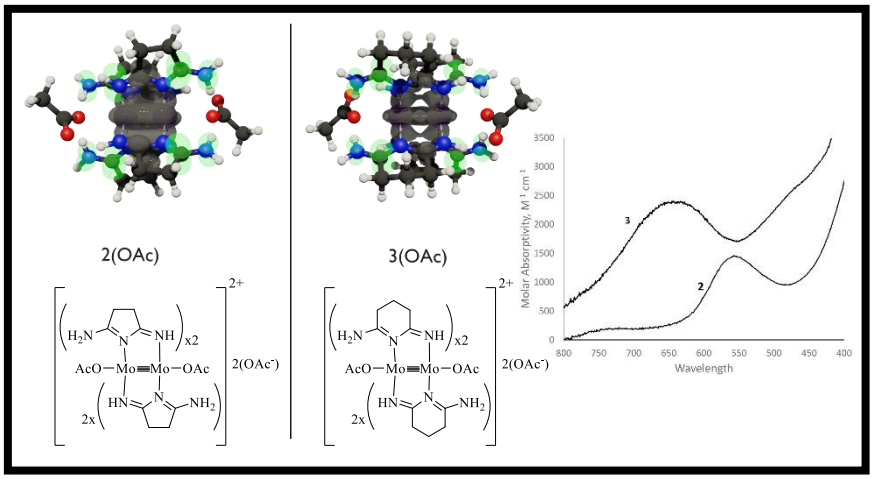

2.2.1 Abstract: Through ligand and anion exchange synthetic techniques, four new dimolybdenum complexes, $[Mo_2(HNNN5)_4(OAc)_2](OAc)_2$, **2(OAc)**, $[Mo_2(HNNN6)_4(OAc)_2](OAc)_2$, **3(OAc)**, $[Mo_2(HNNN5)_4Cl_2]Cl_2$, **2(Cl)**, and $[Mo_2(HNNN6)_4Cl_2]Cl_2$, **3(Cl)**, (HNNN5 = 2-imino-3,4-dihydro-2H-pyrrol-5-amine (succinimidine) and HNNN6 = 6-imino-3,4,5,6-tetrahydro-2-pyridinamine (glutaroimidine)) were prepared and characterized. These compounds are rare examples of quadruply-bonded

Mo_2^{4+} compounds bearing four neutral equatorial bridging ligands. The tetracationic $[Mo_2(HNNN)_4]^{4+}$ core binds two axial anionic ligands, either acetate or chloride, which also engage in hydrogen bonding with the ligand framework. These compounds show unusually high molar absorptivity in the lowest energy transitions in their electronic spectrum, which arises due to mixing of δ-δ* character with MLCT character. These features were identified through a combination of experimental and computational methods.

2.2.2 Introduction:

The ligand 2,2'-dipyridylamine, Hdpa, Chart 1, has been extensively explored for its ability to support multimetallic coordination complexes,[1] particularly trimetallic metal-metal bonded compounds called extended metal atom chains (EMACs) and heterometallic extended metal atom chains (HEMACs).[2-5] We have recently focused on the preparation and properties of new dpa-supported heterometallic complexes containing a Mo≡Mo–M chain, which has led to a rich chemistry of new metal atom incorporation,[6, 7] axial site modification,[8] and stabilization of one-electron oxidized monocationic species.[9, 10] Related Mo≡Mo–M complexes have been investigated for single-molecule conductance by Peng and coworkers.[11]

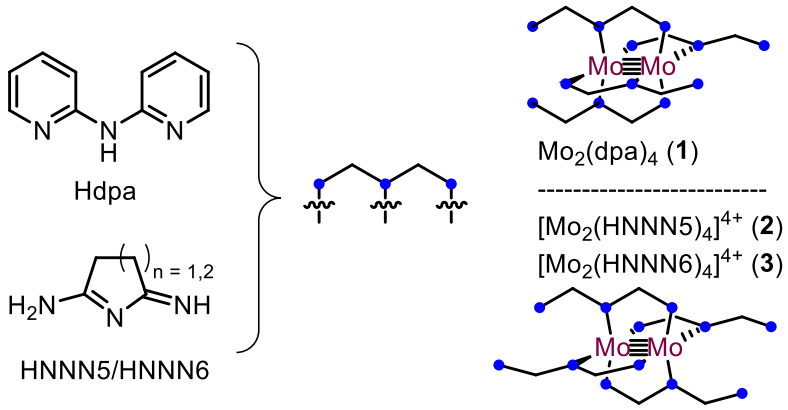

Chart 1. Structures of the Hdpa, HNNN5, and HNNN6 ligands, along with the corresponding Mo_2 complexes.

For the preparation of Mo≡Mo–M HEMACs, we take a metalloligand approach in which the Mo_2 coordination complex $Mo_2(dpa)_4$, **1**, is first synthesized,[12] and then the heterometal is added in a second step.[13, 14] We have also explored alternative ligands containing a mix of S, N, and O donors that have allowed us to make use of hard/soft acid/base concepts to prepare Mo≡Mo–M complexes by self-assembly[15, 16] or metal-atom substitution.[17]

Here, we report our first steps toward the preparation of novel Mo≡Mo–M HEMACs supported by N, N, N donor ligands 2-imino-3,4-dihydro-2H-pyrrol-5-amine (succinimidine), HNNN5, and 6-imino-3,4,5,6-tetrahydro-2-pyridinamine (glutaroimidine), HNNN6 (Chart 1). Although these organic species were known since the mid 1950's,[18, 19] no reported investigations into their coordination chemistry have been performed. Like the SNO ligands described above, the new NNN ligands contain a central, aliphatic ring rather than the conjugated pyridine arms of the dpa ligand. In their free base form, the HNNN ligands are able to tautomerize to give either symmetric or unsymmetric structures; the form shown in Chart 1 is what we have determined to be the major tautomer in the solid state.[20] The HNNN ligands react with $Mo_2(OAc)_4$ preserving this unsymmetric structure and act as neutral bridging ligands to the Mo_2 unit. Thus, while the

HEMAC precursor **1** is a neutral molecule, the Mo_2 cores of HNNN5 and HNNN6 are tetracationic, which bind axial acetate ligands in compounds **2(OAc)** and **3(OAc)**, or chloride ligands, as in compounds **2(Cl)** and **3(Cl)**, respectively. The preparation and properties of these compounds are described here.

2.2.3 Results and Discussion

2.2.3.1 Synthesis. The compounds $[Mo_2(HNNN5)_4(OAc)_2](OAc)_2$ (**2(OAc)**) and $[Mo_2(HNNN6)_4(OAc)_2](OAc)_2$ (**3(OAc)**) were formed in solution through a room temperature reaction between $Mo_2(OAc)_4$ and four molar equivalents of HNNN5 or HNNN6 in anhydrous methanol, Scheme 1. Large crystals of **2(OAc)** (purple) and **3(OAc)** (teal) were obtained by vapor diffusion of anhydrous diethyl ether into the reaction filtrate. The products were found to be readily soluble in protic and/or polar solvents (MeOH, EtOH, DMSO). Additionally, the Mo_2 complexes, like the ligands themselves, were observed to be very moisture sensitive and hygroscopic. Unlike reactions with HSNO,[16] the HNNN5/6 ligands are not deprotonated during the reaction with $Mo_2(OAc)_4$, and instead bridge the Mo_2 core as neutral species. By treating the reaction mother liquor with a saturated solution of LiCl in MeOH, the chloride species, **2(Cl)** and **3(Cl)** could be precipitated. No distinct color change is overserved during the anion exchange. Reactions of **2** with lithium ethoxide, sodium bis(trimethylsilyl)amide, and proton sponge were performed in attempt to deprotonate the coordinated HNNN5 ligands; these reactions yielded mixtures of unidentifiable materials.

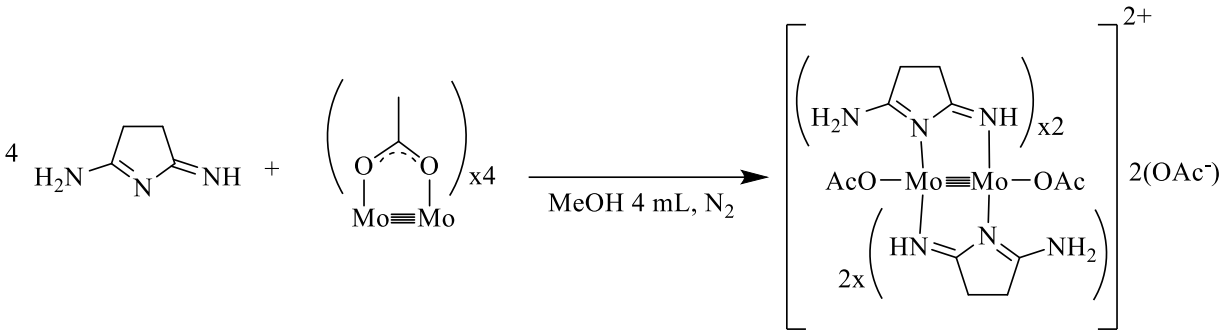

Scheme 1. Reaction of $Mo_2(OAc)_4$ with HNNN5 in the preparation of **2(OAc)**.

2.2.3.2 Structures. The reactions of HNNN5 and HNNN6 with $Mo_2(OAc)_4$ yield a dimolybdenum species with four bridging HNNN ligands bound in a 2,2-*cis* conformation with four acetate anions, as shown in Figure 1. The equatorial ligands each retain three N-H protons in the form of an imine and an amine group, and therefore bind neutrally to the metal core. The acetate anions can be swapped for chloride anions by treating the product with excess LiCl. In the structures of **2(OAc)** and **3(OAc)**, two of the anionic ligands occupy axial sites along the Mo≡Mo vector, while the other two do not coordinate to the Mo_2 unit. In both **2(OAc)** and **3(OAc)**, the axial acetate counterions are stabilized by three intramolecular O···H–N hydrogen bonding interactions, as seen in Figure 1. The axial acetate ligands are also buttressed by intramolecular hydrogen bonding interactions to NH groups of the equatorial ligands, two that target the Mo-bound oxygen atom and one to the

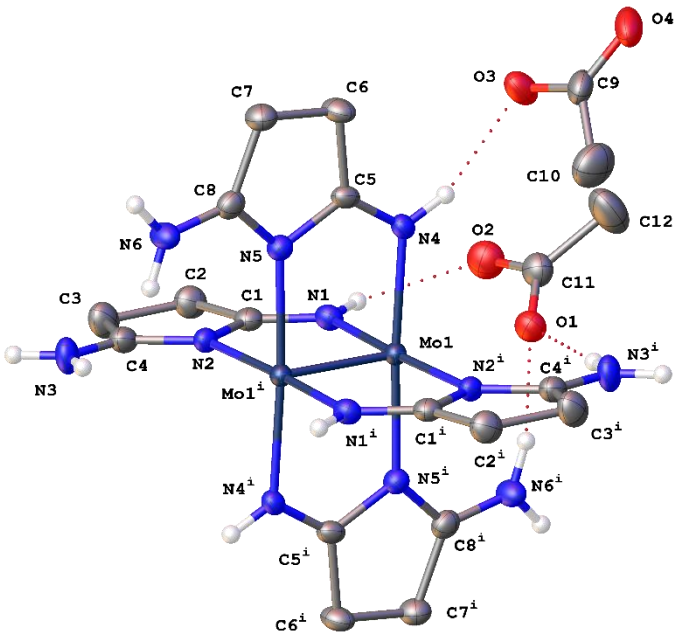

Figure 1. A molecular drawing of **2(OAc)** shown with 50% probability ellipsoids. Most H atoms, solvent molecules, and two acetate counter ions are omitted. [Symmetry code: i = 3/2-X, 3/2-Y, 1-Z].

free oxygen atom. The previous examples of Mo_2 species with axially bound carboxylate counterion do not have any intramolecular hydrogen bonds to stabilize the structures.[21, 22] In the structures with Cl^- counterions, the axial chlorides form a Mo-Mo-Cl bond angle of 171° and 160° in **2(Cl)** and **3(Cl)** respectively. These chloride ligands engage in two hydrogen bonding interactions to the HNNN ligand N–H groups, seen in Figure 2, which cause the deviation from a linear interaction that is more severe for the HNNN6 ligand than the smaller HNNN5 ligand. A similar effect is seen with the acetate counter ions. In all four of these structures, the axial counterions are stabilized by multiple hydrogen bonding interactions with the HNNN ligands. The Mo≡Mo distances in the structures reported here range from 2.10 to 2.14 Å, within the expected range for Mo≡Mo quadruple bonds,[23] with the NNN5 structures having slightly longer Mo≡Mo distances (Table 1), likely an effect of the divergent bite angle of the ligand.[24, 25] The identity of the weakly bound axial ligand has little impact on the Mo≡Mo distance, which is not unexpected. The Mo≡Mo distances nonetheless compare well to those of other Mo_2^{4+} complexes supported only by neutral equatorial ligands (Table 2).[26-32] There is slight asymmetry in the Mo–N bond distances, with the bonds from the Mo atom to the ring N atom being slightly longer (2.17 to 2.22 Å) than the bonds from the Mo atoms to the imino -NH groups (2.12 and 2.15 Å). For **2(OAc)** and **3(OAc)**, the axially bound acetate counter ions were observed to have Mo···O distances of 2.561(3) and

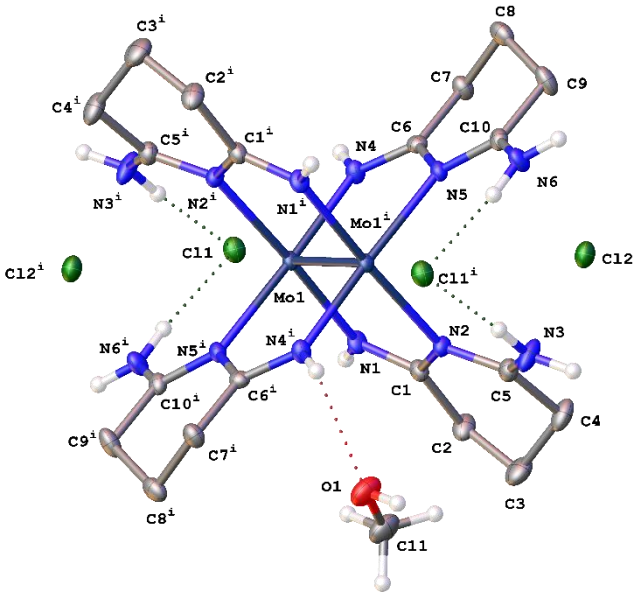

*Figure 2. A molecular drawing of **3(Cl)** shown with 50% probability ellipsoids. All H atoms not bound to solvent or Nitrogen are omitted. [Symmetry code: i=1-X,1-Y,1-Z.]*

2.606(3) Å, respectively, which is ~0.4 Å longer than the equatorial Mo-O bonds, 2.159(3) Å, in $Mo_2(OAc)_4$.[33] These Mo···O distances are, however, shorter than the intramolecular Mo···O distances in $Mo_2(OAc)_4$, 2.645(4) Å.[33] The axial Mo···O distances here are comparable to the Mo···O of 2.575(4) Å to the axial acetate ligand in $Mo_2(OAc)_4 \cdot NaOAc$.[21] Shorter intermolecular Mo···O axial distances are also encountered with trifluoroacetate (2.399(2) Å, 2.3492(13) Å)[34] and pivalate (2.298(5) Å) ligands.[22] The axial Mo···Cl distances in **2(Cl)** and **3(Cl)** (2.933(1) and 2.992(1) Å, respectively) are much longer than the Mo–Cl bonds of ~2.45 Å in the $[Mo_2Cl_8]^{4-}$ ion,[35] and are also slightly longer than those reported previously in Mo≡Mo species with four bridging ligands, 2.71 – 2.89 Å,[16, 36-38] and Cl-ligated Mo_2M HEMACs supported by the dpa ligand, 2.63 – 2.79 Å.[8-10, 13, 14]

2.2.3.3 Spectroscopic Properties. As was noted in our report of the free HNNN5 and HNNN6 ligands,[20] the ^{1}H NMR spectra contain two sets of signals. The main signals are indicative of a symmetric tautomer of the ligands, and minor signals arise from the unsymmetric tautomer, which is the form of the ligands when bound to Mo_2^{4+}. The ^{1}H NMR signals for the unsymmetric tautomers are complex, indicating a second order splitting pattern. Similar NMR features are observed for the Mo_2 complexes **2(OAc)** and **3(OAc)**. Most easily identifiable in these spectra are the signals corresponding to the acetate groups, which appear as singlets at 1.78 and 1.73 ppm for **2(OAc)** and **3(OAc)**, respectively. The fact that we do not see distinct signals for coordinated vs outer-sphere acetate groups indicates that the acetate ions exchange rapidly

Table 1. Selected bond distances and angles in the Mo_2 complexes examined here.

Compound:	Mo–Mo (Å)	Mo–N_{ring} (Å)	Mo–N_{term} (Å)	Mo–Axial (Å)	Mo-Mo-Axial (°)	Reference
1	2.098(1)	2.179[7]	2.166[7]	NA	NA	[12]
2(OAc)	2.1354(8)	2.180[6]	2.152[6]	2.561(3)	178.52(6)	This work
2(Cl)	2.1318(8)	2.181[6]	2.151[6]	2.933(1)	171.09(3)	This work
3(OAc)	2.104(1)	2.197[4]	2.130[4]	2.606(3)	166.91(4)	This work
3(Cl)	2.1115(6)	2.219[4]	2.127[5]	2.992(1)	160.02(2)	This work

relative to the NMR timescale. The signals for the ligand methylene groups are identifiable, if not assignable, and integrate with the proper ratio against the acetate signals. Due to the idealized C_{2h} molecular symmetry, all four HNNN ligands for each complex are chemically equivalent. However, within each ligand, all proton signals are inequivalent with each CH_2 group being a diastereotopic pair. This situation leads to second order multiplet splitting patterns that we are unable to deconvolute.

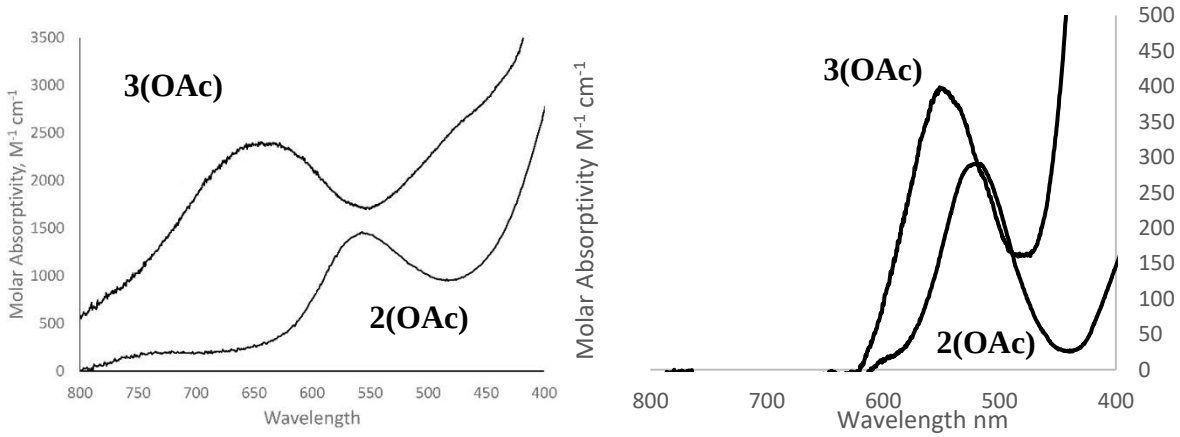

Figure 3. Visible absorption spectra of **2(OAc)** and **3(OAc)** Left: In DMSO, Right in MeOH. These spectra highlight the region of the δ-δ* transitions.

In DMSO, the electronic spectra of **2(OAc)** and **3(OAc)** show several features at ~260, ~296, ~347, and ~553 nm and ~296, ~321, 394, ~464, and 628 nm, respectively, across the visible and ultraviolet range, with the lowest energy bands, featured in Figure 3, most likely being the Mo_2 δ-δ* transitions. The δ-δ* transition for **3(OAc)** at 632 nm is significantly lower in energy than that for **2(OAc)** at 533 nm, and it's also 65% higher in intensity. However, in MeOH, the molar absorptivity sharply decreases, and for **2(OAc)** and **3(OAc)**, the peak excitation shift from ~553 to ~520 and from 632 nm to ~550 nm respectively. Interestingly, the charge transfer bands in

3(OAc) become less intense than those of **2(OAc)** in these dilute MeOH solutions as compared to the excitations in the DMSO solution. The full MeOH UV-Vis spectra can be found in the supplemental information. A comparison between these species and Mo_2 complexes bearing neutral ligands is shown in Table 2. These unusual features prompted an investigation of the electronic structure of the compounds using DFT and time-dependent DFT (TD-DFT) methods.

2.2.3.4 Computational Analysis. We used crystallographic coordinates as a starting point for computational analysis of **2(OAc)** and **3(OAc)** and focused on the structures with axial acetate ligands. The geometry optimized structures of **2(OAc)** and **3(OAc)** show excellent agreement with the experimental crystal structures as seen in Table 3. The Mo≡Mo bond distances optimized to 2.142 Å and 2.118 Å as compared to the distances 2.1354(8) Å and 2.104(1) Å found experimentally for **2(OAc)** and **3(OAc)**, respectively. Similar trends were observed in the asymmetric binding distances for the Mo-N_{ring} and Mo-N_{term} as were described in the crystallographic section. The Mo···O distances to the axial acetate ligands optimized to 2.615 Å for **2(OAc)** and 2.558 Å for **3(OAc)**, in good agreement with the experimental structures.

Table 2. Structural and electronic features of tetracationic Mo_2 complexes.[a]

Compound	Mo–Mo, Å	δ-δ*, nm (ε, M^{-1} cm^{-1})	Ref
$[Mo_2(NH_3)_8]^{4+}$	NR	400	26
$[Mo_2(R\text{-}1,2\text{-propanediamine})_4]^{4+}$	NR	~475	27
$[Mo_2(en)_4]^{4+}$	NR	478 (483)	28
$[Mo_2(H_2O)_8]^{4+}$	NR	504 (337)	28
$[Mo_2(DMF)_8]^{4+}$	NR	514	26
$[Mo_2(HDPyF)_2(NCCH_3)_4]^{4+}$	2.13	533	29
$[Mo_2(NCCH_3)_{10}]^{4+}$	2.19	597 (1127)	30
$[Mo_2(NP)_4]^{4+}$	2.10	699 (717)	31
$[Mo_2(NP\text{-}tz)_2(NCCH_3)_4]^{4+}$	2.17	747 (1800)	32
$[Mo_2(NP\text{-}fu)_2(NCCH_3)_4]^{4+}$	2.12	765 (380)	32
2(OAc)	2.13	553 (1400)	This work
3(OAc)	2.10	632 (2400)	This work

[a]Abbreviations: NR = not reported, en = ethylenediamine, DMF = N,N-dimethylformamide, HDPyF = di-2-pyridylformamidine, NP = 1,8-naphthyridine, NP-tz = 2-(2-thiazolyl)-1,8-naphthyridine; NP-fu = 2-(2-furyl)-1,8-naphthyridine.

Table 3. Selected bond lengths and angles from the computational and experimental structures of **2(OAc)** and **3(OAc)**.

Compound	Mo–Mo Å	Mo–N_{ring} Å	Mo–N_{term} Å	Mo–Axial Å	Mo-Mo-O °
2(OAc) crystal	2.1354(8)	2.180[6]	2.152[6]	2.56r1(3)	178.52(6)
2(OAc) Comp	2.142	2.173	2.122	2.615	177
3(OAc) crystal	2.104(1)	2.197[4]	2.130[4]	2.606(3)	166.91(4)
3(OAc) Comp.	2.118	2.210	2.108	2.558	167

Frequency calculations showed no imaginary modes, indicating that an energetic minimum was reached during the optimizations.

The optimized structures were used to predict the electronic transitions using TD-DFT. Consistent with the experimental data, TD-DFT predicts four major transitions; a comparison of the experimental and computational electronic spectra for **2(OAc)** in DMSO can be seen in Figure 4, and the corresponding data for **3(OAc)** are found in the SI. To achieve the best agreement between computational and experimental results, we found that inclusion of the two axial acetates was necessary.

From the TD-DFT results, we assign the four electronic features as HOMO-LUMO ($\delta_u \rightarrow \delta_g^*$) charge transfer (CT) for the lowest energy peak, metal-to-equatorial-ligand CT (MLCT) for both middle features, and metal-to-axial-ligand (MLCT) for the high energy feature. The electron density difference map (EDDM) plots of these features are seen in

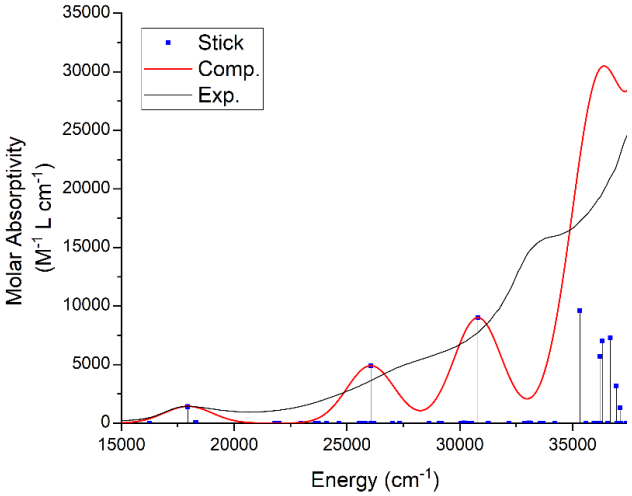

Figure 4. The experimental and TD-DFT-calculated electronic spectra of **2(OAc)** overlayed with each other.

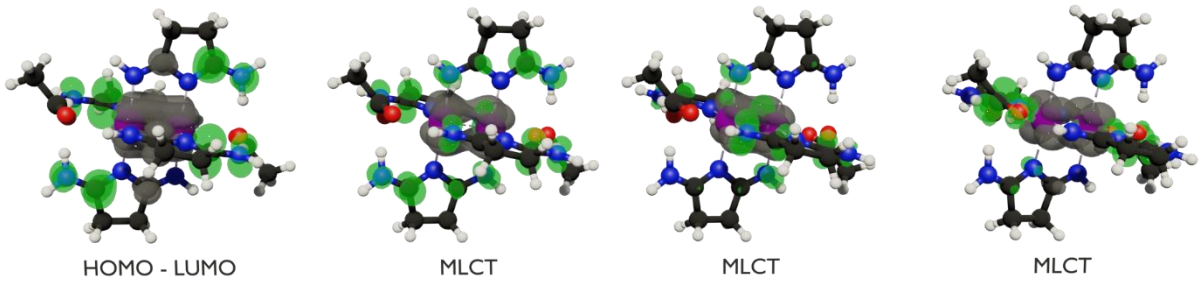

Figure 5. EDDM plots for the four computationally predicted excitations in **2(OAc)**. The right two plots illustrate the importance of including the axially bound acetate in the calculations.

Figure 5, and a comparison between experimental and calculated electronic spectra is given in Figure 5. Of particular interest to us is the lowest energy feature, which is the $\delta_u \rightarrow \delta_g^*$ transition as anticipated. However, the LUMO contains significant contributions from the terminal, non-metal-bound amine, as seen in Figure 3. In **2(OAc)** the LUMO orbital is comprised of only 40.8% Mo character, with 59.2% equatorial-ligand character with most of that character being in out-of-phase *p*-orbitals on the C-NH_2 terminal group. This was also noted in **3(OAc)** where the LUMO was composed of 35.4% Mo character with 64.6% equatorial-ligand character. Notably, the LUMO of neither **2(OAc)** nor **3(OAc)** had axial acetate character. Because of the orbital composition, the lowest energy excitation has significant MLCT character, which results in a more intense and lower energy HOMO-LUMO transition than observed for most other Mo_2^{4+} complexes. The only notable difference between the HOMO-LUMO transitions of **2(OAc)** and **3(OAc)** is the inclusion of a small contribution (3.4%) of a $\sigma \rightarrow \delta^*$ transition in **3(OAc)**. This $\sigma \rightarrow \delta^*$ transition is not observed as being a component of the lowest energy excitation in **2(OAc)**.

2.2.3.5 Concentration Dependent Color-Shift: To understand the nature of the observed concentration dependent molar absorptivity/color we examined both the crystal structures and the TD-DFT results. In extremely concentrated solutions, the colors of **2(OAc)** and **3(OAc)** match the colors of their solids, purple and green respectively. However, as additional solvent is

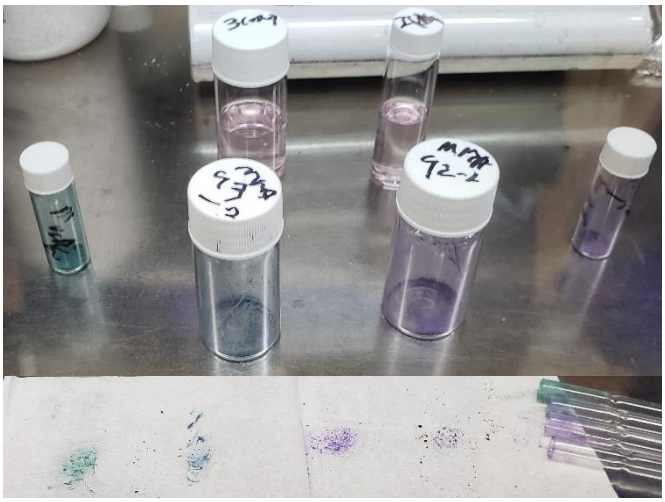

Figure 4. Top Left: A pink dilute solution of 3(OAc) in MeOH. Top right a pink dilute solution of 2(OAc). These solutions were used to collect the spectra shown in Figure 3. The solids from left to right are 3(OAc) (green), 3(Cl) (blue), 2(Cl) purple, 2(OAc) dark purple.

added, solutions of these species become faint pink and indistinguishable. The colors of all these solids, and the mentioned pink solutions are shown in Figure 6. When these pink solutions are allowed to dry, they return to the purple and green of **2(OAc)** and **3(OAc)**. These reversible color changes are noted in both MeOH and DMSO, however, DMSO is unable to dissolve enough of either **2(OAc)** or **3(OAc)** to reach the concentrations necessary to see the purple and green coloration. In the crystal structures, both **2(OAc)** and **3(OAc)** have two axially bound, inner sphere counter ions and two outer-sphere acetate counter ions. All four of these counter ions engaged in hydrogen bonding interactions with the terminal -NH_2, a portion of the ligand that we previously showed to be a part of the both the LUMO orbital and the $\delta_u \rightarrow \delta_g^*$ excitation responsible for the complexes' color. We hypothesized that in dilute solutions of these species, the out-sphere and axial counterions are stripped from the $[Mo_2(NNNx)]^{4+}$ core, and therefore they lose their hydrogen bonding interactions with the terminal -NH_2. The loss of this hydrogen bonding interaction could be responsible for the observed color change. To test this, we performed additional geometry optimizations, frequency calculations, and TD-DFT calculations on $[Mo_2(HNNNX)_4]^{4+}$. From these calculations, we noted a distinct decrease blue shift in energies of the δ-δ* transition, 693 nm (1409 M^{-1} cm^{-1}) → 630 nm (1419 M^{-1} cm^{-1}) and 775 nm (2205 M^{-1} cm^{-1}) → 667 nm (2150 M^{-1} cm^{-1}) for **2(OAc)** and **3(OAc)** as the axial acetate

anions was excluded. However, there was no observed changed in molar absorptivity for these features.

2.2.4 Conclusion. We describe here a set of new cationic dimolybdenum species: **2(OAc)**, **2(Cl)**, **3(OAc)**, and **3(Cl)**. These species show unusually low energy δ-δ* features in their electronic spectra, and these features were identified through a combination of experimental and computational methods to also contain significant MLCT character. The accumulation of electron density on the terminal amine group in the excited state may provide use in future photochemical reactivity studies. In future work, we aim to use this material as a starting material for the generation of novel HEMAC species.

2.2.5 Acknowledgements. We thank NSF for funding via CHE-1953294, and we thank the NSF-GRFP for funding via DGE-1747503. NMR spectrometers were supported by NSF grant CHE-1048642 and a generous gift from Paul J. and Margaret M. Bender. The mass spectrometer was supported by NIH grant 1S10 OD020022-1. The Bruker D8 VENTURE Photon III X-ray diffractometer was partially funded by NSF Award #CHE-1919350 to the UW–Madison Department of Chemistry. The Bruker Quazar APEX2 was purchased by the UW–Madison Department of Chemistry with a portion of a generous gift from Paul J. and Margaret M. Bender. Molecular orbital graphics were generated with UCSF Chimera, developed by the Resource for Biocomputing, Visualization, and Informatics at the University of California, San Francisco, with support from NIH grant P41-GM103311.

2.2.6 Associated Content

Supporting information

The Supporting Information contains information on computational methods, physical measurements, general methods, synthesis, figures for NMR (Figures S1-S2), figures for IR (Figures S3-S4), additional electronic absorption spectra (Figures S5), crystallographic information and figures (Figures S5-10), and optimized XYZ coordinates for all calculated structures (Tables S2 and S3).

CCDC codes 2196147-2196150 contain the supplementary crystallographic data for this paper.

Corresponding Authors

John F. Berry – berry@chem.wisc.edu

ORCID

Michael M. Aristov**:** 0000-0003-1161-5126
Han Geng: 0000-0002-8433-9671
Amelia M. Wheaton: 0000-0002-7743-9922
James W. Harris: 0000-0003-1941-7407
John F. Berry: 0000-0002-6805-0640

2.2.7 References.

1. Brogden, D. W.; Berry, J. F., Coordination Chemistry of 2,2'-Dipyridylamine: The Gift That Keeps on Giving. *Comments Inorg. Chem.* **2016,** *36* (1), 17-37.
2. Berry, J. F.; Roy, M., 2-Aminopyridine and Related Ligands to Support Metal-Metal Bonded Compounds. In *Comprehensive Coordination Chemistry III (Third Edition)*, 2021; Vol. 1.
3. Chipman, J. A.; Berry, J. F., Paramagnetic Metal–Metal Bonded Heterometallic Complexes. *Chem. Rev.* **2020,** *120* (5), 2409-2447.
4. Hua, S.-A.; Cheng, M.-C.; Chen, C.-h.; Peng, S.-M., From Homonuclear Metal String Complexes to Heteronuclear Metal String Complexes. *Eur. J. Inorg. Chem.* **2015,** *2015* (15), 2510-2523.
5. Cotton, F. A.; Murillo, C. A.; Walton, R. A., *Multiple Bonds Between Metal Atoms*. Springer Science & Business Media: 2005.
6. Brogden, D. W.; Christian, J. H.; Dalal, N. S.; Berry, J. F., Completing the Series of Group VI Heterotrimetallic $M_2Cr(dpa)_4Cl_2$ (M_2= Cr_2, Mo_2, MoW and W_2) Compounds and Investigating Their Metal–Metal Interactions Using Density Functional Theory. *Inorg. Chim. Acta* **2015,** *424*, 241-247.
7. Brogden, D. W.; Berry, J. F., Heterometallic Multiple Bonding: Delocalized Three-Center σ and π Bonding in Chains of 4d and 5d Transition Metals. *Inorg. Chem.* **2014,** *53* (21), 11354-11356.
8. Chipman, J. A.; Berry, J. F., Facile axial ligand substitution in linear Mo≣ Mo–Ni complexes. *Inorg. Chem.* **2018,** *57* (15), 9354-9363.
9. Chipman, J. A.; Berry, J. F., Extraordinarily Large Ferromagnetic Coupling (J≥ 150 cm− 1) by Electron Delocalization in a Heterometallic Mo≣ Mo− Ni Chain Complex. *Chemistry–A European Journal* **2018,** *24* (7), 1494-1499.
10. Brogden, D. W.; Berry, J. F., Heterometallic Second-Row Transition Metal Chain Compounds in Two Charge States: Syntheses, Properties, and Electronic Structures of $[Mo–Mo–Ru]^{6+/7+}$ Chains. *Inorg. Chem.* **2015,** *54* (15), 7660-7665.

11. Chang, W.-C.; Chang, C.-W.; Sigrist, M.; Hua, S.-A.; Liu, T.-J.; Lee, G.-H.; Jin, B.-Y.; Chen, C.-h.; Peng, S.-M., Nonhelical heterometallic [Mo2M(npo)4(NCS)2] string complexes (M = Fe, Co, Ni) with high single-molecule conductance. *Chem. Commun.* **2017,** *53* (63), 8886-8889.
12. Suen, M.-C.; Wu, Y.-Y.; Chen, J.-D.; Keng, T.-C.; Wang, J.-C., Dimolybdenum Complexes of Bis(2-pyridyl)amine (Hdpa) :Ligand and its Anion (dpa−); Transformation of Chelating η2-Hdpa to Bridging η2-dpa−. *Inorg. Chim. Acta* **1999,** *288* (1), 82-89.
13. Nippe, M.; Victor, E.; Berry, J. F., Do Metal–Metal Multiply-Bonded "Ligands" Have a trans Influence? Structural and Magnetic Comparisons of Heterometallic Cr≡Cr··· Co and Mo≡Mo··· Co Interactions. *Eur. J. Inorg. Chem.* **2008,** (36), 5569 - 5572.
14. Nippe, M.; Bill, E.; Berry, J. F., Group 6 Complexes with Iron and Zinc Heterometals: Understanding the Structural, Spectroscopic, and Electrochemical Properties of a Complete Series of MM··· M' Compounds. *Inorg. Chem.* **2011,** *50* (16), 7650-7661.
15. Dolinar, B. S.; Berry, J. F., Lewis Acid Enhanced Axial Ligation of $[Mo_2]^{4+}$ Complexes. *Inorg. Chem.* **2013,** *52* (8), 4658-4667.
16. Dolinar, B. S.; Kozimor, S. A.; Berry, J. F., $K_3[Mo_2(SNO5)_4Cl]_3[Mo_2(SNO5)_4]$: the First example of a Heterometallic Extended Metal Atom Node (HEMAN). *Dalton Transactions* **2016,** *45* (44), 17602-17605.
17. Dolinar, B. S.; Berry, J. F., Influence of Lewis acid charge and proximity in MoMo··· M linear chain compounds with M= Na^+, Ca^{2+}, Sr^{2+}, and Y^{3+}. *Polyhedron* **2016,** *103*, 71-78.
18. Elvidge, J. A.; Linstead, R. P., Heterocyclic imines and amines. Part III. Succinimidine. *Journal of the Chemical Society (Resumed)* **1954,** (0), 442-448.
19. Elvidge, J. A.; Linstead, R. P.; Salaman, A. M., 37. Heterocyclic imines and amines. Part IX. Glutarimidine and the imidine from α-phenylglutaronitrile. *Journal of the Chemical Society (Resumed)* **1959,** (0), 208-215.
20. Aristov, M. M.; Geng, H.; Harris, J. W.; Berry, J. F., Updated Synthesis and Characterization of Imidines: Using Crystallographic Characterization to Identify Tautomers and Localized Systems of π-Bonding. *Manuscript in Preparation* **2022**.
21. Kepert, D.; Skelton, B. W.; White, A. H., Crystal Structure of the Acetic Acid Solvate of the Molybdenum (II) Acetate/Sodium Acetate Double Salt. *Aust. J. Chem.* **1980,** *33* (8), 1847-1852.
22. Cayton, R.; Chacon, S.; Chisholm, M. H.; Folting, K., The Dimolybdenum Pentapivalate Anion: X-ray Crystal Structure and Dynamic Solution Behaviour and Comments on the Substitutional Lability of Containing Compounds. *Polyhedron* **1993,** *12* (4), 415-422.
23. Cotton, F. A.; Daniels, L. M.; Hillard, E. A.; Murillo, C. A., The Lengths of Molybdenum to Molybdenum Quadruple Bonds: Correlations, Explanations, and Corrections. *Inorg. Chem.* **2002,** *41* (9), 2466-2470.
24. Cotton*, F. A.; Daniels, L. M.; Murillo*, C. A.; Zhou, H.-C., The Effect of Divergent-Bite Ligands on Metal–Metal Bond Distances in Some Paddlewheel Complexes. *Inorg. Chim. Acta* **2000,** *300-302*, 319-327.
25. Cotton, F. A.; Murillo, C. A.; Wang, X.; Wilkinson, C. C., Homologues of the Easily Ionized Compound Mo2(hpp)4 Containing Smaller Bicyclic Guanidinates. *Inorg. Chem.* **2006,** *45* (14), 5493-5500.
26. Comrie, A. G.; McVITIE, A.; Peacock, R. D., Preparation and Spectroscopic Characterization of the Elusive Octamminodimolybdenum Cation: $[Mo_2(NH_3)_8][TFMS]_4$. *Polyhedron* **1994,** *13* (2), 193-197.
27. Peacock, R. D.; Fraser, I. F., Preparation and Circular Dichroism Spectrum of the Tetrakis ((R)-1, 2-Diaminopropane) Dimolybdenum Cation: Evidence for a Bridged Structure. *Inorg. Chem.* **1985,** *24* (7), 988-989.
28. Bowen, A.; Taube, H., New Molybdenum(II) and Molybdenum(III) Species. *Inorg. Chem.* **1974,** *13* (9), 2245-2249.
29. Yen, Y.-S.; Yeh, C.-W.; Chen, J.-D.; Wang, J.-C., Dimolybdenum Complex Containing N–H··· Mo Interactions. Synthesis and Structure of cis-$[Mo_2(HDpyF)_2(CH_3CN)_4](BF_4)_4$ and its Transformation to

$[Mo_2(DpyF)_2(py)_4](BF_4)_2$ [HDpyF= Bis (2-pyridyl) formamidine; py= pyridine]. *J. Cluster Sci.* **2008,** *19* (1), 109-119.
30. Cotton, F. A.; Wiesinger, K. J., Synthesis and Characterization of Octaacetonitriledimolybdenum (II) Tetrafluoroborate. *Inorg. Chem.* **1991,** *30* (4), 871-873.
31. Døssing, A.; Larsen, S.; van Lelieveld, A.; Bruun, R. M., Preparation and Crystal Structure of Tetrakis-(u-1, 8-naphthyridine) Dimolybdenum (II). *Acta Chem. Scand.* **1999,** *999* (53), 230-234.
32. Patra, S. K.; Kannan, M.; Dunbar, K. R.; Bera, J. K., Role of Axial Donors in the Ligand Isomerization Processes of Quadruply Bonded Dimolybdenum (II) Compounds. *Inorg. Chem.* **2008,** *47* (6), 2212-2222.
33. Cotton, F.; Mester, Z.; Webb, T., Dimolybdenum Tetraacetate. *Acta Crystallographica Section B: Structural Crystallography and Crystal Chemistry* **1974,** *30* (11), 2768-2770.
34. Zhang, G.; Zhao, J.; Raudaschl-Sieber, G.; Herdtweck, E.; Kühn, F. E., Syntheses and Characterization of Dimolybdenum and Dirhodium Complexes Containing 2-pyridylphosphine Ligands. *Polyhedron* **2002,** *21* (17), 1737-1746.
35. Brencic, J. V.; Cotton, F. A., Octachlorodimolybdate (II) ion. Species with a quadruple metal-metal bond. *Inorg. Chem.* **1969,** *8* (1), 7-10.
36. Udović, B.; Leban, I.; Šegedin, P., The Chaotropically Synthesized Dimolybdenum (II, II) Compound. *Croat. Chem. Acta* **1999,** *72* (2-3), 477-499.
37. Apfelbaum, F.; Bino, A., Complexes of Dimolybdenum(II) with DL-Amino Acids. 2. Crystal Structure of Compounds Containing DL-Valine and DL-Leucine. *Inorg. Chim. Acta* **1989,** *155* (2), 191-195.
38. Wu, Y.-Y.; Chen, J.-D.; Liou, L.-S.; Wang, J.-C., Quadruply Bonded Dimolybdenum Complexes Containing Pairs of Bridging Diphosphine and Acetate Ligands; Synthesis and Structural Characterization of Trans-$Mo_2Cl_2(OAc)_2(\mu\text{-dppa})_2$ and its Transformation to $Mo_2Cl_4(\mu\text{-dppa})_2$, where dppa is N,N-bis(diphenylphosphino)amine. *Inorg. Chim. Acta* **1997,** *258* (2), 193-199.

Supporting Information for Subchapter 2.2: A Study of the Unusual Absorptivity of $[Mo_2(HNNNy)_4(X)_2](X)_2$ (where x=OAc^- or Cl^- and y=5 or 6) Resulting from Ligand Contribution to a Metal Based LUMO

Michael M. Aristov, Han Geng, James W. Harris, Amelia M. Wheaton, John F. Berry

Department of Chemistry, University of Wisconsin-Madison, 1101 University Ave., Madison, Wisconsin 53706, United States

Email: berry@chem.wisc.edu

Table of Contents:

1. Computational Methods
2. Synthesis
3. Characterization
    a. NMR
    b. IR
    c. UV-VIS
    d. Crystal Structures
4. Geometry Optimized Coordinates

2.2.8.1 Computational Methods:

Geometry optimizations, frequency calculations, single-point (SP) calculations, and Time-Dependent DFT (TD-DFT) calculations, were carried out using ORCA version 5.0.1.[1, 2] For the geometry optimizations and frequency calculations, the BP86 exchange-correlation functional was used.[3-6] For single point and TD-DFT calculations, the B3LYP functional was used.[4-7] The TD-DFT predicted electronic spectra of **2(OAc)** and **3(OAc)** were shifted by +3512 cm^{-1} and +2496 cm^{-1} respectively to provide the best comparison with their experimental spectra. Crystallographic coordinates, excluding solvent molecules and outer sphere anions were used as the starting point for all geometry optimizations. All geometric parameters were optimized. All calculations used the resolution of identity and correlation of spheres, RIJCOSX approximation.[8-10] The segmented all-electron relativistic contracted (SARC) basis set, SARC-DKH-TZVPP,[11-13] was used for the Mo atoms. The def2-SVP basis set was used for all other atoms.[14] The auxiliary coulomb basis set, def2/J,[15] was used for all atoms. Dispersion corrections to the calculations were accounted for with the atom pairwise dispersion correction employing the Becke-Johnson damping scheme (D3BJ).[16, 17] All molecules were calculated in their open shell singlet state using unrestricted Kohn Sham (UKS) theory. The grids for all atoms were set to 6. Frequency calculations were performed by numerical differentiation with a central-differences increment of 0.01. Visualizations of the orbitals from self-consistent field calculations were carried out with the UCSF Chimera package.[18] Structure comparisons were made using Mercury.[19] All data were plotted with OriginPro.[20]

2.2.8.2 General Methods: $Mo_2(OAc)_4$ was synthesized from $Mo(CO)_6$, acetic acid, and acetic anhydride according to literature procedures.[21, 22] The HNNN5 and HNNN6 ligands were synthesized according to literature procedures and used without additional purification and were stored in a nitrogen atmosphere glovebox.[23] Anhydrous methanol was purchased from Sigma-Aldrich and dried over CaH_2 and stored under N_2 before use. Inhibitor-free anhydrous diethyl ether was purchased from Sigma-Aldrich, stored over molecular sieves, and filtered before use. All disposable glassware was washed with milli-q water and acetone prior to use. All synthetic work was performed in a nitrogen atmosphere glovebox.

Synthesis of **2(OAc)** ($[Mo_2(HNNN5)_4(OAc)_2](OAc)_2$)

A 12 mL scintillation vial was loaded with 105 mg (0.245 mmol) of $Mo_2(OAc)_4$. A second 12 mL scintillation vial was loaded with 102 mg (1.05 mmol) of HNNN5. To each vial, ~2.5 mL of anhydrous MeOH was added. The ligand fully dissolved whereas $Mo_2(OAc)_4$ did not. The dissolved ligand was then transferred via pipet into the vial with the suspended $Mo_2(OAc)_4$ and a stir bar was added. The solution was allowed to stir overnight at room temperature, during which time all solid dissolved and the reaction mixture turned dark purple. The resulting mixture was filtered through a syringe filter and the filtrate layered with anhydrous diethyl ether. After two days, 27 mg (0.033 mmol, 13.5% yield) of crystalline solid was collected. MW: 816.53. IR (ATR, cm^{-1}): 3111, 2971, 2934, 2359, 2342, 1679, 1540, 1467, 1385, 1352, 1334, 1320, 1290, 1243, 1214, 1178, 1038, 1015, 955, 920, 890, 851, 822, 689, 669, 645, 617. UV/vis in DMSO: λ_{max}, nm (ε, M^{-1} cm^{-1}) = 260 (27,000), 296 (16,000), 347 (5,000), 553 nm (1,000). ^{1}H NMR (**2(OAc)** in CD_3OD): (500 MHz, **2(OAc)** in MeOD) δ 3.48 – 3.33 (m, 3H), 1.78 (s, 4H). ^{13}C NMR (126 MHz, **2(OAc)** in MeOD) δ 31.36 30.19, 24.48.

$[Mo_2(HNNN5)_4(OAc)_2](OAc)_2$•3(MeOH) Calcd C 35.53 H 5.74 N 18.42, found C 35.52 H 5.35

N 18.15. Crystals for X-ray diffraction were grown by diethyl ether diffusion into a MeOH solution.

Synthesis of **2(Cl)** ($[Mo_2(HNNN5)_4(Cl)_2]Cl_2$)

A solution on HNNN5 (114 mg, 1.17 mmol) in ~2.5 mL anhydrous methanol, was added to a suspension of $Mo_2(OAc)_4$ (98 mg, 0.229 mmol) in ~2.5 mL anhydrous methanol. The resulting reddish-yellow suspension was allowed to stir overnight at room temperature, during which time all solid dissolved and the reaction mixture turned dark purple. To this purple solution, 1.5 mL of saturated LiCl in MeOH was added. Immediately, a purple solid precipitated out. The mixture was allowed to stir overnight and then the solid was collected by filtration and washed with 2 x 5 mL of MeOH and 20 mL of diethyl ether. The solid was dried on the frit and collected, yielding 85 mg (0.12 mmol, 52% yield) of purple solid. Crystals for X-ray diffraction were grown by dissolving this solid in hot pyridine and layering with diethyl ether. MW: 722.16. IR (ATR, cm^{-1}): 3201, 3132, 3073, 2989, 2815 1697, 1630, 1550, 1460, 1434, 1411, 1375, 1291, 1247, 1198, 1133, 1066, 1027, 891, 812, 710, 689, 670, 662, 648, 640. ^{1}H NMR (500 MHz, **2(Cl)** in MeOD) δ 3.54 – 3.39 (m, 1H). ^{13}C NMR (126 MHz, **2(Cl)** in MeOD) δ 185.47, 185.33, 49.85, 31.75, 29.84. $[Mo_2(HNNN5)_4][OAc]_4$•3(MeOH) Calcd C 35.53 H 5.74 N 18.42, found Submitted (waiting on results).

Synthesis of **3(OAc)** ($[Mo_2(HNNN6)_4(OAc)_2](OAc)_2$)

3(OAc) was synthesized in a manner almost identical to **2(OAc)**. A 12 mL scintillation vial was loaded with 105 mg (0.245 mmol) of $Mo_2(OAc)_4$. A second 12 mL scintillation vial was loaded with 115 mg (1.03 mmol) of HNNN6. To each vial, ~2.5 mL of anhydrous MeOH was added. The ligand fully dissolved whereas $Mo_2(OAc)_4$ did not. The dissolved ligand was then

transferred via pipet into the vial with the suspended $Mo_2(OAc)_4$ and a stir bar was added. The solution was allowed to stir overnight at room temperature, during which time all solid dissolved and the reaction turned green. The resulting solution was filtered through a syringe filter and allowed to diffuse with anhydrous diethyl ether. After one week 127 mg (0.146 mmol, 59.4% yield) of crystalline solid was collected. MW: 872.63. IR (ATR, cm^{-1}): 3172, 2906, 2815, 1662, 1587, 1524, 1466, 1466, 1391, 1330, 1318, 1224, 1194, 1152, 1063, 1041, 1014, 984, 921, 898, 830, 689, 647, 630, 615. UV/vis in DMSO λ_{max}, nm (ε, M^{-1} cm^{-1}) = 296 (17948), 321 (13240), 394 (4540), 464 nm (2687), 628 (2395). ^1H (**3(OAc)** in DMSO-d_6) NMR (500 MHz, DMSO) δ 11.52 (s, 1H), 11.11 (s, 0H), 10.95 (s, 1H), 10.64 (s, 0H), 10.21 (s, 1H), 9.64 (s, 0H), 9.17 (s, 1H), 3.14 – 2.89 (m, 7H), 2.80 – 2.53 (m, 9H), 1.91 (ddt, *J* = 32.1, 20.7, 6.6 Hz, 7H), 1.77 (p, *J* = 6.5 Hz, 2H), 1.57 (s, 12H). $[Mo_2(HNNN6)_4(OAc)_2](OAc)_2\cdot(CH_3OH)\cdot0.5(CH_2Cl_2)$ Calcd C 37.41 H 5.64 N 17.75, found C 37.21 H 5.62 N 17.82. Crystals for X-ray diffraction were grown by diethyl ether diffusion into a MeOH solution.

Synthesis of **3(Cl)** ($[Mo_2(HNNN6)_4(Cl)_2]Cl_2$)

A solution on HNNN6 (104 mg, 0.935 mmol) in ~2.5 mL anhydrous methanol, was added to a suspension of $Mo_2(OAc)_4$ (100 mg, 0.233 mmol) in ~2.5 mL anhydrous methanol. The resulting dark-yellow suspension was allowed to stir overnight at room temperature, during which time all solid dissolved and the reaction mixture turned green. To this green solution, 1.5 mL of saturated LiCl in MeOH was added. Immediately, a green-blue solid precipitated out. The mixture was allowed to stir overnight and then the solid was collected by filtration and washed with 2 x 5 mL of MeOH and 20 mL of diethyl ether. The solid was dried on the frit and collected, yielding 145 mg (0.19 mmol, 83% yield) of purple solid. Crystals for X-ray diffraction were grown by dissolving this solid in hot pyridine and layering with diethyl ether. MW: 778.27. IR (ATR, cm^{-}

^{1}): 3347, 3316, 3171, 3114, 2994, 2811, 1676, 1599, 1522, 1447, 1399, 1351, 1336, 1262, 1212, 1157, 1133, 1100, 1069, 1022, 984, 935, 863, 787, 676, 649, 631, 622. ^{1}H NMR (500 MHz, MeOD) δ 3.32 – 3.18 (m, 2H), 3.09 – 2.81 (m, 2H), 2.24 – 2.09 (m, 2H). ^{13}C NMR (126 MHz, MeOD) δ 177.50, 177.13, 49.85, 32.38, 32.28, 28.98, 19.98. $[Mo_2(HNNN5)_4][OAc]_4$•3(MeOH) Calcd C 35.53 H 5.74 N 18.42, found (Submitted, waiting on results). Crystals for X-ray diffraction were grown by diethyl ether diffusion into a pyridine solution.

2.2.8.3.2 Characterization Data

Physical Measurements: IR spectra were recorded with a Bruker Tenser 27 spectrometer using an ATR adapter. Elemental analysis was performed by Midwest Microlab, LLC in Indianapolis, IN, USA. ^{1}H NMR spectra were recorded on a 400 MHz Bruker Avance III spectrometer. UV−visible absorption spectra were acquired using a Varian Cary 50 spectrophotometer. All electronic absorption spectra were recorded at ambient temperatures in quartz cells with a 1 cm path length.

2.2.8.3.2 NMR

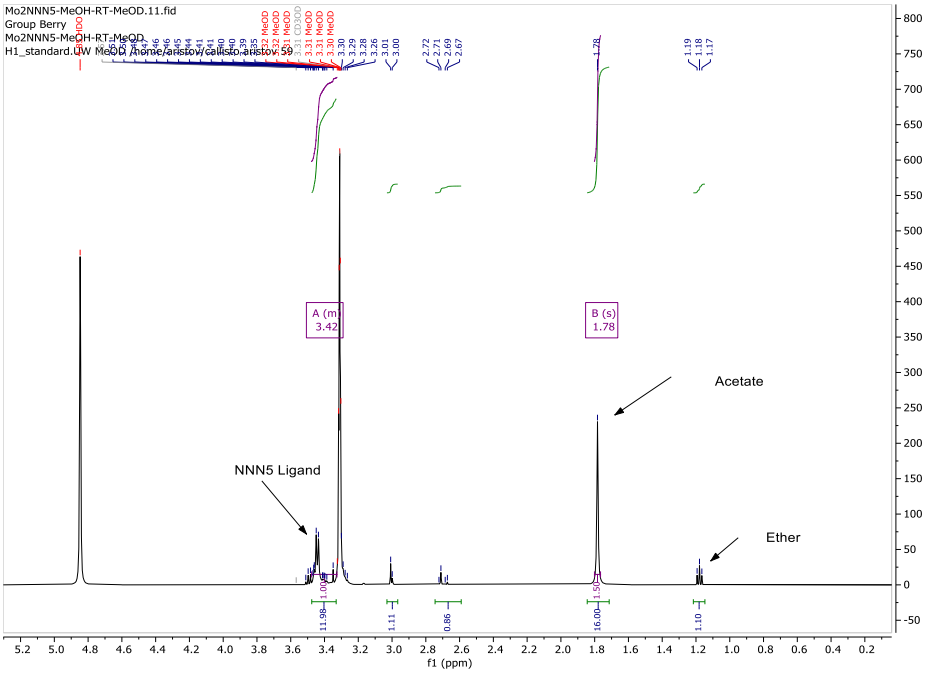

Figure S1: NMR of **(2(OAc))** ^{1}H NMR (500 MHz, MeOD) δ 3.48 – 3.33 (m, 1H), 1.78 (s, 1H)

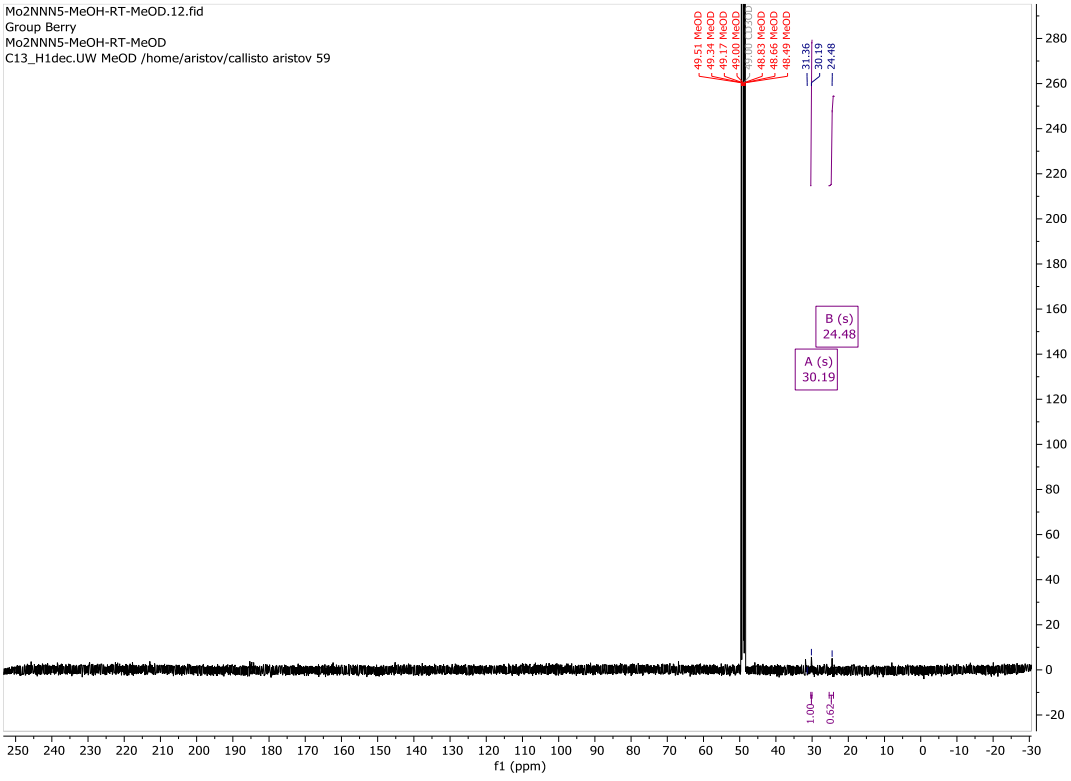

Figure S2: NMR of **(2(OAc))** ^{13}C NMR (126 MHz, MeOD) δ 31.36 30.19, 24.48.

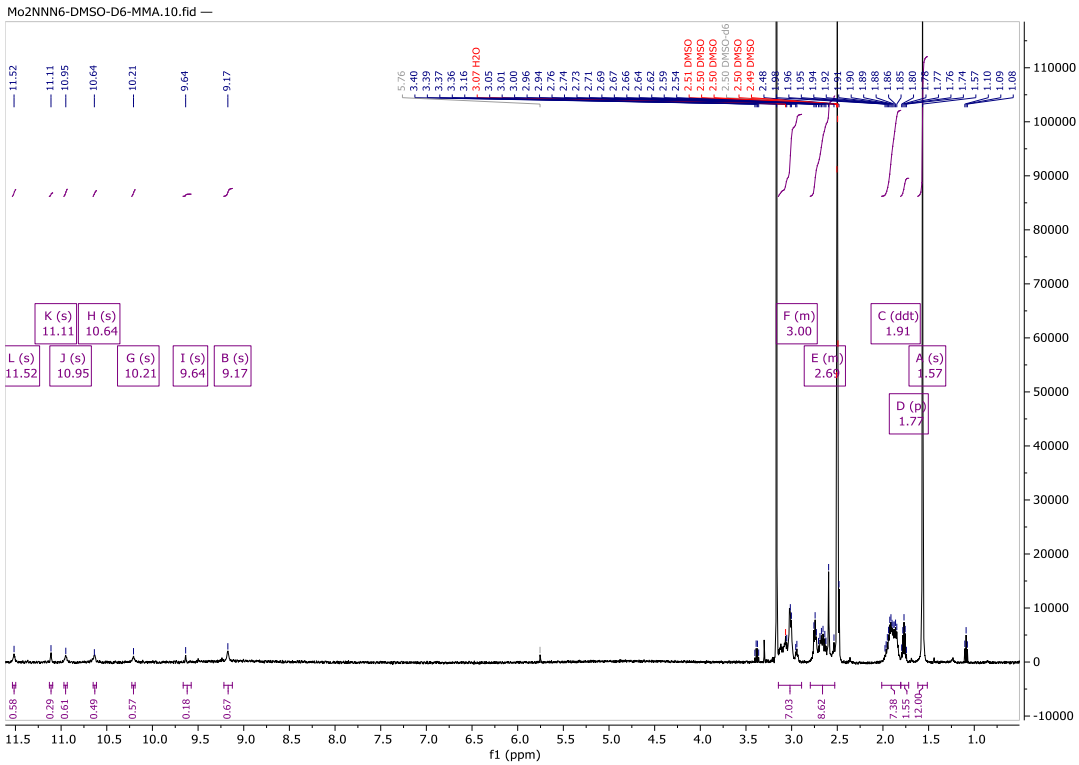

Figure S3: NMR of **(3(OAc))** ^{1}H NMR (500 MHz, DMSO) δ 11.52 (s, 1H), 11.11 (s, 0H), 10.95 (s, 1H), 10.64 (s, 0H), 10.21 (s, 1H), 9.64 (s, 0H), 9.17 (s, 1H), 3.14 – 2.89 (m, 7H), 2.80 – 2.53 (m, 9H), 1.91 (ddt, *J* = 32.1, 20.7, 6.6 Hz, 7H), 1.77 (p, *J* = 6.5 Hz, 2H), 1.57 (s, 12H).

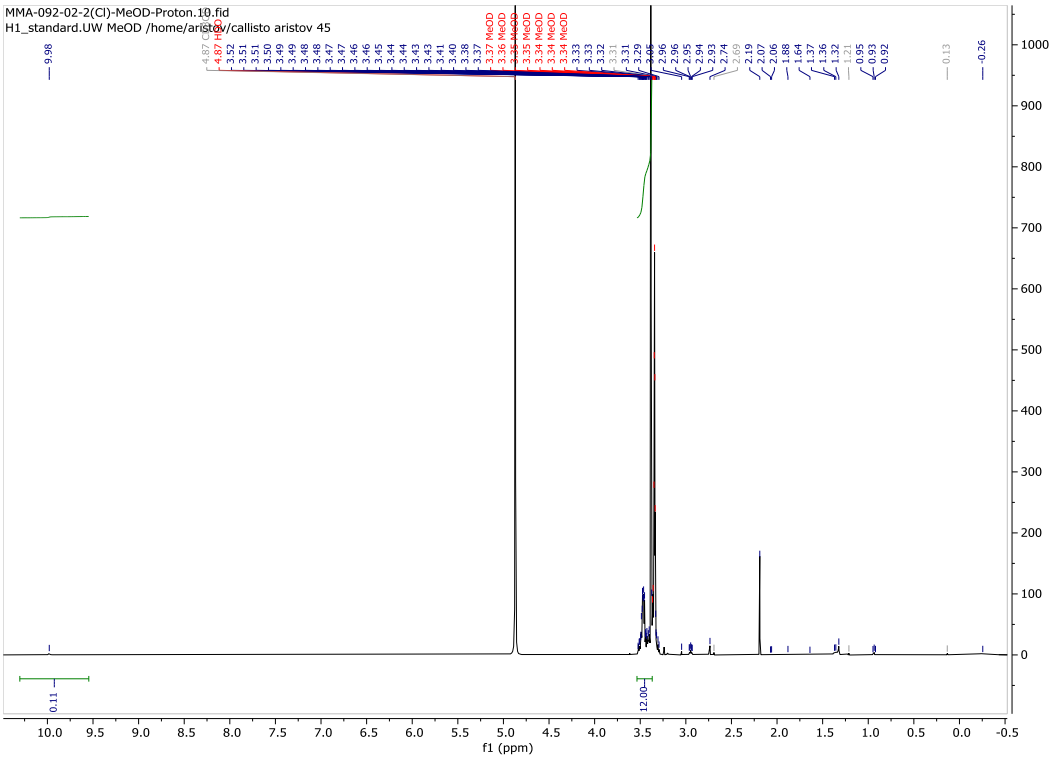

Figure S5: NMR of **2(Cl)** ^{1}H NMR (500 MHz, MeOD) δ 3.54 – 3.39 (m, 1H).

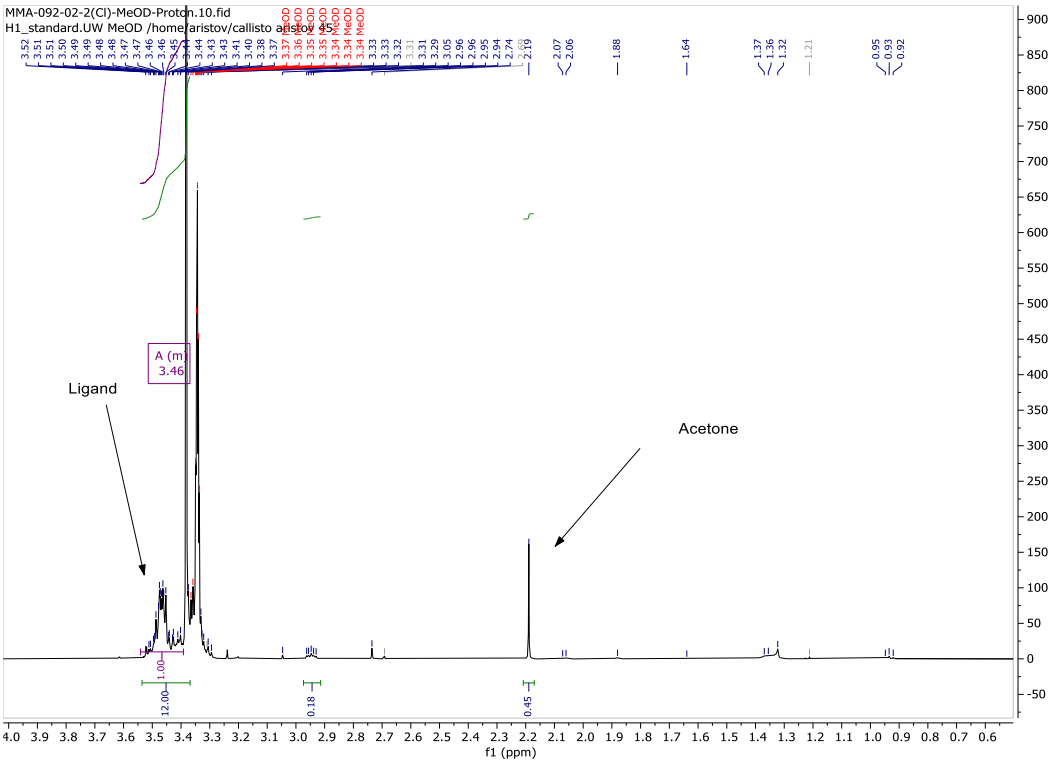

Figure S6: ^{1}H of NMR **2(Cl)** ^{1}H NMR (500 MHz, MeOD) δ 3.54 – 3.39 (m, 1H).

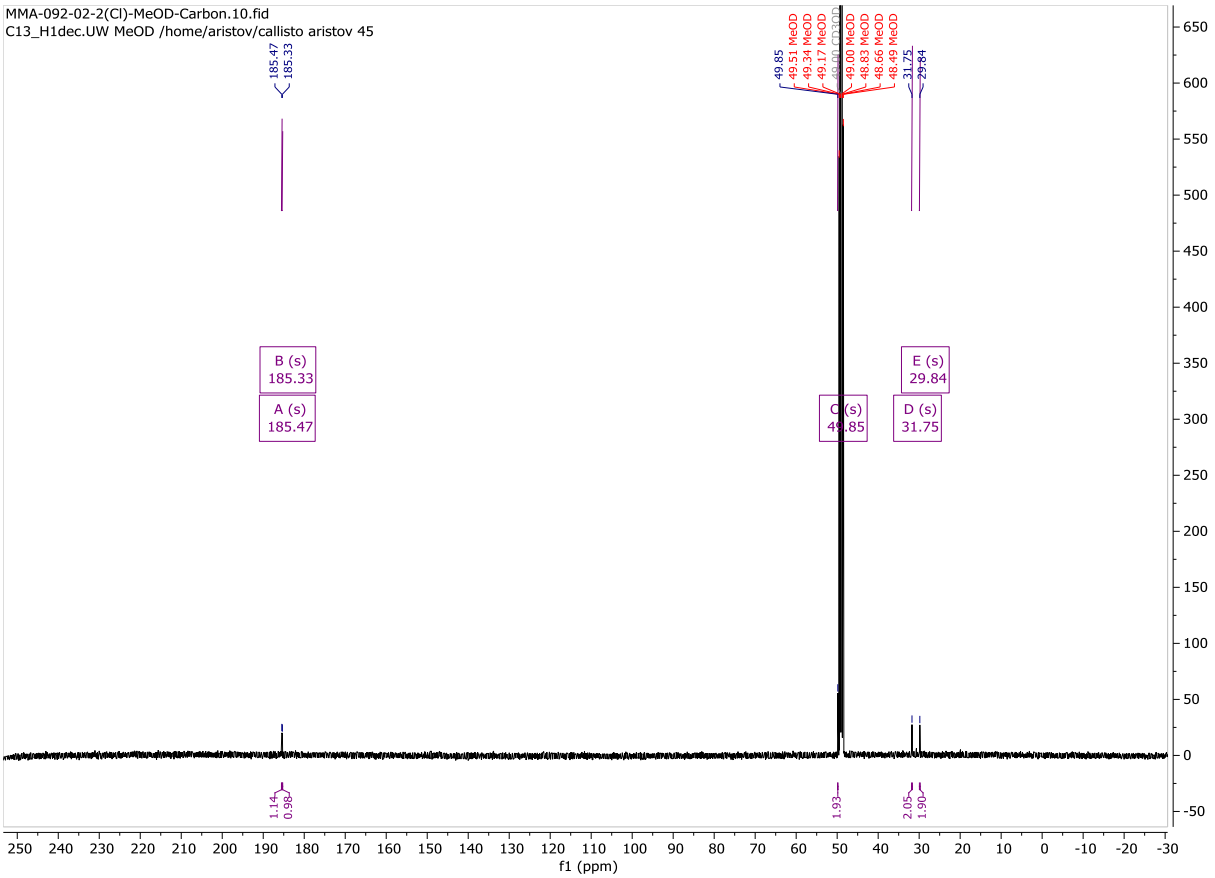

Figure S7: NMR of **2(Cl)** ^{13}C NMR (126 MHz, **2(Cl)** in MeOD) δ 185.47, 185.33, 49.85, 31.75, 29.84

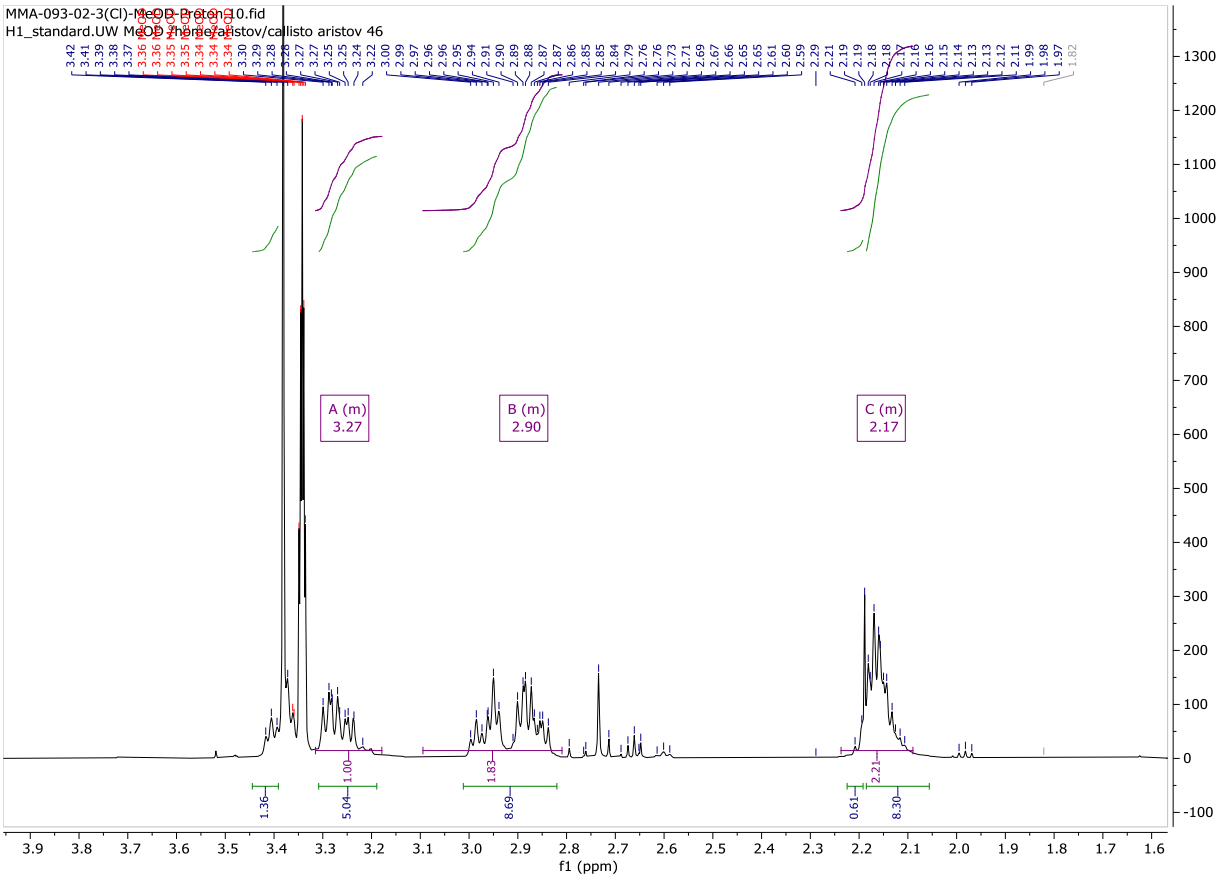

Figure S8: NMR of **(3(Cl))** ^{1}H NMR (500 MHz, MeOD) δ 3.32 – 3.18 (m, 2H), 3.09 – 2.81 (m, 2H), 2.24 – 2.09 (m, 2H).

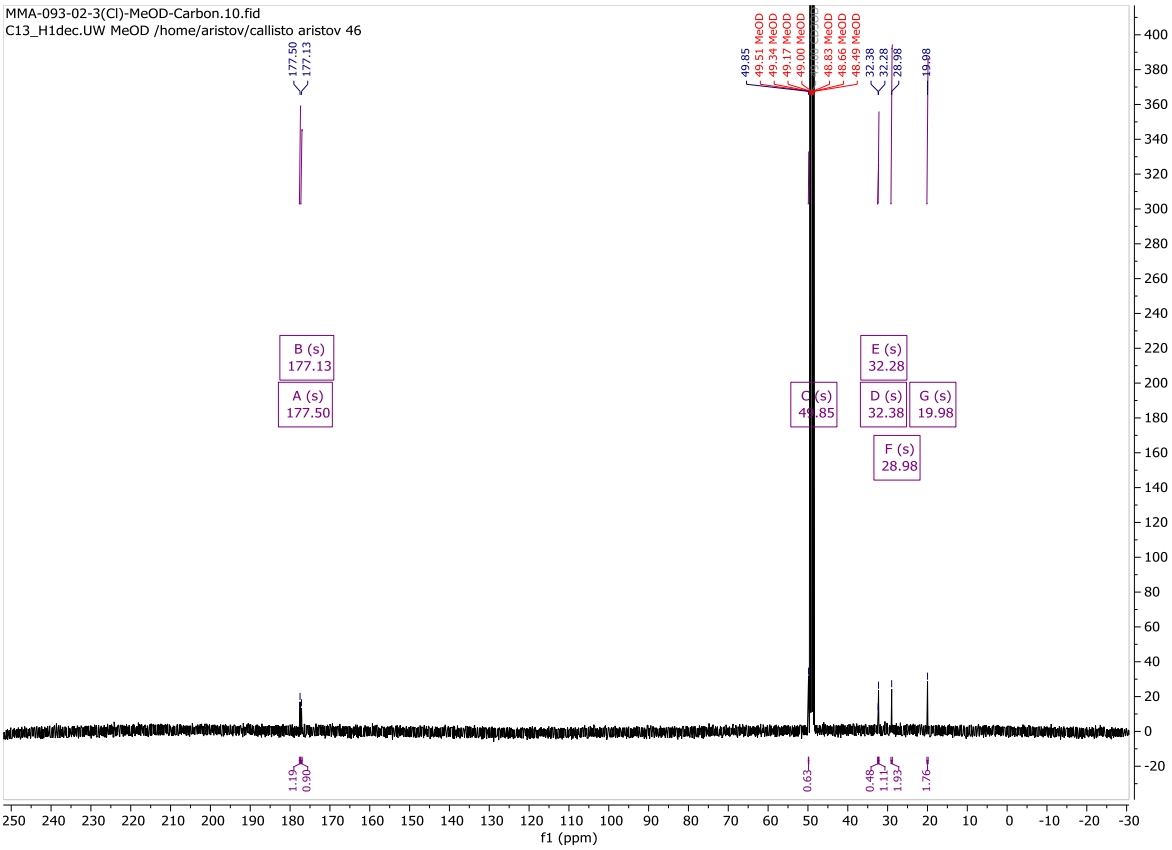

Figure S9: NMR of 3(Cl) ^{13}C NMR (126 MHz, MeOD) δ 177.50, 177.13, 49.85, 32.38, 32.28, 28.98, 19.98.

2.2.8.3.3 IR

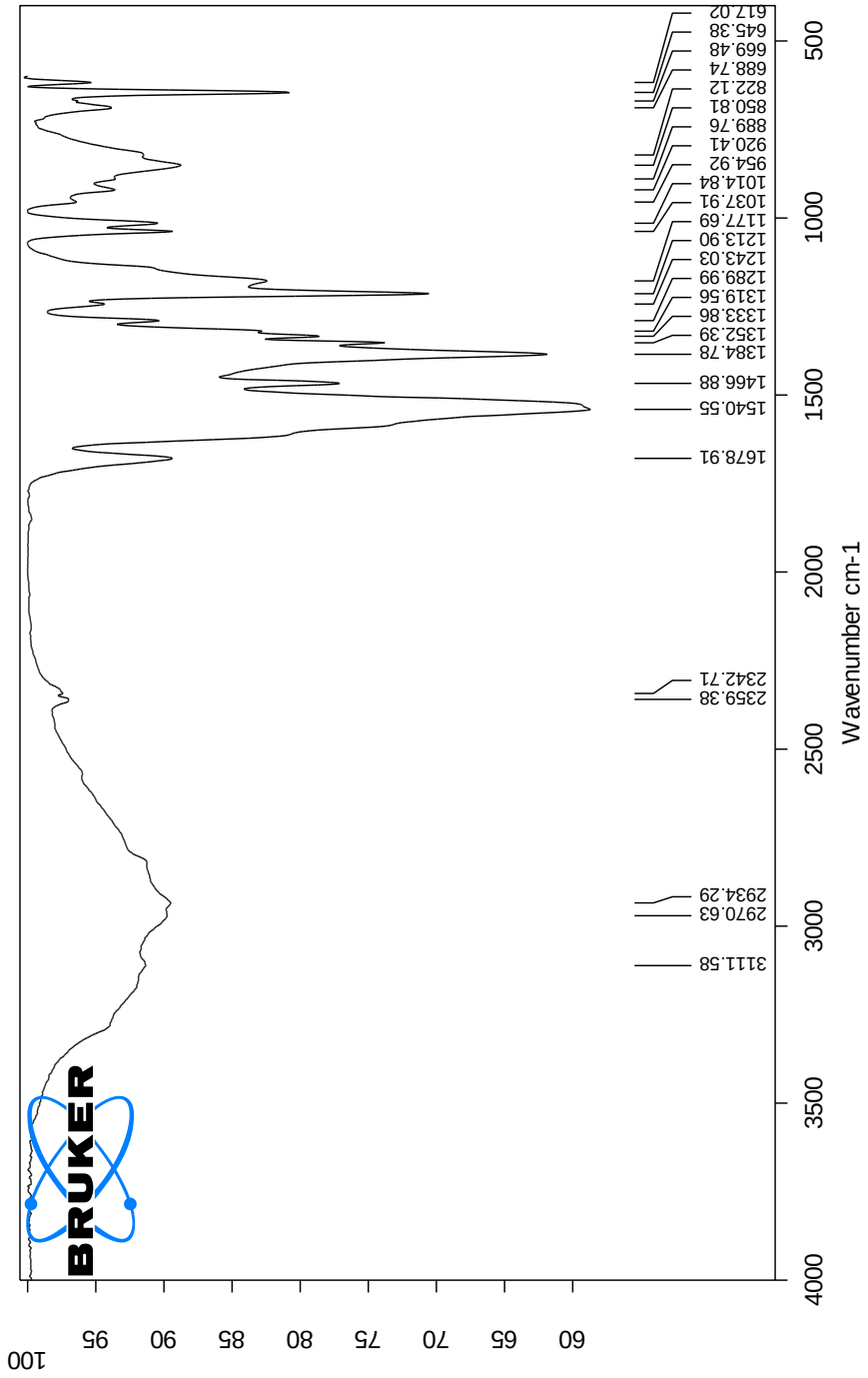

Figure S10: IR data for **2(OAc)**.

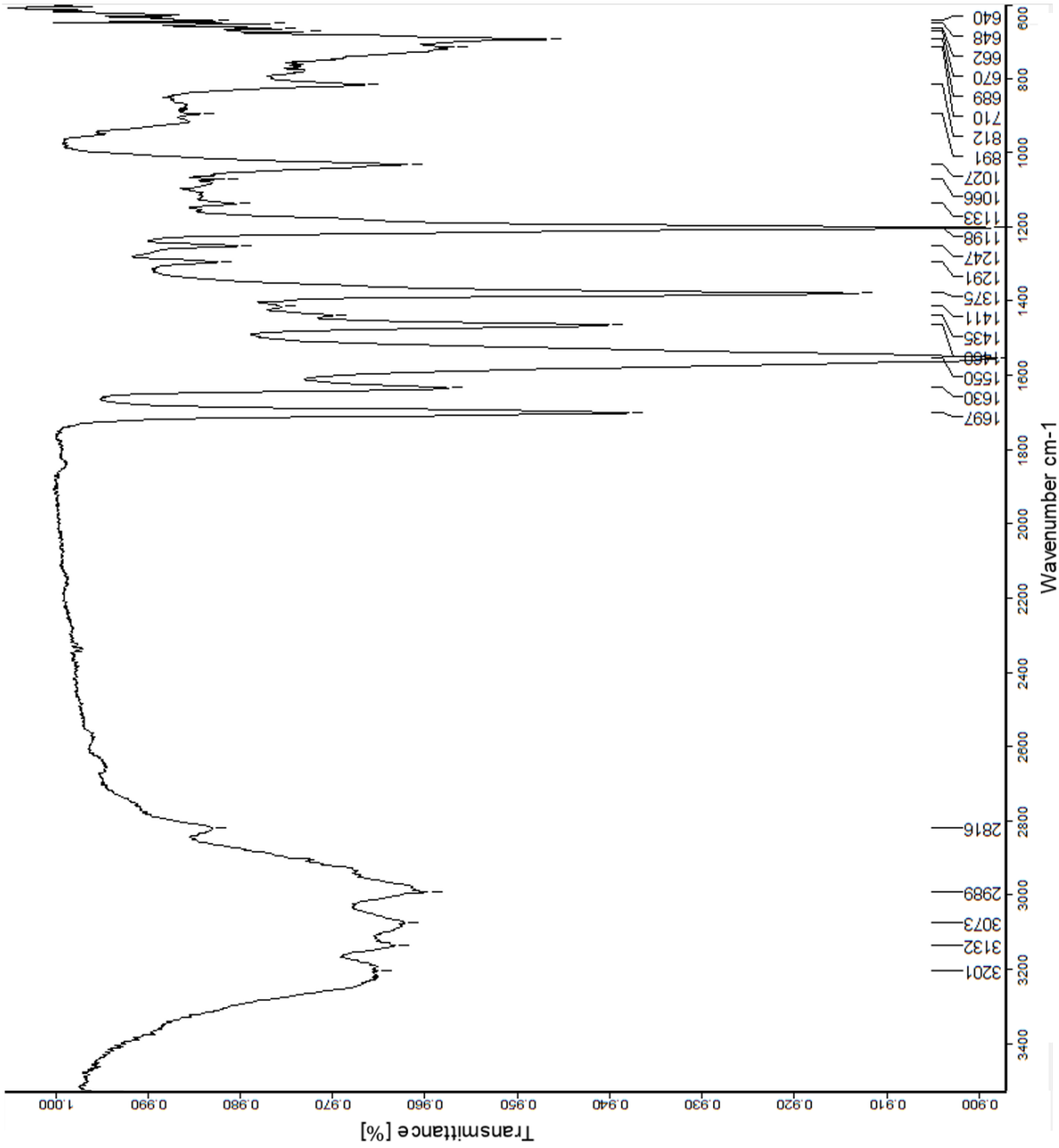

Figure S11: IR data for **2(Cl)**.

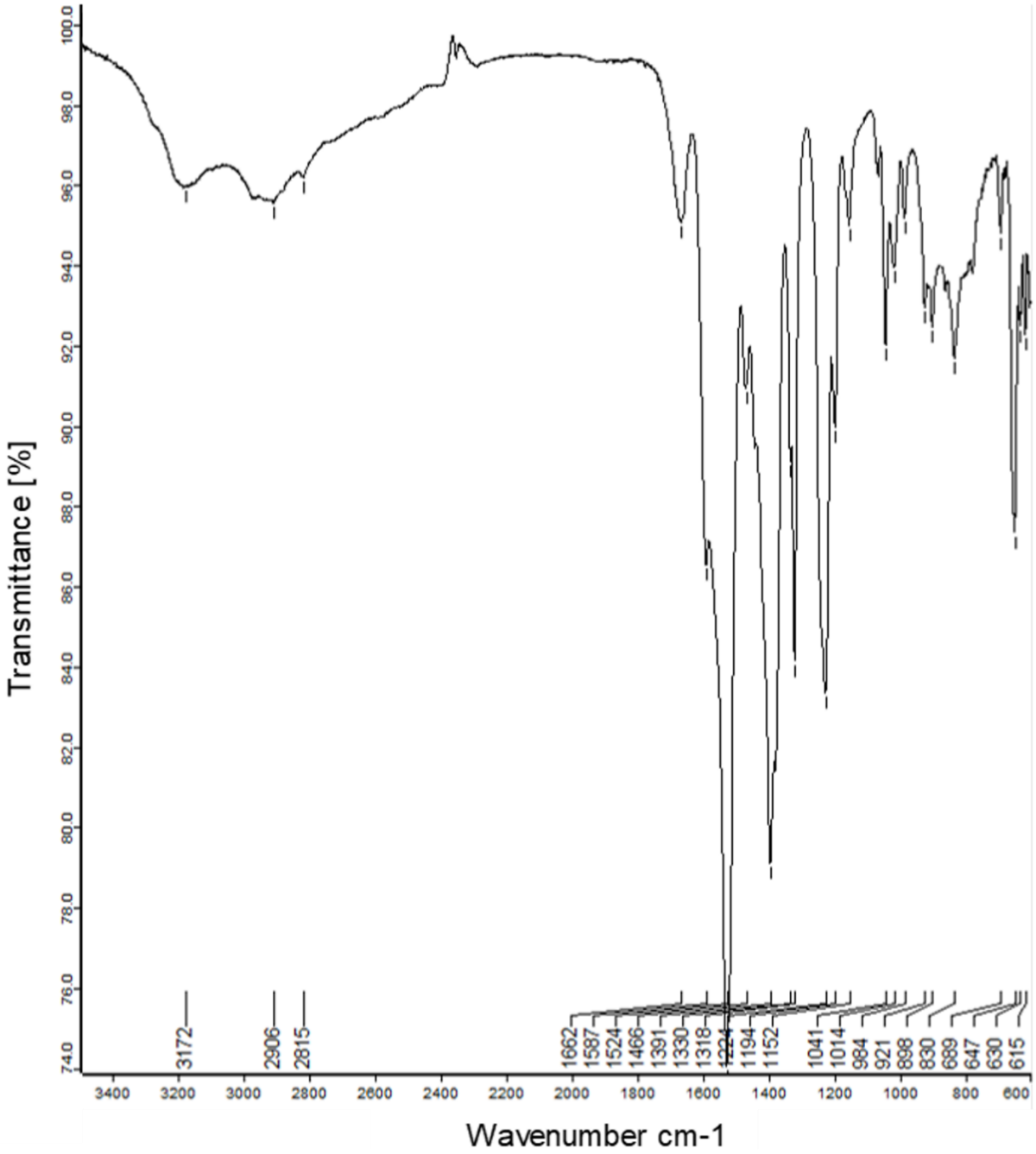

Figure S12: IR data for **3(OAc)**.

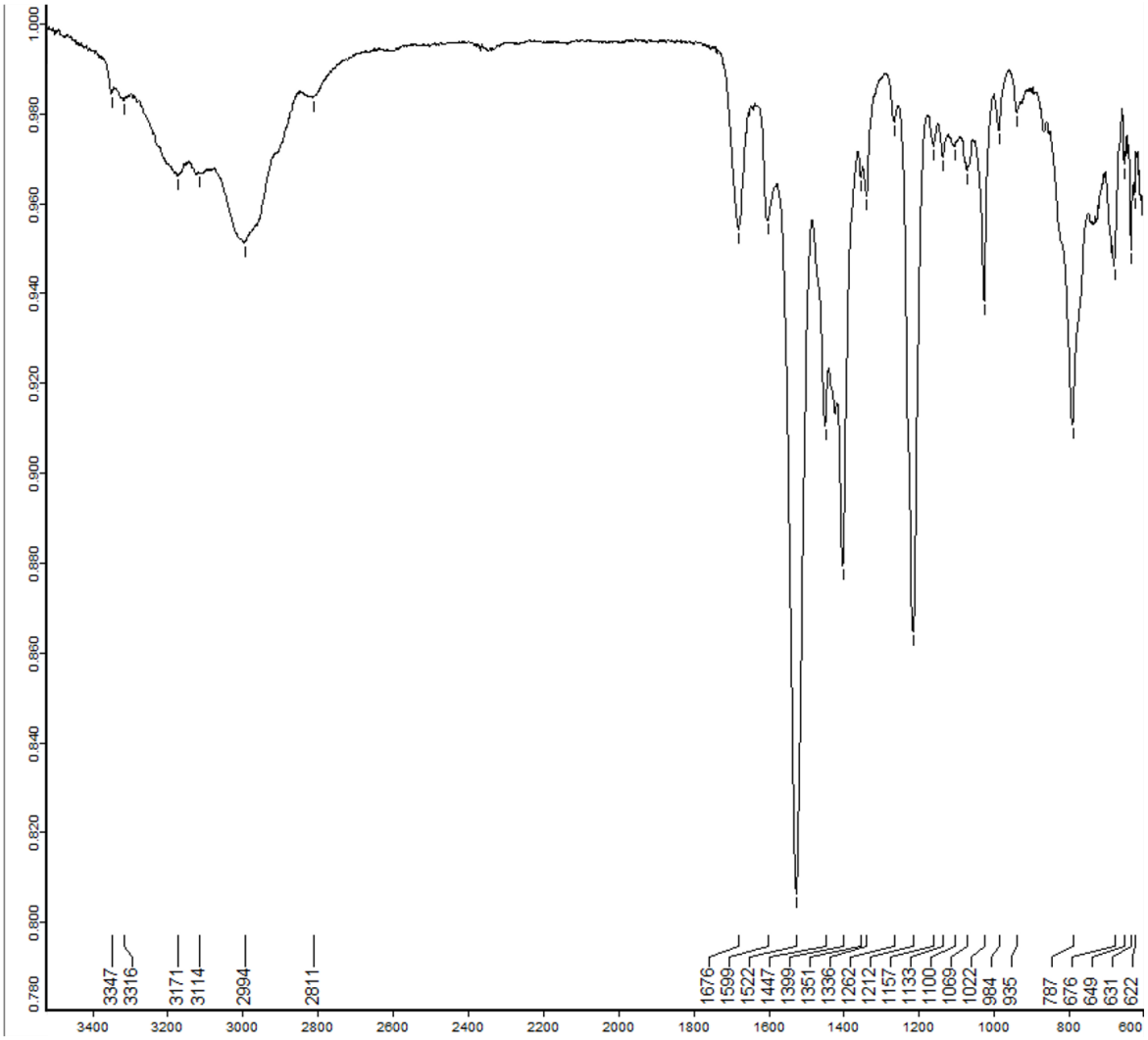

Figure S13: IR data for **3(Cl)**.

2.2.8.3.4 UV-Vis of 2(OAc)

A 0.033 mM solution of **2(OAc) (**0.023 mM solution of **3(OAc))** in anhydrous DMSO was prepared in a nitrogen atmosphere glove box and filtered before being transferred into a screw cap, 6Q cuvette to protect it from air. A second blank cuvette was prepared with the same filtered, anhydrous DMSO. Data were collected on a Cary 50 UV-Vis spectrometer. The spectrum was recorded from 200 nm to 800 nm at a scan rate of 600 nm/minute with a 1 nm data interval. This same procedure was followed for all MeOH samples, (0.22 mM for **2(OAc)** and 0.080 mM for **3(OAc)**).

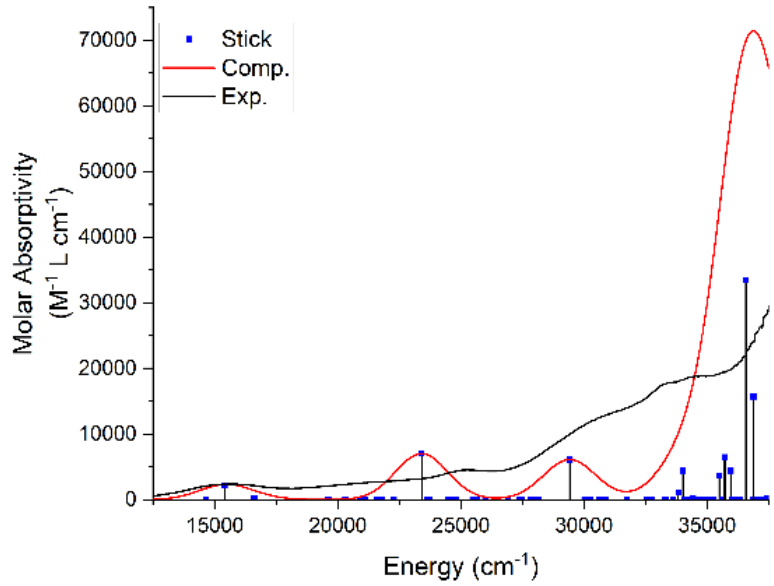

*Figure S14. The experimental and TD-DFT-calculated electronic spectra of **3(OAc)** overlapped with each other.*

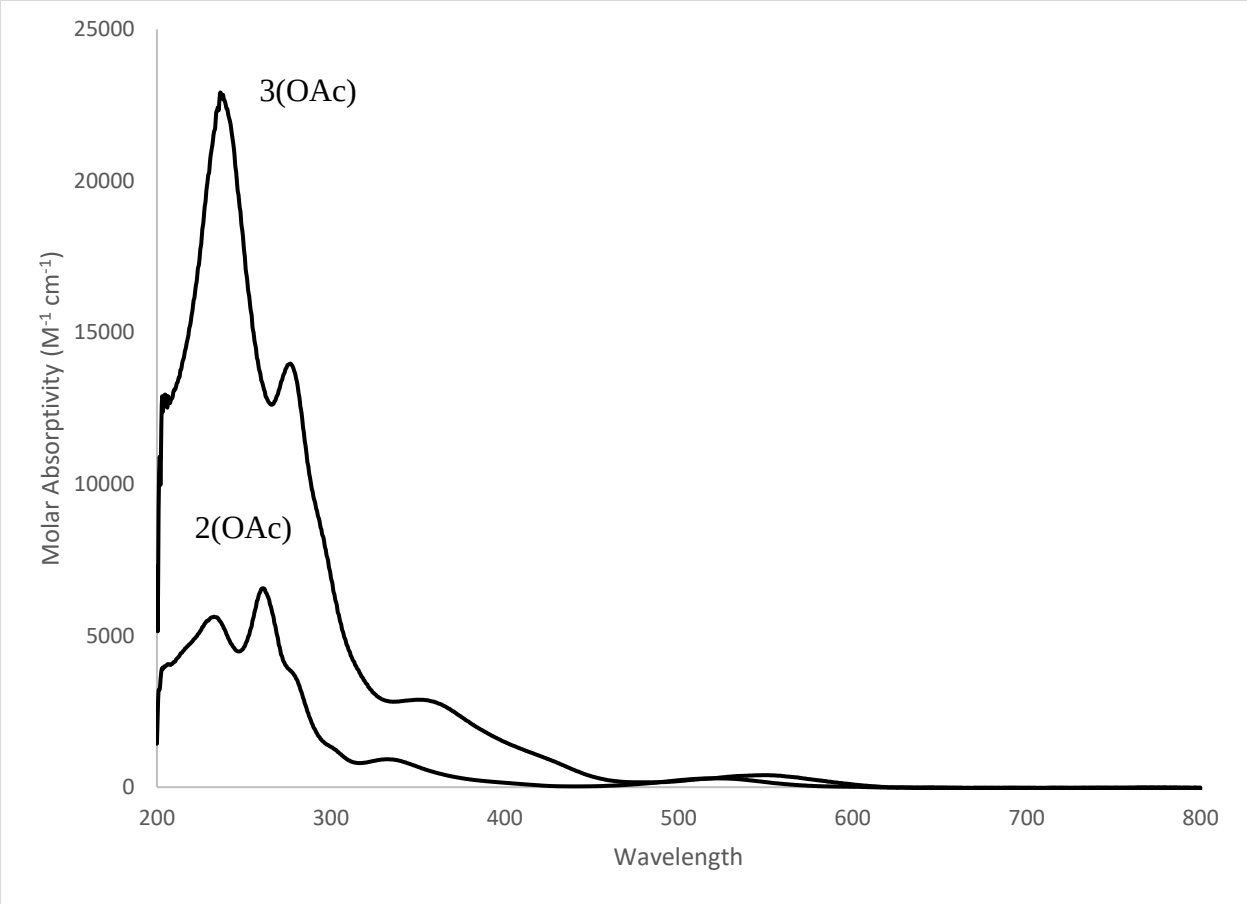

Figure S15. UV-Vis spectra of MeOH solutions of 3(OAc) and 2(OAc) overlayed on top of each other.

2.2.8.3.5 Crystal Structures

Data Collection:

All crystals were selected under oil under ambient conditions and attached to the tip of a MiTeGen MicroMount©. The crystal was mounted in a stream of cold nitrogen at 100(1) K and centered in the X-ray beam by using a video camera.

The crystal evaluation and data collection were performed either on a Bruker Quazar SMART APEXII diffractometer with Mo K_α (λ = 0.71073 Å) radiation and the diffractometer to crystal distance of 4.96 cm[24] or on a Bruker D8 VENTURE PhotonIII four-circle diffractometer with Cu Kα (λ = 1.54178 Å) radiation with the detector to crystal distance of 4.0 cm.[25]

For data collected with a Bruker Quazar SMART APEXII, the initial cell constants were obtained from three series of ω scans at different starting angles. Each series consisted of 12 frames collected at intervals of 0.5º in a 6º range about ω . The reflections were successfully indexed by an automated indexing routine built in the APEX3 program suite. For crystals collected on the on a Bruker D8 VENTURE PhotonIII, the initial cell constants were obtained from a 180° φ scan conducted at a 2θ = 50° angle with an exposure time of 1 second per frame. The reflections were successfully indexed by an automated indexing routine built in the APEX3 program.

All data were collected by using the full sphere data collection routine to survey the reciprocal space to the extent of a full sphere. The absorption correction was based on fitting a function to the empirical transmission surface as sampled by multiple equivalent measurements.[26]

Refinement:

For the structure of **2(OAc)**, the systematic absences in the diffraction data were consistent for the space groups *C*2/*c* and *Cc*. The *E*-statistics strongly suggested the centrosymmetric space group *C*2/*c* that yielded chemically reasonable and computationally stable results of refinement. For the structure of **2(Cl) t**he systematic absences in the diffraction data were uniquely consistent for the space group $P2_1/n$ that yielded chemically reasonable and computationally stable results of refinement. For the structure of **3(OAc)** The systematic absences in the diffraction data were consistent for the space groups $P\bar{1}$ and *P*1. The *E*-statistics strongly suggested the centrosymmetric space group $P\bar{1}$ that yielded chemically reasonable and computationally stable results of refinement. For **3(Cl)** the systematic absences in the diffraction data were uniquely consistent for the space group $P2_1/c$ that yielded chemically reasonable and computationally stable results of refinement.[27-31]

For all structures a successful solution by the direct methods provided most non-hydrogen atoms from the *E*-map. The remaining non-hydrogen atoms were located in an alternating series of least-squares cycles and difference Fourier maps. All major component, non-hydrogen atoms were refined with anisotropic displacement coefficients. All hydrogen atoms were included in the structure factor calculation at idealized positions and were allowed to ride on the neighboring atoms with relative isotropic displacement coefficients.

For **2(OAc)** single crystals suitable for X-ray diffraction of **2** were obtained overnight by vapor diffusion of anhydrous ether into the reaction liquor. The complex crystallizes in the C2/*c* space group. The asymmetric unit consists of half of the cationic $[Mo2(HNN5)_4]^{4+}$ unit with the Mo≡Mo quadruple bond residing on an inversion center, two acetate anions, one occupying a Mo_2 axial site, and partially occupied MeOH solvent. The three solvent methanol sites showed disorder

and their occupancies were freely refined. All atoms with less than 50% occupancy were modeled with isotropic displacement parameters. Distance restraints were applied to all solvent molecules.

For **2(Cl)** the asymmetric unit contains ½ ($[Mo_2(N_3C_4H_7)_4]Cl_4$) situated on the *n*-glide and one methanol solvent molecule. One chloride anion, Cl2, is disordered over two positions with a major occupancy of 83.1(15)%. The methanol is disordered over two positions, with major occupancy of 55.4(11)%, and these solvent molecules were modeled with restraints. The final difference Fourier map contained a max peak of 1.6 $e^{-1}/Å^3$, which resided near the heavy metal center and is therefore noise.

For **3(OAc)** the asymmetric unit consists of ½ of $[Mo_2(HNNN6)_4(OAc)_2](OAc)_2$ and two methanol solvent molecules. One of the MeOH solvent molecules is partially occupied at 92.4(8)%. There are numerous hydrogen bonding ineractions between the metal complex, the inner sphere acetate counter ions, the outer sphere acetate counter ions, and the MeOH solvent. Hydrogen atom H6a was restrained to atom N6.

For **3(Cl) t**he asymmetric unit is comprised of ½ of the ($(C_5N_3H_9)_4Mo_2Cl_4$) complex as well as one half occupied methanol molecule located near a special position. Restraints and constraints were used to model the poorly behaved methanol molecule. The final difference Fourier map contained one peak of ~ 1.2 $e^-/Å^3$. This peak resided near the poorly behaved methanol solvent molecule but could not be refined as an addition disordered methanol. This peak is likely arises from dynamic disorder of the methanol solvent molecule.

Summary

Crystal Data for **2(OAc)** ($[Mo_2(C_4N_3H_7)_4(O_2C_2H_3)_2]$ $(O_2C_2H_3)_2$•$1.29CH_3OH$) (*M* =899.63 g/mol): monoclinic, space group C2/c (no. 15), *a* = 25.729(9) Å, *b* = 9.741(3) Å, *c* = 16.992(7) Å, *β* = 109.154(19)°, *V* = 4023(3) Å^3, *Z* = 4, *T* = 100.02 K, μ(MoKα) = 0.688 mm^{-1}, *Dcalc* = 1.485 g/cm^3, 30396 reflections measured (3.352° ≤ 2Θ ≤ 55.322°), 4690 unique (R_{int} = 0.0673, R_{sigma} = 0.0441) which were used in all calculations. The final R_1 was 0.0374 (I > 2σ(I)) and wR_2 was 0.1068 (all data).

Crystal Data for **2(Cl)** $[Mo_2(C_4N_3H_7)_4]Cl_4$•CH_3OH (*M* =786.27 g/mol): monoclinic, space group $P2_1/n$ (no. 14), *a* = 8.837(2) Å, *b* = 8.631(3) Å, *c* = 19.125(6) Å, *β* = 90.857(10)°, *V* = 1458.6(7) Å^3, *Z* = 2, *T* = 99.99 K, μ(MoKα) = 1.267 mm^{-1}, *Dcalc* = 1.790 g/cm^3, 30674 reflections measured (4.26° ≤ 2Θ ≤ 52.906°), 2998 unique (R_{int} = 0.0508, R_{sigma} = 0.0244) which were used in all calculations. The final R_1 was 0.0360 (I > 2σ(I)) and wR_2 was 0.0981 (all data).

Crystal Data for **3(OAc)** $[Mo_2(C_4N_3H_7)_4(O_2C_2H_3)_2]$ $(O_2C_2H_3)_2$•$3.8CH_3OH$ (*M* =996.01 g/mol): triclinic, space group P-1 (no. 2), *a* = 8.889(7) Å, *b* = 11.066(7) Å, *c* = 12.755(8) Å, *α* = 112.08(3)°, *β* = 96.35(3)°, *γ* = 99.74(4)°, *V* = 1124.8(14) Å^3, *Z* = 1, *T* = 100.0 K, μ(CuKα) = 5.137 mm^{-1}, *Dcalc* = 1.470 g/cm^3, 19506 reflections measured (7.62° ≤ 2Θ ≤ 161.69°), 4799 unique (R_{int} = 0.0526, R_{sigma} = 0.0417) which were used in all calculations. The final R_1 was 0.0298 (I > 2σ(I)) and wR_2 was 0.0727 (all data).

Crystal Data for **3(Cl)** $C_{10.5}H_{20}Cl_2MoN_6O_{0.5}$ (*M* =405.16 g/mol): monoclinic, space group $P2_1/c$ (no. 14), *a* = 11.243(4) Å, *b* = 14.141(5) Å, *c* = 10.708(3) Å, *β* = 110.273(18)°, *V* = 1597.0(10) Å^3, *Z* = 4, *T* = 100.0 K, μ(MoKα) = 1.158 mm^{-1}, *Dcalc* = 1.685 g/cm^3, 28764 reflections measured (3.862° ≤ 2Θ ≤ 53.696°), 3422 unique (R_{int} = 0.0458, R_{sigma} = 0.0256) which were used in all calculations. The final R_1 was 0.0292 (I > 2σ(I)) and wR_2 was 0.0636 (all data).

Table S1: Selected crystallographic data for the compounds described in this manuscript.				
Compound	**2(OAc)**	**2(Cl)**	**3(OAc)**	**3(Cl)**
Deposition #	2196149	2196147	2196150	2196148
Formula	$[Mo_2(C_4N_3H_7)_4(O_2C_2H_3)_2](O_2C_2H_3)_2 \cdot 1.29\,CH_3OH$	$[Mo_2(C_4N_3H_7)_4]Cl_4 \cdot CH_3OH$	$[Mo_2(C_4N_3H_7)_4(O_2C_2H_3)_2](O_2C_2H_3)_2 \cdot 3.8CH_3OH$	$[Mo_2(C_5N_3H_9)_4]Cl_4 \cdot CH_3OH$
Formula weight	899.63	786.27	996.01	405.16
Temperature/K	100.02	99.99	100.0	100.0
Crystal system	Monoclinic	Monoclinic	Triclinic	monoclinic
Space group	*C*2/*c*	$P2_1/n$	$P\bar{1}$	$P2_1/c$
a/Å	25.729(9)	8.837(2)	8.889(7)	11.243(4)
b/Å	9.741(3)	8.631(3)	11.066(7)	14.141(5)
c/Å	16.992(7)	19.125(6)	12.755(8)	10.708(3)
α/°	90	90	112.08(3)	90
β/°	109.154(19)	90.857(10)	96.35(3)	110.273(18)
γ/°	90	90	99.74(4)	90
Volume/$Å^3$	4023(3)	1458.6(7)	1124.8(14)	1597.0(10)
Z	4	2	1	4
$\rho_{calc}g/cm^3$	1.485	1.790	1.470	1.685
μ/mm^{-1}	0.688	1.267	5.137	1.158
Radiation	MoKα (λ = 0.71073)	MoKα (λ = 0.71073)	CuKα (λ = 1.54178)	MoKα (λ = 0.71073)
R_{int}	0.0673	0.0508	0.00526	0.0458
Data/restraints/parameters	4690/4/253	2998/2/187	4799/1/285	3422/1/194
Goodness-of-fit on F^2	1.059	1.085	1.033	1.070
Final R indexes	R_1 = 0.374	R_1 = 0.0360	R_1 = 0.0298	R_1 = 0.0292
[I>=2σ (I)][a, b]	wR_2 = 0.0971	wR_2 = 0.00942	wR_2 = 0.0700	wR_2 = 0.0608
Final R indexes	R_1 = 0.0572	R_1 = 0.0426	R_1 = 0.0340	R_1 = 0.0376
[all data]	wR_2 = 0.1068	wR_2 = 0.0981	wR_2 = 0.0727	wR_2 = 0.0636

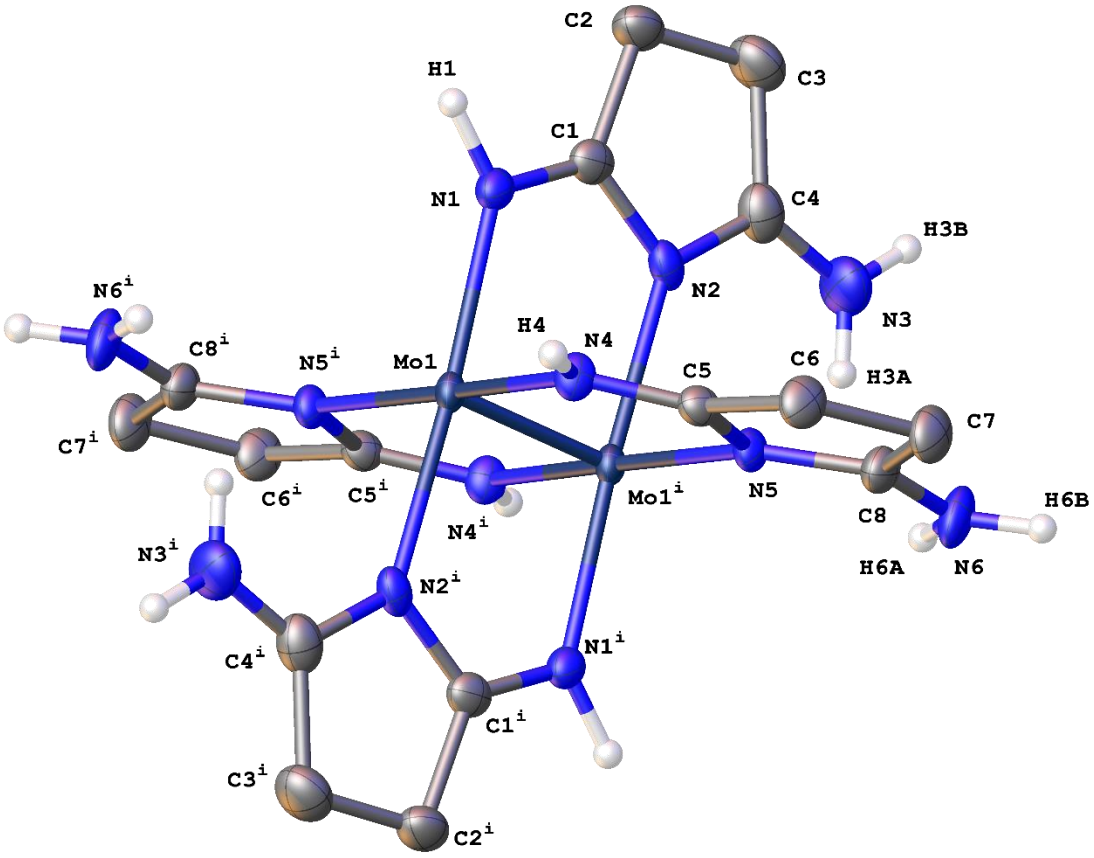

Figure S16. A molecular drawing of the dimolybdenum tetra-cation from **2(OAc)** shown with 50% probability ellipsoids. Counterions and solvent molecules and Carbon bound hydrogens were excluded for clarity. [Symmetry code: i=-1 1-X,-Y,1-Z].

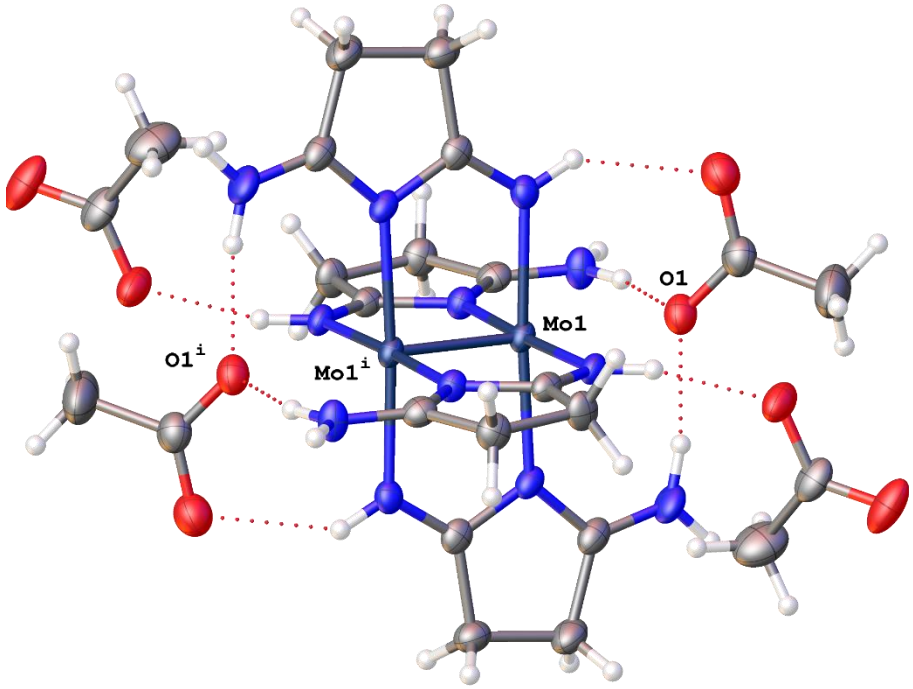

Figure S17. A molecular drawing of **2(OAc)** shown with 50% probability ellipsoids. Solvent molecules were excluded for clarity. [Symmetry code: i=-1 1-X,-Y,1-Z].

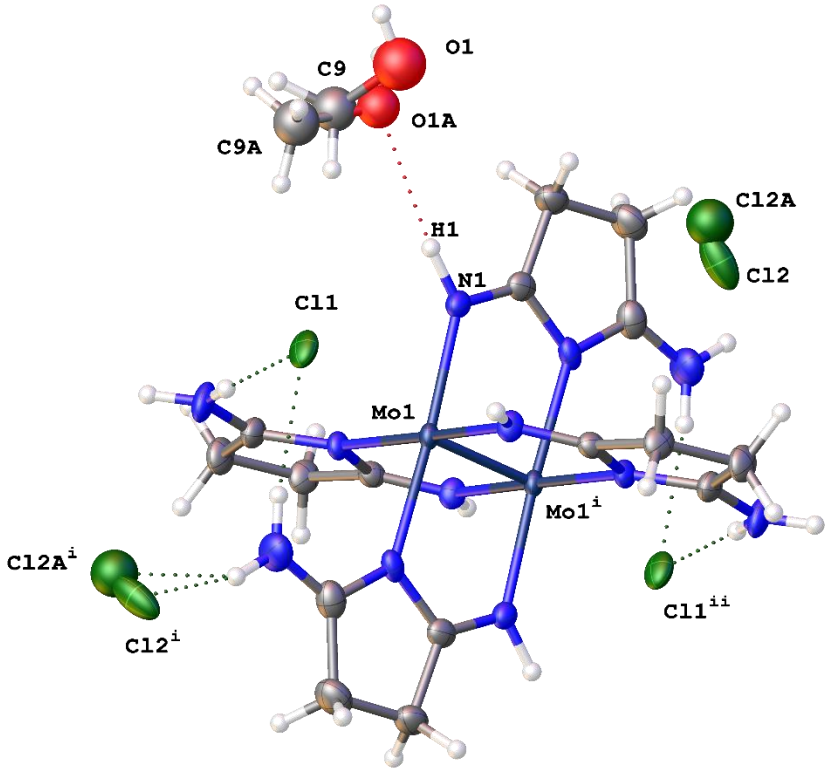

Figure S18. A molecular drawing of **2(Cl)** shown with 50% probability ellipsoids. [Symmetry code: i=-1 1-X,-Y,1-Z]. Positional disorder of the methanol and outer-sphere chloride ions is shown.

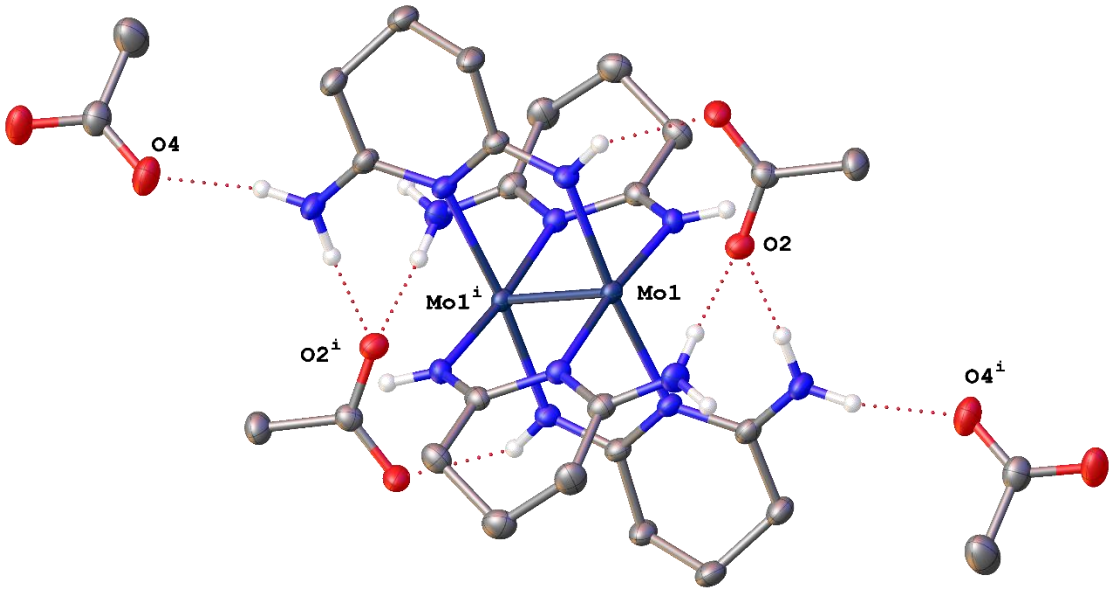

Figure S19. A molecular drawing of **3(OAc)** shown with 50% probability ellipsoids. All C-H atoms and MeOH solvent molecules are omitted. [Symmetry code: i= -X, -Y, 1-Z]

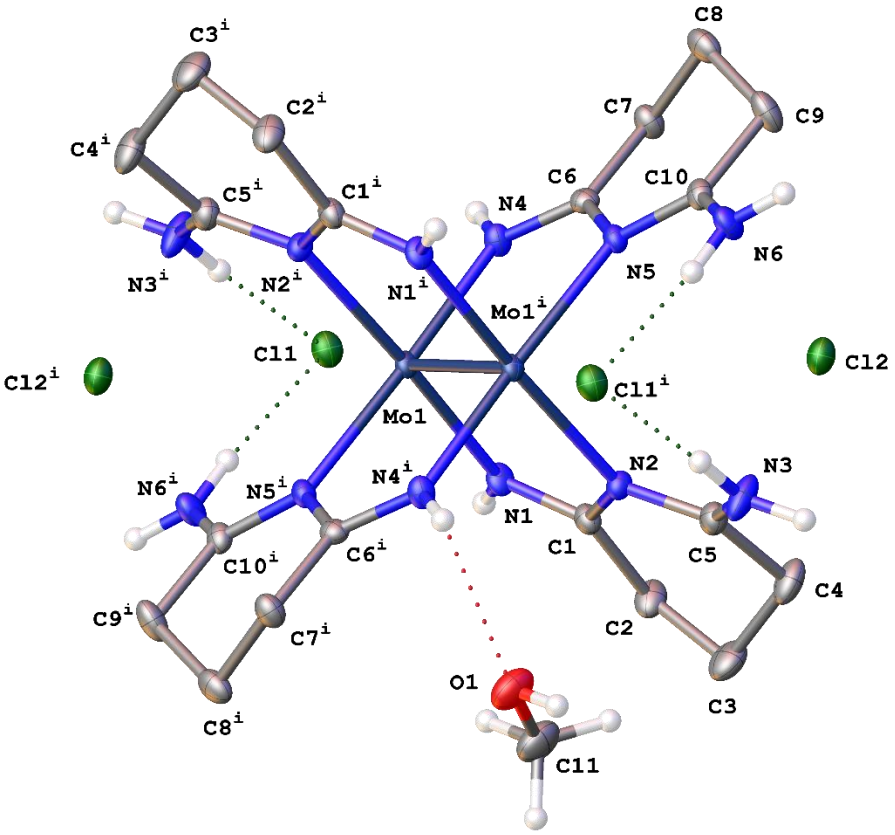

Figure S20. A molecular drawing of Berry971 shown with 50% probability ellipsoids. All H atoms not bound to solvent or nitrogen are omitted. [Symmetry code: i=1-X,1-Y,1-Z.]

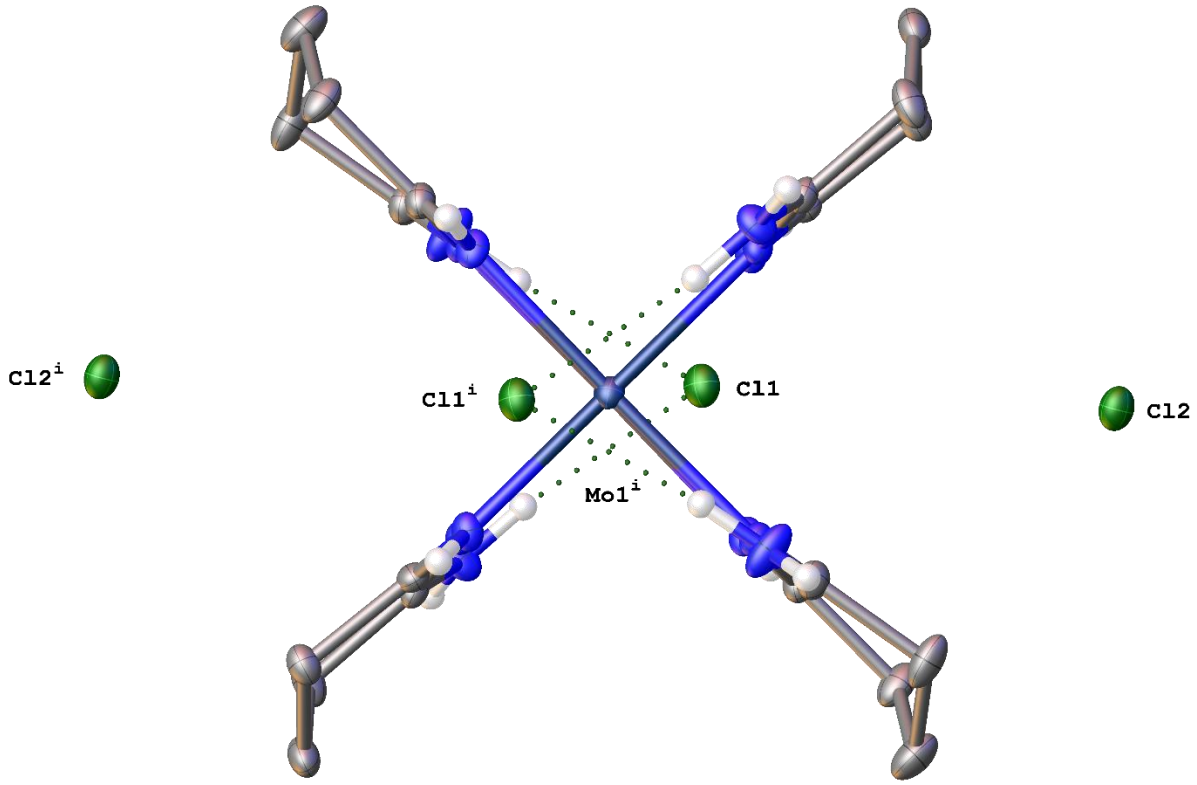

Figure S21. A molecular drawing of Berry971 shown with 50% probability ellipsoids. All H atoms not bound to nitrogen and solvent molecules are omitted. [Symmetry code: i=1-X,1-Y,1-Z.]

2.2.8.4 Geometry Optimized Coordinates

Table S2. Geometry Optimized XYZ coordinates for **2(OAc)**

Atom	X	Y	Z
Mo	17.31604	7.915744	8.377089
N	16.07898	9.615944	8.547114
H	16.51116	10.47606	8.946831
N	14.30387	8.361637	7.77908
N	12.27415	7.544707	6.949218
H	12.70738	6.569588	6.807847
H	11.29355	7.719655	6.719659
N	16.93671	7.438289	10.42382
H	17.45209	7.813402	11.22975
N	15.20239	6.102037	9.700149
N	13.46842	4.561621	9.43844
H	13.49656	4.735334	8.375629
H	12.81988	3.887774	9.851052
C	14.81465	9.576811	8.243853
C	13.74407	10.64463	8.302796
H	14.0425	11.54451	7.728993
H	13.583	10.97734	9.348732
C	12.50868	9.930505	7.709788
H	11.63691	9.913566	8.395535
H	12.156	10.38904	6.76269
C	13.00413	8.522546	7.450297
C	15.96265	6.62171	10.73722
C	15.5001	6.115425	12.08615
H	15.103	6.949619	12.70119
H	16.33573	5.66666	12.6596
C	14.40659	5.090685	11.71114
H	14.68175	4.049627	11.9803
H	13.42624	5.292825	12.18815
C	14.30679	5.22021	10.20663
O	19.36837	9.334175	9.16089
O	18.04267	10.9909	9.922017
C	19.00736	10.23324	10.07583
C	19.86148	10.26112	11.33011
H	19.9256	9.249429	11.78204
H	19.45582	10.9768	12.06651
H	20.89819	10.55687	11.06883
Mo	15.70221	6.695794	7.674235

N	16.93925	4.995584	7.504239
H	16.50708	4.135483	7.104502
N	18.71439	6.249911	8.272184
N	20.74422	7.06689	9.101749
H	20.31107	8.042064	9.242976
H	21.72485	6.891937	9.331217
N	16.08159	7.173234	5.627502
H	15.56624	6.798094	4.821559
N	17.81584	8.509538	6.351209
N	19.54967	10.05002	6.61308
H	19.5214	9.876318	7.675883
H	20.19821	10.72392	6.200552
C	18.20359	5.03472	7.807475
C	19.27416	3.96689	7.748522
H	18.97575	3.067043	8.322381
H	19.43517	3.634137	6.702592
C	20.50958	4.681034	8.341427
H	21.38131	4.697913	7.655635
H	20.8623	4.222555	9.288537
C	20.01417	6.089018	8.600851
C	17.05563	7.989843	5.314115
C	17.51823	8.496147	3.965214
H	17.9154	7.661968	3.350198
H	16.68261	8.944879	3.391723
C	18.61169	9.520935	4.340279
H	18.3365	10.56198	4.071107
H	19.59208	9.318834	3.863319
C	18.71141	9.391408	5.844799
O	13.64986	5.27745	6.890305
O	14.97549	3.620375	6.129827
C	14.01094	4.378134	5.975634
C	13.15698	4.349972	4.721252
H	13.09283	5.361577	4.269135
H	13.56277	3.634178	3.985032
H	12.12026	4.054183	4.982476

Table S3. Geometry Optimized XYZ coordinates for **3(OAc)**.

Atom	X	Y	Z
Mo	-1.35121	-1.88891	5.290949
N	-2.12204	-1.17297	7.107755
H	-2.75877	-0.33788	7.041458

N	-0.81082	-2.59713	8.335194
N	0.299848	-4.22663	9.555007
H	0.667183	-4.71958	8.682907
H	0.55718	-4.60738	10.46792
N	0.120879	-0.36888	5.353626
H	-0.06357	0.573961	4.987781
N	1.58281	-1.7425	6.450545
N	3.128013	-3.22941	7.312431
H	2.435829	-4.04397	7.236499
H	4.070736	-3.41635	7.660629
C	-1.76047	-1.56449	8.298966
C	-2.32857	-0.96452	9.562006
H	-3.29246	-1.47384	9.791786
H	-2.58036	0.096917	9.369307
C	-1.36503	-1.13256	10.73701
H	-0.45239	-0.5207	10.57571
H	-1.82599	-0.7859	11.68102
C	-0.99208	-2.61119	10.8382
H	-0.2375	-2.80336	11.62756
H	-1.88959	-3.21062	11.11512
C	-0.48148	-3.15281	9.521748
C	1.306908	-0.49143	5.906692
C	2.313468	0.63387	5.931798
H	1.774373	1.599437	6.008415
H	2.84803	0.651853	4.954071
C	3.323314	0.454522	7.065559
H	4.124219	1.215058	7.004386
H	2.824286	0.583819	8.048941
C	3.912498	-0.9513	6.958115
H	4.505185	-1.0461	6.019353
H	4.609116	-1.18162	7.78878
C	2.831123	-2.00476	6.910031
Mo	-0.06629	-3.20505	6.341724
N	0.704576	-3.92096	4.524914
H	1.341361	-4.75602	4.591214
N	-0.6067	-2.49685	3.297485
N	-1.71751	-0.86744	2.077704
H	-2.08486	-0.37452	2.949813
H	-1.97488	-0.4867	1.164793
N	-1.53836	-4.7251	6.278998
H	-1.35389	-5.66795	6.644807
N	-3.00033	-3.35146	5.182156
N	-4.54564	-1.86454	4.320447

H	-3.8535	-1.04993	4.396432
H	-5.48839	-1.67762	3.972302
C	0.343009	-3.52944	3.333704
C	0.911117	-4.12939	2.070658
H	1.874972	-3.62	1.84087
H	1.162975	-5.19081	2.263349
C	-0.05244	-3.9614	0.895663
H	-0.96505	-4.57331	1.056966
H	0.408526	-4.30802	-0.04836
C	-0.42549	-2.48279	0.794479
H	-1.1801	-2.29067	0.005132
H	0.471979	-1.88331	0.517542
C	-0.93609	-1.9412	2.110936
C	-2.72439	-4.60255	5.725941
C	-3.73092	-5.72787	5.7008
H	-3.1918	-6.69342	5.624121
H	-4.26546	-5.74592	6.678539
C	-4.74079	-5.54849	4.567071
H	-5.54167	-6.30906	4.628216
H	-4.24178	-5.67771	3.583669
C	-5.33001	-4.1427	4.674615
H	-5.92268	-4.04798	5.613395
H	-6.02666	-3.91235	3.843981
C	-4.24867	-3.0892	4.72273
O	1.293162	-5.16873	7.258851
O	1.863158	-6.24704	5.366419
C	1.507508	-6.27337	6.552604
C	1.288212	-7.57876	7.293059
H	0.268744	-7.61366	7.730427
H	1.998761	-7.65207	8.141687
H	1.435231	-8.44084	6.619266
O	-2.71068	0.07477	4.373816
O	-3.28059	1.153117	6.266253
C	-2.92493	1.179421	5.080068
C	-2.70539	2.484799	4.33967
H	-1.68597	2.519491	3.902173
H	-3.41603	2.558327	3.491135
H	-2.85214	3.34688	5.013527

Table S4. Geometry Optimized XYZ coordinates for $[Mo_2(NNN5)_4]^{4+}$

Atom	X	Y	Z

Mo	17.29173	7.902791	8.38055
N	16.03672	9.606953	8.595474
H	16.32555	10.51871	8.978758
N	14.26294	8.354243	7.775528
N	12.19856	7.652201	6.856295
H	12.55741	6.745097	6.547168
H	11.2211	7.862046	6.617422
N	16.89255	7.403518	10.40959
H	17.38652	7.786574	11.2287
N	15.16946	6.025039	9.690192
N	13.47637	4.379009	9.539588
H	13.49099	4.348659	8.516849
H	12.83879	3.721959	10.00686
C	14.76413	9.555791	8.287013
C	13.70725	10.62387	8.388682
H	13.99626	11.53137	7.818424
H	13.57344	10.94993	9.441778
C	12.45836	9.930846	7.811881
H	11.62065	9.855467	8.538931
H	12.04082	10.444	6.919145
C	12.95838	8.557917	7.447663
C	15.92005	6.585293	10.72905
C	15.46116	6.120798	12.08613
H	15.10672	6.976999	12.69828
H	16.29279	5.656375	12.65596
C	14.33832	5.121827	11.74835
H	14.54082	4.091584	12.11254
H	13.35105	5.405448	12.17337
C	14.28912	5.147903	10.24359
Mo	15.72655	6.708708	7.670775
N	16.98156	5.004547	7.455851
H	16.69274	4.092793	7.072566
N	18.75535	6.257258	8.275797
N	20.81972	6.9593	9.195029
H	20.46087	7.866403	9.504158
H	21.79719	6.749454	9.433901
N	16.12573	7.207982	5.641734
H	15.63176	6.824927	4.822624
N	17.84882	8.58646	6.361134
N	19.54191	10.23249	6.511738
H	19.52729	10.26284	7.534477
H	20.1795	10.88954	6.044469
C	18.25415	5.055709	7.764312

C	19.31103	3.987634	7.662642
H	19.02202	3.080131	8.2329
H	19.44484	3.66157	6.609545
C	20.55992	4.680655	8.239441
H	21.39763	4.756036	7.512391
H	20.97746	4.167505	9.132177
C	20.0599	6.053585	8.603661
C	17.09823	8.026206	5.322276
C	17.55712	8.490702	3.965195
H	17.91157	7.6345	3.353046
H	16.7255	8.955126	3.395362
C	18.67997	9.489671	4.30298
H	18.47746	10.51991	3.938789
H	19.66724	9.206048	3.877958
C	18.72917	9.463596	5.807734

Table S4. Geometry Optimized XYZ coordinates for $[Mo_2(NNN6)_4]^{4+}$

Atom	X	Y	Z
Mo	-1.298478908	-1.86664	5.306792
N	-2.071804316	-1.0658	7.108855
H	-2.704745127	-0.25494	7.163029
N	-0.836986376	-2.57027	8.326531
N	0.152524586	-4.26074	9.570076
H	0.285890833	-4.83978	8.736322
H	0.423860708	-4.67949	10.46775
N	0.21174338	-0.38185	5.376414
H	0.095584744	0.584573	5.0395
N	1.612841712	-1.83604	6.469378
N	3.157327522	-3.35906	7.292741
H	2.588625193	-4.15163	6.981877
H	4.069576723	-3.58359	7.707697
C	-1.72754272	-1.49276	8.307633
C	-2.269649256	-0.88834	9.573928
H	-3.206479454	-1.43023	9.843744
H	-2.566758056	0.162362	9.384729
C	-1.254522039	-1.00322	10.7135
H	-0.362324346	-0.3765	10.50628
H	-1.689879878	-0.63607	11.6616
C	-0.861380864	-2.47188	10.85132
H	-0.024813867	-2.62418	11.5657
H	-1.711742038	-3.06537	11.26566

C	-0.506985004	-3.10437	9.532679
C	1.386024872	-0.55825	5.949007
C	2.426580268	0.525278	6.024956
H	1.932831054	1.516299	5.978868
H	3.068880239	0.457686	5.115605
C	3.285625625	0.36722	7.281973
H	4.098884679	1.11661	7.295667
H	2.676374421	0.536608	8.193969
C	3.870549193	-1.04291	7.279794
H	4.642379976	-1.14311	6.479054
H	4.399113612	-1.28722	8.22558
C	2.834916312	-2.09946	7.004426
Mo	-0.11900089	-3.22733	6.325902
N	0.654323388	-4.02817	4.523839
H	1.287263056	-4.83903	4.469666
N	-0.580492731	-2.5237	3.306163
N	-1.570003755	-0.83322	2.062619
H	-1.7033697	-0.25419	2.896374
H	-1.841339387	-0.41448	1.164942
N	-1.629223814	-4.71212	6.256279
H	-1.513065418	-5.67854	6.593194
N	-3.03032165	-3.25793	5.163312
N	-4.574804693	-1.73491	4.339942
H	-4.006102018	-0.94235	4.650804
H	-5.487053144	-1.51038	3.924983
C	0.310062809	-3.60121	3.325061
C	0.852168905	-4.20563	2.058766
H	1.788999875	-3.66374	1.78895
H	1.149276475	-5.25633	2.247964
C	-0.162957455	-4.09075	0.919191
H	-1.055155896	-4.71747	1.12641
H	0.272400855	-4.4579	-0.02891
C	-0.55609755	-2.62209	0.781376
H	-1.39266406	-2.46979	0.066995
H	0.294264344	-2.0286	0.367031
C	-0.910493938	-1.9896	2.100015
C	-2.803504852	-4.53572	5.683684
C	-3.844060643	-5.61925	5.607736
H	-3.350312406	-6.61027	5.653827
H	-4.486361895	-5.55165	6.517086
C	-4.703104332	-5.46119	4.350718
H	-5.516363567	-6.21058	4.337024
H	-4.093851998	-5.63058	3.438723

C	-5.288027569	-4.05106	4.352892
H	-6.059860138	-3.95086	5.153631
H	-5.816589846	-3.80675	3.407104
C	-4.252394765	-2.99451	4.62826

2.2.8.5 References

1. Neese, F., The ORCA program system. *WIREs Computational Molecular Science* **2012,** *2* (1), 73-78.
2. Neese, F., Software update: The ORCA program system—Version 5.0. *WIREs Computational Molecular Science* **2022,** *n/a* (n/a), e1606.
3. Becke, A. D., Density-functional exchange-energy approximation with correct asymptotic behavior. *Phys Rev A Gen Phys* **1988,** *38* (6), 3098-3100.
4. Stephens, P. J.; Devlin, F. J.; Chabalowski, C. F.; Frisch, M. J., Ab initio calculation of vibrational absorption and circular dichroism spectra using density functional force fields. *The Journal of physical chemistry* **1994,** *98* (45), 11623-11627.
5. Becke, A. D., Density-functional thermochemistry. III. The role of exact exchange. *The Journal of Chemical Physics* **1993,** *98* (7), 5648-5652.
6. Lee, C.; Yang, W.; Parr, R. G., Development of the Colle-Salvetti correlation-energy formula into a functional of the electron density. *Physical review B* **1988,** *37* (2), 785.
7. Vosko, S. H.; Wilk, L.; Nusair, M., Accurate spin-dependent electron liquid correlation energies for local spin density calculations: a critical analysis. *Can. J. Phys.* **1980,** *58* (8), 1200-1211.
8. Guevara-Vela, J. M.; Rocha-Rinza, T.; Pendás, Á. M., Performance of the RI and RIJCOSX approximations in the topological analysis of the electron density. *Theor. Chem. Acc.* **2017,** *136* (5), 57.
9. Neese, F., An improvement of the resolution of the identity approximation for the formation of the Coulomb matrix. *J. Comput. Chem.* **2003,** *24* (14), 1740-1747.
10. Neese, F.; Wennmohs, F.; Hansen, A.; Becker, U., Efficient, approximate and parallel Hartree–Fock and hybrid DFT calculations. A 'chain-of-spheres' algorithm for the Hartree–Fock exchange. *Chem. Phys.* **2009,** *356* (1-3), 98-109.
11. Weigend, F., Accurate Coulomb-Fitting Basis Sets for H to Rn. *Physical Chemistry Chemical Physics* **2006,** *8*, 1057-1065.
12. Pantazis, D. A.; Chen, X.-Y.; Landis, C. R.; Neese, F., All-Electron Scalar Relativistic Basis Sets for Third-Row Transition Metal Atoms. *Journal of Chemical Theory and Computation* **2008,** *4* (6), 908-919.
13. Peterson, K. A.; Puzzarini, C., Systematically Convergent Basis Sets for Transition Metals. Ii. Pseudopotential-Based Correlation Consistent Basis Sets for the Group 11 (Cu, Ag, Au) and 12 (Zn, Cd, Hg) Elements. *Theor. Chem. Acc.* **2005,** *114*, 283-296.
14. Weigend, F.; Ahlrichs, R., Balanced Basis Sets of Split Valence, Triple Zeta Valence and Quadruple Zeta Valence Quality hor H To Rn: Design and Assessment of Accuracy. *Physical Chemistry Chemical Physics* **2005,** *7*, 3297-3305.
15. Weigend, F., Accurate Coulomb-fitting basis sets for H to Rn. *Physical Chemistry Chemical Physics* **2006,** *8* (9), 1057-1065.
16. Grimme, S.; Antony, J.; Ehrlich, S.; Krieg, H., A Consistent and Accurate ab initio Parametrization of Density Functional Dispersion Correction (DFT-D) for the 94 Elements H-Pu. *The Journal of Chemical Physics* **2010,** *132*, 154104.
17. Grimme, S.; Ehrlich, S.; Goerigk, L., Effect of the Damping Function in Dispersion Corrected Density Functional Theory. *J. Comput. Chem.* **2011,** *32*, 1456-1465.
18. Pettersen, E. F.; Goddard, T. D.; Huang, C. C.; Couch, G. S.; Greenblatt, D. M.; Meng, E. C.; Ferrin, T. E., UCSF Chimera—A Visualization System for Exploratory Research and Analysis. *J. Comput. Chem.* **2004,** *25*, 1605-1612.
19. Macrae, C. F.; Sovago, I.; Cottrell, S. J.; Galek, P. T. A.; McCabe, P.; Pidcock, E.; Platings, M.; Shields, G. P.; Stevens, J. S.; Towler, M.; Wood, P. A., Mercury 4.0: from visualization to analysis, design and prediction. *J. Appl. Crystallogr.* **2020,** *53* (1), 226-235.
20. *OriginPro 2022 (Learning Edition)*. OriginLab Corporation: Northampton, MA, USA, 2022.

21. Holste, G.; Schäfer, H., Mo2 (CH3COO) 4, Mo2 (C6H5COO) 4 und [Mo6Cl8] Cl2 (CH3COO) 2. *Z. Anorg. Allg. Chem.* **1972,** *391* (3), 263-270.
22. Dolinar, B. S.; Berry, J. F., Electronic tuning of Mo2(thioamidate)4 complexes through π-system substituents and cis/trans isomerism. *Dalton Transactions* **2014,** *43* (16), 6165-6176.
23. Aristov, M. M.; Geng, H.; Harris, J. W.; Berry, J. F., Updated Synthesis and Characterization of Imidines: Using Crystallographic Characterization to Identify Tautomers and Localized Systems of π-Bonding. *Manuscript in Preparation* **2022**.
24. APEX3, Bruker-AXS **2016,** *Version 2016.5-0*, Madison, Wisconsin, USA.
25. APEX3, Bruker-AXS **2018,** *Version 2018.1-0*, Madison, Wisconsin, USA.
26. Krause, L.; Herbst-Irmer, R.; Sheldrick, G. M.; Stalke, D., Comparison of silver and molybdenum microfocus X-ray sources for single-crystal structure determination. *J. Appl. Crystallogr.* **2015,** *48* (Pt 1), 3-10.
27. Sheldrick, G. M., XPREP. Version 2013/1. *Georg-August-Universität Göttingen, Göttingen, Germany* **2013**.
28. Sheldrick, G. M., The SHELX homepage. *http://shelx.uni-ac.gwdg.de/SHELX/* **2013**.
29. Sheldrick, G. M., SHELXT–Integrated space-group and crystal-structure determination. *Acta Crystallographica Section A: Foundations and Advances* **2015,** *71* (1), 3-8.
30. Dolomanov, O. V.; Bourhis, L. J.; Gildea, R. J.; Howard, J. A.; Puschmann, H., OLEX2: a complete structure solution, refinement and analysis program. *J. Appl. Crystallogr.* **2009,** *42* (2), 339-341.
31. Guzei, I. A., Programs Gn. *University of Wisconsin-Madison, Madison, Wisconsin, USA*.

Chapter 3: *Computational Examination of Unusual Au Atom Bonding Environments*

Subchapter 3.1: Computational studies of the stabilization of various conformers of $[(bipy)Au(PEt_3)]^+$

Michael M. Aristov and John F. Berry

Department of Chemistry, University of Wisconsin, Madison, 1101 University Ave., Madison WI 53706

Email: berry@chem.wisc.edu

3.1.0 Author Contribution: This work was written by MMA and JFB. All computations were set up by MMA.

3.1.1 Introduction: When d^{10} metal centers are forced into a three-coordinate geometry, they become strained due to their filled shells.[1-3] This effect becomes much more apparent when looking at chelating ligands, as the binding distances to the chelating ligand may become asymmetric.[6, 7] An asymmetric binding motif was noticed in $[(bipy)Au(PEt_3)]^+$ (bipy = 2,2'-bipyridine), and we performed a computational study in an effort to understand the origin and energetics of the asymmetrically binding bipy ligand. This report details the result of that study.

3.1.2 Computational Methods

3.1.2.1 Geometry Optimization and Frequency Calculations: Initial coordinates of $[(bipy)Au(PEt_3)]^+$ for the calculations were obtained from the crystallographic data for ll123 with the counterion removed. Geometry optimizations and frequency calculations were carried out using Gaussian 09.[8] The CAM-B3LYP[9] functional and the SDD[10, 11] basis set were used for all atoms that included relativistically contracted effective core potentials for gold. Five structures

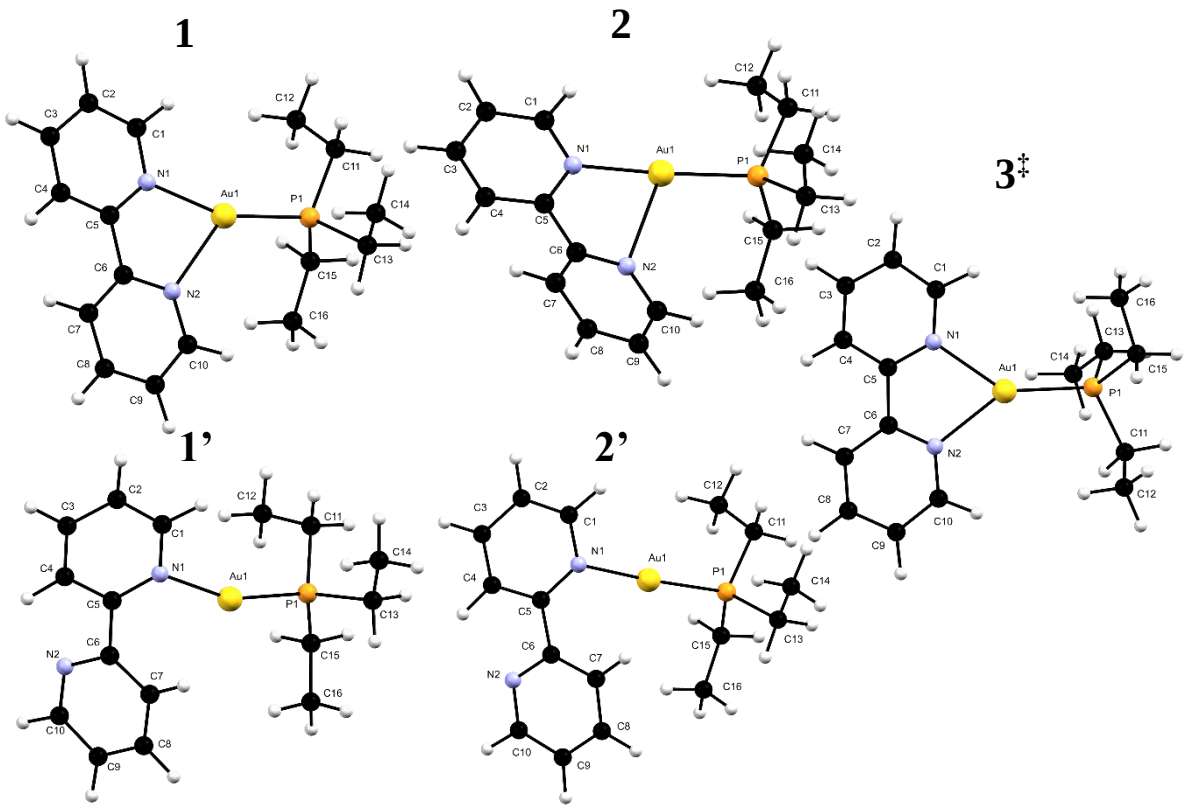

*Figure 1. Top left: Computationally optimized structure of [(bipy)AuPEt₃]⁺, **1**. Top center: Computationally optimized structure of [(bipy)AuPEt₃]⁺ with the P-Au-N₁ angle constrained to be equal to the P-Au-N₁ angle in **2'**, **2**. Bottom left: Computationally optimized structure of [(bipy)AuPEt₃]⁺ with the P-Au-N₁ angle constrained to be equal to the P-Au-N₁ angle in **1**, **1'**. Bottom center: Computationally optimized structure of two-coordinate [(bipy)AuPEt₃]⁺, **2'**. Center right: Computationally optimized structure of [(bipy)AuPEt₃]⁺ with Au-N distances constrained to be equivalent, **3‡**.*

were examined, an asymmetric structure, **1**, based on crystallographic coordinates, a 2-coordinate bent structure, **1'**, a distorted T-shaped structure, **2**, a 2-coordinate linear structure, **2'**, and a symmetric structure, **3‡**, Figure 1. Structures **1**, **2**, and **3‡** contain a planar bidentate bipy ligand with an N-C-C-N dihedral angle of <50°, and structures **1'** and **2'** contain a twisted monodentate bipy ligand with an N-C-C-N dihedral angle of <180° but >60°. Structures **1**, **1'**, **2**, and **2'** were optimized to have no imaginary frequencies. Structure **3‡** was optimized using a modified z-Matrix to constrain the two Au—N bond distances to the same, freely refining variable. Structure **3‡** as optimized was found to have one imaginary frequency of -17 cm^{-1} that interconverts **3‡** to **1**. Structures **1'** and **2** were optimized with the N-Au-P angle constrained to 159.00° and 176.20° respectively.

3.1.2.2 Single Point and Natural Resonance Theory (NRT) Calculations: Single-point and NRT calculations were carried out using ORCA version 4.0.0.2.[12] For the single-point calculations, the CAM-B3LYP[9] exchange-correlation functional was used. The Stuttgart-Dresden effective core potential (ECP), def2-SVP,[13] was used along with the valence basis sets def2-TZVPP[14] and density fitting basis set def2-TZVPP/C [14] for Au. The def2-SVP[13] basis set, def2/J[15] auxiliary basis, and def2-SVP/C[16] density fitting basis set were used for all other atoms. The atom-pairwise dispersion corrections were accounted for with the Becke-Johnson damping scheme (D3BJ).[17, 18] Normal optimization and normal self-consistent field convergence criteria were employed with grid4 and finalgrid5 for all calculations. Visualizations of the orbitals were carried out with the UCSF Chimera package.[4] The relative contributions of the resonance structures were determined from NRT using NBO 7.0.1.[5, 19]

3.1.3 Computational Discussion: In an effort to understand the origins of the asymmetric gold-nitrogen bond distances in the three-coordinate $[(bipy)Au(PEt_3)]^+$ complexes, five structures were optimized. The first structure, **1**, was optimized from crystallographic coordinates. In structure **1'** the bipy ligand was forced to be a monodentate ligand by twisting about the bridging C—C bond. In addition to this twist, the P-Au-N angle was also constrained to 159.00°, which was the optimized bent angle found from **1**. In structure **2'** a monodentate bipy ligand was also utilized with a twist about the central C—C bridge, comparable to **1'**, and this allowed for only one N atom to interact with the Au center. In structure **2** one P-Au-N angle was fixed to 176.20°, as this was the optimized linear angle found from **2'.** In structure **3**‡ the two Au—N bonds were both fixed to a single distance, r1, that itself was optimized. The resulting structures of **1** and **3**‡ maintained a planar bonding motif about the Au center in an extended Y-shape geometry whereas **2'** was structurally linear about the Au center, Figure 1.[3] The hypothetical **2** was found to have the distal

N_2 atom nearly in the plane formed by P-Au-N_1 (deviation of 0.77°) with a 20.32° twist of N-C-C-N dihedral angle in the bipy ligand. The hypothetical **1'** was found to have a distorted geometry with the gold center bending 10.36° away from the plane of the pyridine ring. The Au—N_1 and Au—P bond distances in **1** were slightly overestimated by the calculations, Table 1, as is common for DFT results.[1, 20, 21] The Au—N_2 distance in **1** was ~0.019 Å shorter than expected, most likely due to the overestimation of the stronger Au—P bond. Frequency calculations indicate that **1**, **1'**, **2**, and **2'** occupy local minima, whereas **3**‡ was found to have one imaginary frequency corresponding to an asymmetric distortion of the two gold-nitrogen bonds. From the nature of this imaginary frequency, the geometry optimization and frequency calculations strongly imply that **3**‡

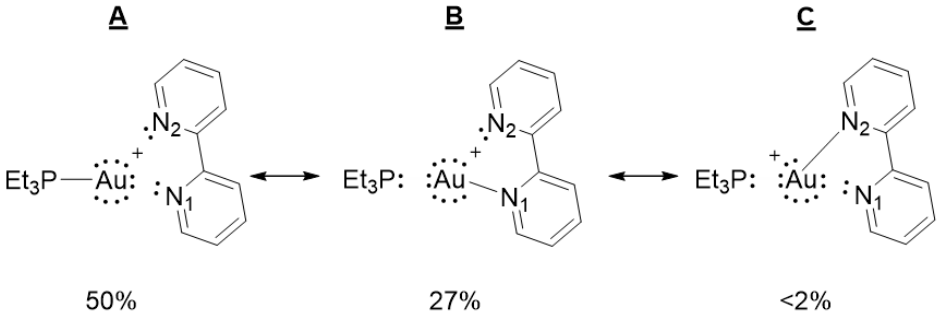

*Figure 2. Resonance structures of [(bipy)AuPEt$_3$]$^+$as described from NRT calculations performed on **1**.*

is best described as a transition state between the two limiting geometries of **1**. Overall, **3**‡ was found to be higher in energy than **1** by 7 kJ/mol, similar to the 5 kJ/mol estimation of the symmetric form of [(phen)AuPPh$_3$]$^+$.[22] Relative to **1**¸ the free energy changes at 298.15 K induced by the distortions were 33, 8.5, and 23 kJ/mol for **1'**, **2**, and **2'**, respectively.

3.1.4 Three-center Four-Electron (3c/4e) Bond and the *anti*-Chelate Effect: We interpret the bonding in [(bipy)Au(PEt$_3$)]$^+$ via Natural Resonance Theory (NRT) calculations using the "12 electron rule" formalism of Landis and Weinhold.[23] The most dominant Lewis structure for both **1** and **3**‡ is one with five lone pairs on Au and one bond to the P atom, **A** in Figure 2. This structure results in a saturated (12 electron) gold center, and thereby inhibits the formation of any classical,

2 e^- bonds between the gold and either of the bipy nitrogen atoms. The nitrogen atoms may instead donate a lone pair into an empty Au—P anti-bonding orbital, resulting in a three-center four-electron (3c/4e) P-Au-N bond, Figure 3, including the resonance forms **B** and **C** of Figure 2.[2, 24] The 3c/4e bonding interaction is maximized when the three atoms approach a linear geometry, as observed by a 146.1 kJ/mol stabilization of the lone pair on N_1 in **1** due to its donation into the P—Au antibonding orbital. This contrasts with the 39.6 kJ/mol stabilization experienced by the donation of the N_2 lone pair, which is significantly diminished due to the poor orbital overlap. This energetic mismatch is also reflected in the distinct Au—N bond lengths, with Au—N_1 being shorter as determined crystallographically by 0.278(4) Å, Table 1.

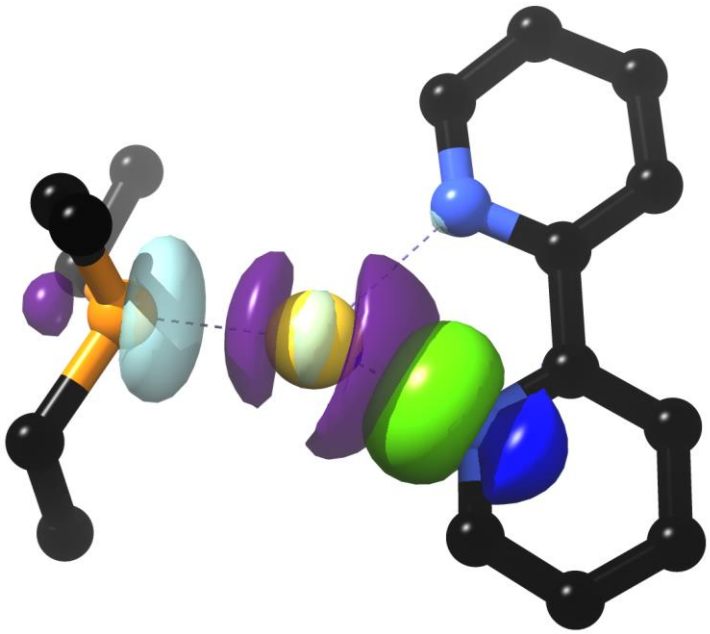

Figure 3. Plot showing the 94% probability for electron density of two orbitals involved in the P-Au-N_1 3c/4e bond. The green and blue lobes represent the positive and negative phases for the lone pair on N_1 respectively, and the blue and purple lobes represent the positive and negative phases for the empty Au—P anti-bonding orbital. The image was generated with chimera from NBO output.[4, 5]

*Table 1. Experimental and computational bond distances and angles for **1-5**.*

	Experimental	Computational				
	Crystallographic	**1**	**1'**	**2**	**2'**	**3**‡
N1-Au1-N2	69.40(8) °	71°	------	70°	------	72°
N1-Au1-P1	157.63(8) °	159°	159°	176°	176°	144°
N2-Au1-P1	132.61(7) °	130°	------	113°	------	144°
Au1-N1	2.190(2) Å	2.19 Å	2.12	2.13	2.10 Å	2.30 Å
Au1-N2	2.468(2) Å	2.45 Å	------	2.66	------	2.30 Å
Au1-P1	2.231(1) Å	2.35 Å	2.36 Å	2.35	2.35 Å	2.34 Å

The asymmetric bidentate binding of the bipy ligand is a manifestation of the *anti*-chelate effect, known to occur between Au^+ and chelating ligands.[25] For this complex, the *anti*-chelate effect arises from the combination of the fixed bite angle of the chelating bipy ligand and the Au center's preference for a linear geometry to satisfy the 3c/4e P-Au-N_1 bond.

Three additional structures were studied computationally in addition to **1** and **3**‡ in an effort to estimate the energies associated with bending the P-Au-N_1 3c/4e bond and the dissociation energy of atom N_2 from Au. Comparing structures **2'** and **1'**, a 10 kJ/mol difference was found, and this destabilization energy may be attributed to the bending of the N_1-Au-P 3c/4e bond. Distorting structure **1** to **1'** resulted in a 33 kJ/mol destabilization. Accounting for the ~20 kJ/mol stabilization energy associated with twisting the N-C-C-N dihedral angle in bipy[26] from 0.14° in **1** to 139.94° in **2'** along with the 10 kJ/mol stabilization gained from unbending the N_1-Au-P interaction as determined from the **2'** to **1'** transformation, then a total destabilization energy associated with breaking the Au—N_2 bond can be estimated at 53 kJ/mol. Comparing **2** and **2'** we find a 14.5 kJ/mol destabilization, and accounting for the bipy torsion, we can estimate a total destabilization of 34.5 kJ/mol that can be attributed to loss of the Au—N_2 bond. These estimated Au—N_2 bond energies are large enough to the structurally important, and thus contribute to the experimentally observed structure.

3.1.5 Conclusion: Through the use of computationally methods, we were able to show that the asymmetric bind motif was energetically favorable, and that the symmetric system was a transition state between the two asymmetric forms. The energetics of the asymmetric form were bracketed, and evidence for both the *anti*-chelate effects and a 3c-4e bond were found in the computational results.

3.1.6 References:

1. Boom, D. H. A.; Ehlers, A. W.; Nieger, M.; Devillard, M.; Bouhadir, G.; Bourissou, D.; Slootweg, J. C., Gold(I) Complexes of the Geminal Phosphinoborane $tBu_2PCH_2BPh_2$. *ACS Omega* **2018,** *3*, 3945-3951.
2. Cheung, Y.-S.; Ng, C.-Y.; Chiu, S.-W.; Li, W.-K., Application of Three-Center-Four-Electron Bonding for Structural and Stability Predictions of Main Group Hypervalent Molecules: The Fulfillment of Octet Shell Rule. *Journal of Molecular Structure: THEOCHEM* **2003,** *623*, 1-10.
3. Davis, T. L.; Watts, J. L.; Brown, K. J.; Hewage, J. S.; Treleven, A. R.; Lindeman, S. V.; Gardinier, J. R., Structural Classification of Metal Complexes with Three-Coordinate Centres. *Dalton Trans.* **2015,** *44*, 15408-15412.
4. Pettersen, E. F.; Goddard, T. D.; Huang, C. C.; Couch, G. S.; Greenblatt, D. M.; Meng, E. C.; Ferrin, T. E., UCSF Chimera—A Visualization System for Exploratory Research and Analysis. *J. Comput. Chem.* **2004,** *25*, 1605-1612.
5. Glendening, E. D.; Landis, C. R.; Weinhold, F., NBO 7.0: New Vistas in Localized and Delocalized Chemical Bonding Theory. *J. Comput. Chem.* **2019,** *40*, 2234-2241.
6. Chen, S. Gas Phase Ion/Molecule Reactions Between Monocationic Metal-Bipyridyl (Metal= Cu, Ag, Au) Complexes and Small Gas Molecules Using Ion Trap Mass Spectrometer. University of New Hampshire, 2021.
7. Ryan, P. E.; Guénée, L.; Canard, G.; Gumy, F.; Bünzli, J.-C. G.; Piguet, C., Structural, spectroscopic, and thermodynamic consequences of anti-chelate effect in nine-coordinate lanthanide podates. *Inorg. Chem.* **2009,** *48* (6), 2549-2560.
8. M. J. Frisch, G. W. T., H. B. Schlegel, G. E. Scuseria, M. A. Robb,; J. R. Cheeseman, G. S., V. Barone, G. A. Petersson, H. Nakatsuji, X. Li, M. Caricato, A.; Marenich, J. B., B. G. Janesko, R. Gomperts, B. Mennucci, H. P. Hratchian, J. V. Ortiz, A. F.; Izmaylov, J. L. S., D. Williams-Young, F. Ding, F. Lipparini, F. Egidi, J. Goings, B. Peng,; A. Petrone, T. H., D. Ranasinghe, V. G. Zakrzewski, J. Gao, N. Rega, G. Zheng, W. Liang, M.; Hada, M. E., K. Toyota, R. Fukuda, J. Hasegawa, M. Ishida, T. Nakajima, Y. Honda, O. Kitao, H.; Nakai, T. V., K. Throssell, J. A. Montgomery, Jr., J. E. Peralta, F. Ogliaro, M. Bearpark, J. J. Heyd,; E. Brothers, K. N. K., V. N. Staroverov, T. Keith, R. Kobayashi, J. Normand, K. Raghavachari, A.; Rendell, J. C. B., S. S. Iyengar, J. Tomasi, M. Cossi, J. M. Millam, M. Klene, C. Adamo, R. Cammi,; J. W. Ochterski, R. L. M., K. Morokuma, O. Farkas, J. B. Foresman, and D. J. Fox, Gaussian, Inc. Wallingford CT, Gaussian 09, Revision B.01. **2016**.
9. Yanai, T.; Tew, D. P.; Handy, N. C., A New Hybrid Exchange–Correlation Functional Using the Coulomb-Attenuating Method (CAM-B3LYP). *Chem. Phys. Lett.* **2004,** *393*, 51-57.
10. Andrae, D.; Häußermann, U.; Dolg, M.; Stoll, H.; Preuß, H., Energy-Adjusted ab initio Pseudopotentials for the Second and Third Row Transition Elements. *Theoretica chimica acta* **1990,** *77*, 123-141.
11. Schwerdtfeger, P.; Dolg, M.; Schwarz, W. H. E.; Bowmaker, G. A.; Boyd, P. D. W., Relativistic Effects in Gold Chemistry. I. Diatomic Gold Compounds. *The Journal of Chemical Physics* **1989,** *91*, 1762-1774.
12. Neese, F., Software Update: The Orca Program System, Version 4.0. *Wiley Interdisciplinary Reviews: Computational Molecular Science* **2018,** *8*, e1327.
13. Weigend, F.; Ahlrichs, R., Balanced Basis Sets of Split Valence, Triple Zeta Valence and Quadruple Zeta Valence Quality hor H To Rn: Design and Assessment of Accuracy. *Physical Chemistry Chemical Physics* **2005,** *7*, 3297-3305.

14. Peterson, K. A.; Puzzarini, C., Systematically Convergent Basis Sets for Transition Metals. Ii. Pseudopotential-Based Correlation Consistent Basis Sets for the Group 11 (Cu, Ag, Au) and 12 (Zn, Cd, Hg) Elements. *Theor. Chem. Acc.* **2005,** *114*, 283-296.
15. Weigend, F., Accurate Coulomb-Fitting Basis Sets for H to Rn. *Physical Chemistry Chemical Physics* **2006,** *8*, 1057-1065.
16. Hellweg, A.; Hättig, C.; Höfener, S.; Klopper, W., Optimized Accurate Auxiliary Basis Sets for RI-MP_2 And RI-CC_2 Calculations for the Atoms Rb to Rn. *Theor. Chem. Acc.* **2007,** *117*, 587-597.
17. Grimme, S.; Ehrlich, S.; Goerigk, L., Effect of the Damping Function in Dispersion Corrected Density Functional Theory. *J. Comput. Chem.* **2011,** *32*, 1456-1465.
18. Grimme, S.; Antony, J.; Ehrlich, S.; Krieg, H., A Consistent and Accurate ab initio Parametrization of Density Functional Dispersion Correction (DFT-D) for the 94 Elements H-Pu. *The Journal of Chemical Physics* **2010,** *132*, 154104.
19. NBO 7.0. E. D. Glendening, J. K. Badenhoop, A. E. Reed, J. E. Carpenter, J. A. Bohmann, C. M. Morales, P. Karafiloglou, C. R. Landis, and F. Weinhold, Theoretical Chemistry Institute, University of Wisconsin, Madison, WI (2018).
20. Schwerdtfeger, P.; Hermann, H. L.; Schmidbaur, H., Stability of the Gold(I)−Phosphine Bond. A Comparison with Other Group 11 Elements. *Inorg. Chem.* **2003,** *42*, 1334-1342.
21. Shawkataly, O. b.; Goh, C.-P.; Tariq, A.; Khan, I. A.; Fun, H.-K.; Rosli, M. M., Synthesis, Spectral Characterization and Crystals Structure of some Arsane Derivatives of Gold (I) Complexes: A Comparative Density Functional Theory Study. *PLOS ONE* **2015,** *10*, e0119620.
22. Yang, Y.; Eberle, L.; Mulks, F. F.; Wunsch, J. F.; Zimmer, M.; Rominger, F.; Rudolph, M.; Hashmi, A. S. K., Trans Influence of Ligands on the Oxidation of Gold(I) Complexes. *Journal of the American Chemical Society* **2019**, ASAP.
23. Weinhold, F.; Landis, C., *Valency and Bonding: A Natural Bond Orbital Donor-Acceptor Perspective*. 2005; p 365-367.
24. Berry, J. F., The Role of Three-Center/Four-Electron Bonds in Superelectrophilic Dirhodium Carbene and Nitrene Catalytic Intermediates. *Dalton Trans.* **2012,** *41*, 700-713.
25. Weinhold, F.; Landis, C., *Valency and Bonding: A Natural Bond Orbital Donor-Acceptor Perspective*. 2005; p 526-530.
26. Göller, A.; Grummt, U.-W., Torsional Barriers in Biphenyl, 2,2′-Bipyridine and 2-Phenylpyridine. *Chem. Phys. Lett.* **2000,** *321* (5), 399-405.

Supporting Information for Subchapter 3.1*:* Computational studies of the stabilization of various conformers of $[(bipy)Au(PEt_3)]^+$

Michael M. Aristov and John F. Berry

Department of Chemistry, University of Wisconsin, Madison, 1101 University Ave., Madison WI 53706

Email: berry@chem.wisc.edu

3.1.7.1 Geometry Optimized Coordinates

*Table S1: Cartesian coordinates from **1** geometry optimization.*

Au	0	0	0
N	1.821138	1.637919	-0.00056
N	1.912377	-1.07614	0.002019
P	-2.32086	0.341387	0.010119
C	1.893962	-2.42957	0.004862
H	0.919454	-2.90006	0.007594
C	3.062879	-3.19119	0.004867
H	3.004107	-4.27271	0.00718
C	4.292749	-2.52214	0.001901
H	5.224349	-3.07761	0.001463
C	4.307784	-1.12419	-0.00015
H	5.254764	-0.60164	-0.002
C	3.098981	-0.41314	0.000287
C	3.051673	1.07757	0.000464
C	1.687959	2.977031	0.001384
C	2.793065	3.835915	0.003823
C	4.073535	3.268673	0.004105
C	4.206349	1.875132	0.002458
H	5.194684	1.43479	0.003087
H	4.956029	3.899301	0.005753
H	2.649898	4.909897	0.005386
H	0.675967	3.365419	0.000713
C	-3.35066	-1.22004	0.097242
H	-3.11128	-1.71236	1.044719
H	-4.40503	-0.92047	0.138654

C	-3.10457	-2.17978	-1.0754
H	-3.67803	-3.10097	-0.93286
H	-2.0455	-2.45108	-1.15118
H	-3.41424	-1.74758	-2.03287
C	-2.92152	1.370764	1.454927
H	-2.48312	2.368199	1.351267
H	-4.00853	1.478402	1.356469
C	-2.55587	0.772355	2.821641
H	-3.02875	-0.20236	2.982493
H	-2.89488	1.435167	3.623882
H	-1.47226	0.647062	2.925544
C	-2.9615	1.237305	-1.50473
H	-2.79622	0.582754	-2.36578
H	-4.04521	1.35601	-1.38515
C	-2.28804	2.596713	-1.74093
H	-2.68303	3.057293	-2.65177
H	-1.20519	2.484472	-1.8673
H	-2.47198	3.295062	-0.91672

*Table S2: Cartesian coordinates from **1'** geometry optimization.*

P1	0	0	0
Au1	2.248483	-0.52509	0.478612
N1	4.076218	-1.59517	0.460091
C1	3.979482	-2.95295	0.487755
H	2.996486	-3.36603	0.675133
C2	5.07733	-3.77794	0.269845
H	4.95482	-4.8537	0.301473
C3	6.32091	-3.18733	-0.0047
H	7.193118	-3.80248	-0.19778
C4	6.421706	-1.7951	-0.01906
H	7.355379	-1.2899	-0.22869
C5	5.288048	-1.01203	0.240752
C6	5.414699	0.470159	0.274902
C7	4.748001	1.262536	1.22398
C8	4.945535	2.650573	1.198743
C9	5.799013	3.198823	0.234075
C10	6.444217	2.330655	-0.66157
N2	6.261709	0.99777	-0.63891
H	7.130777	2.707866	-1.41187
H	5.981413	4.266044	0.1823
H	4.458273	3.286245	1.93079
H	4.138643	0.80863	1.9987

C11	-0.6626	-1.14146	-1.3278
H	-0.62074	-2.16135	-0.93383
H	-1.72004	-0.89	-1.47405
C12	0.105581	-1.05121	-2.65475
H	-0.30438	-1.77034	-3.37043
H	1.168454	-1.28246	-2.52199
H	0.026314	-0.0585	-3.11002
C13	-1.17165	-0.19496	1.445896
H	-0.90542	0.564632	2.187008
H	-2.18019	0.038289	1.083868
C14	-1.13219	-1.59243	2.081916
H	-1.44335	-2.37375	1.380166
H	-1.81537	-1.63172	2.935717
H	-0.12894	-1.83761	2.448316
C15	-0.29561	1.730971	-0.64513
H	0.254904	1.827973	-1.58564
H	-1.36352	1.818114	-0.87869
C16	0.138877	2.827908	0.338076
H	-0.02399	3.813387	-0.10879
H	1.203879	2.745023	0.582758
H	-0.43242	2.795186	1.27195

*Table S3: Cartesian coordinates from **2** geometry optimization.*

Au1	0	0	0
N1	1.989242	-0.76859	0.014712
P1	-2.24119	0.701588	0.010704
N2	1.729437	1.982231	-0.39226
C1	2.12022	-2.12061	0.015583
H	1.203801	-2.6939	0.064885
C2	3.359753	-2.75349	-0.04119
H	3.413509	-3.83517	-0.03856
C3	4.510586	-1.95872	-0.10738
H	5.494252	-2.41181	-0.16665
C4	4.374513	-0.56839	-0.105
H	5.253563	0.057645	-0.18246
C5	3.100782	0.016931	-0.03397
C6	2.937115	1.498397	-0.02654
C10	1.530347	3.312746	-0.43085
C9	2.532111	4.233648	-0.09855
C8	3.78045	3.740321	0.301641
C7	3.987489	2.356307	0.340267
H	4.940808	1.964792	0.672327

H	4.57799	4.41906	0.584013
H	2.334563	5.298011	-0.14808
H	0.546599	3.646541	-0.74318
C11	-3.48867	-0.58207	0.555257
H	-3.24856	-0.84993	1.588504
H	-4.47608	-0.1045	0.558828
C12	-3.49454	-1.83778	-0.32857
H	-4.19943	-2.57282	0.07192
H	-2.5045	-2.30601	-0.36034
H	-3.80206	-1.61692	-1.35625
C13	-2.53679	2.163201	1.142644
H	-1.92261	2.991363	0.775952
H	-3.58683	2.459953	1.032009
C14	-2.20618	1.870502	2.613963
H	-2.84907	1.088333	3.031125
H	-2.35626	2.771131	3.217399
H	-1.1637	1.555618	2.734988
C15	-2.83978	1.267301	-1.67052
H	-2.81733	0.397386	-2.33359
H	-3.88771	1.572525	-1.56362
C16	-1.99842	2.405609	-2.26653
H	-2.36632	2.657483	-3.26592
H	-0.94635	2.114544	-2.36141
H	-2.05665	3.316875	-1.66036

*Table S4: Cartesian coordinates from **2'** geometry optimization.*

Au1	-0.36399	-0.50899	0.069297
P1	-2.57359	0.276051	-0.12003
N2	1.573227	-1.32247	0.164251
C1	1.657348	-2.68245	0.195711
H	0.726055	-3.22343	0.306002
C2	2.867839	-3.35502	0.075276
H	2.885584	-4.43754	0.106887
C3	4.040058	-2.60462	-0.10464
H	4.99901	-3.09768	-0.22192
C4	3.955102	-1.21145	-0.12495
H	4.82806	-0.58766	-0.26549
C5	2.711462	-0.58379	0.034459
C6	2.650987	0.90348	0.062609
C7	1.865547	1.610112	0.987701
C8	1.905189	3.011554	0.970591
C9	2.72163	3.658272	0.034969
C10	3.489377	2.873559	-0.84054
N1	3.461144	1.528268	-0.82292
H	4.151433	3.32965	-1.56872
H	2.783477	4.739578	-0.00906
H	1.324934	3.584633	1.686406
H	1.280384	1.083627	1.733827
C11	-3.78475	-1.05571	-0.63039
H	-3.77592	-1.8228	0.149657
H	-4.7843	-0.60446	-0.63548
C12	-3.4645	-1.68175	-1.99608
H	-4.17921	-2.48091	-2.21471
H	-2.46019	-2.1198	-2.01298
H	-3.53285	-0.9524	-2.80994
C13	-3.2594	0.981793	1.471383
H	-2.64251	1.844524	1.740318
H	-4.2681	1.354728	1.256584
C14	-3.28923	-0.03196	2.62516
H	-3.95291	-0.87678	2.413352
H	-3.65842	0.450737	3.535126
H	-2.28987	-0.42733	2.83983
C15	-2.76782	1.634695	-1.39164
H	-2.47476	1.219263	-2.36032
H	-3.8351	1.880409	-1.44848
C16	-1.93661	2.887915	-1.07884
H	-2.05942	3.623046	-1.88001

H	-0.86886	2.653837	-1.0032
H	-2.25173	3.367535	-0.14582

*Table S5: Cartesian coordinates from **3**‡ geometry optimization.*

Au	0	0	0
N	1.861631	-1.35198	-0.00141
N	1.868449	1.342538	0.003482
P	-2.34469	0.001425	0.00928
C	1.770456	-2.69774	0.001885
H	0.772034	-3.11723	0.004307
C	2.901133	-3.51953	0.002944
H	2.789656	-4.59708	0.005614
C	4.163724	-2.91381	0.000657
H	5.065096	-3.5171	0.001404
C	4.252685	-1.51731	-0.00205
H	5.225435	-1.04351	-0.00277
C	3.077291	-0.75303	-0.00301
C	3.081004	0.737303	-0.00342
C	1.783825	2.688763	0.00715
C	2.918651	3.504832	0.002563
C	4.178154	2.892739	-0.00633
C	4.260124	1.495816	-0.0092
H	5.230454	1.017134	-0.01587
H	5.082544	3.491495	-0.01081
H	2.812568	4.582921	0.005832
H	0.78741	3.11301	0.014417
C	-3.14099	-1.68868	-0.12982
H	-2.84113	-2.26145	0.753303
H	-4.22785	-1.55111	-0.07821
C	-2.75061	-2.44219	-1.40945
H	-3.18072	-3.44857	-1.40018
H	-1.66244	-2.54171	-1.49817
H	-3.11785	-1.93926	-2.31031
C	-3.0854	0.728973	1.568101
H	-2.80383	1.785932	1.600126
H	-4.17681	0.681525	1.470296
C	-2.62287	0.020608	2.850014
H	-2.93758	-1.02827	2.876343
H	-3.05533	0.512464	3.726898
H	-1.53229	0.052917	2.951675
C	-3.12096	0.985076	-1.38338
H	-2.85912	0.485963	-2.32131

H	-4.20955	0.917231	-1.26767
C	-2.66908	2.451419	-1.42402
H	-3.13262	2.963291	-2.27313
H	-1.58212	2.525623	-1.54235
H	-2.95617	2.995942	-0.51774

3.1.7.2 Computational Bond Lengths

Table S6. Computational bond lengths for all 5 structures.

		Computational Length Å				
Atom 1	Atom 2	**1**	**1'**	**2**	**2'**	**3**
Au1	N1	2.19	2.12	2.13	2.10	2.30
Au1	N2	2.45	N/A	2.66	N/A	2.30
Au1	P1	2.35	2.36	2.35	2.35	2.34
N1	C1	1.35	1.36	1.36	1.36	1.35
N1	C5	1.36	1.36	1.36	1.36	1.36
P1	C11	1.87	1.87	1.87	1.87	1.87
P1	C13	1.87	1.87	1.87	1.87	1.87
P1	C15	1.87	1.87	1.87	1.87	1.87
N2	C6	1.35	1.35	1.35	1.35	1.36
N2	C10	1.35	1.35	1.35	1.35	1.35
C1	H	1.08	1.08	1.08	1.08	1.08
C1	C2	1.40	1.39	1.39	1.39	1.40
C2	H	1.08	1.08	1.08	1.08	1.08
C2	C3	1.40	1.40	1.40	1.40	1.40
C3	H	1.08	1.08	1.08	1.08	1.08
C3	C4	1.40	1.40	1.40	1.40	1.40
C4	H	1.08	1.08	1.08	1.08	1.08
C4	C5	1.40	1.40	1.40	1.40	1.40
C5	C6	1.49	1.49	1.49	1.49	1.49
C6	C7	1.40	1.40	1.40	1.40	1.40
C10	C9	1.40	1.40	1.40	1.40	1.40
C10	H	1.08	1.08	1.08	1.08	1.08
C9	C8	1.40	1.40	1.40	1.40	1.40
C9	H	1.08	1.09	1.08	1.08	1.08
C8	C7	1.40	1.40	1.40	1.40	1.40
C8	H	1.08	1.09	1.08	1.09	1.08
C7	H	1.08	1.09	1.08	1.08	1.08
C11	H	1.09	1.09	1.09	1.09	1.09
C11	H	1.10	1.10	1.10	1.10	1.10
C11	C12	1.54	1.54	1.54	1.54	1.54
C12	H	1.09	1.09	1.09	1.09	1.09
C12	H	1.10	1.10	1.10	1.10	1.10

C12	H	1.10	1.10	1.10	1.10	1.10
C13	H	1.09	1.09	1.09	1.09	1.09
C13	H	1.10	1.10	1.10	1.10	1.10
C13	C14	1.54	1.54	1.54	1.54	1.54
C14	H	1.10	1.10	1.10	1.10	1.10
C14	H	1.09	1.09	1.09	1.09	1.09
C14	H	1.10	1.10	1.10	1.10	1.10
C15	H	1.09	1.09	1.09	1.09	1.09
C15	H	1.10	1.10	1.10	1.10	1.10
C15	C16	1.54	1.54	1.54	1.54	1.53
C16	H	1.09	1.09	1.09	1.09	1.09
C16	H	1.10	1.10	1.10	1.10	1.10
C16	H	1.10	1.10	1.10	1.10	1.10

Subchapter 3.2: Computational Studies of d^{10}–d^{10} Bonding in $[Au^{I}_{6}(Triphos)_{4}(Cu^{I}X_{2})]^{5+}$ (X = Cl^{-} or Br^{-}) and their Luminescence

Michael M. Aristov, Daniel J. SantaLucia, and John F. Berry

Department of Chemistry, University of Wisconsin–Madison, 1101 University Ave., Madison, WI 53706

Email: berry@chem.wisc.edu

3.2.0 Author contributions: This work was written by MMA and JFB. All computations were designed and carried out by MMA and DJS.

3.2.1 Introduction: Systems containing multiple Au(I) centers frequently exhibit luminescent properties, and the origin of this luminescent stems from the interactions of the Au(I) with other metals and/or its environment.[1-6] By using computational techniques to probe crystallographic Au(I) structures we can determine the origin of these excitations.[7-9] With this understanding, we may be able to further tune the luminescent properties of the system.[10-12] In this study, we examined two crystalized, multimetallic Au(I) species $[Au^{I}_{6}(Triphos)_{4}(Cu^{I}Cl_{2})]^{5+}$ **(1)** and $[Au^{I}_{6}(Triphos)_{4}(Cu^{I}Br_{2})]^{5+}$ **(2)**, and using computational methods, we describe the nature of the Au-Cu interaction, the source of the luminisence, and the origin of the experimentally observed difference in Au-Cu between systems.

3.2.2 Computational Methods: Density-functional theory (DFT) calculations were carried out using ORCA version 4.0.0.2.[13] Initial structures were obtained from crystallographic coordinates and were not optimized due to the computational expense required to optimize these compounds. For single point calculations, the BP86[14] exchange-correlation functional and the resolution of

identity (RI) [15] approximation were used. The segmented all-electron relativistically contracted (SARC) basis set, SARC-DKH-TZVPP,[16-18] was used for the Au atoms. The relativistically recontracted Karlsruhe basis set, DKH-def2-TZVPP,[18] was used for Cu and Br atoms, while DKH-def2-SVP[17, 19] was used for all other atoms. The auxiliary coulomb basis set, SARC/J,[16] was used for all atoms. Dispersion corrections to the calculations were accounted for with the atom pairwise dispersion correction employing the Becke-Johnson damping scheme (D3BJ).[20, 21] All self-consistent field calculations used Grid4 (Lebedev quadrature with 302 points) and FinalGrid5 (Lebedev quadrature with 434 points) for numerical integration. Time-dependent DFT calculations were done for 150 roots, with a Davidson expansion space of 1500, and a convergence criterion of 10^{-4}. Visualizations of the orbitals from self-consistent field calculations were carried out with the UCSF Chimera package and Blender.[22]

3.2.3 Results and Discussion: Single point calculations were conducted to visualize the orbitals involved in d^{10}-d^{10} bond in order to understand the nature of the Au−Cu interaction, while TD-DFT calculations were conducted to model the excitations contributing to the photoluminescence observed in the species, $[Au^{I}_{6}(Triphos)_4(Cu^{I}Cl_2)]^{5+}$ **(1)** and $[Au^{I}_{6}(Triphos)_4(Cu^{I}Br_2)]^{5+}$ **(2)** cations. In both **(1)** and **(2)** the two Au−Cu distances are symmetry equivalent, by an *n*-glide and an inversion center respectively and are therefore discussed in the singular.

3.2.3.1 The Nature of d^{10}–d^{10} Bonding: In 1978 Dedieu and Hoffman established the theoretical framework for d^{10}–d^{10} interactions.[23] Metal–metal partial bonding between closed-shell ions arises from hybridization of the filled metal–metal σ* orbital with empty (n+1)s and p orbitals on each metal center. This hybridization adds nonbonding character to the σ* orbital, effectively removing antibonding contributions to the total energy while preserving the bonding character of the lower-energy σ orbital. In 1990, this framework was first applied by Arkhireeva

Table 1. Experimental and computation values relating to the Au—Cu interaction in **(1)** and **(2)**.

		Crystallographic Bond Distance	Mayer Bond Order	FSR
$[Au^{I}_{6}(Triphos)_4(Cu^{I}Cl_2)]^{5+}$	Au1−Cu1	3.1645(10) Å	0.20	1.26
$[Au^{I}_{6}(Triphos)_4(Cu^{I}Br_2)]^{5+}$	Au3−Cu1	3.2172(4) Å	0.16	1.28

et al. to multinuclear Cu(I) complexes.[24] This bonding interaction is often accompanied by luminescence, stemming from the excitation of an electron from the filled σ* orbital to linear combinations (with constructive overlap) of the (n+1)s and p atomic orbitals.[25] The partial d^{10}–d^{10} bonding interaction is dubbed metallophilicity.[26]

3.2.3.2 The Au−Cu ground state d^{10}–d^{10} bonding interaction: The Au−Cu Mayer bond orders of 0.16-0.20, Table 1, indicate a small metal–metal bonding interaction between the central Cu atom and the facial Au atoms for both cations. Consistent with the small Mayer bond orders, the formal shortness ratios (FSR, defined as the interatomic metal-metal distance divided by the sum of single bond metallic radii) of 1.26 and 1.28 for (**1)** and (**2)**, respectively, exceed the expected value for a single metal–metal bond (1.00-1.05).[27, 28] The metallophilicity was found to vary between **(1)** and **(2)**, as reflected by the range of Au−Cu distances and the span of Mayer bond orders. The calculated electronic structures have highest occupied molecular orbitals (HOMOs) that are characterized by an anti-bonding interaction between the Au and Cu atoms, for both **(1)**

Table 2. Percent contributions of atomic orbitals to the Au−Cu filled σ* donor molecular orbital.

	Atom	Contributions (%)
$[Au^{I}_{6}(Triphos)_4(Cu^{I}Cl_2)]^{5+}$		
	Cu286	d: 56.4; s: 8.4
	Au0	d: 5.5; s: 2; p: 3.5
	Au143	d: 5.5; s: 2; p: 3.5
$[Au^{I}_{6}(Triphos)_4(Cu^{I}Br_2)]^{5+}$		
	Cu1	d: 54.4; s: 6.5
	Au2	d: 4.8; s: 2; p: 2.8
	Au145	d: 4.8; s: 2; p: 2.8

and **(2)**, and hybridization between the (n+1)s and p orbitals is apparent, as seen in Figures 1 and 2. Table 2 displays the orbital contributions, indicating mixing of the σ* orbital with 4s/3d character on Cu, and 6s/6p/5d character on Au. This hybridization demonstrates that the Au−Cu distances in the ground state support metallophilic interactions, which are further evidenced by the observed luminescence.[29]

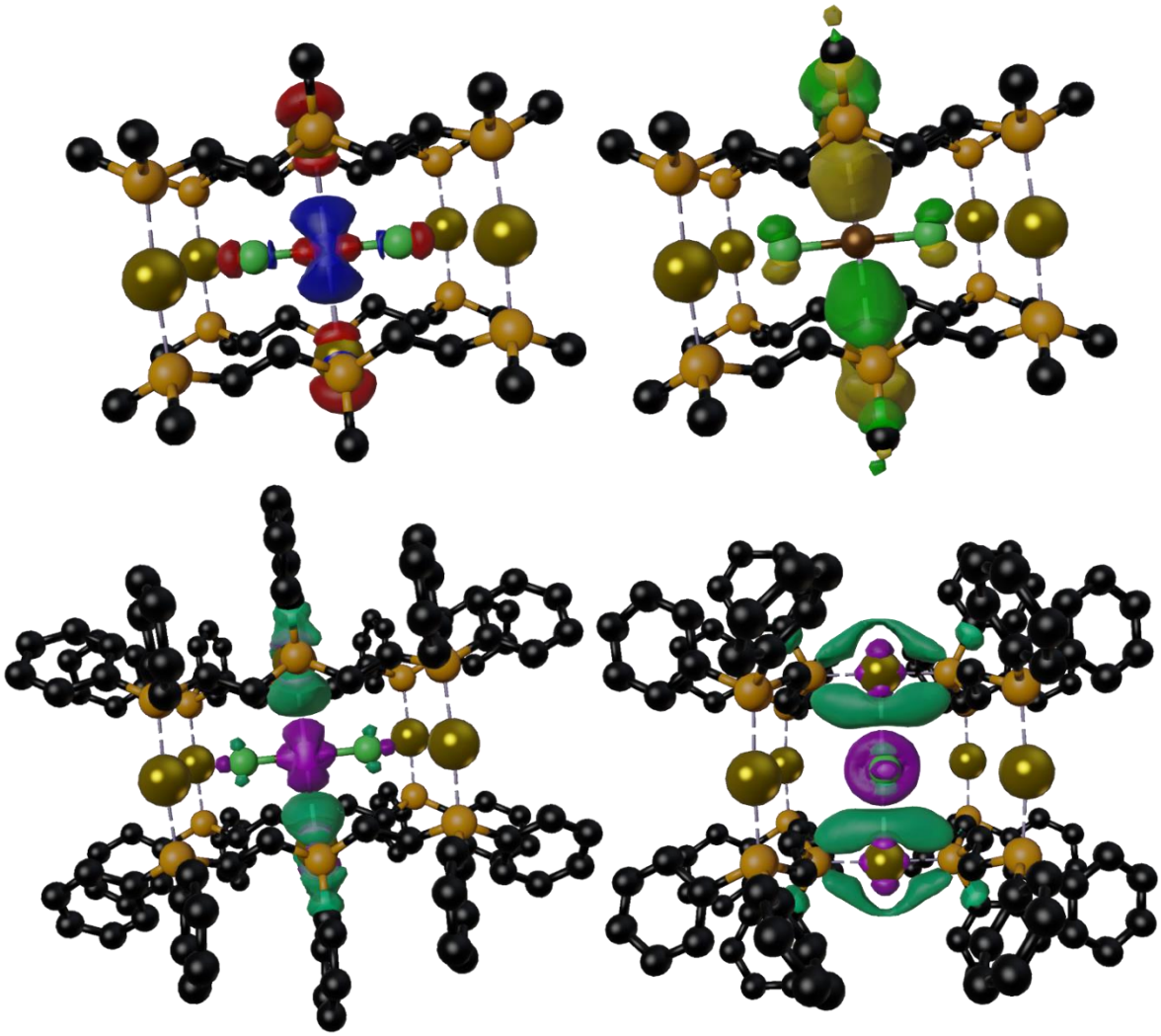

Figure 1. Top left: Filled Au−Cu σ* orbital for **(1)**, which is the primary metal-based donor orbital for the observed excitation. The phenyl rings are omitted for clarity. Top right: Empty Au−Cu σ orbital, which is the primary metal-based acceptor orbital for the observed excitation. The phenyl rings are omitted for clarity. Bottom: Two views of the electron density difference map calculated for the most intense electronic excitation. Purple indicates a loss of electron density and teal indicates a gain in electron density.

3.2.3.3 The Nature of the Luminescence: Analysis of the TD-DFT outputs for **(1)** and **(2)** revealed a primary excitation around 320 nm responsible for the observed UV absorption feature as has been previously seen in other Au−Cu containing species.[30] For both complexes, the excitation was calculated to be a composite of multiple, one-electron excitations, including ligand-to-metal and metal-to-metal charge transfer transitions. The primary contribution to the absorption feature is a metal-to-metal (Cu-to-Au) charger transfer as seen in Figures 1 and 2. This charge transfer originates from the filled Au−Cu weakly antibonding orbital, described above in Table 2, donating into an empty Au−Cu weakly bonding orbital, as seen in the electron difference density plots in Figure 1 and Figure 2. The acceptor orbital comprises a 4p orbital on the Cu atom with bonding overlap with the primarily p orbitals on the Au atoms. This suggests that the excitation increases the strength of the Au−Cu metal-metal bonding interaction in the excited state, a hallmark of metallophilic luminescence.

3.2.3.4 Origin of the Asymmetry in the Au–Cu distances. The crystal structure of $[(Triphos)_4Au_6(CuBr_2)](OTf)_5$-•$(CH_2Cl_2)_3$•$(CH_3OH)_3$•$(H_2O)_4$ has two molecules in the asymmetric unit with two strikingly distinct Au–Cu distances, 3.2172(4) Å and 3.0738(4) Å. Since it is unusual for two instances of the same molecule in the same crystal structure to have distances that differ by > 0.1 Å, we decided to investigate the energetics of these species using DFT. Single-point calculations on the bare pentacations fixed to their crystallographic geometries revealed a rather large energetic difference of 58.06 kJ/mol, the structure with the *long* Au–Cu distance being more stable. This energy difference between the *long* and *short* geometries is too large to be accounted for by normal packing forces, so we looked beyond the molecule for a possible explanation. Analysis of the crystal structure revealed triflate counter ions positioned nearby the facial Au atoms. The distance between the nearest triflate O atom and

the facial Au atom is 2.966(12) Å for the *long* and 3.7905(4) Å for the *short* geometry. By including the two triflate anions located adjacent to these facial Au atoms in the calculations, the energetic difference dropped to 4.42 kJ/mol with the *long* still being more stable. From these calculations, we propose that the difference in the Au–Cu lengths between *long* and *short* arises from a weak interaction between the Au center and the triflate anion. In the *long* geometry this Au−triflate interaction stabilizes the box at the cost of the Au–Cu interaction. Whereas in the *short* geometry the Au−triflate interaction is almost non-existent due to physical separation, resulting in a less stable box that favors a stronger and shorter Au–Cu interaction.

3.2.4 Conclusion: Through computational studies, we were able to determine the both the presence and nature of the Au-Cu interaction. We also identified the source of the luminisence and how it strengthened the Au-Cu interaction. Lastly, we found that the the origin of the experimentally observed difference in Au-Cu between systems was due to the interaction and lack-there-of the interstitial triflate counter-ion on the Au atom center.

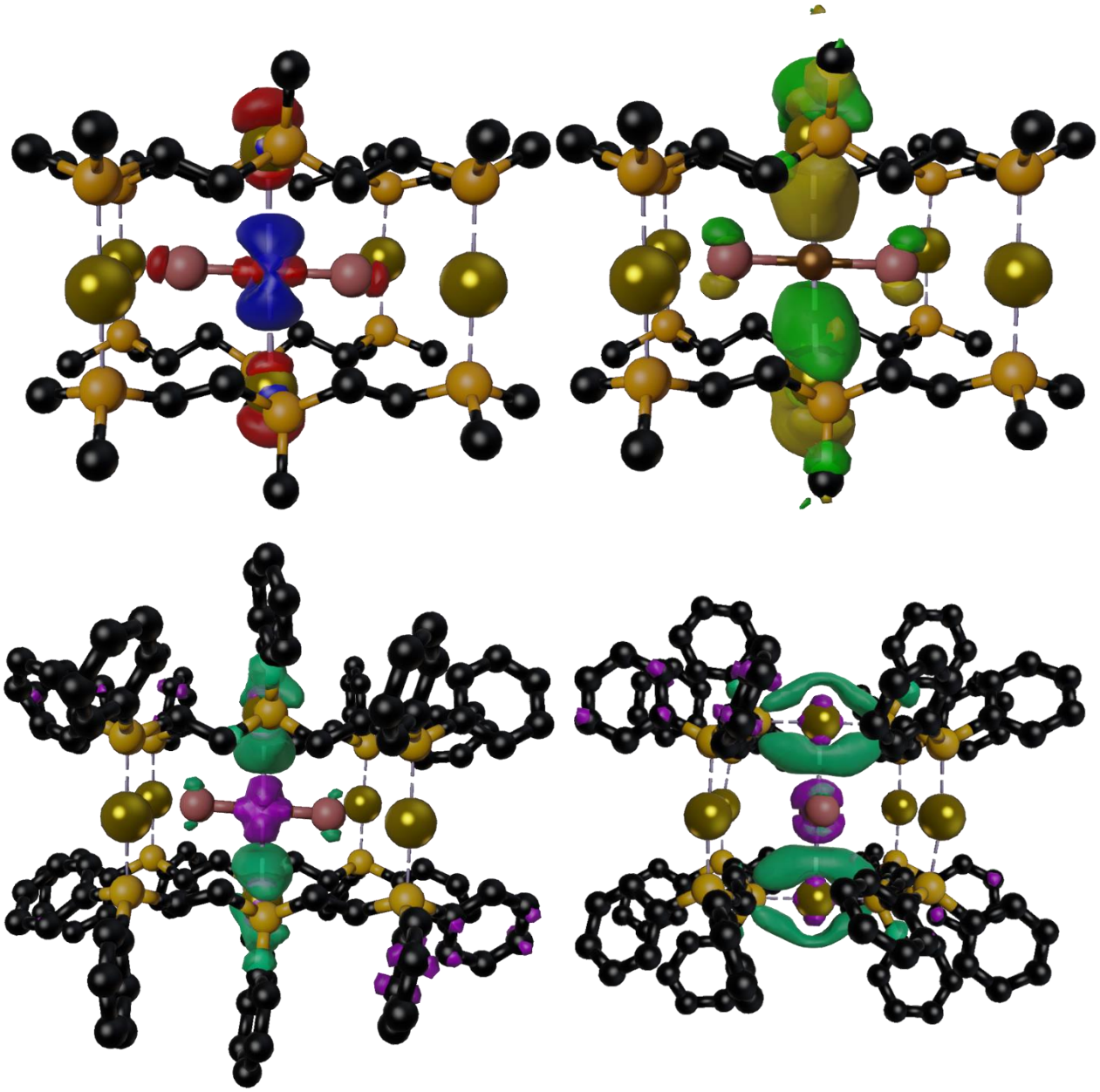

Figure 2. Top left: Filled Au−Cu σ* orbital for **(2)**, which is the primary metal-based donor orbital for the observed excitation. The phenyl rings are omitted for clarity. Top right: Empty Au−Cu σ orbital, which is the primary metal-based acceptor orbital for the observed excitation. The phenyl rings are omitted for clarity. Bottom: Two views of the electron density difference map calculated for the most intense electronic excitation. Purple indicates a loss of electron density and teal indicates a gain in electron density.

3.2.5 References

1. Fernández, E.; Laguna, A.; López-de-Luzuriaga, J., Luminescence in Complexes with Au (I)–Tl (I) Interactions. *Coord. Chem. Rev.* **2005,** *249* (13-14), 1423-1433.

2. King, C.; Wang, J. C.; Khan, M. N. I.; Fackler Jr, J. P., Luminescence and Metal-Metal Interactions in Binuclear Gold (I) Compounds. *Inorg. Chem.* **1989,** *28* (11), 2145-2149.
3. White-Morris, R. L.; Olmstead, M. M.; Jiang, F.; Tinti, D. S.; Balch, A. L., Remarkable Variations in the Luminescence of Frozen Solutions of $[Au\{C(NHMe)_2\}_2](PF_6)\odot 0.5$(Acetone). Structural and Spectroscopic Studies of the Effects of Anions and Solvents on Gold (I) Carbene Complexes. *J. Am. Chem. Soc.* **2002,** *124* (10), 2327-2336.
4. Tiekink, E. R.; Kang, J.-G., Luminescence Properties of Phosphinegold (I) Halides and Thiolates. *Coord. Chem. Rev.* **2009,** *253* (11-12), 1627-1648.
5. Pintado-Alba, A.; de la Riva, H.; Nieuwhuyzen, M.; Bautista, D.; Raithby, P. R.; Sparkes, H. A.; Teat, S. J.; López-de-Luzuriaga, J. M.; Lagunas, M. C., Effects of Diphosphine Structure on Aurophilicity and Luminescence in Au(I) Complexes. *Dalton Trans.* **2004,** (21), 3459-3467.
6. Barnard, P. J.; Wedlock, L. E.; Baker, M. V.; Berners-Price, S. J.; Joyce, D. A.; Skelton, B. W.; Steer, J. H., Luminescence Studies of the Intracellular Distribution of a Dinuclear Gold (I) N-heterocyclic Carbene Complex. *Angew. Chem., Int. Ed.* **2006,** *45* (36), 5966-5970.
7. Latouche, C.; Lin, Y.-R.; Tobon, Y.; Furet, E.; Saillard, J.-Y.; Liu, C.-W.; Boucekkine, A., Au–Au Chemical Bonding Induced by UV Irradiation of Dinuclear Gold (I) Complexes: A Computational Study with Experimental Evidence. *Phys. Chem. Chem. Phys.* **2014,** *16* (47), 25840-25845.
8. Lim, S. H.; Schmitt, J. C.; Shearer, J.; Jia, J.; Olmstead, M. M.; Fettinger, J. C.; Balch, A. L., Crystallographic and Computational Studies of Luminescent, Binuclear Gold (I) Complexes, AuI2 (Ph2P (CH2) n PPh2) 2I2 (n= 3–6). *Inorg. Chem.* **2013,** *52* (2), 823-831.
9. Luong, L. M.; Aristov, M. M.; Adams, A. V.; Walters, D. T.; Berry, J. F.; Olmstead, M. M.; Balch, A. L., Unsymmetrical Coordination of Bipyridine in Three-Coordinate Gold (I) Complexes. *Inorg. Chem.* **2020,** *59* (6), 4109-4117.
10. Runowski, M.; Stopikowska, N.; Goderski, S.; Lis, S., Luminescent-Plasmonic, Lanthanide-Doped Core/Shell Nanomaterials Modified with Au Nanorods–Up-Conversion Luminescence Tuning and Morphology Transformation after NIR Laser Irradiation. *J. Alloys Compd.* **2018,** *762*, 621-630.
11. Liu, C.-Y.; Wang, H.-F.; Ren, Z.-G.; Braunstein, P.; Lang, J.-P., Fine-Tuning of Luminescence through Changes in Au–S Bond Lengths as a Function of Temperature or Solvent. *Inorg. Chem.* **2019,** *58* (13), 8533-8540.
12. Donamaria, R.; Lippolis, V.; Lopez-de-Luzuriaga, J. M.; Monge, M.; Nieddu, M.; Olmos, M. E., Tuning Au (I)⋯ Tl (I) Interactions via Mixed Thia–Aza Macrocyclic Ligands: Effects on the Structural and Luminescence Properties. *Inorg. Chem.* **2017,** *56* (20), 12551-12563.
13. Neese, F., Software Update: The Orca Program System, Version 4.0. *Wiley Interdisciplinary Reviews: Computational Molecular Science* **2018,** *8*, e1327.
14. Becke, A. D., Density-Functional Exchange-Energy Approximation with Correct Asymptotic Behavior. *Phys. Rev. A Gen. Phys.* **1988,** *38*, 3098-3100.
15. Whitten, J. L., Coulombic Potential Energy Integrals and Approximations. *J. Chem. Phys.* **1973,** *58*, 4496-4501.
16. Weigend, F., Accurate Coulomb-Fitting Basis Sets for H to Rn. *Phys. Chem. Chem. Phys.* **2006,** *8*, 1057-1065.

17. Pantazis, D. A.; Chen, X.-Y.; Landis, C. R.; Neese, F., All-Electron Scalar Relativistic Basis Sets for Third-Row Transition Metal Atoms. *J. Chem. Theory Comput.* **2008,** *4*, 908-919.
18. Peterson, K. A.; Puzzarini, C., Systematically Convergent Basis Sets for Transition Metals. II. Pseudopotential-Based Correlation Consistent Basis Sets for the Group 11 (Cu, Ag, Au) and 12 (Zn, Cd, Hg) Elements. *Theor. Chem. Acc.* **2005,** *114*, 283-296.
19. Weigend, F.; Ahlrichs, R., Balanced Basis Sets of Split Valence, Triple Zeta Valence and Quadruple Zeta Valence Quality for H To Rn: Design and Assessment of Accuracy. *Phys. Chem. Chem. Phys.* **2005,** *7*, 3297-3305.
20. Grimme, S.; Antony, J.; Ehrlich, S.; Krieg, H., A Consistent and Accurate ab initio Parametrization of Density Functional Dispersion Correction (DFT-D) for the 94 Elements H-Pu. *J. Chem. Phys.* **2010,** *132*, 154104.
21. Grimme, S.; Ehrlich, S.; Goerigk, L., Effect of the Damping Function in Dispersion Corrected Density Functional Theory. *J. Comput. Chem.* **2011,** *32*, 1456-1465.
22. Pettersen, E. F.; Goddard, T. D.; Huang, C. C.; Couch, G. S.; Greenblatt, D. M.; Meng, E. C.; Ferrin, T. E., UCSF Chimera—A Visualization System for Exploratory Research and Analysis. *J. Comput. Chem.* **2004,** *25*, 1605-1612.
23. Dedieu, A.; Hoffmann, R., Platinum(0)-Platinum(0) Dimers. Bonding Relationships in a d^{10}-d^{10} System. *J. Am. Chem. Soc.* **1978,** *100*, 2074-2079.
24. Arkhireeva, T. M.; Bulychev, B. M.; Sizov, A. I.; Sokolova, T. A.; Belsky, V. K.; Soloveichik, G. L., Copper(I) Complexes with Metal-Metal (d^{10}–d^{10}) bond. Crystal and Molecular Structures of Adducts of Tantalocene Trihydride with Copper(I) Iodide of Composition: $(\eta^5\text{-}C_5H_5)_2TaH[(\mu_2\text{-}H)Cu(\mu_2\text{-}I)_2Cu(\mu_2\text{-}H)]_2HTa(\eta^5\text{-}C_5H_5)_2$, $(\eta^5\text{-}C_5H_4But)_2TaH(\mu_2\text{-}H)_2Cu(\mu_2\text{-}I)_2Cu(\mu_2\text{-}H)_2HTa(\eta^5\text{-}C_5H_4Bu^t)_2\cdot CH_3CN$ and $\{Cu(\mu_3\text{-}I)\cdot P[N(CH_3)_2]_3\}_4$. *Inorg. Chim. Acta* **1990,** *169*, 109-118.
25. Romanova, J.; Ranga Prabhath, M. R.; Jarowski, P. D., Relationship between Metallophilic Interactions and Luminescent Properties in Pt(II) Complexes: TD-DFT Guide for the Molecular Design of Light-Responsive Materials. *J. Phys. Chem. C* **2016,** *120*, 2002-2012.
26. Sculfort, S.; Braunstein, P., Intramolecular d^{10}–d^{10} Interactions in Heterometallic Clusters of the Transition Metals. *Chem. Soc. Rev.* **2011,** *40*, 2741-2760.
27. *Multiple Bonds Between Metal Atoms*. 3rd ed.; Springer-Verlag New York: 2005.
28. Chipman, J. A.; Berry, J. F., Paramagnetic Metal–Metal Bonded Heterometallic Complexes. *Chem. Rev.* **2020,** *120*, 2409-2447.
29. Ai, P.; Mauro, M.; Gourlaouen, C.; Carrara, S.; De Cola, L.; Tobon, Y.; Giovanella, U.; Botta, C.; Danopoulos, A. A.; Braunstein, P., Bonding, Luminescence, Metallophilicity in Linear Au_3 and Au_2Ag Chains Stabilized by Rigid Diphosphanyl NHC Ligands. *Inorg. Chem.* **2016,** *55*, 8527-8542.
30. Galassi, R.; Ghimire, M. M.; Otten, B. M.; Ricci, S.; McDougald, R. N.; Almotawa, R. M.; Alhmoud, D.; Ivy, J. F.; Rawashdeh, A.-M. M.; Nesterov, V. N.; Reinheimer, E. W.; Daniels, L. M.; Burini, A.; Omary, M. A., Cupriphication of Gold to Sensitize d^{10}–d^{10} Metal–Metal Bonds and Near-Unity Phosphorescence Quantum Yields. *Proc. Natl. Acad. Sci. U.S.A* **2017,** *114*, E5042.

Supporting Information for Subchapter 3.2: Computational Studies of d10–d10 Bonding in $[Au^{I}_{6}(Triphos)_{4}(CuIX_{2})]^{5+}$ (X = Cl^{-} or Br^{-}) and their Luminescence

Michael M. Aristov, Daniel J. SantaLucia, and John F. Berry

Department of Chemistry, University of Wisconsin–Madison, 1101 University Ave., Madison, WI 53706

Email: berry@chem.wisc.edu

Table 3. Percent contributions of atomic orbitals to the Au−Cu empty σ acceptor molecular orbital.

	Atom	Contributions (%)
$[Au^{I}_{6}(Triphos)_{4}(Cu^{I}Cl_{2})]^{5+}$		
	Cu286	p: 12.8
	Au0	f: 0.2; d: 0.3; p: 22.4
	Au143	f: 0.2; d: 0.3; p: 22.4
$[Au^{I}_{6}(Triphos)_{4}(Cu^{I}Br_{2})]^{5+}$		
	Cu286	p: 11.8
	Au2	f: 0.1; d: 0.3; p: 21.3
	Au145	f: 0.1; d: 0.3; p: 21.3

Subchapter 3.3: Single Crystal Structural Isomers of $Au_2(DPPE)_2I_2$ and the Elongation of the Au–Au Metallophilic Interaction

Michael M. Aristov and John F. Berry

Department of Chemistry, University of Wisconsin, Madison, 1101 University Ave., Madison WI 53706

Email: berry@chem.wisc.edu

3.3.0 Author Contribution: This work was written by MMA and JFB. All computations were set up by MMA.

3.3.1 Abstract: A pair of polymorphs containing $Au_2(DPPE)_2I_2$·acetone were investigated computationally to better understand the different Au···Au distances of 3.32 and 3.67 Å in the two structures. The two structures were used as a basis for two computational models, **Geom(Short)** and **Geom(Long)**, having Au···Au distances fixed to those of the two polymorphs. A third model, **Geom(Very_Short)**, with an even shorter Au–Au distance of 2.96 Å was also examined. Consistent with the experimental observations, the **Geom(Short)** and **Geom(Long)** models were found to differ in energy by only ~ 10 kJ/mol, a small enough energy to be attributable to crystal packing forces. An analysis of Au···Au interactions was made considering all three models, highlighting the changes in electronic structure that occur as the Au atoms are brought together from a non-bonding range into the aurophilic bonding range. Notably, an increase in 6p contribution to the Au–Au highest filled metal orbital (HFMO) changes the nature of this orbital from Au–Au antibonding to Au–Au non-bonding as the two Au atoms are brought together.

3.3.2 Computational Methods: Geometry optimizations, frequency calculations, and single-point (SP), were carried out using ORCA version 5.0.1.[1, 2] For the geometry optimizations and frequency calculations the BP86 exchange-correlation functional was used.[3-6] Crystallographic coordinates, excluding solvent molecules were used as the starting point for all geometry optimizations. The two experimental crystal structures were used as a basis for two computational models, **Geom(Short)** and **Geom(Long)**, having Au···Au distances fixed to those of the two polymorphs.[7] All other geometric parameters were optimized. A third model, **Geom(Very_Short)**, with an even shorter Au–Au distance of 2.99 Å, resulted from a full geometry optimization without fixing the Au···Au distances. All calculations used the resolution of identity and correlation of spheres, RIJCOSX approximation.[8-10] The segmented all-electron relativistic contracted (SARC) basis set, SARC-DKH-TZVPP,[11-13] was used for the Au atoms. The SARC contracted Karlsruhe basis set, SARC-DKH-TZVP,[14] was used for I atoms, while def2-SVP[15] was used for all other atoms. The auxiliary coulomb basis set, def2/J,[16] was used for all atoms. Dispersion corrections to the calculations were accounted for with the atom pairwise dispersion correction employing the Becke-Johnson damping scheme (D3BJ).[17, 18] All molecules were calculated in their open shell singlet state using unrestricted Kohn Sham (UKS) theory. The radial grid of the Au atoms was set to 10, whereas the grids for all other atoms were set to 6. Frequency calculations were performed by numerical differentiation with a central-differences increment of 0.01. Visualizations of the orbitals from self-consistent field calculations were carried out with the UCSF Chimera package.[19] Structure comparisons were made using Mercury.[20]

3.3.3 Results and Discussion.

3.3.3.1 Structural Comparisons: Computational methods were employed to better understand the energetics and the nature of the Au···Au interactions in the two distinct structures of the $Au_2(DPPE)_2I_2$ system. In the $Au_2(DPPE)_2I_2$ compound, each gold center is three-coordinate, bound to a P atom from each of two bridging DPPE ligands and an inner sphere iodine atom. The distorted trigonal-planar/trigonal pyramidal gold centers stack on top of each other held together by the bridging DPPE ligands in a slipped-anti configuration, as seen in Figure 2. Crystals of $Au_2(DPPE)_2I_2$·acetone occur in two polymorphs having the same general structure, but with differing interatomic Au···Au distances. One polymorph (called **Au(Short)**) has an Au···Au distance of 3.3177(7) Å, at the sum of the Au van der Waals radii, and the other polymorph (**Au(Long)**) has an Au···Au distance of 3.6720(2) Å, well outside the sum of the Au van der Waals radii, and outside the traditional range for "aurophilic" interactions (2.5-3.5 Å).[21, 22] There were no other significant differences noted between these two structures. Additionally, a related crystal structure of $[Au_2(DPPE)_2](OTf)_2$·2MeOH has only outer sphere counterions and a dramatically decreased Au–Au distance of 2.959(1) Å, within the sum of the van der Waals radii. This third experimental structure contains linear, two-coordinate Au centers bound to DPPE P atoms on either end, where the DPPE ligands both adopt a bridging coordination mode, and outer-sphere triflate counter-ions.

Geometry optimizations starting from crystallographic coordinates were used to locate energetic minima corresponding to these structures, which we call **Geom(Short)** and **Geom(Long)**. To optimize geometries for these two structures, the Au···Au distances were constrained while all other distances were allowed to optimize. A third hypothetical structure, **Geom(Very_Short)**, with an Au–Au distance of 2.987 Å, well below the sum of the Au van der Waals radii was also

optimized by running a full geometry optimization starting from **Geom(Short)** but freely refining the Au···Au distance. Selected measurements and comparisons between the computational structures and their experimental counterparts are noted in Table 1. A notable difference between **Geom(Short)** and **Geom(Long)** is the Au···I interaction between the gold center and the iodine atom bound to the other gold center. As the Au···Au distance shrinks, so does this Au···I interaction, and in the **Geom(Very_Short)** this distance is smaller than the sum of the Van Der Walls radii, 3.64 Å. No significant differences in other non-covalent interactions were observed between the three optimized structures. Frequency calculations confirm that all three structures occupy local energetic minima, and allow comparison of the Gibbs free energies, ΔG, of the structures. **Geom(Very_Short)** was found to be lowest in ΔG (at 298.15 K), followed by **Geom(Short)** (+9.2 kJ mol^{-1}), followed by **Geom(Long)** (+18.4 kJ mol^{-1}). The change in calculated energy between the Short and Long structures (< 10 kJ/mol) is within the associated range of crystal packing effects, which, for this system, are predominantly weak hydrogen-bonding interactions, namely solvent – aryl-proton (2-20 kJ/mol) and proton-to-phenyl π-stacking (>3 kcal/mol).[23-28] The <10 kJ/mol difference in energies between the two calculated structures and notable intermolecular forces in the packed structure strongly suggest that the differences in Au···Au distances in the two polymorphs are primarily a result of crystal packing effects.

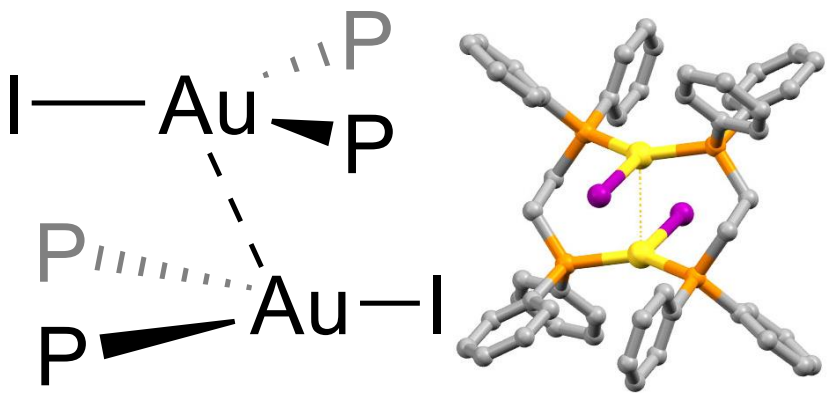

*Figure 2. Left: Simplified Chemdraw of the Au-Au interaction in the $Au_2(DPPE)_2I_2$ system. Right: Computation output from the **Geom(Very_Short)** geometry optimization.*

Table 1. Selected geometric features of $Au_2(DPPE)_2I_2$ from the experimental crystal structures and the computed systems.

	Au–Au, Å	Au–P Å	Au–I Au···I Å	I–Au–Au Angle	P–Au–P Angle	P–Au–I Angle	Origin
Geom(Short)	3.395 (fixed)	2.321	2.871 3.695	71.7°	146.0°	109.7° 104.3°	DFT
Au(Short)	3.3955 (2)	2.316 (2)	2.9759 (2) 3.7143 (2)	70.97(2)°	152.98 (2)°	103.57(2)° 102.79(2)°	crystal
Geom(Long)	3.6720 (fixed)	2.321	2.871 3.842	70.7°	146.1°	108.8° 104.8°	DFT
Au(Long)	3.6720(2)	2.314 (1)	2.9106 (2) 3.937 (2)	72.43(2)°	154.33 (2)°	103.34(2)° 102.27(2)°	crystal
Geom(Very_Short)	2.987	2.327	2.865 3.576	75.3°	143.5°	111.5° 103.4°	DFT

3.3.3.2 Analysis of Au···Au Interactions: Single point calculations on the three gold structures were used to determine the nature of the interactions between the two Au atoms in each structure using the calculated Mayer bond orders (MBO).[29-31] The **Geom(Very_Short)** structure was calculated to have a Au–Au MBO of 0.11, indicating a weak but non-zero Au–Au bonding interaction. Both the **Geom(Short)** and **Geom(Long)** structures returned MBO values less than the default reporting cutoff of 0.10. Thus, Au–Au bonding interactions in these two structures are minimal. These bond order results agree well with the comparison of the Au···Au distances to the sum of the Au van der Waals radii, described above.

Metal-metal bonding between the d^{10} Au(I) ions can occur at short Au–Au distances when the Au–Au antibonding HFMO (consisting of an out-of-phase combination of 5d orbitals) is raised close enough in energy to mix significantly with the empty 6s and 6p orbitals.[32-37] This mixing, particularly with the 6p orbitals, causes the HFMO to have non-bonding, rather than antibonding, character, as the orbital lobes bulge out away from the Au–Au centroid. The structures **Geom(Very_Short)**, **Geom(Short)**, and **Geom(Long)**, provide snapshots of this effect best seen via analysis of the orbital compositions given in Table 2 and Figure 3. Starting with **Geom(Long)**, beyond the sum of the Au van der Waals radii, we see that the HFMO is essentially a hybrid of 5d and 6s orbitals with little 6p character (<3% of the metal contribution per Au atom). **Geom(Short)**, which is very close to the sum of the Au van der Waals radii, has ~5% 6p character, while **Geom(Very_Short)** has ~20% p character.

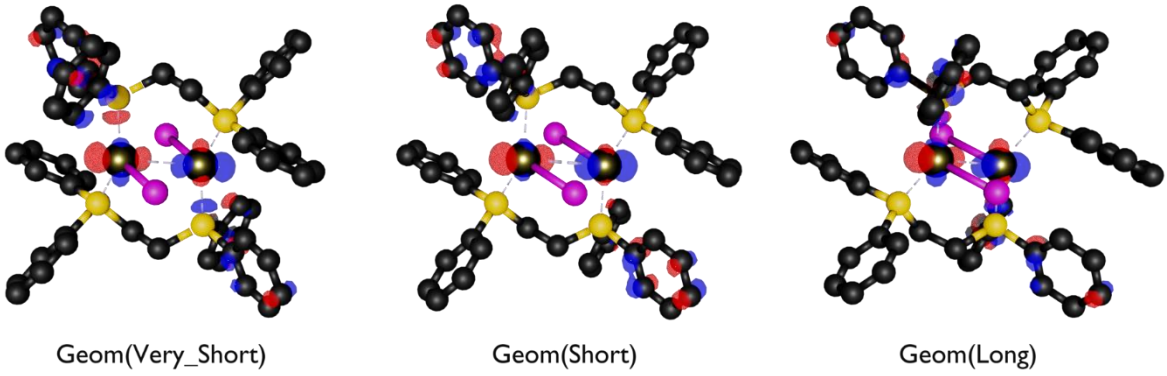

Figure 3. Isosurface plots (at 50%) of the highest filled metal orbitals for **Geom(Very_Short)**, **Geom(Short)**, and **Geom(Long)**, highlighting the increasing degree of Au–Au antibonding character across the series.

3.3.4 Conclusion: A pair of polymorphs containing $Au_2(DPPE)_2I_2$·acetone were investigated computationally to better understand the origin of their different Au···Au distances. These two structures were computationally predicted to differ in energy by only ~ 10 kJ/mol, a small enough energy to be attributable to crystal packing forces. An analysis of Au···Au interactions highlighted the changes in electronic structure that occurred as the Au atoms were brought together from a non-bonding range into the aurophilic bonding range. Notably, an increase in 6p contribution to the Au–Au highest filled metal orbital (HFMO) changes the nature of this orbital from Au–Au antibonding to Au–Au non-bonding as the two Au atoms were brought together. However, this effect was minimal over the crystallographically observed Au···Au distances, and only became relevant at hypothetical Au−Au distance of <3.2 Å. Overall, the structural differences between the Au dimers were found to likely originate primarily from crystal packing effects with minimal aurophilic influence.

Table 2. Percentage contributions of atomic orbitals to the filled Au–Au σ and σ* molecular orbitals.

	System	Contributions (%)
Geom(Very_Short)		
Highest Occupied Metal Orbital	Au 1	d: 9.4; s: 2.4; p: 2.9

	Au 2	d: 9.4; s: 2.4; p: 2.9
	other	70.6
Geom(Short)		
Highest Occupied Metal Orbital	Au 1	d: 8.8; s: 4.2; p: 0.7
	Au 2	d: 8.8; s: 4.2; p: 0.7
	other	72.6
Geom(Long)		
Highest Occupied Metal Orbital	Au 1	d: 4.8; s: 2.8; p: 0.2
	Au 2	d: 4.8; s: 2.8; p: 0.2
	other	84.4

3.3.5 References:

1. Neese, F., The ORCA program system. *WIREs Computational Molecular Science* **2012,** *2* (1), 73-78.
2. Neese, F., Software update: The ORCA program system—Version 5.0. *WIREs Computational Molecular Science* **2022,** *n/a* (n/a), e1606.
3. Becke, A. D., Density-functional exchange-energy approximation with correct asymptotic behavior. *Phys Rev A Gen Phys* **1988,** *38* (6), 3098-3100.
4. Stephens, P. J.; Devlin, F. J.; Chabalowski, C. F.; Frisch, M. J., Ab initio calculation of vibrational absorption and circular dichroism spectra using density functional force fields. *The Journal of physical chemistry* **1994,** *98* (45), 11623-11627.
5. Becke, A. D., Density-functional thermochemistry. III. The role of exact exchange. *The Journal of Chemical Physics* **1993,** *98* (7), 5648-5652.
6. Lee, C.; Yang, W.; Parr, R. G., Development of the Colle-Salvetti correlation-energy formula into a functional of the electron density. *Physical review B* **1988,** *37* (2), 785.
7. Lim, S. H.; Olmstead, M. M.; Balch, A. L., Inorganic topochemistry. Vapor-induced solid state transformations of luminescent, three-coordinate gold(i) complexes. *Chemical Science* **2013,** *4* (1), 311-318.
8. Guevara-Vela, J. M.; Rocha-Rinza, T.; Pendás, Á. M., Performance of the RI and RIJCOSX approximations in the topological analysis of the electron density. *Theoretical Chemistry Accounts* **2017,** *136* (5), 57.
9. Neese, F., An improvement of the resolution of the identity approximation for the formation of the Coulomb matrix. *Journal of computational chemistry* **2003,** *24* (14), 1740-1747.
10. Neese, F.; Wennmohs, F.; Hansen, A.; Becker, U., Efficient, approximate and parallel Hartree–Fock and hybrid DFT calculations. A 'chain-of-spheres' algorithm for the Hartree–Fock exchange. *Chemical Physics* **2009,** *356* (1-3), 98-109.
11. Weigend, F., Accurate Coulomb-Fitting Basis Sets for H to Rn. *Physical Chemistry Chemical Physics* **2006,** *8*, 1057-1065.
12. Pantazis, D. A.; Chen, X.-Y.; Landis, C. R.; Neese, F., All-Electron Scalar Relativistic Basis Sets for Third-Row Transition Metal Atoms. *Journal of Chemical Theory and Computation* **2008,** *4* (6), 908-919.

13. Peterson, K. A.; Puzzarini, C., Systematically Convergent Basis Sets for Transition Metals. Ii. Pseudopotential-Based Correlation Consistent Basis Sets for the Group 11 (Cu, Ag, Au) and 12 (Zn, Cd, Hg) Elements. *Theoretical Chemistry Accounts* **2005,** *114*, 283-296.
14. Rolfes, J. D.; Neese, F.; Pantazis, D. A., All-electron scalar relativistic basis sets for the elements Rb–Xe. *Journal of Computational Chemistry* **2020,** *41* (20), 1842-1849.
15. Weigend, F.; Ahlrichs, R., Balanced Basis Sets of Split Valence, Triple Zeta Valence and Quadruple Zeta Valence Quality hor H To Rn: Design and Assessment of Accuracy. *Physical Chemistry Chemical Physics* **2005,** *7*, 3297-3305.
16. Weigend, F., Accurate Coulomb-fitting basis sets for H to Rn. *Physical Chemistry Chemical Physics* **2006,** *8* (9), 1057-1065.
17. Grimme, S.; Antony, J.; Ehrlich, S.; Krieg, H., A Consistent and Accurate ab initio Parametrization of Density Functional Dispersion Correction (DFT-D) for the 94 Elements H-Pu. *The Journal of Chemical Physics* **2010,** *132*, 154104.
18. Grimme, S.; Ehrlich, S.; Goerigk, L., Effect of the Damping Function in Dispersion Corrected Density Functional Theory. *Journal of Computational Chemistry* **2011,** *32*, 1456-1465.
19. Pettersen, E. F.; Goddard, T. D.; Huang, C. C.; Couch, G. S.; Greenblatt, D. M.; Meng, E. C.; Ferrin, T. E., UCSF Chimera—A Visualization System for Exploratory Research and Analysis. *Journal of Computational Chemistry* **2004,** *25*, 1605-1612.
20. Macrae, C. F.; Sovago, I.; Cottrell, S. J.; Galek, P. T. A.; McCabe, P.; Pidcock, E.; Platings, M.; Shields, G. P.; Stevens, J. S.; Towler, M.; Wood, P. A., Mercury 4.0: from visualization to analysis, design and prediction. *Journal of Applied Crystallography* **2020,** *53* (1), 226-235.
21. Schmidbaur, H.; Schier, A., Aurophilic interactions as a subject of current research: an up-date. *Chemical Society Reviews* **2012,** *41* (1), 370-412.
22. Schmidbaur, H.; Schier, A., A briefing on aurophilicity. *Chemical Society Reviews* **2008,** *37* (9), 1931-1951.
23. Desiraju, G. R., Hydrogen Bridges in Crystal Engineering: Interactions without Borders. *Accounts of Chemical Research* **2002,** *35* (7), 565-573.
24. Desiraju, G. R., Hydrogen bonds and other intermolecular interactions in organometallic crystals. *Journal of the Chemical Society, Dalton Transactions* **2000,** (21), 3745-3751.
25. Desiraju, G. R., Chemistry beyond the molecule. *Nature* **2001,** *412* (6845), 397-400.
26. Braga, D.; Grepioni, F., Intermolecular Interactions in Nonorganic Crystal Engineering. *Accounts of Chemical Research* **2000,** *33* (9), 601-608.
27. Desiraju, G. R., C–H···O and other weak hydrogen bonds. From crystal engineering to virtual screening. *Chemical Communications* **2005,** (24), 2995-3001.
28. Sinnokrot, M. O.; Sherrill, C. D., Substituent Effects in π–π Interactions: Sandwich and T-Shaped Configurations. *Journal of the American Chemical Society* **2004,** *126* (24), 7690-7697.
29. Bridgeman, A. J.; Cavigliasso, G.; Ireland, L. R.; Rothery, J., The Mayer bond order as a tool in inorganic chemistry. *Journal of the Chemical Society, Dalton Transactions* **2001,** (14), 2095-2108.
30. Mayer, I., Charge, bond order and valence in the AB initio SCF theory. *Chemical Physics Letters* **1983,** *97* (3), 270-274.
31. Mayer, I., Bond order and valence: Relations to Mulliken's population analysis. *International Journal of Quantum Chemistry* **1984,** *26* (1), 151-154.
32. Pyykkö, P., Relativistic quantum chemistry. In *Advances in quantum chemistry*, Elsevier: 1978; Vol. 11, pp 353-409.
33. Pyykko, P.; Desclaux, J. P., Relativity and the periodic system of elements. *Accounts of Chemical Research* **1979,** *12* (8), 276-281.
34. Pyykkö, P., Strong closed-shell interactions in inorganic chemistry. *Chemical reviews* **1997,** *97* (3), 597-636.

35. Schmidbaur, H., The aurophilicity phenomenon: a decade of experimental findings, theoretical concepts and emerging applications. *Gold Bulletin* **2000,** *33* (1), 3-10.
36. Hutchings, G. J.; Brust, M.; Schmidbaur, H., Gold—an introductory perspective. *Chemical Society Reviews* **2008,** *37* (9), 1759-1765.
37. Wang, S.-G.; Schwarz, W. H. E., Quasi-Relativistic Density Functional Study of Aurophilic Interactions. *Journal of the American Chemical Society* **2004,** *126* (4), 1266-1276.

Supporting Information For Subchapter 3.3: Single Crystal Structural Isomers of $Au_2(DPPE)_2I_2$ and the Elongation of the Au–Au Metallophilic Interaction

Michael M. Aristov, Han Geng, James W. Harris, and John F. Berry

Department of Chemistry, University of Wisconsin – Madison, 1101 University Ave. Madison, WI 53703

Email: berry@chem.wisc.edu

3.3.6.1 Geometry Optimized Coordinates

Table S1: Cartesian Coordinates from **Geom(Long)** Geometry Optimization.

Au	3.57938629520458	11.77836280806180	0.40023041693381
Au	7.09746380787977	11.09565777209210	-0.40000132836001
I	4.48082970413236	9.52515494843595	1.93429352201878
P	4.10805027285320	13.63598575529000	1.70174411626712
P	7.87025707428430	11.84975393150870	1.64757264169905
C	3.47776849300082	13.55823661211900	3.42220286866146
C	4.06514478096986	14.27812618637100	4.48424813982787
H	4.93752269201395	14.92443026102720	4.30297727823381
C	3.55149600290186	14.16266511305300	5.78563225115759
H	4.01721812875008	14.72517768235060	6.60937867322041
C	2.45076949197523	13.32560943340090	6.03670675597664
H	2.05268153051054	13.23219044786670	7.05874635570242
C	1.86952128357943	12.59677104357960	4.98549911038184
H	1.01977756112943	11.92525144354140	5.18048384869518
C	2.38479832869550	12.70657154030390	3.68537009818491
H	1.96046440810016	12.11075238905480	2.86188623370365
C	3.51113675980323	15.22113650856930	0.99135306844216
C	3.19704086491037	15.24800106741640	-0.38356186307497
H	3.29777128523559	14.32716316035950	-0.97754557786448
C	2.76489330232371	16.44044036725490	-0.98260601474174
H	2.52499060220352	16.44406906275200	-2.05618692795201
C	2.63336141376542	17.60784051175020	-0.21231286168236
H	2.28757624180958	18.54230514753160	-0.68087653132574
C	2.93533502620666	17.58232275734490	1.16104665409545
H	2.82314751546620	18.49349406907840	1.76875862532566

C	3.37503909870128	16.39322351370380	1.76379803137299
H	3.59374296120160	16.37576513625600	2.84227670014359
C	5.93403920114514	13.87078526224560	1.90986877387266
H	6.30869759031277	13.97232514500010	0.86652106640129
H	6.13713111280551	14.83574830028980	2.41499673046750
C	9.22105921347493	13.09085660956770	1.60673238387065
C	10.05931655691960	13.29139806554170	2.72473964944169
H	9.94596763292914	12.65467207045150	3.61616625471549
C	11.04307218146880	14.29080653145350	2.69250593819106
H	11.69953162682390	14.44059800086050	3.56360297614277
C	11.19054480722900	15.09844598319210	1.55002608444912
H	11.96312352866260	15.88252457952400	1.52774492335393
C	10.35535596113210	14.90136382832160	0.43805229635468
H	10.46696176548190	15.53014643888830	-0.45846688856600
C	9.37401359345152	13.89661715740920	0.45976224610160
H	8.71474487962619	13.74065592691740	-0.41128960590934
C	8.51428020330799	10.48976941455880	2.68813798540633
C	9.74098172807141	9.89439862014368	2.31479238461189
H	10.32096017966210	10.31928519871510	1.48054804811013
C	10.21042811922670	8.76000654581837	2.98861405269360
H	11.16553101866230	8.30316318066004	2.68803843556432
C	9.45528759863218	8.19799087961174	4.03539572848465
H	9.82017471094149	7.30104568859510	4.55896496733365
C	8.23261624329935	8.78059830327424	4.40356907949865
H	7.62934919001829	8.34095442986992	5.21223940865159
C	7.76019329723347	9.92402296670518	3.73655787686962
H	6.78657110013995	10.34784273379320	4.01680974609503
C	6.55697579214043	12.67417395789940	2.65835334987915
H	6.98766866961968	12.97197412512450	3.63487411015724
H	5.80297362394978	11.87727732520640	2.84753301399886
I	6.19601711018360	13.34916095675600	-1.93376343206283
P	6.56912726032021	9.23801767978447	-1.70150409546312
P	2.80670283961128	11.02405508918990	-1.64740560073540
C	7.19918174158541	9.31589262039530	-3.42204220155257
C	6.61180797475161	8.59586151107061	-4.48399724213868
H	5.73959748913810	7.94937190386658	-4.30258368645409
C	7.12523941440371	8.71142354154572	-5.78545651446776
H	6.65952662442602	8.14879654638191	-6.60912998217388
C	8.22573773612638	9.54873103448022	-6.03670065937402
H	8.62365472590637	9.64222962186729	-7.05879967636880
C	8.80697100891165	10.27771544630190	-4.98558814699913
H	9.65653069360166	10.94942980298760	-5.18070471623922
C	8.29191490842692	10.16780603500560	-3.68537810166538

H	8.71623377572770	10.76373020175300	-2.86196363849056
C	7.16634258040291	7.65293928696679	-0.99120308020528
C	7.48068454374400	7.62614258901958	0.38365759389195
H	7.37995582486648	8.54696513264634	0.97765715973846
C	7.91310839588582	6.43377848146877	0.98265058958576
H	8.15320397426119	6.43021061584129	2.05618895426161
C	8.04467859654032	5.26638011469178	0.21236071744038
H	8.39067904094942	4.33197584057549	0.68088617060162
C	7.74247991428715	5.29183399768160	-1.16094932099819
H	7.85471269585691	4.38067509123452	-1.76867182831842
C	7.30250308941520	6.48085968771756	-1.76364953960147
H	7.08364111867908	6.49826919807371	-2.84209574618487
C	4.74312477756881	9.00305914785208	-1.90943595440102
H	4.36853440136842	8.90161288350355	-0.86602802275296
H	4.54003776450255	8.03804481269258	-2.41446657944516
C	1.45582018070665	9.78299536995088	-1.60677381669126
C	0.61807749257128	9.58225721843397	-2.72513499416374
H	0.73194253294628	10.21874354442040	-3.61666587715066
C	-0.36580061182544	8.58295957216817	-2.69315458503861
H	-1.02184014051862	8.43302818750963	-3.56454365137837
C	-0.51393575593153	7.77562126696471	-1.55056096768211
H	-1.28661276474020	6.99163400925440	-1.52847247783562
C	0.32070227780210	7.97290866930742	-0.43821617573540
H	0.20855103217008	7.34438969911007	0.45842022575405
C	1.30215873586290	8.97754775551818	-0.45967258634324
H	1.96087715391255	9.13370662279285	0.41171413659446
C	2.16284064050003	12.38400274224100	-2.68810711352973
C	0.93628204862619	12.97964312467580	-2.31471539672344
H	0.35636272738101	12.55502990892920	-1.48029003052234
C	0.46690996408270	14.11395552745410	-2.98872059648385
H	-0.48808197096326	14.57100644495890	-2.68810903763490
C	1.22199940076439	14.67563239426610	-4.03572469903702
H	0.85718217923688	15.57252202471530	-4.55943763680090
C	2.44453307395140	14.09276071501720	-4.40393842447133
H	3.04774989877016	14.53213643082650	-5.21279146266644
C	2.91686633653167	12.94940082517790	-3.73675075728328
H	3.89034950178836	12.52532806803230	-4.01709270427500
C	4.12013347875461	10.19960789728890	-2.65798729746509
H	3.68955470599897	9.90176840092743	-3.63454621028089
H	4.87411180619376	10.99653776898970	-2.84711658386723

Table S2: Cartesian Coordinates from **Geom(Short)** Geometry Optimization.

Au	6.90978486722774	5.23204702021905	0.75633663537211

Au	9.92143808601299	5.64579265616301	-0.75627928066766
I	8.77503103781120	3.40350892441624	1.94729956108205
P	5.85981784942118	4.21494496007489	-1.03819297802812
P	9.78035006244457	3.73751172107775	-2.08277407051395
C	5.00620055383381	2.63033256480824	-0.67783994592563
C	5.39889121843959	1.88091578375405	0.44955360159303
H	6.17840203458156	2.27632376645590	1.12299523602709
C	4.80621911813569	0.63212007077255	0.69953899332308
H	5.12119820732596	0.04927707091879	1.57856420262523
C	3.81731495646123	0.13353950961651	-0.16414066508970
H	3.35062273121867	-0.84315863578545	0.03697088261311
C	3.41909794210274	0.88406383654983	-1.28568339071866
H	2.64039158844288	0.49712464802938	-1.96103495067481
C	4.01264055020876	2.12800657375411	-1.54571893903023
H	3.69672285097462	2.71981462644996	-2.41929708758774
C	4.56857633896415	5.27288764404573	-1.78607251525783
C	3.37994757130799	5.48219523756827	-1.05051954959592
H	3.22136649966049	4.93985411490683	-0.10518270574778
C	2.41459521005547	6.38717265405763	-1.50937614735785
H	1.49382954062171	6.54420765556787	-0.92733545811201
C	2.62993165575078	7.10367174188163	-2.70168634903062
H	1.87498112448904	7.82125048070249	-3.05800384539838
C	3.81316271526765	6.90579801143955	-3.43033704247289
H	3.99480208971654	7.47134032063415	-4.35679870316299
C	4.78205105295200	5.99335908802866	-2.97876551069861
H	5.71507949296858	5.87266689813580	-3.54520332020324
C	7.00882166009865	3.77329574698454	-2.41940401270849
H	6.42587009574474	3.30724177693230	-3.23830892704591
H	7.39631223089252	4.74760617084173	-2.79102424417366
C	9.91776521967153	4.07931355404830	-3.88070021738629
C	10.55269360890090	5.27465906384350	-4.27725223426479
H	10.92817252102690	5.96319210511294	-3.50412689328799
C	10.67108009801540	5.59599813379393	-5.63759799874720
H	11.16293577369970	6.53437493146742	-5.93514078774977
C	10.14334016542410	4.73380382769559	-6.61319229928126
H	10.22679483455820	4.99126541213822	-7.68022639976161
C	9.49422133201410	3.54905701556683	-6.22531508781697
H	9.06893423560574	2.87720378371343	-6.98666660575737
C	9.37986918563571	3.22269431678715	-4.86470062540278
H	8.85612280769098	2.29932463797263	-4.57346008992986
C	11.05245452822590	2.46919929409527	-1.69987151280341
C	11.39620877220810	1.44778279298688	-2.61004039342816
H	10.91777573519960	1.40242164247620	-3.60009727169808

C	12.37184427765890	0.49958629732942	-2.26479835154761
H	12.64232115171830	-0.29115748573956	-2.98152111251624
C	13.00657360533080	0.56471417124102	-1.01148447421741
H	13.77330597122070	-0.17923540524513	-0.74503260542336
C	12.66877084588580	1.58357097353880	-0.10526290238683
H	13.16420627636150	1.65148494659186	0.87459500082306
C	11.69871350092250	2.53734214370989	-0.44799788505893
H	11.43229380452440	3.34180881377089	0.25404137438815
C	8.15507571765965	2.86063324210254	-1.93162438268325
H	8.07819273246198	2.60631829318384	-0.85106738650576
H	8.18797571402698	1.90002396581463	-2.48267087872711
I	8.05617507110982	7.47435129747879	-1.94732697498672
P	10.97140440932180	6.66290294392318	1.03823000411285
P	7.05083134305131	7.14037618181083	2.08279930351592
C	11.82501883175910	8.24752035660021	0.67789566283989
C	11.43223001383670	8.99701866692128	-0.44940852055116
H	10.65263340223750	8.60168066522003	-1.12279037354196
C	12.02490207693680	10.24581580292330	-0.69937310475307
H	11.70984105573860	10.82872271454000	-1.57832651621830
C	13.01391084864100	10.74431997532820	0.16423496206839
H	13.48060885245230	11.72101826728660	-0.03686497794505
C	13.41222772801740	9.99371219311952	1.28568527264914
H	14.19101709538500	10.38058646163920	1.96097847465981
C	12.81868558205360	8.74976356456605	1.54569773810074
H	13.13468231320340	8.15788779383775	2.41920023159953
C	12.26265509607250	5.60498030988739	1.78613259110643
C	13.45128557104030	5.39568439448932	1.05058054216729
H	13.60985688603420	5.93802083435341	0.10523943969193
C	14.41665337260280	4.49071881369152	1.50943600353694
H	15.33742006955680	4.33369595648522	0.92739361609102
C	14.20133233071900	3.77422405052543	2.70175088549615
H	14.95629092372440	3.05665994793651	3.05808185243653
C	13.01810228567440	3.97208682295333	3.43040232575458
H	12.83647194153630	3.40654457590010	4.35686451866619
C	12.04919865425850	4.88451007181142	2.97883366309633
H	11.11616829860030	5.00517428296438	3.54528200558663
C	9.82236750680845	7.10450922438663	2.41942449762717
H	10.40529522531480	7.57051105471748	3.23837537008698
H	9.43485836755572	6.13017057380753	2.79097192693086
C	6.91335254154240	6.79863859102308	3.88073447505999
C	6.27831650268326	5.60336128904578	4.27731584660677
H	5.90278831655464	4.91483655225949	3.50420626466844
C	6.15987892959282	5.28207785752682	5.63767037102602

H	5.66793398801336	4.34375513110980	5.93523635605446
C	6.68768307516006	6.14425507063448	6.61324467926136
H	6.60418943182781	5.88683517440792	7.68028602413345
C	7.33691979452864	7.32892824308508	6.22533865126498
H	7.76226269486518	8.00076413182246	6.98667466857059
C	7.45132445728951	7.65523369017617	4.86471542517824
H	7.97516826453142	8.57854017980278	4.57344958984848
C	5.77877281738370	8.40870509586461	1.69979053216705
C	5.43475868048607	9.42998793362442	2.61001194117570
H	5.91294763202639	9.47523808365738	3.60019138986684
C	4.45916328981770	10.37818784999890	2.26466160050304
H	4.18847762609428	11.16882151308190	2.98142737095132
C	3.82473800557544	10.31320230312480	1.01118483832709
H	3.05803933303773	11.05715668346310	0.74464920247804
C	4.16281012631995	9.29448772534612	0.10490392158817
H	3.66761525263823	9.22667662247717	-0.87508382460240
C	5.13282788569491	8.34071549577480	0.44774469373938
H	5.39945367576855	7.53635780883500	-0.25434252831170
C	8.67613427010318	8.01721240158959	1.93167251056963
H	8.75301759348394	8.27153981116246	0.85111888582298
H	8.64327031295283	8.97781685500117	2.48272924196481

Table S2: Cartesian Coordinates from **Geom(Very_Short)** Geometry Optimization.

Au	7.08699214931219	5.25810724754077	0.65729983412845
Au	9.74421080813918	5.61977685339057	-0.65725172928783
I	8.82140693308992	3.41904118855476	2.00585627514552
P	5.92897340427987	4.22566862444650	-1.06438808658865
P	9.72372073179778	3.74233163901655	-2.04589251531271
C	5.03598049813708	2.69189016882349	-0.58507852778400
C	5.42941501672595	1.99931076876465	0.57727083834621
H	6.24353970260268	2.40364181460495	1.20286643500392
C	4.79382215034561	0.79527200088897	0.92387557913928
H	5.11067546228575	0.25782175849245	1.83073257247482
C	3.76121690821521	0.28488610024811	0.12069959547831
H	3.26059910441226	-0.65596693522967	0.39709679376823
C	3.36235786473861	0.97854130114220	-1.03688388902801
H	2.54914555600445	0.58298347827074	-1.66491677637558
C	3.99802713281669	2.17706717331069	-1.39212556663892
H	3.67938602682566	2.72561741692125	-2.29250157888540
C	4.62115440065086	5.28120914389263	-1.78841060964494
C	3.47467969253671	5.53716716853941	-1.00280030491468
H	3.36147853563435	5.04023700575848	-0.02654984341442

C	2.49323309820496	6.42917356477468	-1.45303606422928
H	1.60616648337910	6.62307184878822	-0.83125519862200
C	2.65100734616811	7.08622469986494	-2.68758348814590
H	1.88348875712486	7.79308941986312	-3.03844237163877
C	3.79377609849409	6.84370478743031	-3.46585883641091
H	3.93060373914021	7.36360808608238	-4.42614140735121
C	4.77826395877825	5.94462723767272	-3.02186553210936
H	5.67958863555692	5.78720045551702	-3.62908640447221
C	6.96330627665057	3.66233102945634	-2.49335441405574
H	6.30754020426797	3.12681319596176	-3.20867418497077
H	7.32878516041439	4.58406915982159	-2.99456526760422
C	9.93811712838735	4.17296231844779	-3.81802356149477
C	10.63249048880180	5.36277195509452	-4.12219551190832
H	10.99966877782440	5.99449390255071	-3.29829236135470
C	10.82361514425760	5.75058577725631	-5.45617662962036
H	11.36244265810870	6.68355333751010	-5.68027610903946
C	10.30755903467480	4.96370497946599	-6.49958571403359
H	10.44654324087520	5.27487220999154	-7.54630386724486
C	9.59995304395084	3.78614843415088	-6.20460072839112
H	9.18413052117867	3.17237467924977	-7.01842317007537
C	9.41563577480943	3.39124816716220	-4.86976558203201
H	8.84877711433570	2.47271328305521	-4.65447288001818
C	11.02748007847910	2.50113167239862	-1.68070337254210
C	11.40500963795080	1.51797112024441	-2.61966402668009
H	10.93507241217290	1.49196238054853	-3.61478631547845
C	12.40202710631860	0.58503433172720	-2.29586052444933
H	12.69826361308200	-0.17637207650627	-3.03386916746083
C	13.02531052008650	0.62828274228601	-1.03555487686580
H	13.80839740317530	-0.10411343507020	-0.78507185652254
C	12.65470941917060	1.61000084496885	-0.10194909412042
H	13.14057613546860	1.66021171274727	0.88363358493755
C	11.66208389277080	2.54855181197425	-0.42295714146107
H	11.36599066602600	3.32061889372224	0.30284104395137
C	8.13927669726497	2.78131477793569	-2.02072069818569
H	8.02711222959936	2.43531001752582	-0.97015173011738
H	8.25031689148965	1.87124119339456	-2.64324422624207
I	8.00977481890028	7.45891477794004	-2.00579471320317
P	10.90222899521600	6.65219962754845	1.06442381476706
P	7.10748575939272	7.13559683808455	2.04590545216986
C	11.79526266351620	8.18594079036473	0.58508888100587
C	11.40179699152730	8.87852028796354	-0.57725109357923
H	10.58762041507900	8.47420624523953	-1.20280042859952
C	12.03741724672200	10.08253265162730	-0.92389737541327

H	11.72054204755150	10.61998629449240	-1.83074482109679
C	13.07007738732550	10.59288799998430	-0.12077152324950
H	13.57071681512050	11.53372055343730	-0.39719974490534
C	13.46896433377800	9.89923018748630	1.03680203730363
H	14.28221998884890	10.29476565189780	1.66479285476994
C	12.83326879480810	8.70073091988462	1.39208581884767
H	13.15193210725180	8.15217609574362	2.29245077771324
C	12.21001474946410	5.59663028024236	1.78846621940460
C	13.35644812986630	5.34057526721110	1.00282896098707
H	13.46963488117490	5.83744762866972	0.02654775861021
C	14.33786804027820	4.44854453471897	1.45307281429170
H	15.22490264685900	4.25457297048136	0.83126932821285
C	14.18010730158140	3.79156343286923	2.68765969875691
H	14.94760281573210	3.08467952437832	3.03853080190120
C	13.03737791923190	4.03417918073019	3.46596248792494
H	12.90055813134820	3.51433055863951	4.42627573933438
C	12.05291746847820	4.93328158042056	3.02195757522016
H	11.15162557201730	5.09077559923711	3.62920723189356
C	9.86790400870539	7.21556883729882	2.49338024908380
H	10.52366996144010	7.75109239379144	3.20869512821755
H	9.50241975652503	6.29383739474868	2.99460222049855
C	6.89305082763724	6.70501652950413	3.81804381020184
C	6.19868593140653	5.51520768567181	4.12223718595395
H	5.83153373911352	4.88345554192790	3.29834580112023
C	6.00753908239566	5.12743146659505	5.45622605946271
H	5.46872022014283	4.19446302203019	5.68034256947411
C	6.52356278709822	5.91435102985837	6.49962206115504
H	6.38456119880265	5.60321359280976	7.54634675721178
C	7.23115740536277	7.09190906553869	6.20461609366606
H	7.64695300245721	7.70571402343922	7.01842868566102
C	7.41549658429967	7.48677120560154	4.86977295174332
H	7.98234484962049	8.40530830389033	4.65446356592454
C	5.80375820671621	8.37681553768640	1.68066369265477
C	5.42623183965161	9.36000475292150	2.61959496833907
H	5.89615082240559	9.38602467752788	3.61472564671094
C	4.42923965546881	10.29295493102870	2.29575308525788
H	4.13300506943530	11.05438277379790	3.03374024042690
C	3.80597762163715	10.24969185632870	1.03543793030780
H	3.02290935924305	10.98209803665750	0.78492600419421
C	4.17657643973961	9.26794751257657	0.10185894762691
H	3.69072468427430	9.21772345417838	-0.88373097057716
C	5.16918038393788	8.32938552262236	0.42290381118852
H	5.46527314858302	7.55729899151669	-0.30287451679941

C	8.69194364958010	8.09659086282549	2.02073577257103
H	8.80411292861294	8.44257942416236	0.97016449659705
H	8.58091234764426	9.00667265972660	2.64324838950938

Chapter 4: Using Blender to Create Educational Tools

Subchapter 4.1: A Library of 3D Visual Teaching Tools for Chemistry Classroom Accessible via Sketchfab and Viewable in Augmented Reality

Michael M. Aristov, John W. Moore, John F. Berry

Department of Chemistry, University of Wisconsin–Madison, 1101 University Ave., Madison, WI 53706

Email: berry@chem.wisc.edu

4.1.0 Author contributions: This work was written by MMA and JFB. All 3D models were created by MMA.

4.1.1 Abstract: Through the implementation of the free website/smartphone application Sketchfab, we have found a simple means to introduce 3D visual tools into the chemistry classroom. Sketchfab stores 3D models and animations with free cross-platform accessibility. Blender is a free 3D modeling tool that has been used to prepare models and animations for dissemination via Sketchfab. By combining these two tools, we have created and are currently maintaining an ever-growing free library of interactive 3D models on various chemistry topics. Through the Sketchfab smartphone application, these models are viewable in augmented reality on most devices. Topics include molecular motion, isomerism, molecular orbital theory, chirality, and polymerization.

Keywords: High School / Introductory Chemistry; First-Year Undergraduate / General; Internet / Web-Based Learning; Multimedia-Based Learning; MO Theory; Polymerization

4.1.2 Introduction: Teaching in a purely virtual setting as a consequence of the COVID-19 pandemic has encouraged the invention and adoption of new visualization tools.[1, 2] Previous efforts have built libraries of freely accessible online teaching resources for chemistry.[3-5] These tools are particularly vital for a hands-on science like chemistry, in which the act of physically manipulating molecular models can be crucial for understanding spatial relationships.[6-8] For this purpose, molecular model kits, computational chemistry programs, and augmented reality tools have been increasingly introduced into the general chemistry classroom as teaching tools.[9-18] Model kits enable students to craft molecules physically, thereby discovering things like the effect of steric encumbrance, rotation about single bonds vs. double bonds, and the non-superposition of enantiomers. Augmented reality offers a middle ground between the intangible computer-generated images and the tactile nature of model kits.[19-21] By coupling this tactile learning with visualization of the complex geometries inherent to molecular orbitals, students achieve a more holistic view of bonding in chemistry.[22-26] Unfortunately, computational chemistry tools often have a steep learning curve, may lack compatibility across operating systems and devices, and may require technical capabilities that many students lack.[27] To circumvent these problems, we have sought a universally accessible tool for manipulating 3D objects that can be implemented both in a virtual learning environment and in the physical classroom of high schools and universities, where the majority of students (>80% for high school and >90% for university) have access to smart phones.[28, 29]

To this end we have created and are currently maintaining an ever-growing library of interactive 3D models that have been uploaded to the free 3D model sharing website, Sketchfab.[30] This website offers a browser-based venue for viewing 3D models and animations, with interactive elements that allow the viewer to pan, zoom, rotate, and play/pause/rewind the contents of a 3D

object or movie. Sketchfab allows for simple upload and distribution of these 3D models and animations across operating systems or devices, allowing mass distribution to a student body without concerns for compatibility. Furthermore, during the Sketchfab upload process, all models are automatically converted into a form that can be viewed through augmented reality via smartphone applications. This background feature of Sketchfab for augmented reality offers potentially one of the simplest means to create and integrate augmented reality models into teaching. We anticipate that these tools will remain relevant once in-person teaching returns to the norm, as students can download the Sketchfab smartphone application, available on both Android and IOS. This smartphone integration allows students to view these models easily on screen in a classroom environment where a computer may not be convenient. Sketchfab also automatically generates embedded code, allowing for the models to be inserted directly into online open education resource (OER) textbooks and websites.[31] This embedding eliminates the need for students to navigate to alternative web pages or programs to view the 3D files.

Currently, our model library details common high school and general chemistry topics such as orbital shapes, molecular motion, chirality and enantiomers, and molecular orbitals. We have limited the use of written descriptors to circumvent language barriers for international students. These models are currently freely accessible online through the Sketchfab website, and they to date have garnered over 5.8 thousand views by chemistry teachers and students.

4.1.3 Methods

All models were made and uploaded through a subset of four free software packages: ORCA,[32] Chimera,[33] Avogadro,[34] and Blender.[35] The models were later uploaded with a free account to Sketchfab, a browser-based 3D model hosting/sharing/viewing platform. Alternatively, 3D

models that could be manipulated in Microsoft Office programs were directly exported from blender, though these models lost their animations.

4.1.4 Workflow: The quantum chemistry program ORCA was used to perform single point (SP) calculations on molecules and/or ions to derive their orbitals. Both Natural Bond Orbitals (NBO)[36] and Molecular Orbitals (MO) were calculated from these SP calculations. To create output files that can be read by the molecular graphics program Chimera, surfaces of these orbitals were converted into .cube files using ORCA_PLOT with a standard file resolution of 100 grid points. This file conversion process also generated .xyz files that contained information about the molecule, specifically the atom types and positions, and this molecule was aligned with the orbital plots.

Visualization and manipulation of the orbital surfaces from the .cube files was performed in Chimera by loading both the .xyz and the .cube files.[33] The alias MySurface, generated by the line "^MySurface volume all style surface level 0.05 color red level -0.05 color blue", was used to set the orbitals to the 95% isosurface and to set their colors. After initial visualization, the surfaces for each NBO and/or MO were saved as the wavefront object (.obj) file type, whereas the ball and stick structure of the molecule was saved as the collada (.dae) file type. Care was taken to not reorient the molecule when saving multiple orbitals through this method, as this reorientation would misalign the orbital's surface from the corresponding molecule's coordinates.

4.1.5 Alternative Workflow Guide

Another route for importing molecules in Blender is outlined in Dr. Joseph G. Manion's guide titled "Blender for Scientists - How to Make ANY Molecule in Blender".[37] This video provides

an excellent step-by-step process for creating any molecule in Blender. Manion did not rely on any quantum chemical methods to make these models, and instead he used the molecular mechanics algorithm embedded in the free Avogadro software package.[34]

4.1.6 Blender Implementation and Final File Export

After the 3D files were generated, they were imported into Blender where any remaining aesthetic changes and/or animations were made. After the 3D files were generated, they were imported into Blender where any remaining aesthetic changes and/or animations were made. These aesthetic changes include modification of an object's color, sheen, roughness, index-of-refraction, and opacity, as well as the refinement of lighting, scaling, and scene-composition. All animations were made through Blender's keyframe system by changing either the object's location, rotation, or scaling over a specified number of frames. These keyframed actions combined with object parenting were used to create animations like "Butane Rotation Smooth", which displays a perfect loop of every C-C bond rotating simultaneously and at different rates in a butane molecule.

Microsoft Office365 compatible 3D files were made by exporting the Blender model as a filmbox (.fbx). These files can be directly inserted into any Word or PowerPoint file with their 3D nature preserved, allowing for real time rotation, scaling, and animation inside Office. It should be noted that some material attributes are lost, like the metallic value, when viewing 3D files in Office365, and we have found that simple base colors and alpha values (opacity) have worked best. A recent guide by Manion, titled "Blender for Scientists - Using 3D Objects Directly in PowerPoint" details an alternative process of generating 3D objects for use in PowerPoint, though this guide favors glTF 2.0 files, and does not detail how alpha values can be used to incorporate transparent objects.[38]

Uploading models to Sketchfab was done either through a freely available Blender extension or by using the Sketchfab website directly. All models were uploaded to Sketchfab as Blender's default save file type (.blend). Once uploaded, Sketchfab's 3D viewer was used to make any final changes to individual materials in the model, which define the appearance of each object in the scene. These changes include scene lighting, initial camera location, model orientation and scale, and to set the animation to auto-play upon loading. Once uploaded, these models were set to public, a title and description were added, and their copyrights were declared.

4.1.7 Pedagogical Framework: Sketchfab automatically generates multiple styles of embed code for every public model on the website. These embed codes allow for simple integration into online resources frequently used in chemistry classes. These embedded files allow for finer control of the material viewed by students and help eliminate distractions and breaks in student workflow that may occur when students are asked to view multiple websites simultaneously.

4.1.8 Current Models and Animations: All of the models we have made using the above procedure are available on Michael Aristov's Sketchfab account at *https://sketchfab.com/Michael.Aristov*. Table 1 below offers a list of some of the models we have made. As we continue to generate more of these models, they will be added to the Sketchfab account. Additionally, all models are downloadable from the Sketchfab website as .blend or .glTF; all of the .blend files for the models described in Table 1 are included in the SI.

Table 1. Selected models currently freely available on Sketchfab. Each entry is accompanied by the model's title as found on Sketchfab, a direct link, a short description, and a snapshot taken of the model or animation.

	Description	Snapshot
MOs and AOs		
Molecular Orbital Diagram from Atomic Orbitals https://skfb.ly/6V9Lu	A diagram showing how 2*s* and 2*p* orbitals on F_2 combine to give rise to its MO diagram.	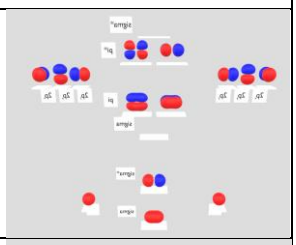
1s, 2s, and 3s, orbitals https://skfb.ly/6UAYF	A model showing the relative sizes and nodes associated with the first three *s*-orbitals.	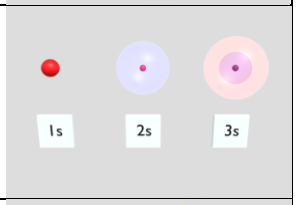
2p, 3p, 4p atomic orbitals on Xe: https://skfb.ly/6WQnr	A model showing the relative sizes and nodes associated with the first three sets of *p*-orbitals.	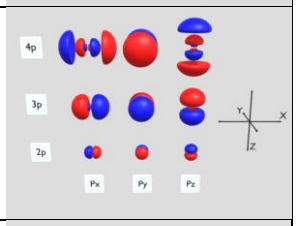
3d and 4d atomic orbitals on Xe https://skfb.ly/6UDVU	A model showing the relative sizes and nodes associated with the first two sets of *d*-orbitals.	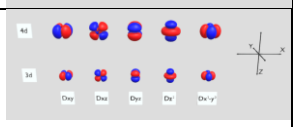
1,3-Butadiene polymerization https://skfb.ly/6UznK	An animation showing the orbitals of 1,3-Butadiene and the changes they undergo during an addition polymerization.	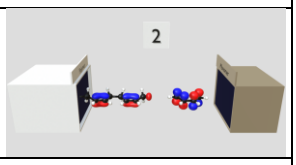
Molecular Motion		
Butane Rotation Smooth https://skfb.ly/6TwYN	A cartoon visualization of how butane can rotate about and C-C bond, and how this rotation affects the structure of butane.	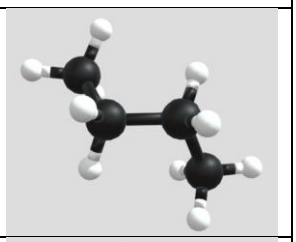
Rotation of Nonane https://skfb.ly/6TNq8	A cartoon visualization of how distorted nonane can appear when rotating about every C-C bond.	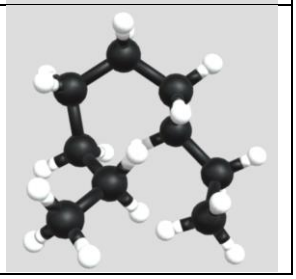

Cis-2-Butene Rotation https://skfb.ly/6TJsN	An animation depicting the limited rotation in a hydrocarbon with a double bond.	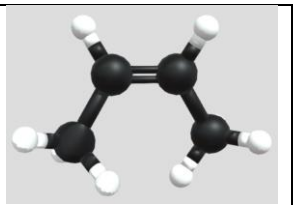
1,2-Dichloroethane Twist https://skfb.ly/6TOVy	An animation showing the energy levels associated with rotating about the C-C bond in dichloroethane.	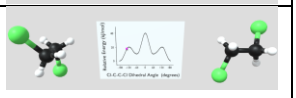
Enantiomers and Chirality		
Superimposing Dichloroiodomethane Mirror Images https://skfb.ly/6XvoX	A simple animation showing Dichloroiodomethane and its mirror image, followed by an overlap of the two molecules in 3D space. This animation demonstrates how non-chiral molecules can be superimposed.	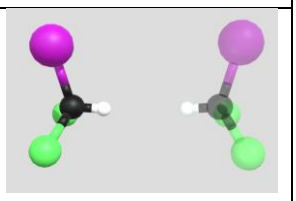
Enantiomers of bromochloroiodomethane https://skfb.ly/6TJsW	A simple animation showing bromochloroiodomethane and its mirror image, followed by two attempts to overlap the molecules using only translation and rotation. The animation demonstrates how chiral molecules cannot be superimposed.	
Isomers		
Fac/Mer Molecular Configurations https://skfb.ly/6ZDLv	A model showing the differences between the *fac* and *mer* isomers of a generic octahedral complex. Triangles were added for emphasis.	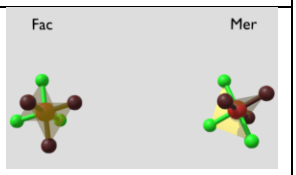
Cis/Trans Molecular Configurations https://skfb.ly/onEQA	A model showing the differences between the *cis* and *trans* isomers of a generic octahedral complex.	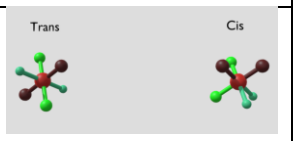
Structures of 2,3-dichlorohexane https://skfb.ly/6UTsI	An animation showing five isomers of 2,3-dichlorohexane. The intent of this animation is for the student to try and identify which pair of isomers are identical, and which pairs are rotamers. This animation starts in a static pose, and the animation must be manually started through the user controls.	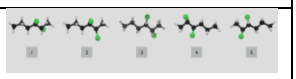
Butane Rotation to Lewis Structure https://skfb.ly/6VTDB	An animation depicting four possible conformations of butane achieved by rotation about a C-C bond. Each conformer is shown sequentially with its associated wedge-dash structure.	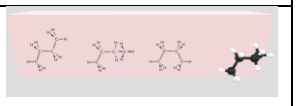
Simple Symmetry		

Single Water Molecule https://skfb.ly/onwrI	A model of a single water molecule. Students are tasked with identifying all symmetry elements present in the molecule. By switching from a static model to display symmetry elements in bottom left of the user interface, the symmetry elements will be displayed.	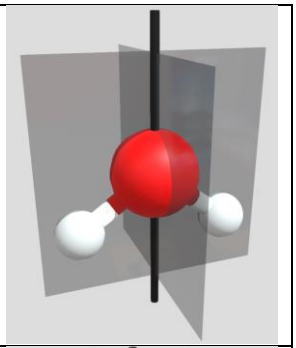
Single Boron Trifluoride Molecule https://skfb.ly/ootFs	A model of a single Boron Trifluoride molecule. Students are tasked with identifying all symmetry elements present in the molecule. By switching from a static model to action in bottom left of the user interface, the symmetry elements will be displayed.	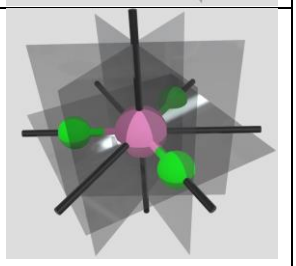
Single Ammonia Molecule https://skfb.ly/onw8w	A model of a single ammonia molecule. Students are tasked with identifying all symmetry elements present in the molecule. By switching from a static model to display symmetry elements in bottom left of the user interface, the symmetry elements will be displayed.	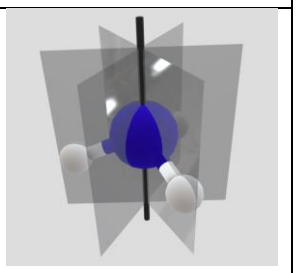

4.1.9 Student Implementation and Classroom Integration: We believe these 3D teaching tools will offer significant benefits over their more classical 2D depictions. Specifically, we seek to replace the static 2D figures of complex systems commonly found in textbooks with dynamic and interactive 3D models. We have started pursuing this replacement by including these 3D models into the open education resource (OER) chemistry textbook pre-class materials for Advanced General Chemistry, Chem 109, at the University of Wisconsin, Madison.[31] Several example pages with these embedded 3D models from the above OER textbook that was used to teach the Fall 2020 chemistry course at UW Madison are provided below.

Molecular conformations: https://wisc.pb.unizin.org/chem109fall2021ver02/chapter/day-11/

Cis-trans isomers: https://wisc.pb.unizin.org/chem109fall2021ver02/chapter/day-11/

Enantiomers: https://wisc.pb.unizin.org/chem109fall2021ver02/chapter/day-11/

Addition polymerization: https://wisc.pb.unizin.org/chem109fall2021ver02/chapter/day-14/

Because these animations were embedded into an OER, we cannot attribute learning gains to the animations separately. However, there is a positive correlation between exam scores and time spent using the OER.

We propose that these 3D models should be used instead of classical 2D figures in online textbooks. For classrooms with physical books, we suggest emailing links to the models as appropriate throughout the course. For interactive work, we suggest allowing students to work in small groups and to view the models on their smartphones with the task of answering scaffolding questions about the model. An example of this type of task is seen in the Single Water Molecule model (https://skfb.ly/6UTsI), where students would be asked to identify all symmetry elements for the water molecule. The students can view the correct answer by selecting “display symmetry elements” in the Sketchfab user interface.

4.1.10 Conclusion: This technical report highlights a new and growing library of 3D models and animations that can be viewed on any device, and thereby allows for simple integration across a variety of learning environments. The animation capabilities of Blender simplify the creation of novel visualizations for otherwise esoteric descriptions of chemistry concepts, like a chiral molecule’s inability to be superimposed on its mirror image or how multiple wedge-dash structures can be drawn for different conformations as seen in Table 1. The free nature and ease of use inherent to Sketchfab allows for students to view these models via computer display or augmented reality. This combination of Blender and Sketchfab provides a simple means by

which an instructor can create and distribute 3D teaching tools for any class. Our initial work has focused on the integration of these models as additional teaching tools in the classroom, and these models have gathered over 5,800 views from students and teachers alike in the 14 months that they have been publicly available.

4.1.11 Associated Content

Supporting information

The Supporting Information is available on the ACS Publications website at DOI: https://pubs.acs.org/doi/10.1021/acs.jchemed.1c00460.

The finalized project files for all models and animations shown in Table 1 as output from and modifiable in Blender (.zip, .blend)

Corresponding Authors

Michael M. Aristov – aristov@wisc.edu
John F. Berry – berry@chem.wisc.edu

ORCID

Michael M. Aristov**:** 0000-0003-1161-5126
John W. Moore: 0000-0001-7652-0668
John F. Berry: 0000-0002-6805-0640

ACKNOWLEDGMENT

We thank NSF for funding via CHE-1953294, and we thank the NSF-GRFP for funding via DGE-1747503.

4.1.12 References:

1. Babinčáková, M.; Bernard, P., Online Experimentation during COVID-19 Secondary School Closures: Teaching Methods and Student Perceptions. *J. Chem. Educ.* **2020,** *97*, 3295-3300.

2. Lee, M. W., Online Teaching of Chemistry during the Period of COVID-19: Experience at a National University in Korea. *J. Chem. Educ.* **2020,** *97*, 2834-2838.
3. Johnston, D. H. Symmetry Resources at Otterbein University. https://symotter.org/ (accessed 06/28/2021).
4. Winter, M. The Orbitron. https://winter.group.shef.ac.uk/orbitron/ (accessed 04/01/2021).
5. Chemistry: LibreTexts. https://chem.libretexts.org/ (accessed 06/28/2021).
6. Eastwood, M. L., Fastest Fingers: A Molecule-Building Game for Teaching Organic Chemistry. *J. Chem. Educ.* **2013,** *90*, 1038-1041.
7. Ramesh, B. V.; Selvam, A. A. A.; Kulkarni, S.; Manganahalli, A. D.; Bettadapur, K. R., Designing and Using an Atomic Model Kit with H, C, N, and O Model Atoms Having a Mass Ratio of 1:12:14:16 to Teach the Concept of Mole and Associated Stoichiometric Relationships. *J. Chem. Educ.* **2020,** *97*, 986-991.
8. Stull, A. T.; Hegarty, M.; Dixon, B.; Stieff, M., Representational Translation With Concrete Models in Organic Chemistry. *Cogn. Instr.* **2012,** *30*, 404-434.
9. Lyle, S. J.; Flaig, R. W.; Cordova, K. E.; Yaghi, O. M., Facilitating Laboratory Research Experience Using Reticular Chemistry. *J. Chem. Educ.* **2018,** *95*, 1512-1519.
10. Johnson, L. E.; Engel, T., Integrating Computational Chemistry into the Physical Chemistry Curriculum. *J. Chem. Educ.* **2011,** *88*, 569-573.
11. Barradas-Solas, F.; Sánchez Gómez, P. J., Orbitals in chemical education. An analysis through their graphical representations. *Chem. Educ. Res. Pract.* **2014,** *15*, 311-319.
12. M. B. Marcus; Moore, J. W., Impact of a Web-Based Tutorial on VSEPR and Visualization Skills. *Chem. Educator* **2010,** *15*, 18-25.
13. Tee, N. Y. K.; Gan, H. S.; Li, J.; Cheong, B. H.-P.; Tan, H. Y.; Liew, O. W.; Ng, T. W., Developing and Demonstrating an Augmented Reality Colorimetric Titration Tool. *J. Chem. Educ.* **2018,** *95*, 393-399.
14. Eriksen, K.; Nielsen, B. E.; Pittelkow, M., Visualizing 3D Molecular Structures Using an Augmented Reality App. *J. Chem. Educ.* **2020,** *97*, 1487-1490.
15. Yang, S.; Mei, B.; Yue, X., Mobile Augmented Reality Assisted Chemical Education: Insights from Elements 4D. *J. Chem. Educ.* **2018,** *95*, 1060-1062.
16. Sanii, B., Creating Augmented Reality USDZ Files to Visualize 3D Objects on Student Phones in the Classroom. *J. Chem. Educ.* **2020,** *97*, 253-257.
17. Aw, J. K.; Boellaard, K. C.; Tan, T. K.; Yap, J.; Loh, Y. P.; Colasson, B.; Blanc, É.; Lam, Y.; Fung, F. M., Interacting with Three-Dimensional Molecular Structures Using an Augmented Reality Mobile App. *J. Chem. Educ.* **2020,** *97*, 3877-3881.
18. Snyder, H. D.; Kucukkal, T. G., Computational Chemistry Activities with Avogadro and ORCA. *J. Chem. Educ.* **2021,** *98*, 1335-1341.
19. Fernandes, H. S.; Cerqueira, N. M. F. S. A.; Sousa, S. F., Developing and Using BioSIMAR, an Augmented Reality Program to Visualize and Learn about Chemical Structures in a Virtual Environment on Any Internet-Connected Device. *J. Chem. Educ.* **2021**.
20. Abdinejad, M.; Ferrag, C.; Qorbani, H. S.; Dalili, S., Developing a Simple and Cost-Effective Markerless Augmented Reality Tool for Chemistry Education. *J. Chem. Educ.* **2021**.
21. Elford, D.; Lancaster, S. J.; Jones, G. A., Stereoisomers, Not Stereo Enigmas: A Stereochemistry Escape Activity Incorporating Augmented and Immersive Virtual Reality. *J. Chem. Educ.* **2021**.
22. Levy Nahum, T.; Mamlok-Naaman, R.; Hofstein, A.; Taber, K. S., Teaching and Learning the Concept of Chemical Bonding. *Stud. Sci. Educ.* **2010,** *46*, 179-207.
23. Smith, D. W., A Simple Molecular Orbital Treatment of the Barrier to Internal Rotation in the Ethane Molecule. *J. Chem. Educ.* **1998,** *75*, 907.
24. Miller, G. J.; Verkade, J. G., A Pictorial Approach to Molecular Orbital Bonding in Polymers: Non-Mathematical but Honest. *J. Chem. Educ.* **1999,** *76*, 428.

25. Kronik, L.; Levy Nahum, T.; Mamlok-Naaman, R.; Hofstein, A., A New "Bottom-Up" Framework for Teaching Chemical Bonding. *J. Chem. Educ.* **2008,** *85*, 1680.
26. Dhindsa, H. S.; Treagust, D. F., Prospective pedagogy for teaching chemical bonding for smart and sustainable learning. *Chem. Educ. Res. Pract.* **2014,** *15*, 435-446.
27. Trammell, G.; Koehler, P. F. M.; Pratt, D. W.; Garkov, V. N.; Gotwals, R. R.; Wang, M. R.; Bishop, A., Meeting the Challenges of Teaching Chemistry for General Education Students: Summary of the Fall 2007 ConfChem Conference. *J. Chem. Educ.* **2010,** *87* (12), 1455-1457.
28. Alfawareh, H.; Jusoh, S., Smartphones Usage Among University Students: Najran University Case. *J. Acad. Res.* **2014,** *6*, 321-326.
29. Poll, H. Pearson Student Mobile Device Survey 2015 National Report: Students in Grades 4-12. https://www.pearson.com/content/dam/one-dot-com/one-dot-com/us/en/pearson-ed/downloads/2015-Pearson-Student-Mobile-Device-Survey-Grades-4-12.pdf (accessed 06/28/2021).
30. Sketchfab. https://sketchfab.com/ (accessed 6/28/2021).
31. Moore, J. W.; Zhou, J.; Garand, E. Chemistry 109 Fall 2021 OER. https://wisc.pb.unizin.org/chem109fall2021ver02/front-matter/introduction/ (accessed 6/28/2021).
32. Neese, F., Software Update: The Orca Program System, Version 4.0. *Wiley Interdiscip. Rev.: Comput. Mol. Sci.* **2018,** *8*, e1327.
33. Pettersen, E. F.; Goddard, T. D.; Huang, C. C.; Couch, G. S.; Greenblatt, D. M.; Meng, E. C.; Ferrin, T. E., UCSF Chimera—A Visualization System for Exploratory Research and Analysis. *J. Comput. Chem.* **2004,** *25*, 1605-1612.
34. Hanwell, M. D.; Curtis, D. E.; Lonie, D. C.; Vandermeersch, T.; Zurek, E.; Hutchison, G. R., Avogadro: an advanced semantic chemical editor, visualization, and analysis platform. *J. Cheminf.* **2012,** *4*, 17.
35. Blender. https://www.blender.org (accessed 06/28/2021).
36. Glendening, E. D.; Landis, C. R.; Weinhold, F., NBO 7.0: New Vistas in Localized and Delocalized Chemical Bonding Theory. *J. Comput. Chem.* **2019,** *40*, 2234-2241.
37. Manion, J. G. Blender for Scientists - How to Make ANY Molecule in Blender. https://www.youtube.com/watch?v=zXJKYvuCPYY (accessed 6/28/2021).
38. Manion, J. G. Blender for Scientists - Using 3D Objects Directly in PowerPoint. https://www.youtube.com/watch?v=Cr1-01cutHs (accessed 6/28/2021).

Subchapter 4.2: A New Library of 3D Models and Problems for Teaching Crystallographic Symmetry Generated Through Blender for Use with 3D Printers or Sketchfab

Michael M. Aristov, Han Geng, Alex Pavelic**,** and John F. Berry*

Department of Chemistry, University of Wisconsin–Madison, 1101 University Ave., Madison, WI 53706

*Email: berry@chem.wisc.edu

4.2.0 Author contributions: This work was written by MMA and JFB. All 3D models and animations were made by MMA, HG, and AP.

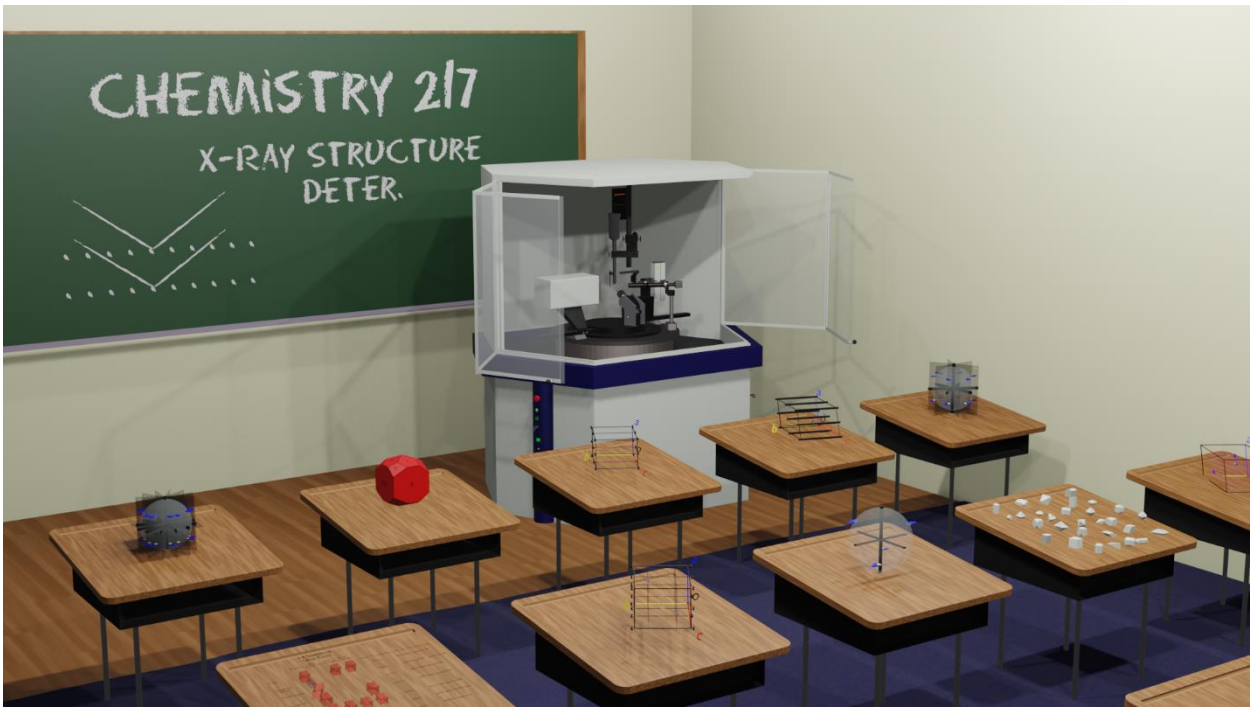

4.2.1 Abstract: We present here a new and growing library of 3D models that can be utilized to illustrate many important concepts in the field of crystallography. These models are accessible in the classroom via computers and smartphones and offer significant advantages over 2D depictions found in crystallography textbooks. Through the use of Blender, a free 3D modeling

and animation program, we were able to create over 100 new models focusing on different aspects of crystallographic education. To simplify distribution/access, we uploaded all of these models to Sketchfab, a model hosting and viewing website that works similarly to YouTube. The current set of models is also given as a list in the supporting information. All of these models are free to view in a web-browser or through a smartphone application. We additionally made all of these models freely downloadable through the SI and Sketchfab, and we encourage users to download and modify these models to best suit their needs. This library of models is part of our ongoing outreach program to create 3D models for free for educational purposes, and we offer our services to create additional models and moderate this library as additional requests or critiques are provided.

4.2.2 Introduction: By its very nature, understanding crystallography requires a strong ability to intuit 3D spatial relationships.(Chapuis, 2011, Grazulis *et al.*, 2015) These relationships can be taught to students via mathematical concepts such as matrix algebra, symmetry, and group theory, though diagrammatic demonstration of symmetry relationships is of prime importance and utility. (Tuvi-Arad & Blonder, 2010, Grafton, 2011, Luxford *et al.*, 2012, Southam & Lewis, 2013, Fuchigami *et al.*, 2016, Girolami, 2016, Penny *et al.*, 2017, Ruiz & Johnstone, 2020) Classically, 2D projections (stereographic projections) of 3D relationships have been used in crystallography.(Hardgrove, 1997, Stroz, 1997, Chen *et al.*, 2015, Duda *et al.*, 2020) Over time, teaching of molecular symmetry has improved significantly from the work of educators to create either physical or virtual libraries of 3-dimensonal (3D) models, including some with 3D printing capabilities,(Scalfani & Vaid, 2014, Casas & Estop, 2015, Rodenbough *et al.*, 2015, Penny *et al.*, 2017, Casas, 2018, 2020, Savchenkov, 2020) to aid in the visualization of this inherently 3D topic.(Graef, 1998, Stróż, 2003, Hitzer *et al.*, 2010, Tuvi-Arad & Blonder, 2010, Antonoglou *et*

al., 2011, Flint, 2011, Carlisle *et al.*, 2015, Johnston, 2021) These libraries capitalize on visualization software such as Jmol, allowing users to manipulate 3D structures through the use of a mouse, and the integration of 3D models onto web pages.(Hanson *et al.*, 2013) Examples of libraries of 3D models on chemistry topics that are now used across campuses include Otterbein symmetry, the orbitron, or other education libraries on Sketchfab.(Aristov *et al.*, 2021, Johnston, 2021, Winter, 2021) While these libraries are excellent resources for visualizing inherently 3D concepts like molecular orbitals or molecular symmetry, more specialized topics like crystallographic symmetry, including translational symmetry and space symmetry, fall outside of their original scope. (Tuvi-Arad & Blonder, 2010, Antonoglou *et al.*, 2011, Flint, 2011, Southam & Lewis, 2013, Carlisle *et al.*, 2015, Penny *et al.*, 2017, Dagnoni H. *et al.*, 2018) Although there are still numerous resources that focus on teaching crystallography, (Grove *et al.*, 2009, Cushman & Linford, 2015, Malbrecht *et al.*, 2016, Bazley *et al.*, 2018) few fully incorporate 3-dimensionality.(Scalfani & Vaid, 2014, Casas & Estop, 2015, Rodenbough *et al.*, 2015, Brannon *et al.*, 2020)

We report here a new, large library of 3D models and animations expressly designed for the purpose of teaching crystallography. Herein, we define a model as any 3-dimensional representation or animation, that can be manipulated and viewed in 3D. In creating these models, we have paid careful attention to convert the historically used 2D projections found throughout textbooks and the International Tables for Crystallography into recognizable 3D counterparts. (Meier, 1984, Borchardt-Ott, 1993, Graef, 1998, Meier, 2001, *International Tables for Crystallography*, 2016, Girolami, 2016) We have sought to make this library easily and globally accessible, barrierless, free, and expandable/curatable. To accomplish these goals, we make use of Sketchfab, a free website for hosting, editing, and viewing 3D models.(*Sketchfab*, 2021) All of

the models are freely available on the Sketchfab website, which can be viewed either in an internet browser on all operating systems or through a smart phone application available on either IOS or Android. As the models can be viewed inside a web browser through Sketchfab, users do not need to download or learn additional software packages to make use of the models. All primary functions for viewing these models on Sketchfab are free, thereby avoiding the potential financial burden that other teaching tools, like physical model kits or proprietary software packages, put on students. Additionally, anyone can freely add their own models to Sketchfab, and by including specific tags, like "Crystallography_education" or "Crystallography_activities" or "Stereographic_Projection", these models can be easily found alongside the initial library we describe here. New models can be curated through feedback via the comment section or by contacting the author, allowing the community to help self-moderate.

The models themselves were made using Blender, a free 3D modeling software program that is compatible with most research grade software packages, including Chimera, Mercury, and PyMol.(Pettersen *et al.*, 2004, *Blender*, 2020, Macrae *et al.*, 2020, The PyMOL Molecular Graphics System, 2021) The Blender guides by Dr. Joseph G. Manion proved to be exceptionally useful for making many of these models and using Blender in general.(Manion, 2021) To help determine the scope of models to make, we communicated with groups of crystallography teachers and students. Currently, this library contains over 130 models/animations including models showing the action of symmetry operations, depictions of point and space symmetry, and illustrations of unit cells from various crystal systems. Although we have constructed a robust set of models for these topics, we plan to expand upon this library as we receive additional nuanced feedback or model requests on previously unconsidered topics.

4.2.3 Technical Considerations

4.2.3.1 General Model Settings: All models uploaded to Sketchfab were made with the following specifications. All models had their field-of-view (FOV) set to 1°, which is an option built into Sketchfab's 3D model editor. This FOV was selected to avoid issues with parallax and minimize distortion during reorientations. The models' shadows were turned off to minimize unnecessary visual information during reorientation of the camera. Either the default, off-white (#dddddd) or the included "clean_dark"/"clean_light" image backgrounds were used depending on which one provided clearer visualization of the model.

4.2.3.2 3D Symbols for Symmetry Elements: Adapting the well-known 2D symbols from stereographic projections to 3D visualization aids proved to be non-trivial. We primarily referenced X-ray Crystallography and the International Tables to construct 3D versions of the historical 2D representations for the symbols.(Paufler, 2007, Girolami, 2016, *International Tables for Crystallography*, 2016) While some symbols, such as the rotational axes or mirror planes had intuitive 3D counterparts, others, like the inversion center or glide planes did not. For mirror planes we used a flat, grey, transparent 2D surface. For rotation axes, we opted for a matte black bar whose end-on profile matches that of the 2D projection. For inversion centers we used a small metallic-red sphere. If another symmetry element passed through an inversion center, we cut a hole through the secondary symmetry element, leaving a void space around the inversion center so that it was not obscured. For roto-inversion axes, we added a white dot to the end-on profile of the $\overline{3}$, whereas $\overline{4}$ and $\overline{6}$ were drawn as white tetragonal/hexagonal prisms with a black 2-fold and 3-fold rotation symbol imposed on their faces respectively. For unit cells, we color coded the axes such that $\vec{a}$ was blue, $\vec{b}$ was yellow, and $\vec{c}$ was red. Glide planes were colored according to the direction of translation, for instance a *c*-glide, regardless of whether it is

perpendicular to $\vec{a}$ or $\vec{b}$, was colored red. The *n*-glide planes were colored according to the combination of translations: e.g., an *n*-glide along *a* and *c* was colored purple (blue+red). Examples of these elements can be seen in Figure 1.

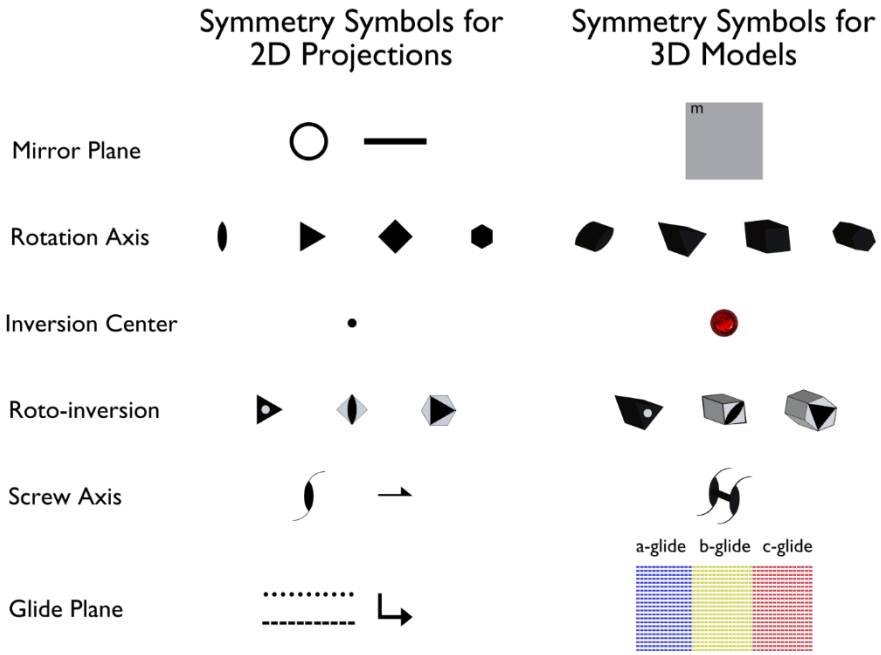

Figure 1. A comparison between the 2D symmetry symbols used in stereographic projections, and our 3D interpretation of those symbols.

4.2.3.3 3D Symbols for Objects

This library contains two primary types of objects to be acted upon by symmetry elements. These objects include the Blender default "Suzanne" model, protected under the creative commons attribution 3.0 un-ported license. The second object is a custom-made blue hand holding a yellow

coin designed to help emphasize chirality, Figure 2. These “hands” are inspired by W. M. Meier’s pamphlet for teaching crystallographic space groups. (Meier, 1984)

Figure 2. A depiction of the model we chose for the chiral object, showing off both the back and the front of the left hand.

4.2.4 Static VS Animated: One benefit from creating these models in Blender is the ease with which animations could be made from the models. This process, although technically simple through Blender’s included options, allows for the generation of animations depicting all of the symmetry operations used in crystallography. Models including animations can be identified easily on the Sketchfab website by their thumbnail showing a small depiction of film in the upper right corner on the animated models.

4.2.5 Availability and Expandability: All of the models that we have made are freely available on Michael Aristov’s Sketchfab account at *https://sketchfab.com/Michael.Aristov*. All models relevant to crystallography are tagged with either “Crystallography_education” or “Crystallography_activities” to make them more visible to the Sketchfab search engine. These models can be viewed either in-browser or through the free Sketchfab smart phone application available on both android and iOS.(*Sketchfab,* 2021) To search for a tag on Sketchfab, the user needs to type “tag:” at the start of their search. Additionally, users need to take care when typing in a tag that they do not use a “ “ instead of an “_”, as tags do not contain spaces. All models described in this publication can also be downloaded from the SI. The SI contains duplicate

models in a variety of file formats depending on their purpose. To make these models easier to navigate, we have included direct links throughout this paper, additionally, there an excel sheet in the SI that contains an interactive link to every model and for every tag search relevant to this project. We encourage students and teachers to download, modify, and reupload these models while including the "Crystallography_education" or "Crystallography_activities" tag as appropriate to help expand this library and provide additional resources for crystallography topics we may have missed.

4.2.6 File Types: 3D file formats have a variety of file types, each with their own specifications and capabilities. All of the models were originally made in Blender and are therefore available as .blend files. Models created for 3D printing are available as .stl files. Additionally, the files uploaded to Sketchfab can be downloaded directly as their original upload file type, a .blend, or as .glTf, a universal 3D file format, or USDZ, an augmented reality file type. For animation purposes, the 3D space group problems were uploaded as paired .obj/.mtl, which contain the 3D coordinates and materials respectively.

4.2.7 3D Printing: 3D printing is rapidly becoming accessible on most university campuses. The capability for 3D printing trivializes the distribution of physical teaching tools, as it eliminates the need for costly shipping. All models in this paper intended for 3D printing are available in the SI as .stl files. To reduce the cost of 3D printing, each model was made hollow to minimize the amount of 3D printing material required. These models can and will need to be scaled to fit the large variety of commercially available 3D printers.

4.2.8 Discussion

4.2.8.1 A Need for New Objects: For point group symmetry in the International Tables, Table 3.2.3.1, open circles and dots are used to denote object(s) above or below the projection plane, respectively. (*International Tables for Crystallography*, 2016) Furthermore, the space group diagrams implement circles, or circles with an inscribed comma (to denote a change in handedness), to represent symmetry operations on the asymmetric unit. While functional at showing the symmetry, the positions of these objects, and a change in chirality, this notation does not indicate directionality. Translating the circles from 2D projections into spheres for 3D models creates certain ambiguities as a sphere is too symmetric to serve as a proper placeholder for an "asymmetric unit". An example of ambiguous symmetry operations arising from a set of these symmetric symbols is shown in Figure 4. In the 2D projection (Figure 4, top), a coordinate system with a symmetry axis normal to the plane is set by the nature of the projection, and students can easily recognize the $(x, y, z) \rightarrow (\bar{x}, \bar{y}, \bar{z})$ relationship between the two points, one open, one filled. When translating this exercise to 3D, however, the two points are now represented with identical black spheres and students are able (and encouraged!) to rotate the model in any way that they like. When small black spheres are used to denote the asymmetric unit, students are rightly able to see that the two highly-symmetric objects could be related to each other by either a 2-fold axis, a mirror plane, or an inversion center. The 2D projection that the International Tables uses in Table 3.2.3.1 to denote the point group $\bar{1}$ actually has $\frac{\infty}{m}m$ symmetry when translated literally into 3-dimensions as a direct result of the spherically symmetric objects being used. (*International Tables for Crystallography*, 2016) Unambiguous 3D exercises for symmetry determination require asymmetric, chiral objects instead of achiral spheres, whereby the symmetry operations for any point symmetry can be unambiguously

determined from the arrangement of the objects alone. For this reason, we developed these 3D renderings using the chiral hand objects introduced in Figure 2.

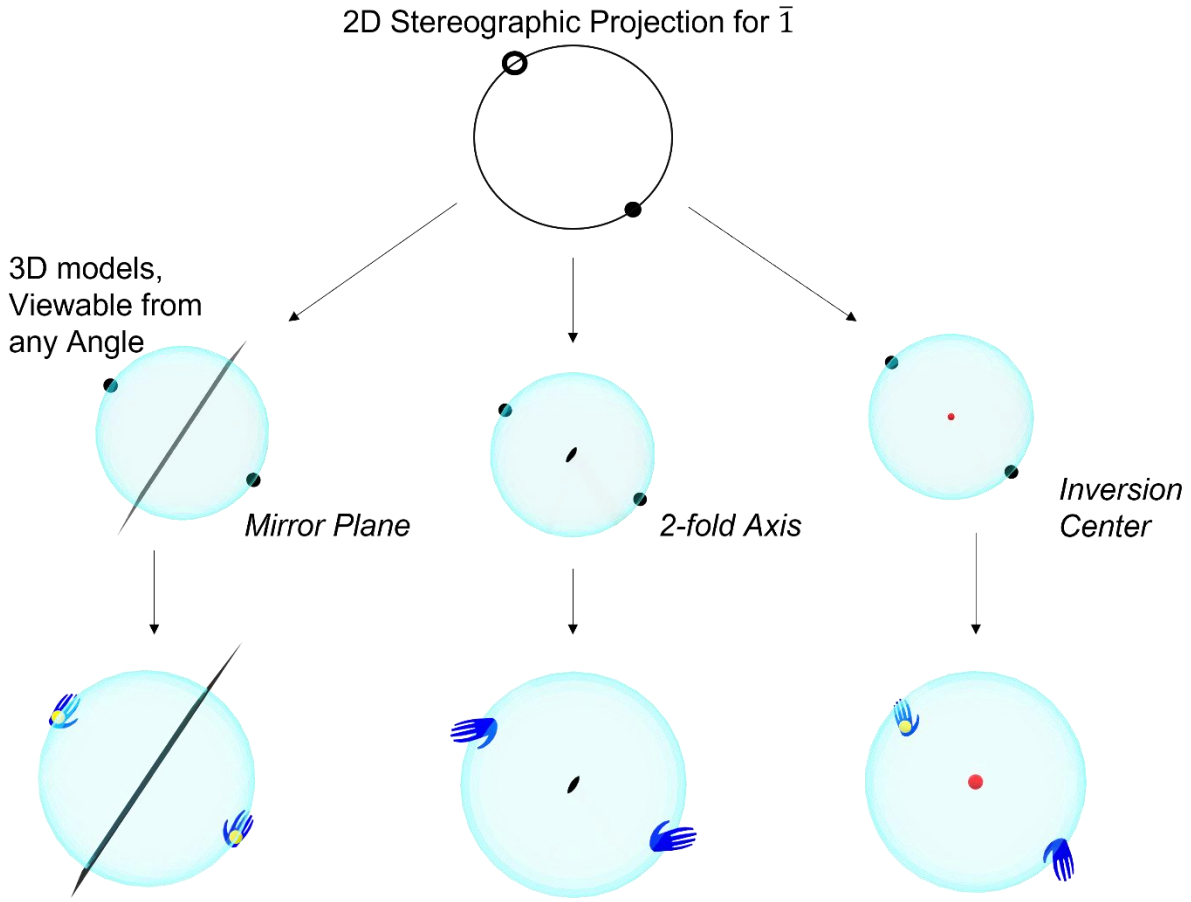

Figure 3. A depiction of how a set of the symmetric circle symbols generated from the objects used in the International Tables, Table 3.2.3.1, for point group symmetry can give rise to multiple, equally correct, interpretations of the absent symmetry operation when translated to 3D as compared to the 3D models with full asymmetric objects. By using the asymmetric hand object, ambiguity is removed and the three different symmetry operations implied by the spheres now give rise to unique diagrams (bottom). (*International Tables for Crystallography*, 2016)

4.2.9 The 3D Library

4.2.9.1 General Considerations: The models in the library described throughout this paper fall into two general classes – 3D visualization aids and 3D activities. The visualization aids provide students with a 3D representation for many of the inherently 3D concepts necessary to understand crystallographic symmetry. The 3D activities allow students to apply the understanding that they garner from the visualization aids through problem solving activities. Topics pertain to specific frequently raised student questions or common student misconceptions. Some of these topics include: why the stereographic projections for cubic groups have curved lines for mirror planes, the difference between 4_1 and 4_3 screw axes, and the obverse vs. reverse rhombohedral centerings. This library of models capitalizes on our existing experience in combining Blender, chemistry education, and Sketchfab.(Aristov *et al.*, 2021) These models are further described in Table 1.

4.2.9.2 Example Models: Symmetry is a foundational topic in crystallography, and its presentation differs from how the topic is introduced in chemistry courses. The use of Hermann-Mauguin definitions in crystallography as opposed to Schönflies definitions in the chemistry context can cause potential confusion for students. A striking example is the handling of improper rotation axes, which are defined as roto-inversion axes in the Hermann-Mauguin system and as roto-reflections in the Schönflies system. To help teach this topic, we created a model for each of the 32-crystallographic point groups. These models contain a semi-transparent sphere to represent the stereographic projection of the objects, the hands with coins, to represent the chiral objects, and the various symmetry elements representative of the group. For space groups, we have modeled many of the lower-symmetry systems. These include all triclinic and monoclinic, as well as some selected higher symmetry systems. Each of these models by default

has color coded axes and a black outline to denote the unit cell, and the hands with coins are used to represent the chiral object. Additionally, by switching from "static pose" to "display symmetry elements", an option available in the bottom left of the UI on the browser based Sketchfab website, the various symmetry elements representative of the group will be displayed. Example images of these types of 3D depictions can be found in Table 1.

Table 1. Selected models currently freely available on Sketchfab. Each entry is accompanied by the model's title as found on Sketchfab, a direct link, a short description, and a snapshot taken of the model or animation.

	Description	Snapshot
Symmetry Elements		
Crystallographic Translational Symmetry (Orth) https://skfb.ly/o7YQq	An animation showing how translation generates symmetry related objects in adjacent unit cells in an orthorhombic system.	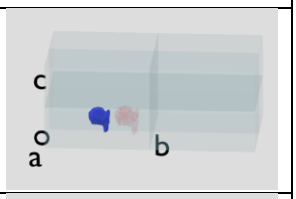
Crystallographic Translational Symmetry (tri) https://skfb.ly/o7YQo	An animation showing how translation generates symmetry related objects in adjacent unit cells in a triclinic system.	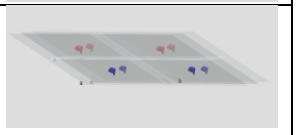
Crystallographic rotation axes https://skfb.ly/o7YPZ	An animation comparing the 2-fold, 3-fold, 4-fold, and 6-fold rotational symmetry axes all side-by-side. This animation shows how the operation generates the symmetry related objects.	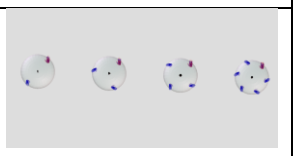
Symmetry: Mirror Plane https://skfb.ly/o7YPX	An animation showing how a mirror plane operates on an object to generate its symmetry related counterpart.	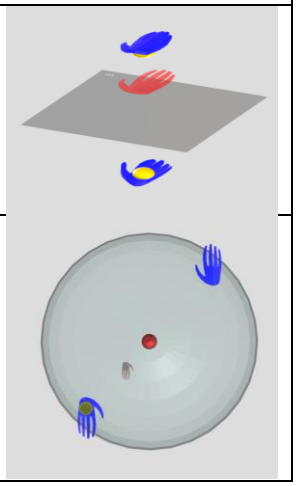
Symmetry: Inversion center https://skfb.ly/o7YQu	An animation showing how an inversion center operates on an object to generate its symmetry related counterpart.	

Symmetry: Roto-inversion https://skfb.ly/o7YQx	An animation showing how a Roto-inversion operates on an object to generate its symmetry related counterpart.	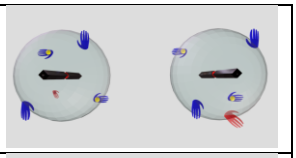
2_1 Screw Axis https://skfb.ly/o7YQC	An animation showing how the 2_1 screw axis acts on an object to generate symmetry related counterparts.	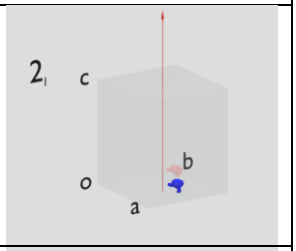
4_1 and 4_3 Screw Axes https://skfb.ly/o7YQE	An animation comparing how the 4_1 and 4_3 screw axes act on an object to generate symmetry related counterparts. The animation shows both operations happening simultaneously side-by-side to emphasize how the counter-clockwise and clockwise arrangements for the objects are generated.	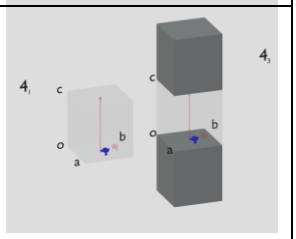
Crystallographic b-Glide Plane https://skfb.ly/o7NsH	An animation showing how the b-glide acts on an object to generate symmetry related objects in subsequent unit cells.	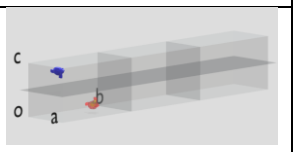
Symmetry Progression for 2/m https://skfb.ly/o7YQJ	An animation showing how the 2/m point group can be constructed by applying sequential symmetry operations through three different routes.	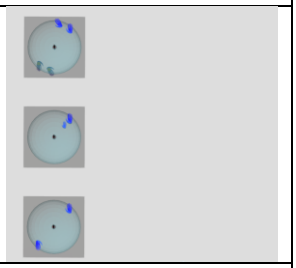
Unit Cells		
The 14 crystallographic unit cells https://skfb.ly/o7Oxp	A static model showing all 14-unit cells along with their cell definitions.	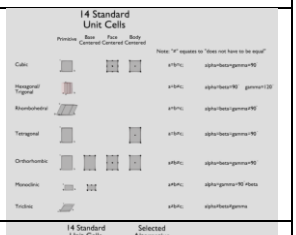
Selected Alternative Settings for Unit Cells https://skfb.ly/o7YQO	A static model showing the 14-unit cells and 3 alternative settings for the standard unit cells. Specifically, obverse and reverse are shown for rhombohedral and the body centered setting for monoclinic.	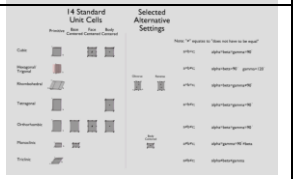

Bravais lattices (collection) https://skfb.ly/ooY6s	A collection of models, each one showing one of the 14 standard setting Bravais lattices with cell definitions.	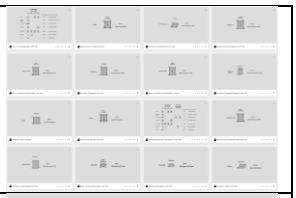
Unit cells for a given lattice https://skfb.ly/o7YQR	A static model showing how several different unit cells can all be drawn within a single lattice.	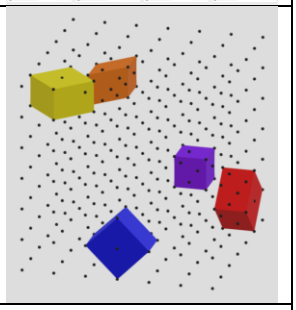
Stereographic Projections		
Why Cubic Groups have "Curved" Mirror Planes https://skfb.ly/o7YQV	An animation showing how the mirror planes in a cubic space group give rise to a "curved" plane in the related stereographic projection.	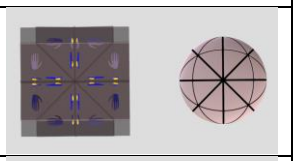
Stereographic projection of a house https://skfb.ly/o7YQY	An animation showing how the stereographic projection for a simple house is generated. These models were inspired by Walter Borchardt-Ott's Crystallography. (Borchardt-Ott, 1993)	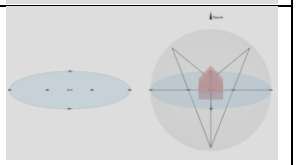
Stereographic projection of a sideways house https://skfb.ly/o7YRn	An animation showing how the stereographic projection for a house rotated onto its side is generated. These models were inspired by Walter Borchardt-Ott's Crystallography. (Borchardt-Ott, 1993)	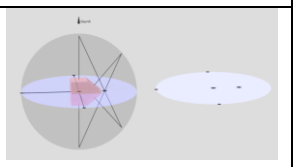
Stereographic Projection Example https://skfb.ly/o7YRp	An animation showing how the stereographic projection for an orthorhombic shape is generated. These models were inspired by Walter Borchardt-Ott's Crystallography. (Borchardt-Ott, 1993)	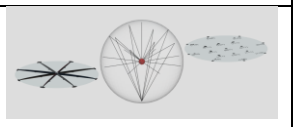
Crystallographic Point Groups		
Crystallographic point groups (collection) Tag: Stereographic_Projection	This collection contains a simple model for each of the 32-point groups. All models in this set include a 3D representation of their respective symmetry elements. These models are all titled "Stereographic projection: *Hermann-Mauguin*", where "Hermann-Mauguin" is replaced with the corresponding symbol of the point group. All models include the tag	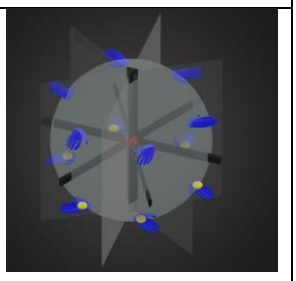

(Direct links for each model can be found in the SI)	"Hermann-Maguguin", "Stereographic_Projection", and "crystallography_education".	
Crystallographic Space Groups		
Crystallographic Space groups (collection) Tag: Space_group (Direct links for each model can be found in the SI)	This collection contains a simple model for selected space groups. These include all triclinic and monoclinic groups, as well as the more frequently observed higher symmetry groups. All models in this set have a 3D representation of their respective symmetry elements. A total of 15 space groups were modeled.	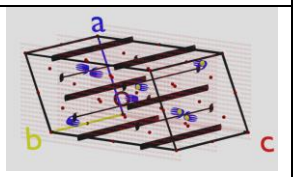
P2/c Symmetry Progression https://skfb.ly/orvnX	An animation showing one possible route to generating the objects in the *P*2/*c* space group. This animation first applies a 2-fold rotation, then an inversion, then the *c*-glide plane.	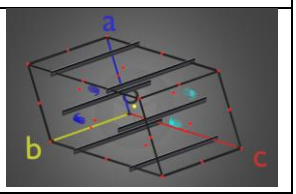
Miller Indecies		
Miller Indices Expansion https://skfb.ly/orDDR	An animation showing how the faces of a crystal can be expanded to intersect with a coordinate system. These points of intersection are used to determine the face index.	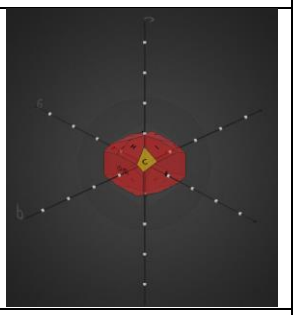
Instrumentation		
Single Crystal Diffractometer https://skfb.ly/oqoKq	An animation of a single crystal diffractometer. The instrument is built roughly to scale with the purpose of demonstrating the size of crystal needed for a data collection. Many parts of the instrument are animated and annotated to provide additional information.	

4.2.10 Crystallography Activities: Many of the activities provided in this 3D library were created with the intent for students to tackle them collaboratively in small groups of 3-4, and many have been tested successfully in this mode. The versatility of Sketchfab allows students to easily access the 3D models either on smartphones through the official Sketchfab application or through a provided web browser link. These links can be emailed to the students beforehand,

added to a course web page, or built into printable QR codes. The specific problems and student expectations are described below.

4.2.10.1 Unit Cell Problems: The unit cell problems each contain a single labeled unit cell that is initially randomly oriented and can be reoriented subsequently through student interaction. The goal of the problem is for the students to determine the centering and type of each unit cell. A total of 15 problems were created; one for each of the 14 standard Bravais lattice settings with an additional nonstandard monoclinic cell added for additional challenge. These problems are labeled "Unit Cell Practice x" where x goes from 1-15, and they can all be found through the "unit_cell_practice" tag. Solutions to these problems are provided in the SI. Links to these problems are provided in the SI.

4.2.10.2 Point Group Problems: The point group problems are designed for students to find symmetry elements and determine the overall point group of a symmetric array of 3D objects. Each problem consists of a set of hands positioned around a sphere with no other symmetry elements present; this problem is meant to integrate well with an exposition of the crystallographic point groups using stereographic projections. One problem exists for each of the 32-point groups, and they are titled "Stereographic Projection Problem x", where x goes from 1 to 32, and they can all be found through the "point_group_practice" tag. Solutions to these problems are provided in the SI. Links to these problems are provided in the SI. We have found that a group of 3-4 students working together can reasonably solve 3-4 of these problems in a 15-minute period.

4.2.10.3 Space Group Problems: The space group problems each contain a unit cell with a set of symmetry related objects but no labeled symmetry elements. The goal of these problems is for students to identify the space group represented. All of these problems can easily be found by using the "space_group_practice" tag. These problems have proven to take more time to solve as higher symmetry unit cells are introduced. For that reason, we recommend starting with triclinic or primitive monoclinic space groups. Currently, problems exist for all triclinic and monoclinic space groups as well as some selected higher symmetry systems. Solutions to all space group problems can be found in the SI. Links to these problems are provided in the SI.

4.2.10.4 Block Problems: A legacy problem set on point groups for our department consists of a collection of wooden blocks from the Krantz geological Warehouse that were created to depict crystal shapes of various types.(Krantz) These wooden blocks were given to students for problem sets or exams who were asked to determine the point group of the shape. To preserve and modernize these exercises, as the blocks have become worn through many years of use, and to further distribute them, the shapes of these wooden blocks along with a few other shapes have been recreated in Blender, uploaded to Sketchfab, and converted into a 3D printing compatible file format (.stl). Examples of the printed blocks can be seen in figure 4. The online versions of these block problems are labeled "Block n" where n goes from 1 to 29, and these names match the 3D file names found in the SI. All of these problems can easily be found by using the "block_problem" tag. The solutions to these problems are listed in the SI. Links to these problems are provided in the SI. Each block contains a number cut-out on one face to help differentiate them after they have been printed. This letter should not be considered when trying to determine the point group of the object.

Figure 4. The 3D printed versions of the blocks. These were printed using ivory color. The 3D printing files have since been modified to fix inhomogeneity in block size.

4.2.10.5 Miller Indices Problem: The Miller indices problems contain five models of an idealized crystal shapes with multiple facets. Two faces of the shape are labeled as (100) and (010) while the remaining faces are labeled with letters. The goal of this problem is for the students to analyze the shape and determine the crystal system, point group, and Miller indices for each of the lettered faces. This assignment is available either via the online model or as a 3D printed version, which is more satisfying to work with. These problems can be found by using the "miller_index" tag. The solutions to these problems are listed in the SI. Links to these problems are provided in the SI.

4.2.11 Conclusion: Blender offers a simple means to generate any 3D model with a variety of animations. Through collaboration with several experienced crystallographers and students, we have used this tool to create a library of short animations and static 3D models to aid in the teaching of crystallographic symmetry. We offer downloads to many of these models in the SI of this paper, and we continue to maintain a library of the models via Sketchfab, the free browser-

based 3D model viewer. We describe methods by which we incorporate these models into crystallography education through Sketchfab's functionality across handheld smart devices. We will continue to grow this freely accessible library as we garner additional feedback and animation requests from the greater crystallography community.

4.2.12 Disclaimer: These 3d models (the "models") are made available as-is for educational purposes, and the Board of Regents of the University of Wisconsin System, its officers, employees, and agents ("UW"), makes no representations or warranties of any kind, express, implied, statutory, or other, concerning the models. UW expressly disclaims all warranties in connection with use of the models, including but not limited to warranties of fitness for a particular purpose, warranties of merchantability, and warranties of non-infringement. Users accept all risk associated with use of the models.

By using the models, you acknowledge and agree to the foregoing and waive any and all claims of any kind and description against the Board of Regents of the University of Wisconsin System, its officers, employees and agents, arising out of or in connection with your use of the models.

Supporting Information for Subchapter 4.2: A New Library of 3D Models and Problems for Teaching Crystallographic Symmetry Generated Through Blender for Use with 3D Printers or Sketchfab

Michael M. Aristov, Han Geng, Alex Pavelic**,** and John F. Berry*

Department of Chemistry, University of Wisconsin–Madison, 1101 University Ave., Madison, WI 53706

*Email: berry@chem.wisc.edu

4.2.13 Supporting Information: The included SI contains all models described in this paper. In the main folder is an excel sheet "Model Index with links", and this excel sheet contains a complete list of the models with their Sketchfab hyperlinks mentioned in this manuscript. The models themselves are subdivided into separate folders. The *Animations* folder contains all models that have animated components, like the screw-axis models. The *Block Problems* folder contains all block problems uploaded to Sketchfab, and they are named with their corresponding problem number. The *Miller index Problems* folder contains the miller index problems as uploaded to Sketchfab, an alternative .blend file that has the precursor to the 3D printable .stl file, and the 3D printable .stl file. The *Solutions* folder contains excel spreadsheets that provide the answer for all problems described in this paper. The *Space Group Problems* contain a mix of .obj/.mtl and .blend files for all space group problems uploaded to Sketchfab. The *Space Groups* folder contains all space groups with symmetry elements that were uploaded to Sketchfab. The *Stereographic Projection Point Groups* folder contains the models for all 32-point groups, and these models are named by their point group symmetry. The *Stereographic Projection Point Groups Problems* folder contains models for all of the 32-point group problems, and these

models are named by their problem number. The *Unit Cell Problems* folder contains all unit cell problems, and these models are named by their problem number. The *Unit Cells* folder contains all models for individual and composite unit cells, and each model is named based on the unit cell it displays.

Corresponding Authors
Michael M. Aristov – aristov@wisc.edu
John F. Berry – berry@chem.wisc.edu

ORCID
Michael M. Aristov**:** 0000-0003-1161-5126
Hang Geng: 0000-0002-8433-9671
Alex Pavelic: 0000-0002-5487-7540
John F. Berry: 0000-0002-6805-0640

ACKNOWLEDGMENT
We thank NSF for funding via CHE-1953294, and we thank the NSF-GRFP for funding via DGE-1747503. We also acknowledge Ilia Guzei, Christine Beavers, Xian Powers, Bruce Noll and the Crystallography Class of Spring 2020 at UW Madison for their help in creating these models.

DEDICATION
This work is dedicated in memory of Prof. Marilyn M. Olmstead and Prof. Larry F. Dahl, two of the most passionate crystallographers and educators these authors ever had the pleasure of learning from and working with. May their influence live on forever in the countless crystallographers that they have fostered.

4.2.14 References

Antonoglou, L. D., Charistos, N. D. & Sigalas, M. P. (2011). *Chem. Educ. Res. Pract.* **12**, 454-468.
Aristov, M. M., Moore, J. W. & Berry, J. F. (2021). *J. Chem. Educ.* **98**, 3032-3037.
Bazley, I. J., Erie, E. A., Feiereisel, G. M., LeWarne, C. J., Peterson, J. M., Sandquist, K. L., Oshin, K. D. & Zeller, M. (2018). *J. Chem. Educ.* **95**, 876-881.
Blender, (2020). https://www.blender.org.
Borchardt-Ott, W. (1993). *Crystallography*. Springer.
Brannon, J. P., Ramirez, I., Williams, D., Barding, G. A., Liu, Y., McCulloch, K. M., Chandrasekaran, P. & Stieber, S. C. E. (2020). *J. Chem. Educ.* **97**, 2273-2279.
Carlisle, D., Tyson, J. & Nieswandt, M. (2015). *Chem. Educ. Res. Pract.* **16**, 478-517.
Casas, L. (2018). *J. Appl. Cryst.* **51**, 901-908.
Casas, L. (2020). *J. Appl. Cryst.* **53**, 1583-1592.
Casas, L. & Estop, E. (2015). *J. Chem. Educ.* **92**, 1338-1343.

Chapuis, G. (2011). *Crystallogr. Rev.* **17**, 187-204.
Chen, L., Sun, H. & Lai, C. (2015). *J. Chem. Educ.* **92**, 1422-1425.
Cushman, C. V. & Linford, M. R. (2015). *J. Chem. Educ.* **92**, 1415-1418.
Dagnoni H., R., Vailati, A. F., Ribeiro de Laia, L., Salvador T., P. & Xavier, F. R. (2018). *J. Chem. Educ.* **95**, 1151-1155.
Duda, M., Rafalska-Łasocha, A. & Łasocha, W. (2020). *J. Chem. Educ.* **97**, 2169-2174.
Flint, E., B. (2011). *J. Chem. Educ.* **88**, 907-909.
Fuchigami, K., Schrandt, M. & Miessler, G. L. (2016). *J. Chem. Educ.* **93**, 1081-1084.
Girolami, G. S. (2016). *X-Ray Crystallography*. Wilsted & Taylor Publishing Services.
Graef, M. D. (1998). *J. Mater. Educ.*, 31-42.
Grafton, A. K. (2011). *J. Chem. Educ.* **88**, 1281-1282.
Grazulis, S., Sarjeant, A. A., Moeck, P., Stone-Sundberg, J., Snyder, T. J., Kaminsky, W., Oliver, A. G., Stern, C. L., Dawe, L. N., Rychkov, D. A., Losev, E. A., Boldyreva, E. V., Tanski, J. M., Bernstein, J., Rabeh, W. M. & Kantardjieff, K. A. (2015). *J. Appl. Cryst.* **48**, 1964-1975.
Grove, N. P., Guerin, N. P., Collins, D. J., López, J. J., Bretz, S. L. & Zhou, H. C. (2009). *J. Chem. Educ.* **86**, 946.
Hanson, R. M., Prilusky, J., Renjian, Z., Nakane, T. & Sussman, J. L. (2013). *Isr. J. Chem.* **53**, 207-216.
Hardgrove, G. L. (1997). *J. Chem. Educ.* **74**, 797.
Hitzer, E. M. S., Perwass, C. & Ichikawa, D. (2010). *Geometric Algebra Computing: in Engineering and Computer Science*, edited by E. Bayro-Corrochano & G. Scheuermann, pp. 385-400. London: Springer London.
International Tables for Crystallography, 2016). Second Online ed. Springer.
Johnston, D. H. (2021). *Symmetry Resources at Otterbein University,* https://symotter.org/.
Krantz, D. F. *Wooden-Crystal Models - Collection* https://www.krantz-online.de/en/wooden-crystal-models-collection/K15.
Luxford, C. J., Crowder, M. W. & Bretz, S. L. (2012). *J. Chem. Educ.* **89**, 211-214.
Macrae, C. F., Sovago, I., Cottrell, S. J., Galek, P. T. A., McCabe, P., Pidcock, E., Platings, M., Shields, G. P., Stevens, J. S., Towler, M. & Wood, P. A. (2020). *J. Appl. Cryst.* **53**, 226-235.
Malbrecht, B. J., Campbell, M. G., Chen, Y. S. & Zheng, S. L. (2016). *J. Chem. Educ.* **93**, 1671-1675.
Manion, J. G. (2021). CG-Figures, YouTube.
Meier, W. M. (1984). *Space Group Patterns*. University College Cardiff Press.
Meier, W. M. (2001). *14 Space Group Patterns*. Cardiff, Wales University College Cardiff Press
Paufler, P. (2007). *Complete Online set of International Tables for Crystallography, Vols. A-G.* .
Penny, M. R., Cao, Z. J., Patel, B., Sil dos Santos, B., Asquith, C. R. M., Szulc, B. R., Rao, Z. X., Muwaffak, Z., Malkinson, J. P. & Hilton, S. T. (2017). *J. Chem. Educ.* **94**, 1265-1271.
Pettersen, E. F., Goddard, T. D., Huang, C. C., Couch, G. S., Greenblatt, D. M., Meng, E. C. & Ferrin, T. E. (2004). *J. Comput. Chem.* **25**, 1605-1612.
The PyMOL Molecular Graphics System (2021). Schrödinger, LLC.
Rodenbough, P. P., Vanti, W. B. & Chan, S. W. (2015). *J. Chem. Educ.* **92**, 1960-1962.
Ruiz, G. N. & Johnstone, T. C. (2020). *J. Chem. Educ.* **97**, 1604-1612.
Savchenkov, A. V. (2020). *J. Chem. Educ.* **97**, 1682-1687.
Scalfani, V. F. & Vaid, T. P. (2014). *J. Chem. Educ.* **91**, 1174-1180.
Sketchfab, (2021). https://sketchfab.com/.
Southam, D. C. & Lewis, J. E. (2013). *J. Chem. Educ.* **90**, 1425-1432.
Stroz, K. (1997). *J. Appl. Cryst.* **30**, 178-181.
Stróż, K. (2003). *Z. Kristallogr. Cryst. Mater* **218**, 642-649.
Tuvi-Arad, I. & Blonder, R. (2010). *Chem. Educ. Res. Pract.* **11**, 48-58.
Winter, M. (2021). *The Orbitron,* https://winter.group.shef.ac.uk/orbitron/.

4.2.15 Additional Supporting Information

All models and animations described in this publication are available for download as a .bin from https://doi.org/10.1107/S1600576721013236/oc5017sup1.bin.

Space Group Models	
Space Group: P1	https://skfb.ly/o7Q9Z
Space Group: P-1	https://skfb.ly/orovG
Space Group: P2	https://skfb.ly/o7LRN
Space Group: $P2_1$	https://skfb.ly/o7LSz
Space Group: C2	https://skfb.ly/o7LSH
Space Group: Pm	https://skfb.ly/o7LST
Space Group: Pc	https://skfb.ly/o7LTw
Space Group: Cm	https://skfb.ly/o7NsY
Space Group: Cc	https://skfb.ly/o7Ntw
Space Group: P2m	https://skfb.ly/o7NtU
Space Group: $P2_1/m$	https://skfb.ly/o7N96
Space Group: C2/m	https://skfb.ly/o7N9x
Space Group: P2/c	https://skfb.ly/o7N9E
Space Group: $P2_1/c$	https://skfb.ly/o7N9V
Space Group: C2/c	https://skfb.ly/o7Nu9

Space Group Problems	
Space Group Practice 1	https://skfb.ly/oqnXD
Space Group Practice 2	https://skfb.ly/oqnXI
Space Group Practice 3	https://skfb.ly/oq67T
Space Group Practice 4	https://skfb.ly/oq67X
Space Group Practice 5	https://skfb.ly/oq6qn
Space Group Practice 6	https://skfb.ly/oq6qq
Space Group Practice 7	https://skfb.ly/oq6qs
Space Group Practice 8	https://skfb.ly/oq6q9
Space Group Practice 9	https://skfb.ly/oq6qw
Space Group Practice 10	https://skfb.ly/oqqGp
Space Group Practice 11	https://skfb.ly/oqqGr
Space Group Practice 12	https://skfb.ly/oqqGJ
Space Group Practice 13	https://skfb.ly/oqqGL
Space Group Practice 14	https://skfb.ly/oqqGO
Space Group Practice 15	https://skfb.ly/oqqGQ
Space Group Practice 16	https://skfb.ly/oqqGV
Space Group Practice 17	https://skfb.ly/oqqH6

Space Group Practice 18 https://skfb.ly/oqqHo

Miller Indices Problems	
Miller Indices Problem 1	https://skfb.ly/o7PGT
Miller Indices Problem 2	https://skfb.ly/o7Kwn
Miller Indices Problem 3	https://skfb.ly/orwKL
Miller Indices Problem 4	https://skfb.ly/orwKM
Miller Indices Problem 5	https://skfb.ly/orwKN

Stereographic Projection Problems	
Stereographic Projection Problem 1	https://skfb.ly/o7Ctx
Stereographic Projection Problem 2	https://skfb.ly/o7CtB
Stereographic Projection Problem 3	https://skfb.ly/o7CtE
Stereographic Projection Problem 4	https://skfb.ly/o7CtI
Stereographic Projection Problem 5	https://skfb.ly/o7CtX
Stereographic Projection Problem 6	https://skfb.ly/o7CtY
Stereographic Projection Problem 7	https://skfb.ly/o7C9n
Stereographic Projection Problem 8	https://skfb.ly/o7C97
Stereographic Projection Problem 9	https://skfb.ly/o7C9t
Stereographic Projection Problem 10	https://skfb.ly/o7C9w
Stereographic Projection Problem 11	https://skfb.ly/o7C9z

Stereographic Projection Problem 12	https://skfb.ly/o7C9B
Stereographic Projection Problem 13	https://skfb.ly/o7C9D
Stereographic Projection Problem 14	https://skfb.ly/o7C9F
Stereographic Projection Problem 15	https://skfb.ly/o7C9K
Stereographic Projection Problem 16	https://skfb.ly/o7Cuo
Stereographic Projection Problem 17	https://skfb.ly/o7Cu8
Stereographic Projection Problem 18	https://skfb.ly/o7Cut
Stereographic Projection Problem 19	https://skfb.ly/o7Cuz
Stereographic Projection Problem 20	https://skfb.ly/o7CuC
Stereographic Projection Problem 21	https://skfb.ly/o7CuF
Stereographic Projection Problem 22	https://skfb.ly/o7CuI
Stereographic Projection Problem 23	https://skfb.ly/o7CuN
Stereographic Projection Problem 24	https://skfb.ly/o7CuW
Stereographic Projection Problem 25	https://skfb.ly/o7Cvo

Stereographic Projection Problem 26	https://skfb.ly/o7Cvr
Stereographic Projection Problem 27	https://skfb.ly/o7Cvv
Stereographic Projection Problem 28	https://skfb.ly/o7Cvx
Stereographic Projection Problem 29	https://skfb.ly/o7CvD
Stereographic Projection Problem 30	https://skfb.ly/o7CvG
Stereographic Projection Problem 31	https://skfb.ly/o7CvK
Stereographic Projection Problem 32	https://skfb.ly/o7CvL

Stereographic Projection Point Groups

Stereographic Projection: 1	https://skfb.ly/o7BNP
Stereographic Projection: -1	https://skfb.ly/o7BOq
Stereographic Projection: 2	https://skfb.ly/o7BO9
Stereographic Projection: m	https://skfb.ly/o7BOH
Stereographic Projection: 2/m	https://skfb.ly/o7BOQ
Stereographic Projection: 222	https://skfb.ly/o7BOW
Stereographic Projection: mm2	https://skfb.ly/o7BOY

Animations

Single Crystal Diffractometer	https://skfb.ly/oqoKq
Stereographic Projection Example	https://skfb.ly/o7YRp
Stereographic projection of a house	https://skfb.ly/o7YQY
Stereographic projection of a sideways house	https://skfb.ly/o7YRn
Why Cubic Groups have "Curved" Mirror Planes	https://skfb.ly/o7YQV
Crystallographic rotation axes	https://skfb.ly/o7YPZ
Symmetry: Mirror Plane	https://skfb.ly/o7YPX

Stereographic Projection: mmm	https://skfb.ly/o7BPq
Stereographic Projection: 4	https://skfb.ly/o7BPy
Stereographic Projection: -4	https://skfb.ly/o7BPH
Stereographic Projection: 4/m	https://skfb.ly/o7BPQ
Stereographic Projection: 422	https://skfb.ly/o7BQn
Stereographic Projection: 4mm	https://skfb.ly/o7BQr
Stereographic Projection: -42m	https://skfb.ly/o7BQw
Stereographic Projection: 4/mmm	https://skfb.ly/o7BRt
Stereographic Projection: 3	https://skfb.ly/o7BRC
Stereographic Projection: -3	https://skfb.ly/o7BRH
Stereographic Projection: 32	https://skfb.ly/o7BRQ
Stereographic Projection: 3m	https://skfb.ly/o7BSn
Stereographic Projection: -3m	https://skfb.ly/o7BSt
Stereographic Projection: 6	https://skfb.ly/o7BSx
Stereographic Projection: -6	https://skfb.ly/o7BSF
Stereographic Projection: 6/m	https://skfb.ly/o7BSM
Stereographic Projection: 622	https://skfb.ly/o7BSV
Stereographic Projection: 6mm	https://skfb.ly/o7BTs
Stereographic Projection: -6m2	https://skfb.ly/o7BTP

Symmetry: Inversion Center	https://skfb.ly/o7YQu
Symmetry: Roto-inversion	https://skfb.ly/o7YQx
2_1 Screw Axis	https://skfb.ly/o7YQC
4_1 and 4_3 Screw Axes	https://skfb.ly/o7YQE
Crystallographic b-Glide Plane	https://skfb.ly/o7NsH
Crystallographic Translational Symmetry (tri)	https://skfb.ly/o7YQo
Crystallographic Translational Symmetry (Orth)	https://skfb.ly/o7YQq
Symmetry Progression for 2/m	https://skfb.ly/o7YQJ
1>2>4>4/m Symmetry Progression	https://skfb.ly/orwLO
P2/c Symmetry Progression	https://skfb.ly/orvnX
Miller Indices Expansion	https://skfb.ly/orDDR

Stereographic Projection: 6/mmm	https://skfb.ly/o7BTU
Stereographic Projection: 23	https://skfb.ly/o7BUn
Stereographic Projection: m-3	https://skfb.ly/o7BU8
Stereographic Projection: 432	https://skfb.ly/o7BUA
Stereographic Projection: -43m	https://skfb.ly/o7BUK
Stereographic Projection: m-3m	https://skfb.ly/o7BUO

Block Problems	
Block 1	https://skfb.ly/o7ICo
Block 2	https://skfb.ly/o7ICq
Block 3	https://skfb.ly/o7IC8
Block 4	https://skfb.ly/o7ICt
Block 5	https://skfb.ly/o7ICv
Block 6	https://skfb.ly/o7ICA
Block 7	https://skfb.ly/o7ICF
Block 8	https://skfb.ly/o7ICL
Block 9	https://skfb.ly/o7ICM
Block 10	https://skfb.ly/o7ICN
Block 11	https://skfb.ly/o7ICQ
Block 12	https://skfb.ly/o7ICT
Block 13	https://skfb.ly/o7ICW

Unit Cells	
The 14 crystallographic unit cells	https://skfb.ly/o7Oxp
The 14 crystallographic unit cells CV	https://skfb.ly/o6IqB
Selected Alternative Settings for Unit Cells	https://skfb.ly/o7YQO
Primitive Triclinic Unit Cell	https://skfb.ly/orouU
Primitive Monoclinic Unit Cell	https://skfb.ly/orovA
Base-Centered Monoclinic Unit Cell	https://skfb.ly/orowB
Base-Centered Monoclinic Unit Cell	https://skfb.ly/orovB
Base-Centered Orthorhombic Unit Cell	https://skfb.ly/orovL
Face-Centered Orthorhombic Unit cell	https://skfb.ly/orowD
Primitive Tetragonal Unit Cell	https://skfb.ly/orovC
Body-Centered Orthorhombic Unit Cell	https://skfb.ly/orouX
Body-Centered Tetragonal Unit Cell	https://skfb.ly/orowE
Primitive Rhombohedral Unit Cell	https://skfb.ly/oqQKU

Block 14	https://skfb.ly/o7ICX
Block 15	https://skfb.ly/o7IDo
Block 16	https://skfb.ly/o7IDx
Block 17	https://skfb.ly/o7IDy
Block 18	https://skfb.ly/o7IDF
Block 19	https://skfb.ly/o7IDG
Block 20	https://skfb.ly/o7IDI
Block 21	https://skfb.ly/o7IDN
Block 22	https://skfb.ly/o7IDQ
Block 23	https://skfb.ly/o7IDS
Block 24	https://skfb.ly/o7IDU
Block 25	https://skfb.ly/o7IDW
Block 26	https://skfb.ly/o7IDX
Block 27	https://skfb.ly/o7IEp
Block 28	https://skfb.ly/o7IE8
Block 29	https://skfb.ly/o7IEs

Primitive Hexagonal/Trigonal Unit Cell	https://skfb.ly/oqyn7
Primitive Cubic Unit Cell	https://skfb.ly/o7HME
Face-Centered Cubic Unit Cell	https://skfb.ly/orovn
Body-Centered Cubic Unit Cell	https://skfb.ly/orouW

Unit Cell Problems

Unit Cell Practice 1	https://skfb.ly/orouF
Unit Cell Practice 2	https://skfb.ly/orowF
Unit Cell Practice 3	https://skfb.ly/orouD
Unit Cell Practice 4	https://skfb.ly/orouH
Unit Cell Practice 5	https://skfb.ly/orouR
Unit Cell Practice 6	https://skfb.ly/orowv
Unit Cell Practice 7	https://skfb.ly/orouO

Unit Cell Practice 8	https://skfb.ly/orowV
Unit Cell Practice 9	https://skfb.ly/orowW
Unit Cell Practice 10	https://skfb.ly/orovx
Unit Cell Practice 11	https://skfb.ly/orowX
Unit Cell Practice 12	https://skfb.ly/orowY
Unit Cell Practice 13	https://skfb.ly/oroww
Unit Cell Practice 14	https://skfb.ly/orowx
Unit Cell Practice 15	https://skfb.ly/orowU

Tags

Crystallography_Activities	https://sketchfab.com/tags/crystallography_activities
Crystallography_Education	https://sketchfab.com/tags/crystallography_education
Space_group	https://sketchfab.com/tags/space_group
Space_Group_Practice	https://sketchfab.com/tags/space_group_practice
Block_Problem	https://sketchfab.com/tags/block_problem
Stereographic_Projection	https://sketchfab.com/tags/stereographic_projection
Point_Group_Practice	https://sketchfab.com/tags/point_group_practice
Unit_Cell	https://sketchfab.com/tags/unit_cell
Unit_Cell_Practice	https://sketchfab.com/tags/unit_cell_practice
Miller_Index	https://sketchfab.com/tags/miller_index